TECHNISCHE UNIVERSITÄT MÜNCHEN
Lehrstuhl für Numerische Mechanik

A Finite Element Model for the Human Red Blood Cell

Thomas Klöppel

Vollständiger Abdruck der von der Fakultät für Maschinenwesen der Technischen Universität München zur Erlangung des akademischen Grades eines

Doktor-Ingenieurs (Dr.-Ing.)

genehmigten Dissertation.

Vorsitzender: Univ.-Prof. Dr. rer. nat. Tim C. Lüth

Prüfer der Dissertation:

1. Univ.-Prof. Dr.-Ing. Wolfgang A. Wall
2. Univ.-Prof. Marek Behr, Ph. D.,
   Rheinisch-Westfälische Technische Hochschule Aachen

Die Dissertation wurde am 3. Mai 2012 bei der Technischen Universität München eingereicht und durch die Fakultät für Maschinenwesen am 17. Juli 2012 angenommen.

Abstract

The human red blood cell (RBC, erythrocyte) has become a topic of intensive scientific research in the past decades. The interest in this cell is mainly motivated by three important aspects. First, the mechanical properties of erythrocytes govern the macroscopic rheological behavior of human blood. Second, certain diseases could be shown to alter the mechanical characteristics of the cell significantly. Finally, hemolysis, which is characterized by cell damaging due to external mechanical loading, is the limiting factor for the successful long-term application of artificial blood pumps.

The present work shows the development of a comprehensive numerical model for the human RBC and for its interaction with the surrounding blood plasma. Such a model is necessary in order to evaluate and interpret experimental results. None of the existing numerical models in literature accounts for all the key features of the erythrocyte and certain experimental observations could not be reproduced numerically so far. One objective of this work is, thus, to identify and explain the consequences of an incomplete numerical cell model.

A single RBC can be viewed as a biconcave vesicle, which is a biological, two-layer composite membrane enclosing a concentrated hemoglobin solution. In the present development, accurate continuum mechanical descriptions of the membrane and the fluid fields on the inside and on the outside are derived. Both membrane layers are addressed individually and realistic constitutive models for the fluid-like outer lipid bilayer and for the underlying elastic cytoskeleton network are introduced.

Moreover, a tailored numerical implementation of the mechanical model is presented. State-of-the-art finite element formulations are used to discretize the membrane and the fluid fields. To remedy the ill-conditioning problem resulting from the thinness of the cell membrane, a scaled thickness conditioning approach has been devised. Further, a novel dual mortar based monolithic fluid-structure interaction scheme is proposed that allows to reposition the fluid grid nodes at the interface to avoid fluid mesh distortion due to the rotation of the membrane.

The numerical RBC model is validated with static and dynamic laser trap experiments. The simulation results are in excellent agreement with experimental data found in the literature. Furthermore, the flexibility of the model allows to identify the shortcomings of existing numerical models. The results demonstrate the necessity of realistic boundary conditions and modeling assumptions.

Simulations of RBCs in shear flow do not only accurately predict tumbling and tank-treading, but, for the first time, also the swinging motion of human erythrocytes in moderate shear flow can be reproduced. The ability of the numerical model to recover this behavior can conclusively be attributed to residual stresses in the membrane for the cell at rest, which are not accounted for by any other available numerical model.

Zusammenfassung

Die menschliche rote Blutzelle (RBC, Erythrozyt) ist seit einigen Jahrzehnten Gegenstand intensiver wissenschaftlicher Forschung. Das Interesse an der Zelle lässt sich hauptsächlich anhand dreier Aspekte begründen. Erstens bestimmen die mechanischen Eigenschaften der Erythrozyten die rheologischen Eigenschaften menschlichen Bluts. Zweitens gehen bestimmte Krankheiten einher mit einer messbaren Änderung der mechanischen Eigenschaften der Zelle. Schließlich wird der klinische Einsatz von künstlichen Blutpumpen von der so genannten Hämolyse beschränkt, die auf eine Schädigung der roten Bluttzellen aufgrund äußerer Belastungen zurückzuführen ist.

In der vorliegenden Arbeit wird die Entwicklung eines umfassenden numerischen Modells für den menschlichen Erythrozyten und dessen Wechselwirkung mit dem umgebenden Blutplasma präsentiert. Ein solches Model ist unverzichtbar bei der Auswertung und Interpretation von experimentellen Ergebnissen. Keines der bereits existierenden numerischen Modelle berücksichtigt alle kennzeichnenden mechanischen Eigenschaften der Zelle. Daher konnten bestimmte experimentelle Ergebnisse bislang von keiner numerischen Simulation reproduziert werden. Folglich ist ein Ziel dieser Arbeit, die Auswirkungen einer unvollständigen Modellbeschreibung zu benennen und zu erklären.

Eine einzelne Blutzelle kann als bikonkaves Vesikel aufgefasst werden, das aus einer biologischen, aus zwei Schichten zusammengesetzten Membran und der von ihr eingeschlossenen konzentrierten Hämoglobinlösung besteht. Bei der vorliegenden Modellentwicklung wird zunächst eine präzise, kontinuum-mechanische Beschreibung der Membran und der Fluidgebiete innerhalb und außerhalb der Membran hergeleitet. Hierbei werden beide Schichten der Membran getrennt betrachtet. Sowohl für die fluidartige Lipid-Doppelschicht als auch für das elastische Zytoskelett werden passende Konstitutivmodelle eingeführt.

Darüber hinaus präsentiert diese Arbeit eine maßgeschneiderte numerische Umsetzung der mechanischen Modellierung. Moderne finite Element Formulierung finden Verwendung um die Membran und die Fluide zu diskretisieren. Um das aufgrund der Dünnwandigkeit der Membran auftretende Konditionierungsproblem zu lösen, wurde ein ‘Scaled Thickness Conditioning’ genannter Vorkonditionierungsansatz entwickelt. Außerdem wird ein neuartiges auf der dualen Mortar-Methode basierendes monolithisches Verfahren zur Simulation von Fluid-Struktur Wechselwirkung vorgeschlagen, welches auch große Rotation der Membran durch Neupositionierung der Fluidknoten am Interface erlaubt.

Validierung des numerischen Zellmodells erfolgt anhand von statischen und dynamischen Experimenten mit optischen Fallen. Die Simulationsergebnisse zeigen eine hervorragende Übereinstimmung mit Literaturdaten. Aufgrund seiner Flexibilität kann das Modell außerdem verwendet werden um die Nachteile bestehender numerische Modelle zu identifizieren. In den Simulationen zeigt sich die Wichtigkeit von realistischen Randbedingungen und Modellannahmen.

Die Simulationen einer Zelle im Scherfluss zeigen nicht nur ‘Tumbling’ and ‘Tank-Treading’. Zum ersten Mal, kann auch ‘Swinging’ bei einem numerischen Modell

beobachtet werden. Die Fähigkeit dieses Verhalten wiederzugeben, kann eindeutig auf einen Vorspannungszustand in der Membran in der Ruhelage zurückgeführt werden. Diese Vorspannung wird von keinem anderen bereits existierenden numerischen Model berücksichtigt.

Danksagung

Zu Beginn möchte ich mich bei allen bedanken, die mich unterstützt und so diese Arbeit erst ermöglicht haben.

Der größte Dank gebührt meinem Doktorvater, Herrn Prof. Wolfgang A. Wall, für die Anregung zu dieser Arbeit, die Betreuung und sein Vertrauen. Seine Art den Lehrstuhl für Numerische Mechanik zu führen und zu entwickeln und vor allem seine Leidenschaft für die Forschung haben mich stark geprägt und stets motiviert.

Mein Dank gilt auch den weiteren Mitgliedern der Prüfungskomission, Herrn Prof. Marek Behr für die Übernahme des Mitberichts und Herrn Prof. Tim Lüth für die Übernahme des Vorsitzes.

Einen großen Beitrag zum Gelingen dieser Arbeit haben auch die aktuellen und ehemaligen Mitglieder des Lehrstuhls, denen ich herzlich für die tolle Arbeitsatmosphäre und die vielen interessanten Diskussionen danke. Vor allem bei Dr. Burkhard Bornemann, Dr. Moritz Frenzel, Dr. Ulrich Küttler, Dr. Peter Gamnitzer, Dr. Lena Yoshihara, Alexander Popp, Georg Bauer und Prof. Michael Gee möchte ich mich für die großartige Zusammenarbeit und Freundschaft bedanken.

Schließlich danke ich auch meinen Eltern, die immer an mich geglaubt haben, und meiner Frau, Tine Brülle, für die Geduld und Unterstützung während der letzten Jahre. Ohne diese wäre die vorliegende Arbeit undenkbar.

Thomas Klöppel

Contents

Nomenclature

Acronyms

AFM	atomic force microscope.
ALE	arbitrary Lagrangean-Eulerian.
AMG	algebraic multigrid.
ANS	assumed natural strain.
BI	boundary integral.
DAE	differential algebraic equation.
DOF	degree of freedom.
DPD	dissipative particle dynamics.
EAS	enhanced assumed strain.
FE	finite element.
FEM	finite element method.
FSI	fluid-structure interaction.
IFEM	immersed finite element method.
LBB-condition	Ladyzhenskaya-Babuska-Brezzi-condition.
LSIC	least-squares incompressibility constraint.
MPCD	multiparticle collision dynamics.
NURBS	non-uniform rational B-splines.
ODE	ordinary differential equation.
PDE	partial differential equation.
PSPG	pressure stabilized Petrov-Galerkin.
RBC	red blood cell.
SDC	scaled director conditioning.
STC	scaled thickness conditioning.
SUPG	streamwise upwind Petrov-Galerkin.
XFEM	extended finite element method.

General style for scalars, tensors, and matrices

q	general notation for a scalar quantity.
$\mathbf{f}$, $\mathbf{T}$	general notation for a vector and a tensor.
$\underline{\mathbf{f}}$, $\underline{\underline{\mathbf{T}}}$	matrix representation of a vector $\mathbf{f}$ and a tensor $\mathbf{T}$.

Mappings, domains, boundaries, and coordinate systems

$\Omega_{\mathbf{X}}$	initial domain.
$\Omega_{\mathbf{x}}(t)$	current domain.
$\Omega_{\boldsymbol{\chi}}(t)$	reference domain.
$\boldsymbol{\varphi}$	particle motion mapping between $\Omega_{\mathbf{X}}$ and $\Omega_{\mathbf{x}}(t)$.
$\boldsymbol{\Phi}$	motion mapping between $\Omega_{\boldsymbol{\chi}}(t)$ and $\Omega_{\mathbf{x}}(t)$.
$\boldsymbol{\Psi}$	motion mapping between $\Omega_{\boldsymbol{\chi}}(t)$ and $\Omega_{\mathbf{X}}$.
$\mathbf{c}$, $\mathbf{w}$	ALE convective velocity and particle velocity modulo grid velocity.
$\mathbf{X}$	material coordinates.
$\mathbf{x}(t)$	spatial coordinates.
$\boldsymbol{\chi}(t)$	reference coordinates.
Γ_D	Dirichlet boundary.
Γ_N	Neumann boundary.
Γ_{FSI}	interface between structure and fluid field.

Observer schemes and frames of reference

q^0, q, $q^{\mathcal{G}}$	quantity q in material, spatial, and referential frame of reference.
$\mathbf{f}\|_{\mathbf{X}}(\mathbf{X}, t)$	Lagrangean observer measuring a quantity $\mathbf{f}$.
$\mathbf{f}\|_{\mathbf{x}}(\mathbf{x}, t)$	Eulerian observer measuring a quantity $\mathbf{f}$.
$\mathbf{f}\|_{\boldsymbol{\chi}}(\boldsymbol{\chi}, t)$	ALE observer measuring a quantity $\mathbf{f}$.

Spaces, inner products, and norms

$\mathcal{L}^2(\mathcal{V}_1, \mathcal{V}_2)$	Space of square integrable functions mapping vector space $\mathcal{V}_1$ onto vector space $\mathcal{V}_2$.
$(\cdot\,,\cdot)_\Omega$	$\mathcal{L}^2$-scalar product for scalar functions on Ω.
$(\cdot\,;\cdot)_\Omega$	$\mathcal{L}^2$-scalar product for vector-valued functions on Ω.
$(\cdot\,:\cdot)_\Omega$	$\mathcal{L}^2$-scalar product for tensor-valued functions on Ω.

Mathematical operators

$\dot{f} = \frac{\partial f\|_{\mathbf{x}}}{\partial t}$	partial time derivative in spatial coordinates.
$\mathring{f} = \frac{\partial f\|_{\mathbf{X}}}{\partial t}$	partial time derivative in reference coordinates.
∇q	gradient operator.
$\boldsymbol{\nabla}\,\mathbf{f}$	Jacobian of $\mathbf{f}$.
$\mathrm{div}(\mathbf{f}) = \boldsymbol{\nabla}\cdot\mathbf{f}$	divergence operator applied on a vector $\mathbf{f}$.
$\mathbf{div}(\mathbf{T}) = \boldsymbol{\nabla}\cdot\mathbf{T}$	divergence operator applied on a tensor valued quantity $\mathbf{T}$.
$\mathbf{1}$, $\underline{\mathbf{1}}$	second order identity tensor and matrix.
$\mathbb{1}$	fourth order identity tensor.
$c(\underline{\mathbf{M}})$	condition number of matrix $\underline{\mathbf{M}}$.
$\mathbf{v}_1\cdot\mathbf{v}_2$	standard scalar product for vectors.
$\mathbf{T}_1 : \mathbf{T}_2$	double contraction for tensors.
$S_1 \subset S_2$	the set S_1 is a subset of or equals S_2.

Basic physical quantities and constants

General notation

n^{dim}	number of spatial dimensions.
$\boldsymbol{\sigma}$	Cauchy stress tensor.
ρ	density.
$m(V)$	mass of a volume V.
$\mathbf{b}, \mathbf{t}, \mathbf{T}$	outer loads: body load per unit mass, surface traction, and pseudo surface traction.
t, t_0	time and initial time.

Structure field

$\mathbf{d}$, p	displacement and pressure fields.
$\mathbf{F}$, $J = \det(\mathbf{F})$	Deformation gradient and determinant.
$\mathbf{E}$, $\mathbf{C}$, $\widehat{\mathbf{C}}$	Green-Lagrange strain tensor, right Cauchy-Green tensor, and modified right Cauchy-Green tensor.
I_1, I_2, I_3	invariants of $\mathbf{C}$.
$\widehat{I}_1$, $\widehat{I}_2$, $\widehat{I}_3$	modified invariants of $\mathbf{C}$.
$\mathbf{m}$, $\mathbf{M}$	fiber direction and associated metric tensor.
$\widehat{I}_4 = \mathrm{tr}(\widehat{\mathbf{C}}\mathbf{M})$	modified non-standard invariant.
$\boldsymbol{\Gamma}$	internal strain like control variables.

$\mathbf{P}$, $\mathbf{S}$	first and second Piola-Kirchhoff stress tensor.
$\mathbf{Q}$	non-equilibrium stress-like tensor.
$(\cdot)^{\text{bil}}$	quantity referring to the lipid bilayer.
$(\cdot)^{\text{nw}}$	quantity referring to the cytoskeleton network.
G^{bil}, κ_1, κ_2	material parameters for lipid bilayer.
c_1, c_3, κ	material parameters for cytoskeleton.
B, G_{eff}, μ_{eff}	effective bending modulus, shear modulus, and viscosity of the membrane.
$\mathcal{B}$	algebraic constraint conditions.
$n^{\mathcal{B}}$	number of algebraic constraints.
$\boldsymbol{\lambda}^{\mathcal{S}}$	Lagrange multipliers for structure algebraic constraints.
$\boldsymbol{\kappa}^{\mathcal{S}}$	penalty parameters for structure algebraic constraints.

Fluid field

$\mathbf{u}$, p	velocity and pressure fields.
$\varepsilon(\mathbf{u})$	symmetric velocity gradient.
μ	fluid dynamic viscosity.
Re	Reynolds number.

Fluid grid field

$\mathbf{d}^{\mathcal{G}}$	grid displacements.
$\varepsilon^{\mathcal{G}}$	linear strain measure.
$\lambda^{\mathcal{G}}$, $\mu^{\mathcal{G}}$	Lamé constants for pseudo-structure material.
$\mathbb{C}$	linear constitutive tensor.

Coupling

$\mathbf{d}_{\Gamma}^{\mathcal{G}}$	grid displacements restricted to FSI interface.
$\mathbf{d}_{\Gamma}^{\mathcal{S}}$	structure displacements restricted to FSI interface.
$\mathbf{u}_{\Gamma}^{\mathcal{F}}$	fluid velocities restricted to FSI interface.

Discretization

Finite elements general notation

$(\cdot)^h$	discrete version of a quantity.
$\underline{\mathbf{N}}$	matrix of discrete nodal values for shape functions.
$\underline{\mathbf{y}}$	vector of discrete nodal values.

$(\cdot)^e$	element specific version of a quantity.
n_ℓ^{adj}	number of adjacent elements to an edge ℓ.
n^{dof}	number of DOFs.
n^{nd}	number of nodes.
$\boldsymbol{\mathcal{D}}$	general differential operator.
$\boldsymbol{\mathcal{R}}$	general residual.
N_i	i-th scalar shape function (test space).
$\bar{N}_j$	j-th scalar shape function (trial space).
$\mathbf{N}_i$	i-th vector-valued shape function (test space).
$\bar{\mathbf{N}}_j$	j-th vector-valued shape function (trial space).
$\mathcal{T}$	space of test functions.
$\mathcal{S}$	space of trial functions.
$\mathcal{T}^h$	semi-discrete space of test functions.
$\mathcal{S}^h$	semi-discrete space of trial functions.

Structure Field

$\delta\mathbf{d}$, δp	trial functions for displacements and pressure.
$\underline{\mathbf{d}}$, $\underline{\mathbf{p}}$	vectors of discrete nodal values for displacements and pressure.
$\underline{\mathbf{N}}_\mathbf{d}$, $\underline{\mathbf{N}}_p$	matrices containing shape function entries for displacements and pressure.
$\mathcal{T}_\mathbf{d}$, $\mathcal{T}_p$, $\mathcal{T}_{\bar{\mathbf{E}}}$	test spaces for displacement, pressure, and incompatible strains.
$\mathcal{T}_\mathbf{d}^h$, $\mathcal{T}_p^h$, $\mathcal{T}_{\bar{\mathbf{E}}}^h$	semi-discrete test spaces for displacement, pressure, and incompatible strains.
$\mathcal{S}_\mathbf{d}$, $\mathcal{S}_p$, $\mathcal{S}_{\bar{\mathbf{E}}}$	trial spaces for displacement, pressure, and incompatible strains.
$\mathcal{S}_\mathbf{d}^h$, $\mathcal{S}_p^h$, $\mathcal{S}_{\bar{\mathbf{E}}}^h$	semi-discrete trial spaces for displacement, pressure, and incompatible strains.
$\bar{p}$	discontinuous pressure value.
τ	stabilization parameter.
$\underline{\mathbf{P}}^e$, $\underline{\mathbf{P}}$	element wise and global stabilization matrices.
$\mathcal{C}$	STC scaling parameter.
$\underline{\boldsymbol{\mathcal{C}}}$	STC preconditioning matrix.
$\underline{\mathbf{B}}$	nonlinear B-operator.
$\underline{\bar{\mathbf{B}}}$	modified B-operator.
$\underline{\boldsymbol{\alpha}}$, $\delta\underline{\boldsymbol{\alpha}}$	EAS parameters and corresponding test functions.
$\underline{\mathbf{M}}^\alpha$	element EAS matrix.

$\underline{\boldsymbol{\lambda}}^{\mathcal{S}}$	vector of discrete Lagrange multiplier values.
$\underline{\mathcal{B}}$	constraint matrix containing first derivatives.
$\underline{\mathbb{S}}_{\mathbf{dd}}^{\lambda,\kappa}$	constraint matrix containing decond derivatives.

Fluid Field

$\mathbf{v}$, q	trial functions for velocities and pressure.
$\underline{\mathbf{u}}$, $\underline{\mathbf{p}}$	vectors of discrete nodal values for velocity and pressure.
$\underline{\mathbf{N}}_{\mathbf{u}}$, $\underline{\mathbf{N}}_{p}$	matrices containing shape function entries for velocities and pressure.
$\mathcal{T}_{\mathbf{u}}$, $\mathcal{T}_{p}$	test spaces for velocities and pressure.
$\mathcal{T}_{\mathbf{u}}^{h}$, $\mathcal{T}_{p}^{h}$	semi-discrete test spaces for velocities and pressure.
$\mathcal{S}_{\mathbf{u}}$, $\mathcal{S}_{p}$	trial spaces for velocities and pressure.
$\mathcal{S}_{\mathbf{u}}^{h}$, $\mathcal{S}_{p}^{h}$	semi-discrete trial spaces for velocities and pressure.
τ_{mp}, τ_{m}, τ_{c}	stabilization parameters.

Fluid grid field

$\underline{\mathbf{d}}^{\mathcal{G}}$	vector of discrete nodal grid displacement values.
$\underline{\widetilde{\mathbf{d}}}_{\Gamma}^{\mathcal{G},}$	vector of corrected discrete nodal grid displacement values.
$\underline{\mathbf{N}}_{\mathbf{d}}^{\mathcal{G}}$	matrix containing shape functions for grid displacmenets.
$\underline{\mathbf{B}}^{\mathsf{lin}}$	linear B-operator.

FSI coupling

$\boldsymbol{\lambda}$, $\delta\boldsymbol{\lambda}$	Lagrange multiplier and associated test function.
$\underline{\boldsymbol{\lambda}}$	vector of discrete multiplier values.
$\underline{\mathfrak{M}}$, $\underline{\mathfrak{D}}$	mortar matrices.
$\underline{\mathfrak{P}} = \underline{\mathfrak{D}}^{-1}\underline{\mathfrak{M}}$	mortar projection matrix.

Time integration

α_f, α_m	parameters for generalized-α time integration scheme.
θ	parameter for one-step-θ time integration scheme.
$t^{n+1-\alpha_f}$	generalized midpoint for external and internal forces.
$t^{n+1-\alpha_m}$	generalized midpoint for inertia.

Monolithic FSI system

$\underline{\mathcal{F}}$	effective fluid matrix.
$\underline{\mathcal{S}}$	effective structure matrix.
$\Delta\underline{\mathbf{x}}^{\mathcal{F}}$	vector of fluid increments.
$\Delta\underline{\mathbf{u}}^{\mathcal{F}}$, $\Delta\underline{\mathbf{p}}^{\mathcal{F}}$	velocity and pressure block, respectively, of fluid increments.
$\underline{\mathbf{r}}^{\mathcal{F}}$	fluid residual vector.
$\underline{\mathbf{r}}^{\mathcal{F}}_{\mathbf{u}}$, $\underline{\mathbf{r}}^{\mathcal{F}}_{p}$	velocity and pressure block, respectively, of fluid residual.
$\Delta\underline{\mathbf{x}}^{\mathcal{S}}$	vector of structure increments.
$\Delta\underline{\mathbf{d}}^{\mathcal{S}}$, $\Delta\underline{\mathbf{p}}^{\mathcal{S}}$, $\underline{\boldsymbol{\lambda}}^{\mathcal{S}}$	displacement, pressure, and Lagrange multiplier block, respectively, of structure increments.
$\underline{\mathbf{r}}^{\mathcal{S}}$	structure residual vector.
$\underline{\mathbf{r}}^{\mathcal{S}}_{\mathbf{d}}$, $\underline{\mathbf{r}}^{\mathcal{S}}_{p}$, $\underline{\boldsymbol{\mathcal{B}}}$	displacement, pressure, and constraint block, respectively, of structure residual.

Chapter 1
Introduction

This chapter motivates the scientific interest in human erythrocytes, also known as red blood cells (RBC), in general and addresses the need for a comprehensive numerical model in particular. The first section describes the relevance of erythrocytes for blood flow and blood damage and introduces the main characteristics of the cell. Experimental studies that provide insight into these characteristics are reviewed. The second section shows that the interpretation of the experiments performed on erythrocytes necessitates numerical studies and derives the required complexity of a reasonable numerical model. The section is completed by an overview on existing numerical models, which are commented on with regards to these requirements. The objectives and the outline of this thesis are given in the final section.

1.1 The human red blood cell

This section reviews some aspects that motivate and demonstrate the scientific research on the human RBC within the last decades. To begin with, the relevance of the cell for the rheology of blood in larger vessels, for the flow characteristics in very small capillaries, for the diagnosis of certain diseases, and for the biomedical applications is discussed. Subsequently, an overview on morphology and on main mechanical properties of erythrocytes is given. These properties are derived from experimental results, which are addressed in the final subsection. Qualitative observations and quantitative measurements for erythrocytes in optical tweezers, atomic force microscopes, shear flow, and microfluidic devices are summarized.

1.1.1 Biological relevance

Erythrocytes have become a field of intensive research over the last decades and many groups are still working on this subject. In many cases the interest in erythrocytes is motivated by an interest in the rheological properties of blood flow. Blood is a complex fluid that can be viewed as a suspension of different blood cells (red cells, white cells and platelets) in a Newtonian fluid. From a micromechanical point of view,

the mechanical properties of the suspended cells, their interaction with each other, the interaction between cells and fluid, and the properties of the plasma have to be considered. The composition of the suspension shows the importance of the RBC: the human erythrocyte constitutes more than 99% of the particulate matter in blood and 40 to 45% of the blood by volume.

On the macroscopic level, the suspended RBCs give rise to a non-Newtonian, viscoelastic behavior. First of all, a shear thinning behavior for increasing shear rates can be observed. Experimental studies of Chien et al. [38, 39] showed that the high viscosity measured for low shear rates is due to cell aggregation into rouleaux structures, whereas for high shear rates these structures break up and the relatively low viscosity is a consequence of cell deformability. Furthermore, it has also been shown, for example, by Schmid-Schönbein and Wells [170] and Chien [37] that the apparent viscosity of blood increases for increasing *hematocrit*. Hematocrit refers to the volume fraction of red cells in the suspension. The viscoelastic properties of the red cell itself yield a viscoelasticity of the whole suspension, i.e. blood, which has been established by Thurston [185] for oscillatory flow in cylindrical tubes. Today, blood is generally accepted to be a shear thinning viscoelastic fluid.

From a modeling point of view, when a macroscopic constitutive model for blood is considered, rather complex material models have to be introduced. Common choices for the human blood are, for example, the Carreau-Yasuda model, which only accounts for shear thinning effects, the Oldroyd-B model, which represents a viscoelastic behavior, or microstructure-based models. The latter aims to translate certain aspects of the micro-rheology into a macroscopic material formulation. This thesis does not consider macroscopic models for blood and their impact on the numerical methods. Therefore, details are omitted here and the reader is referred to the literature. For example, a comprehensive review on finite element (FE) based models for viscoelastic fluids is given by Baaijens [5]. Details on the Carreau-Yasuda model can be found in the textbook by Bird et al. [16] or in the publication by Leuprecht and Perktold [127]. Oldroyd-B fluids and their numerical treatment are thoroughly addressed in the work of Behr et al. [11], Coronado et al. [41, 42], and in the theses by Yeleswarapu [199] and by Arora [2]. Microstructure-based models have, for example, been proposed by Fang and Owens [57], Owens [148], and Iolov et al. [114].

The influence of erythrocytes on blood flow behavior becomes even more apparent if the flow through the terminal branches of the circulatory system is considered. In this so-called *microcirculation*, vessel diameters range from a few hundred μm to a few μm. A significant decrease in flow resistance and, thus, in apparent viscosity with decreasing blood vessel diameter below 1 mm is measurable. This effect known as *Fåhraeus-Lindqvist effect* was first described by Fåhraeus and Lindqvist [56] and results from a non-continuum behavior of blood near the vessel wall, where a cell-free or cell-depleted layer forms.

In contrast, for even smaller vessels with a diameter below 8 μm, the so-called *capillaries*, the apparent viscosity increases rapidly with decreasing vessel size. This limiting

diameter corresponds to the diameter of a single erythrocyte. The effect has been quantified by Secomb [171] and Pries et al. [160, 161, 162] both experimentally and theoretically. For the considered vessel sizes, erythrocytes frequently flow in single file and are compressed into narrow shapes, which explains the drastically increasing flow resistance. Nevertheless, in the human body, the erythrocytes passe vessels with diameter as low as 3 μm, demonstrating the deformability of those cells.

The mechanics of the RBC is not only important in order to characterize blood rheology and to understand the flow behavior in small vessels, but it has also a potential to help diagnose certain diseases. For example, cells infected with malaria are known to have a stiffened membrane behavior, see for example work by Cranston et al. [43] and by Suresh et al. [179]. Therefore, an experimental set-up which is easy to use, cheap to produce, and, most importantly, sensitive with respect to altered cell mechanics, would provide the possibility to diagnose this kind of diseases.

Finally, for the design process and the application of artificial devices such as artificial blood pumps, the mechanics of erythrocytes plays a major role. So far, damaging of erythrocytes, the so-called *hemolysis*, is the limiting factor for the long-term success of these devices. An indicator for the damage is the amount of freed hemoglobin measured in the plasma. It is no longer stored inside the erythrocyte due to temporal leakage caused by large deformations or even due to rupturing of the cell. Theoretical studies that provide some explanation for the process of hemolysis based on the molecular structure of the cell membrane are for example given by Borsos et al. [24], Seeman [172] and Arora et al. [3]. A general, theoretically rigorous, and quantitative model relating hemolysis to mechanical loads is still an open question.

Nevertheless, there are several experimental studies measuring the amount of freed hemoglobin for shear flow (for example by Paul et al. [150]), for different blood pumps (for example by Kameneva et al. [115]), or for turbulent jets (for example by Lu et al. [135]). Those measurements have been used to develop empirical relations between shear stress and hemolysis as, for example, shown by Bludszuweit [19], Lu et al. [135], Paul et al. [150], or Grigioni et al. [88, 89]. However, the quality of the blood damage prediction is generally found to be relatively poor and often restricted to the considered experimental set-up. A more promising approach was proposed by Arora et al. [3, 4]. Instead of relating cell damage with the shear stress, hemolysis, or more precisely the rate of leaking hemoglobin, was assumed to depend on the strain state of the RBCs.

1.1.2 Morphology

The unloaded, but not necessarily stress-free shape of a human red cell (at least under physiological conditions) is a biconcave disc, the shape of which has been measured by Canham [34] and Evans and Fung [53]. The *cytosol*, a concentrated incompressible viscous hemoglobin solution, is surrounded by a two-layer, viscoelastic membrane, cf. Figure 1.1(a). This membrane has been the subject of many scientific studies, which have been reviewed recently in an article of Mohandas and Gallagher [143]. Briefly, it is a composite of a *lipid bilayer* and an underlying *cytoskeleton network*, which is linked

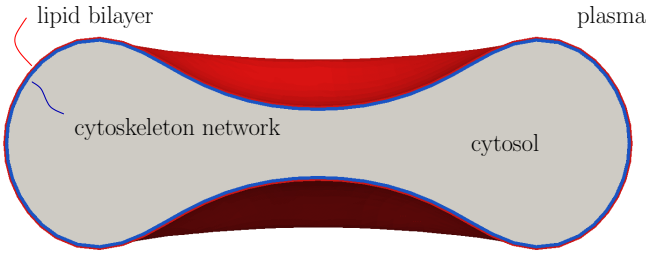

(a) cut through the cell

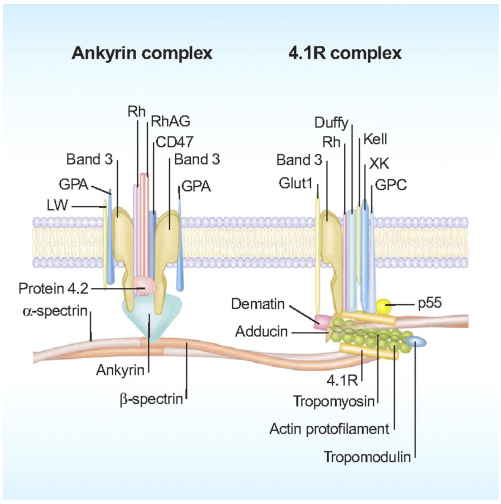

(b) Schematic drawing of the red cell membrane, taken from [143]

Figure 1.1: *Basic morphology of the human erythrocyte*

to intramembrane proteins in the lipid bilayer. A schematic drawing of the set-up taken from reference [143] is shown in Figure 1.1(b).

The outer and very thin lipid bilayer consists mainly of cholesterol and phospholipids and exhibits a fluid-like character, as could be shown by Discher et al. [47] and Discher and Mohandas [46]. Subjected to a large deformation, a measurable gradient in lipid concentration could be observed, but self-diffusion achieved an equilibrium distribution within several minutes. Furthermore, incompressibility and a large resistance to changes of the surface area, as measured by Evans and Waugh [55] and by Katnik and Waugh [117], are generally attributed to this plasma membrane layer. Even an increase of 3% to 4% in surface area leads to cell lysis as pointed out by Arora et al. [3]. This is remarkable, since the cell membrane can nevertheless undergo extremely large deformations and the cell, which as already mentioned has a diameter of 8 μm, can squeeze through capillaries with diameters of about 3 μm.

The experiments of Discher et al. [47] and Discher and Mohandas [46] also show a solid-like behavior of the cytoskeleton, which is a 2D spectrin network tethered by junctunal complexes of actin filaments, globular band 4.1, and other proteins to intramembrane proteins band 3 and glycophorin in the lipid bilayer, cf. the work of Heinrich et al. [99] and Mohandas and Gallagher [143]. Spectrin is a highly extensible and elastic molecule. Consequently, the cytoskeleton is the source of shear elasticity for the composite and its network topology implies a strain-hardening effect for large shear deformations.

The basic assumption to explain the biconcave shape of the cell at rest is that it represents the state with minimal mechanical energy of the lipid bilayer/membrane skeleton composite under the constraint of given surface area and given cell volume. Helfrich [100] proposed that the minimization process is dominated by the bending

energy stored in the membrane. This implies that the unstressed shape of erythrocytes is controlled by the mechanical properties of the lipid bilayer, since its bending elastic modulus is several orders of magnitude larger than the bending resistance of the 2D cytoskeleton network as reported by Waugh and Evans [195] and Fischer [65]. The relatively high bending elastic modulus of the fluid-like membrane can be explained by its resistance against local differences in area between the outer and inner leaflet. The numerical studies by Canham [34], Feng and Klug [62], and Lim et al. [132] supported this argumentation.

It is important to distinguish between the cell shape at rest and the stress-free state of the membrane. Today, it is widely accepted that the biconcave shape of an unloaded cell is not stress-free. Furthermore, a spherical stress-free state can be ruled out since it would contradict the *shape memory effect* of the erythrocyte, which was observed by Fischer [65]. Even though the membrane had been rotated around the cytosol by a steady shear flow, at equilibrium, the rim of the cell was always formed by the same parts of the membrane.

Although the basic structure of the erythrocyte is well known, the material properties of the single membrane constituents and of the cytosol cannot be accessed by direct measurement. Instead, they have to be deduced from experimental observations of the overall behavior of the cell, focused on in the following subsection.

1.1.3 Experimental studies on single erythrocytes

Several different experimental set-ups have been proposed to investigate the behavior of individual RBCs. They have brought great insight into cell morphology and mechanical properties. In following paragraphs, the response of a cell in laser traps, atomic force microscope (AFM), shear flow, and microfluidic devices is reviewed in more detail. The main advantages and drawbacks of the respective experimental method are discussed and the most important results in the literature are briefly summarized.

Laser trap experiments

The first, static *laser trap (optical tweezers)* experiments on RBCs have been reported by Henon et al. [102]. For this kind of experiments, the cells are prepared by attaching two rigid silica beads at the diametrically opposite ends of the cell. A laser exerts a force on the beads and, thus, stretches the cell. The experiments reported in [102] realized only small trap forces, a limitation that was overcome by Lim et al. [130, 131] and by Mills et al. [142], who generated forces large enough to stretch the cell by more than 100 %. Pictures of a deformed cell subjected to two different stretching forces (taken from [142]) are exemplarily shown in Figure 1.2. Till today, the results of those experiments have become the core data on which several numerical studies are based upon. Therefore, the experiments and their results reported in [142] are discussed here in some more detail.

(a) Stretching force of 67 pN

(b) Stretching force of 193 pN

Figure 1.2: *Deformed cell in laser traps taken from [142]*

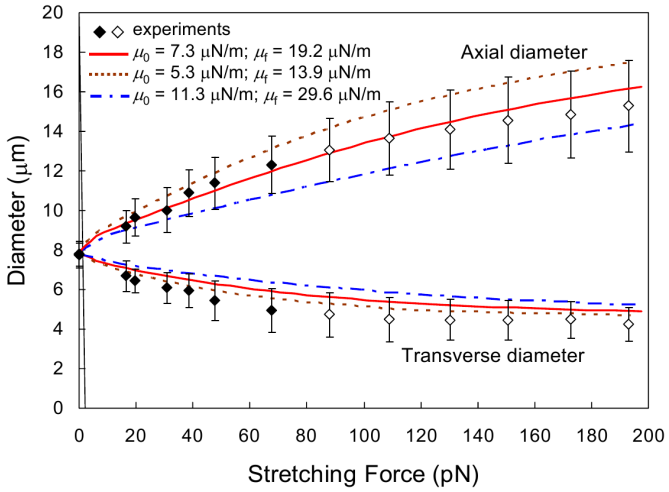

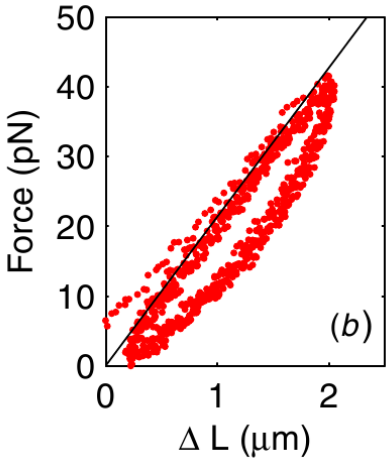

(a) Response to quasi-static deformation. Experimental and numerical results taken from [142]

(b) Hysteresis behavior for dynamic deformation with a trap speed of 5 μm/s *[201]*

Figure 1.3: *Literature results for laser trap experiments*

In the experiments by Mills et al. [142], only one bead was trapped by the laser and the other one was attached to a glass slide, which was slowly translated to stretch the cell. Depending on the current laser power, which determines the maximal trapping force, the trapped bead eventually escaped. Measurements of the axial and of the transverse cell diameter just before the escape resulted in a displacement over force diagram as shown in Figure 1.3(a). The mechanical response of the whole cell to quasi-static deformation is clearly dominated by the shear elasticity of the cytoskeleton. Thus, it is not surprising that the results revealed a hardening behavior of the whole cell for large strains, which reflects well the network topology of the cytoskeleton.

As described above, eventually the cell escaped the laser trap. Recording the recovery of the cell to its biconcave initial shape allows for an analysis of viscoelastic creeping behavior of a RBC associated with a sudden drop in stretching force. In both studies, [102] and [142], the progressions of the axial diameter were fitted by exponential curves.

Averaging the relaxation times yielded a characteristic recovery time, which could then be compared to other creeping experiments. One problem of these studies is that the recovery always started from different deformed states and that the sensitivity of the recovery time with respect to these deformed states was not considered.

More recently, Yoon et al. [201] presented experiments, where the dynamic deformations of the cell were induced by fast movements of the laser trap. The motion of both beads was controlled with a laser beam steered via a pair of accousto-optic deflectors. The position of one trap was again held fixed, whereas the other one was translated following a triangle wave pattern. Three different trap speeds were considered. During those experiments, a difference between bead position and known laser position in the immobile trap could be observed depending on the trapping force. Therefore, the trap could no longer be assumed to be rigid but was modeled as a harmonic spring. As results, the actual bearing force could be determined and hysteresis curves plotting force over displacement were obtained. Those curves allow for the definition of energy dissipation and apparent stiffness. For a trap speed of $5\,\mu\mathrm{m/s}$, such a hysteresis plot is exemplarily shown in Figure 1.3(b).

In laser trap experiments, forces and displacements can easily and accurately measured. However, the set-up only allows a very small throughput and, more importantly, the contact surface between cell and laser trap can only be estimated, which makes it difficult to apply realistic boundary conditions in numerical simulations. For dynamic experiments, a further source of uncertainty can be identified in the approximation of the trap as harmonic spring.

Atomic force microscope

A group of the Ludwig Maximilian Universität in Munich started probing the human RBC with an AFM. Instead of using silica beads as in optical tweezers to exert forces on the cell, here, the erythrocyte membrane is adhered to a glass surface on one side and to the tip of a cantilever beam with calibrated stiffness on the other side. The beam is fixed to a piezo actor, which enables a precise and extremely fast streching and compression of the erythrocyte. Force measurement is carried out by recording the tip deflection of the cantilever.

The goal of the measurements is to get an insight into the recovery behavior of the cell, starting always with the same deformed state. After a fast compression or tension, the cell is allowed to relax for 15 s and the progression of the force over time is measured and fitted with a double exponential decay. One application of this experimental set-up is to access the change in viscoelastic behavior of the cells when treated with a chemical called latrunculin. It turned out to reduce both recovery times, which govern the double exponential decay. The hypothesis is that latrunculin destroys the connection between the two membrane layers of the erythrocyte.

These experiments share most of the advantages and the disadvantages of the laser trap experiments. Forces and displacements are easily accessible, but the contact zones between cell and cantilever and between cell and glass surface cannot be controlled.

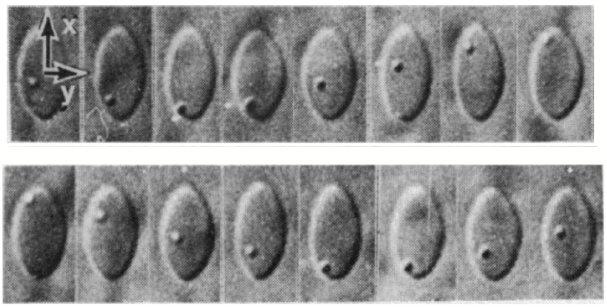

Figure 1.4: *Tank-treading cell motion, taken from [170] (x flow direction, y axis of rotation)*

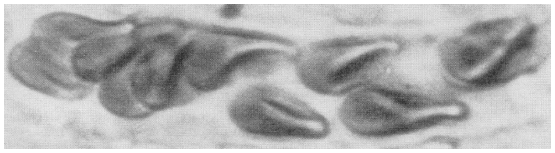

(a) Tube diameter 12 μm

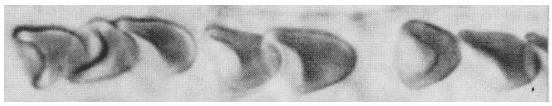

(b) Tube diameter 7 μm

Figure 1.5: *In vivo images of cells in capillary flow, taken from [176]*

Shear Flow

Given the shortcomings of the experiments introduced above, set-ups are appealing, where the cell is deformed by an external shear flow. Here, the level of deformation depends on two factors, the viscosity of the external fluid and the shear rate.

First measurements of cells in simple shear flow have been carried out in the pioneering work of Schmid-Schönbein and Wells [170], Goldsmith and Marlow [83], and Fischer et al. [66]. The important contribution of these studies is the discovery of the characteristic erythrocyte motions in flow: At low shear rate and low external viscosity, the cells behave solid-like, i.e. they do not deform, but undergo a *flipping* (also-called *tumbling*) motion. At high shear rates and high external viscosity, erythrocytes behave like a fluid-drop, i.e. they deform into prolate ellipsoids aligned with the flow and exhibit a *tank-treading* motion, which is characterized by a membrane rotation around the cell while cell shape and orientation do not change, exemplarily shown in Figure 1.4.

Tank-treading is not only found for high shear stresses, but it was also observed for medium shear stresses. A detailed investigation of the cell motion was presented by Abkarian et al. [1] and Viallat et al. [189], who detected a swinging motion of the cell. Swinging is characterized by a tank-treading around a biconcave cell with oscillating inclination angle. The deformation of the cell shape was reported to be negligible.

In the so-called *go-and-stop experiments* reported by Fischer [65], the cells were subjected to simple shear flow that induced a tank-treading motion of the membrane. After the flow was stopped, the cell returned to its unloaded biconcave shape relatively fast. However, the relaxation was not completed by the shape transition. With latex spheres attached to the rim of the cell at rest, Fischer [65] could show that the membrane tended to tank-tread around the biconcave cell, until the attached sphere was again positioned at the rim of the cell.

Microfluidic circulation

Shear flow experiments in the previous paragraph aim to simulate the flow through large blood vessels. As discussed in section 1.1.1, a macroscopic fluid description assuming shear thinning and viscoelastic behavior yields good results for this type of problems. The mechanics of single erythrocytes, however, is of great importance for the flow through very narrow tubes. Depending on flow rate and diameter of the tube, the cells will adopt different shapes when flowing through the tube as shown and discussed, for example, by Gaehtgens et al. [73], Guest et al. [91], and Skalak and Branemark [176]. For relatively large capillary vessels, erythrocytes will assume a slipper-like form as shown in Figure 1.5(a), whereas in very narrow tubes parachute-like shaped cells can be observed as depicted in Figure 1.5(b). Pries et al. [159, 160] investigated the flow of erythrocytes in microvascular bifurcations and developed a theoretical model to predict blood flow through large microcirculatory networks.

The flow through single capillary vessels can be simulated *in vitro* as flow through narrow glass tubes as presented, for example, by Risso et al. [168] and Seshadri et al. [173]. However, systematic *in vitro* investigations of erythrocytes flowing through curved vessels, tubes with varying diameters, different pore geometries, or bifurcating capillaries require more flexible experimental set-ups.

This flexibility is provided by recent developments in lithography, which allow to produce microfluidic devices of almost arbitrary shape. One advantage of these very small devices is that they require only a very little fluid volume to be operational. Microchannels with modulated width have been realized by Braunmüller et al. [28]. The transition of the cells from discocyte to slipper to parachute shapes can be observed and related with channel width and fluid velocities, cf. Figure 1.6(a). Quinn et al. [167] presented a microfluidic design to study how erythrocyte squeeze through narrow restrictions. Since the cell has to undergo extremely large deformations and stresses during the experiments, it might be possible to study damaging scenarios of single cells. However, a damaging of the erythrocyte was not considered in the work of Quinn et al. [167].

Microfluidic devices are relatively cheap to produce, require only a small quantity of blood, and can still operate a relatively large number of erythrocytes in parallel. Therefore, these devices meet many requirements stated in 1.1.1 in order to serve as a diagnosis tool. The design proposed by Bow et al. [25] consisted of periodically spaced, triangle-shaped pillars and was able to mechanically identify a small number of infected cells within a population of uninfected erythrocytes, cf. Figure 1.6(b).

1.2 Numerical studies of the red blood cell

Due to the complexity of erythrocyte morphology and of experimental set-ups introduced in section 1.1, numerical studies focusing on erythrocytes have become very popular in the scientific community over the past 20 years. The first subsection of this section elaborates the motivation for and the necessity of a numerical model for the human

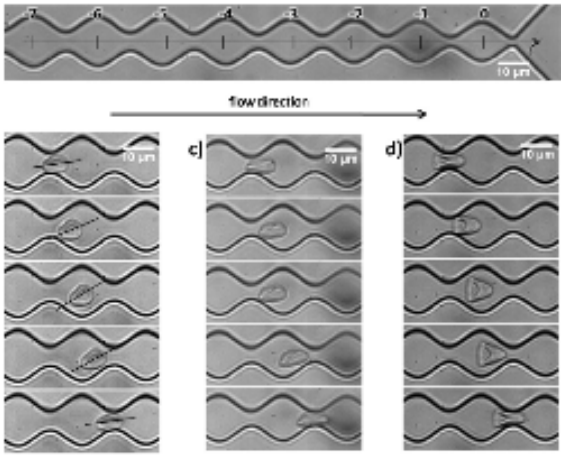

(a) Microchannel with modulated width as presented in [28]

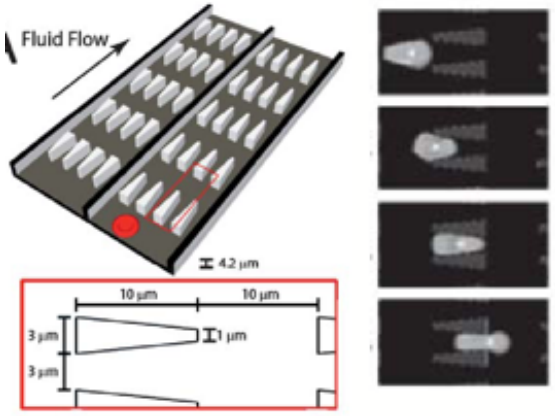

(b) Periodically spaced, triangle shaped pillars as used in [25]

Figure 1.6: *Exemplary geometries realized in microfluidic devices*

RBC in more detail. In subsection 1.2.2, the requirements for a comprehensive model are derived based on the discussions in the previous section. An overview of existing numerical studies and a discussion on how they meet these requirements closes the section in subsection 1.2.3.

1.2.1 The necessity of numerical simulations

Compared to other cells, the morphology of the human erythrocyte is relatively simple in that it is a biological membrane containing a homogeneous viscous fluid but no nucleus. On the other hand, the mechanical response of the whole cell, as obtained by most experimental studies, is governed by the interaction between two membrane layers with different qualitative and quantitative material properties and by the interaction of the membrane with cytosol on the inside and with blood plasma on the outside. General solutions for the nonlinear mechanics of such a fluid-filled composite structure are not available. The biconcave unloaded shape even adds geometrical complexity to the problem.

Analytical approximations are only available for regular geometries, such as spherical or 2D disk-like structures, and for relatively simple membrane descriptions. Earlier studies used those approximations in order to deduce material parameters from experimental observations, cf. the experimental studies by Chien et al. [36] and Henon et al. [102]. Those simplifications clearly have an effect on the resulting parameters, but a quantification of the influence is hardly possible. Furthermore, analytical approaches do not seem to be promising for dynamic experiments. Therefore, in more recent studies, numerical models have become standard in deducing material parameters.

Moreover, numerical modeling allows for an easy change of material parameters, which is an important aspect when planning experiments that are designed to detect cells

with altered cell mechanics. An example for such an experiment is the microfluidic device presented by Bow et al. [25], in which malaria infected cells could be detected based on the increased membrane stiffness resulting from the infection. By simulating the experiments numerically, the sensitivity of an experimental design with respect to the expected changes in cell mechanics is accessible and allows for a relatively easy optimization process of the design.

The changes caused by malaria are known and relatively well-understood. However, physiological defects caused by other diseases or chemical treatments are not fully understood. Nevertheless, a significant change in the mechanical response of affected cells can be observed in experiments. Here, by comparing the effect of altered membrane mechanics observed in numerical simulations with experimental data, simulations can help to identify the alterations caused in the erythrocyte.

Furthermore, numerical simulations of a single cell or of multiple cells in fluid flow have great potential in the context of hemolysis prediction. Strain and stress states of the erythrocyte are thought to be the key parameters in the evolution of hemolysis as already discussed in section 1.1.1. These states are readily accessible for numerical simulations of discrete cells, but have to be estimated in case of macroscopic descriptions. For the continuum-based model proposed by Arora et al. [3, 4], the approximation of the cell strains was motivated by the work of Maffettone and Minale [138] on fluid droplets. Given strain rate and vorticity of the fluid, the so-called *droplet morphology tensor* was calculated in order to approximate the shape of an tank-treading ellipsoidal erythrocyte. The rate of leaking hemoglobin was then assumed to depend on the instantaneous distortion defined by the eigenvalues of this tensor. Thus, two major simplifications are made in the derivation. First, the deformation of the cell is assumed to be reasonably described by the droplet morphology tensor. Second, hemolysis is related to the global deformation. A more detailed representation of the erythrocyte mechanics including local membrane effects can probably further improve the quality of hemolysis prediction and may provide the chance for an even better calibration of the macroscopic model.

It is widely accepted that the biconcave shape, which the cell adopts at rest under physiological conditions, is not stress-free. The experiments reported by Abkarian et al. [1] and Viallat et al. [189] may help to answer the question of a realistic stress-free state of erythrocytes. The existence of a swinging motion of a single erythrocyte in shear flow with relatively low shear rate and viscosity of the surrounding fluid has been attributed to the residual stress in the membrane for the cell at rest. Numerically, it is possible to test this hypothesis by varying the stress-free state of the membrane in order study its effect on the response to external loading.

After having discussed the general necessity for a numerical model of human erythrocytes, the mentioned characteristics, experiments and open questions are utilized to deduce particular requirements for this model.

1.2.2 Requirements for a comprehensive numerical model

First of all, a numerical model should respect the morphology of the cell and account for the properties of the membrane as well as of the cytosol. Therefore, a fluid-structure interaction (FSI) approach of some kind has to be included, where an incompressible fluid domain is completely enclosed by a viscoelastic membrane. Numerically, this kind of balloon-type problems limits the number of applicable FSI approaches significantly as discussed by Küttler et al. [124].

Simulations of erythrocytes in shear flow or microfluidic devices additionally require a second FSI interface between the membrane and the surrounding blood plasma. The additional complexity does not arise from the second coupling itself but from the fact that in the experiments the cell undergoes large rotations or large displacements.

Of course, the results of the FSI simulation can only be relied on if the models of the single physical fields, i.e. fluid and structure, are reliable. In the case of RBCs, both fluid descriptions are rather standard. It is essential that the incompressibility condition of the cytosol is fulfilled. The membrane model has to account for the properties of both a fluid-like lipid bilayer as well as a spectrin network. To briefly review the characteristics discussed in section 1.1.2, the lipid layer is incompressible and provides viscosity, bending elasticity and a large resistance against changes of the surface area. The cytoskeleton layer is the source of shear elasticity of the membrane and shows a hardening effect for large strains.

Since the shape of the unstressed cell membrane is still an open question, the model should provide some flexibility with regards to the stress-free state of the membrane and, hence, allow to numerically investigate the influence of a pre-stressing of the membrane on the response of the cell.

Naturally, the model should be able to predict the outcome of different experimental set-ups. In particular, in order to realistically simulate the cell stretching in laser traps or atomic force microscopes, appropriate boundary conditions have to be applicable. In both cases, a rigid structure, i.e. a bead or a cantilever beam, is connected to the cell and controls the deformation of the cell by applying a force. This way, the response of the cell is constrained at the surface in contact with the experimental device.

1.2.3 Outline of existing numerical studies

In general, the numerical approaches existing in literature can be divided into two big classes of models: macroscopic continuum approaches and molecular based models. Their development has been motivated by different experimental set-ups and their application is, thus, often restricted to the corresponding experiment due to the particular numerical method or due to an incomplete cell description.

First molecular based methods designed to simulate the whole cell membrane in static experiments were published by Discher et al. [48]. The formulation was based on a coarse-graining approach of an earlier network model for the microscopic make-up of

the cytoskeleton developed by Boal [20] and Boey et al. [22]. The model in [48] mainly focused on the elastic properties of the erythrocyte membrane. Both shear and bending elasticity were included, but neither viscous behavior of the membrane nor of the cytosol was considered. The model was adapted for the simulation of laser trap experiments by Li et al. [128]. In that work, another issue of this numerical approach was evident, since realistic boundary conditions for optical tweezers can hardly be implemented. The issue was circumvented by applying simple Neumann boundary conditions. Furthermore, Li et al. [128] pointed out that a variation of the stress-free shape would be desirable but not possible for the proposed numerical method.

Even though the issue of imposing boundary conditions on the membrane remained, remedies for other restrictions and shortcomings of the original model of Discher et al. [48] were proposed by Fedosov et al. [60, 61] and Pivkin and Karniadakis [152]. In the latter publication, a detailed discussion on a systematic coarse-graining and an extension to dynamic FSI simulations can be found. Viscoelasticity of the membrane was included in the formulation and the fluid was simulated with a dissipative particle dynamics (DPD) approach, which was developed by Groot and Warren [90] and Hoogerbrugge and Koelman [108]. This method is a mesoscopic approach that includes random forces due to thermal fluctuation of the fluid particles and, in case of pure fluid problems, converges to the solutions of the incompressible Navier-Stokes equations. In the publications of Fedosov et al. [60, 61] and in more detail in the thesis of Fedosov [59], the application of the model to different experimental set-ups such as laser traps, capillary flow, and shear flow was shown. The influence of varying material parameters of the membrane on the outcome of the simulations were also considered to some extent. Yet, a variation of the stress-free state of the membrane was not reported.

Another mesoscopic approach was proposed by Gompper and Noguchi [84, 145, 146]. The fluid description of this numerical method is based on a so-called multiparticle collision dynamics (MPCD) approach, which exhibits similar properties as the DPD approach. It was combined with a dynamically triangulated surface model for the erythrocyte membrane, which includes shear and bending elasticity. Viscosity of the membrane was controlled by the bond-flip rate of the dynamical triangulation algorithm. This model was exclusively used to simulate flow through narrow capillaries. As it is true for any of the particle based methods discussed here, an implementation of realistic boundary conditions for the simulation of laser trap experiments or probing with atomic force microscopes seems impossible.

One advantage of such mesoscopic, particle based methods as described so far is that they can relatively easily be extended to simulate flow of multiple cells, even though very simple contact algorithms are most often used to account for cell-cell interaction, see for example the work of Imai et al. [113]. Even though not as straightforward as for the particle based methods, cell-cell interaction could also be accounted for by continuum based models. The study by Liu and Liu [134] employed an immersed finite element method (IFEM) to deal with contacting structures within a FSI simulation. Besides shortcomings of the numerical method itself, the chosen model for the membrane considered only shear elasticity.

The majority of continuum based models consider the behavior of a single cell, but only few of them consider the interaction between the membrane and the fluid fields. Among them are the models developed by Pozrikidis [155, 157, 158], which are based on a boundary integral (BI) formulation. This method is restricted to Stokes flow, which is a reasonable assumption for flow of erythrocytes in most experiments and physiological situations. Drawbacks of the method are the complicated application of correct flow boundary conditions and the very simplistic elastic membrane description. Even a realistic bending behavior is hard to incorporate into the formulation as shown by Pozrikidis [156]. Therefore, the group of Barthès-Biesel applied a very similar model mostly for the simulation of artificial capsules in fluid flow [126, 129, 166, 194], where bending elasticity can reasonably be neglected.

More comprehensive continuum-based membrane models were also published. Especially for laser trap experiments, where the results can be assumed to be unaffected by the surrounding fluid, a variety of proposed models can be found in the literature. The results reported by Chee et al. [35] were obtained by a FSI simulation including only the cytosol. The FE model accounted for the rigidity of the laser trap and for most characteristic membrane properties found in the bilayer-network composite. However, the surface area preservation provided by the bilayer was neglected completely. Bending elasticity was realized by a relatively very thick membrane in comparison to the physiological membrane thickness. Static and very fast dynamic laser trap experiments were simulated and especially the dynamic results showed good agreement to the experimental results given by Mills et al. [142], although the latter were reported to be obtained from static experiments.

The work of Mills et al. [142] does not only contain an experimental but also a numerical study. Due to the slow movement of the trap, the influence of the cytosol was assumed to reduce to its incompressibility. Thus, an additional algebraic constraint was implemented to preserve the volume enclosed by the membrane. Very similar to the later work of Chee et al. [35], the FE based model used in [142] considered the rigidity of the trap and elastic contributions of the cytoskeleton, but the properties of the lipid-bilayer in general and the resistance against dilatation of the surface area in particular were neglected. Nevertheless, the model realistically predicted the outcome of static laser trap experiments.

The more sophisticated model proposed by Peng et al. [151] considered both membrane layers separately in a multiscale-based FE model. The coupling between a single unit of protein network and the bilayer, which was used in [151] on the smaller scale, was originally introduced by Zhu et al. [203]. Validation was again performed with static experiments, i.e. with data taken from [142] and from micropipette aspiration experiments. Again, the cytosol contribution was reduced to its incompressibility. Hartmann [96] also proposed a multiscale approach. However, on the largest scale the whole cell was modeled as a viscoelastic solid. Results obtained for dynamic deformations of the cell were not reported.

None of the above mentioned numerical models is able to reproduce the swinging motion that was observed by Abkarian et al. [1] and Viallat et al. [189]. In those

experimental studies, tank-treading was detected for a biconcave red cell. In contrast, numerical studies predicted tank-treading for cells that already had been deformed into an ellipsoidal shape. None of these studies considered a stress-free state other than a biconcave disc determined by Evans and Fung [53]. This may suggest, that the swinging motion of the cell indeed can be attributed to the pre-stressing of the biconcave cell as suggested by Viallat et al. [189].

1.3 Objectives and outline

As it is apparent from the small survey in the previous section, none of the available models meets all the requirements that have been deduced from the erythrocytes morphology and experimental observations. In most cases, only some aspects of the cell mechanics are addressed depending on the experiments considered. Moreover, none of the models gives flexibility in choosing a stress-free state other than that of a biconcave disc. Some experimental observations could not be reproduced by any of the available models. Thus, it is of great importance to identify and understand the implications of such incomplete RBC model descriptions.

Therefore, a novel FE model for the human RBC has been devised in this work. It is an extension of an earlier model proposed by the author in [119], which already included all the key features of the membrane and the coupling between the membrane and the cytosol. This model accurately predicted the outcome of static and dynamic laser trap experiments and allowed to investigate the cell's sensitivity with respect to certain parameters. Furthermore, different stress-free states could be realized. The influence on the simulation of laser trap experiments was found to be negligible. The blood plasma was not yet included and, consequently, a simulation of erythrocytes in shear flow was not yet possible.

The development of an improved model is the main objective of this work. It can be subdivided into three parts. First, the cell properties discussed in section 1.2.2 have to be translated into continuum mechanical equations, which add up to a comprehensive continuum model of the cell and its surroundings. Second, the numerical discretization of the continuum model is necessary. In this thesis, the finite element method (FEM) will be used for this task. Due to particular features of the model such as the incompressibility and thinness of the membrane, this is not straightforward and necessitates special numerical treatment. Furthermore, a FSI method that can deal with the enclosed incompressible fluid field as well as with rotating structures is to be devised. Third, the final numerical model is to be validated and has to accurately predict the outcome of different experiments with the same set of parameters.

The three tasks mentioned above can also be found in the outline of this thesis, which is organized as follows. Following this introduction, chapter 2 shows the development of the continuum model for the human erythrocyte. It starts with a brief introduction into basic continuum mechanics, where the formulations of kinematics and balance equations are given in an arbitrary Lagrangean-Eulerian (ALE) framework. From these

rather general equations, particular descriptions for the fluid flow inside and outside the erythrocyte membrane as well as for the erythrocyte membrane itself are deduced. As can be seen from the previous sections, especially the membrane necessitates a tailored formulation. The second chapter is closed by introducing necessary algebraic constraints to complete the membrane formulation and the coupling conditions between fluid fields and membrane.

The third chapter introduces the computational framework used to derive a numerical model from the continuum model. All implementation was done in the in-house research platform BACI [193], a FE software written in C++ and utilizing the open-source libraries of the trilinos project [103]. The research code BACI is a joint development of the Institute for Computational Mechanics at the Technische Universität München. As a consequence, important general features such as, for example, different FE formulations, time integration schemes, and state-of-the-art iterative linear solvers could be used without modification. Hence, the basic ideas of the FEM and its application to the fluid field and the fluid grid field are only briefly addressed in the first three sections of chapter 3. The discretization of the structural membrane is derived in some more detail in section 3.4, since tailored FE formulations are used. Subsequently, some new features complementing the research code BACI are discussed, which have been devised in order to obtain a numerical efficient and robust erythrocyte model. In particular, the scaled thickness conditioning (STC) approach, proposed in [120], and an extension of the dual mortar based monolithic FSI approach introduced in [121] are presented.

Chapters 4, 5, and 6 present the results of numerical computations and show that the model is able to accurately predict the outcome for several experiments with one set of parameters. The fourth chapter addresses the shape of a cell at rest and shows its numerical construction based on different stress-free membrane configurations. Chapter 5 presents the response of the cell in laser traps both for static and dynamic motion. Furthermore, the influence of the stress-free state, of material parameters, and the assumed boundary conditions are discussed and compared with other numerical studies. The behavior of erythrocytes in steady shear flow is addressed in the fifth chapter. Particular focus is put on the influence of the fluid shear stresses and of the stress-free state of the membrane on the cell response. The chapter is completed by a numerical investigation of the shape memory effect.

The last chapter concludes the findings and gives an outlook on possible future work. The application of the presented model on potential further numerical investigations as well as reasonable extensions of the model are discussed.

Chapter 2

From basic continuum mechanics to governing equations for human erythrocytes

As has been discussed in the previous chapter, the challenges in describing the behavior of the human red blood cell (RBC) results from the two-layer nature of the membrane as well as its interaction with blood plasma and with cytosol. This chapter translates the particular features of the individual cell components and of the coupling between them into continuum mechanical equations.

From basic continuum mechanical principles, which are briefly stated in sections 2.1 and 2.2, nonlinear governing equations for both fluid fields and the membrane are derived in sections 2.3 and 2.4, respectively. Due to its complexity, the development of the membrane formulation is given in some more detail compared to the rather standard fluid description. Finally, algebraic constraints for the membrane and coupling conditions for the interaction of fluid and membrane, both in a continuous setting, are addressed in the last sections of this chapter.

2.1 Kinematics

In this first section, a general description of kinematics in an arbitrary Lagrangean Eulerian (ALE) framework is introduced. From this formulation, the kinematics of fluid flow and the motion of a structural body can both be obtained as special cases. The objective of this section is to provide basic notations and equations that are necessary to derive the governing equations for the individual fields. Since this section is kept very short, the interested reader is referred to textbooks on general continuum mechanics, for example, the ones by Truesdell and Noll [187] and by Gurtin [92].

2.1.1 Mappings and domains

Let $\Omega_{\mathbf{X}}$ be the *initial domain* or *material domain* covered by the fluid under observation or the structural body at initial time $t = t_0$. For every time $t > t_0$ the motion of a particle

is described by the motion mapping $\boldsymbol{\varphi}$, given as

$$\begin{aligned} &\boldsymbol{\varphi}(\,\cdot\,,t) : \Omega_{\mathbf{X}} \to \Omega_{\mathbf{x}}(t), \quad \mathbf{X} \mapsto \boldsymbol{\varphi}(\mathbf{X},t), \\ &\det\left(\frac{\partial \boldsymbol{\varphi}}{\partial \mathbf{X}}\right) > 0, \quad \forall \mathbf{X} \in \Omega_{\mathbf{X}},\, t \geq t_0, \\ &\boldsymbol{\varphi}(\mathbf{X},t_0) = \mathbf{X}, \quad \forall \mathbf{X} \in \Omega_{\mathbf{X}}. \end{aligned} \tag{2.1}$$

The homeomorphism $\boldsymbol{\varphi}$ introduces the *current* or *spatial domain* $\Omega_{\mathbf{x}}(t) = \boldsymbol{\varphi}(\Omega_{\mathbf{X}},t)$, i.e. the domain covered by the fluid or the structure at fixed time t. In order to have a general formulation suitable for both, fluid and structure motion, it is beneficial to define a so-called *reference domain* $\Omega_{\boldsymbol{\chi}}(t)$ which coincides with $\Omega_{\mathbf{X}}$ and $\Omega_{\mathbf{x}}(t)$ at initial time $t = t_0$. On this domain, a second homeomorphism $\boldsymbol{\Phi}$ can be defined as

$$\begin{aligned} &\boldsymbol{\Phi}(\,\cdot\,,t) : \Omega_{\boldsymbol{\chi}}(t) \to \Omega_{\mathbf{x}}(t), \quad \boldsymbol{\chi} \mapsto \boldsymbol{\Phi}(\boldsymbol{\chi},t), \\ &\det\left(\frac{\partial \boldsymbol{\Phi}}{\partial \boldsymbol{\chi}}\right) > 0, \quad \forall \boldsymbol{\chi} \in \Omega_{\boldsymbol{\chi}}(t),\, t \geq t_0, \\ &\boldsymbol{\Phi}(\boldsymbol{\chi},t_0) = \boldsymbol{\chi}, \quad \forall \boldsymbol{\chi} \in \Omega_{\boldsymbol{\chi}}(t_0) = \Omega_{\mathbf{X}}. \end{aligned} \tag{2.2}$$

In general, the reference domain and the associated mapping $\boldsymbol{\Phi}$ are arbitrary. If fluid flow is considered, most often not the motion of the whole fluid domain, which might undergo extremely large deformations, but the flow through a control volume $V(t)$ is of interest. While in many classical fluid application, $V(t)$ can be assumed to be fixed in space, a deformation of the control volume, e.g. the domain taken by the cytosol, is a crucial part of the problem definition in this work. Hence, if not stated otherwise, the map $\boldsymbol{\Phi}$ refers to the deformation of the control volume $V(t)$ within the remainder of this thesis.

The homeomorphisms $\boldsymbol{\varphi}$ and $\boldsymbol{\Phi}$ allow for a third mapping $\boldsymbol{\Psi}$, that relates the reference configuration to the initial configuration:

$$\boldsymbol{\Psi}(\,\cdot\,,t) := \left(\boldsymbol{\varphi}^{-1} \circ \boldsymbol{\Phi}\right) : \Omega_{\boldsymbol{\chi}}(t) \to \Omega_{\mathbf{X}}, \quad \boldsymbol{\chi} \mapsto \boldsymbol{\varphi}^{-1}(\boldsymbol{\Phi}(\boldsymbol{\chi},t),t). \tag{2.3}$$

Due to its construction, the function $\boldsymbol{\Psi}$ also defines a homeomorphism on the reference domain $\Omega_{\boldsymbol{\chi}}(t)$ with a positive determinant $\det\left(\partial\boldsymbol{\Phi}/\partial\boldsymbol{\chi}\right) > 0$. It coincides with the identity mapping on $\Omega_{\mathbf{X}}$ at initial time $t = t_0$. Given the brief discussion above, the inverse mapping $\boldsymbol{\Psi}^{-1} = (\boldsymbol{\Phi}^{-1} \circ \boldsymbol{\varphi})$ can be interpreted as the motion of an infinitesimal fluid volume modulo the motion of the fluid control volume $V(t)$, which by definition stays unchanged by $\boldsymbol{\Psi}$.

To ease the notation for subsequent derivations, it will be useful to define the *Jacobian determinants*

$$J(\mathbf{X},t) := \det\left(\frac{\partial \boldsymbol{\varphi}}{\partial \mathbf{X}}\right)(\mathbf{X},t) \tag{2.4}$$

$$J^{\mathcal{G}}(\boldsymbol{\chi},t) := \det\left(\frac{\partial \boldsymbol{\Phi}}{\partial \boldsymbol{\chi}}\right)(\boldsymbol{\chi},t). \tag{2.5}$$

2.1.2 Observers

The above introduced maps and domains give rise to three different *observers* measuring a physical quantity $\mathbf{f}$. For modeling the behavior of structures, usually a *Lagrangean* or *material observer* scheme is employed, which travels with material points. Consequently, the quantity $\mathbf{f}$ is measured with respect to fixed material points $\mathbf{X} \in \Omega_{\mathbf{X}}$:

$$\mathbf{f} = \mathbf{f}|_{\mathbf{X}}(\mathbf{X}, t). \tag{2.6}$$

This approach allows for a relatively easy description of the domain boundaries and, thus, of the motion of the whole domain.

A disadvantage of this approach becomes evident when fluid motion is considered. In most applications, the fluid domain undergoes very large deformations and, if described within a Lagrangean framework, the motion of all material points has to be tracked. However, tracking single fluid particles is usually not necessary, since only the flow through the control volume $V(t)$ is of interest. If the position of $V(t)$ is fixed in space, the *Eulerian observer* scheme is most feasible. Here, the observer is assumed to measure the quantity $\mathbf{f}$ of material points momentarily being at a fixed spatial position $\mathbf{x} \in \Omega_{\mathbf{x}}(t)$:

$$\mathbf{f} = \mathbf{f}|_{\mathbf{x}}(\mathbf{x}, t). \tag{2.7}$$

As already mentioned previously, a constant control volume $V(t)$ in time is not suitable when modeling erythrocytes, since the domain of interest changes over time. Thus, an *arbitrary Lagrangean-Eulerian (ALE) observer* scheme will be employed. It is the most general approach and measures the quantity $\mathbf{f}$ with respect to points $\boldsymbol{\chi} \in \Omega_{\boldsymbol{\chi}}(t)$ that are fixed in the reference domain

$$\mathbf{f} = \mathbf{f}|_{\boldsymbol{\chi}}(\boldsymbol{\chi}, t). \tag{2.8}$$

This implies that the observer is neither fixed to a material point nor fixed to a position in space, but can move arbitrarily with the given motion map $\boldsymbol{\Phi}$ defined in (2.2). The classical observer schemes can, therefore, be viewed as special cases of the ALE approach. For $\boldsymbol{\Phi} = \boldsymbol{\varphi}$, the observer moves with the domain, i.e. a Lagrangean scheme is obtained. On the other hand, if $\boldsymbol{\Phi}$ is identified with the identity mapping $\mathbf{1}$, the control volume $V(t)$ does not move and the Eulerian observer is recovered.

Having measured the quantity $\mathbf{f}$ with respect to one of the given observer schemes, this quantity can easily be expressed in terms of the other observers as

$$\mathbf{f}|_{\mathbf{X}}(\mathbf{X}, t) = \mathbf{f}|_{\mathbf{x}}(\boldsymbol{\varphi}(\mathbf{X}, t), t) = \mathbf{f}|_{\boldsymbol{\chi}}(\boldsymbol{\Psi}^{-1}(\mathbf{X}, t), t), \tag{2.9}$$

$$\mathbf{f}|_{\mathbf{x}}(\mathbf{x}, t) = \mathbf{f}|_{\mathbf{X}}(\boldsymbol{\varphi}^{-1}(\mathbf{x}, t), t) = \mathbf{f}|_{\boldsymbol{\chi}}(\boldsymbol{\Phi}^{-1}(\mathbf{x}, t), t), \tag{2.10}$$

$$\mathbf{f}|_{\boldsymbol{\chi}}(\boldsymbol{\chi}, t) = \mathbf{f}|_{\mathbf{X}}(\boldsymbol{\Psi}(\boldsymbol{\chi}, t), t) = \mathbf{f}|_{\mathbf{x}}(\boldsymbol{\Phi}(\boldsymbol{\chi}, t), t). \tag{2.11}$$

2.1.3 Displacements and velocities

With the motion maps of a body at hand, it is now possible to introduce *displacement* and *velocity* quantities. The particle displacement $\mathbf{d}$ is defined as the difference between

current and initial position. Particle velocities $\mathbf{u}$ and accelerations $\mathbf{a}$ are given as first and second time derivatives of the displacements, respectively. For a particle with initial position $\mathbf{X} \in \Omega_{\mathbf{X}}$, these quantities read

$$\mathbf{d}|_{\mathbf{X}}(\mathbf{X},t) = \boldsymbol{\varphi}(\mathbf{X},t) - \boldsymbol{\varphi}(\mathbf{X},t_0) = \boldsymbol{\varphi}(\mathbf{X},t) - \mathbf{X}, \tag{2.12}$$

$$\mathbf{u}|_{\mathbf{X}}(\mathbf{X},t) = \frac{\mathrm{d}\mathbf{d}|_{\mathbf{X}}}{\mathrm{d}t}(\mathbf{X},t) = \frac{\partial \mathbf{d}|_{\mathbf{X}}}{\partial t}(\mathbf{X},t) = \frac{\mathrm{d}\boldsymbol{\varphi}}{\mathrm{d}t}(\mathbf{X},t) = \frac{\partial \boldsymbol{\varphi}}{\partial t}(\mathbf{X},t), \tag{2.13}$$

$$\mathbf{a}|_{\mathbf{X}}(\mathbf{X},t) = \frac{\mathrm{d}^2\mathbf{d}|_{\mathbf{X}}}{\mathrm{d}t^2}(\mathbf{X},t) = \frac{\partial^2 \mathbf{d}|_{\mathbf{X}}}{\partial t^2}(\mathbf{X},t) = \frac{\mathrm{d}^2\boldsymbol{\varphi}}{\mathrm{d}t^2}(\mathbf{X},t) = \frac{\partial^2 \boldsymbol{\varphi}}{\partial t^2}(\mathbf{X},t). \tag{2.14}$$

Similarly, for a point $\boldsymbol{\chi} \in \Omega_{\boldsymbol{\chi}}(t)$ the displacements $\mathbf{d}^{\mathcal{G}}$ and the velocities $\mathbf{u}^{\mathcal{G}}$ of the reference domain are defined as

$$\mathbf{d}^{\mathcal{G}}|_{\boldsymbol{\chi}}(\boldsymbol{\chi},t) = \boldsymbol{\Phi}(\boldsymbol{\chi},t) - \boldsymbol{\Phi}(\boldsymbol{\chi},t_0) = \boldsymbol{\Phi}(\boldsymbol{\chi},t) - \boldsymbol{\chi}, \tag{2.15}$$

$$\mathbf{u}^{\mathcal{G}}|_{\boldsymbol{\chi}}(\boldsymbol{\chi},t) = \frac{\mathrm{d}\mathbf{d}^{\mathcal{G}}|_{\boldsymbol{\chi}}}{\mathrm{d}t}(\boldsymbol{\chi},t) = \frac{\partial \mathbf{d}^{\mathcal{G}}|_{\boldsymbol{\chi}}}{\partial t}(\boldsymbol{\chi},t) = \frac{\mathrm{d}\boldsymbol{\Phi}}{\mathrm{d}t}(\boldsymbol{\chi},t) = \frac{\partial \boldsymbol{\Phi}}{\partial t}(\boldsymbol{\chi},t). \tag{2.16}$$

The map $\boldsymbol{\Phi}$ is associated with the motion of the control volume $V(t)$. In the context of the finite element method (FEM), which will be introduced in the following chapter, this control volume $V(t)$ will be identified with the finite element (FE) grid of the fluid field. Therefore, the terminologies *grid displacement* for $\mathbf{d}^{\mathcal{G}}$ and *grid velocity* for $\mathbf{u}^{\mathcal{G}}$ are commonly used.

The definition of particle and grid velocity give rise to a third physical meaningful velocity, the so-called *ALE convective velocity* $\mathbf{c}$ defined as

$$\mathbf{c}|_{\mathbf{X}}(\mathbf{X},t) = \mathbf{u}|_{\mathbf{X}}(\mathbf{X},t) - \mathbf{u}^{\mathcal{G}}|_{\mathbf{X}}(\mathbf{X},t). \tag{2.17}$$

It is important to distinguish between ALE convective velocity $\mathbf{c}$ and the particle velocity modulo grid velocity $\mathbf{w}$. The latter can easily be identified with the time derivative of the motion mapping $\boldsymbol{\Psi}^{-1}$:

$$\mathbf{w}|_{\mathbf{X}}(\mathbf{X},t) = \frac{\mathrm{d}\boldsymbol{\Psi}^{-1}}{\mathrm{d}t}(\mathbf{X},t) = \frac{\partial \boldsymbol{\Psi}^{-1}}{\partial t}(\mathbf{X},t). \tag{2.18}$$

The next paragraph shows the relation between $\mathbf{c}$ and $\mathbf{w}$ and demonstrates that these velocities are useful quantities in order to derive the material time derivative of an arbitrary physical quantity.

2.1.4 Material time derivative of a physical quantity

Using identities (2.9) and (2.11) and the chain rule, the material time derivative of a physical quantity $\mathbf{f}$ can be expressed in terms of quantities measured in the reference or the spatial domain as

$$\begin{aligned}
\frac{\mathrm{d}\mathbf{f}|_{\mathbf{X}}(\mathbf{X},t)}{\mathrm{d}t} &= \frac{\mathrm{d}\mathbf{f}|_{\boldsymbol{\chi}}\left(\boldsymbol{\Psi}^{-1}(\mathbf{X},t),t\right)}{\mathrm{d}t} \\
&= \frac{\partial \mathbf{f}|_{\boldsymbol{\chi}}}{\partial t}\left(\boldsymbol{\Psi}^{-1}(\mathbf{X},t),t\right) + \frac{\partial \mathbf{f}|_{\boldsymbol{\chi}}}{\partial \boldsymbol{\chi}}\left(\boldsymbol{\Psi}^{-1}(\mathbf{X},t),t\right) \cdot \mathbf{w}|_{\mathbf{X}}(\mathbf{X},t) && (2.19) \\
&= \frac{\partial \mathbf{f}|_{\boldsymbol{\chi}}}{\partial t}\left(\boldsymbol{\Psi}^{-1}(\mathbf{X},t),t\right) + \frac{\partial \mathbf{f}|_{\mathbf{x}}}{\partial \mathbf{x}}\left(\boldsymbol{\varphi}(\mathbf{X},t),t\right) \cdot \frac{\partial \boldsymbol{\Phi}}{\partial \boldsymbol{\chi}}\left(\boldsymbol{\Psi}^{-1}(\mathbf{X},t),t\right) \cdot \mathbf{w}|_{\mathbf{X}}(\mathbf{X},t). && (2.20)
\end{aligned}$$

Here, the time derivatives $\frac{\partial(\cdot)|_{\boldsymbol{\chi}}}{\partial t}$ and $\frac{\partial(\cdot)|_{\mathbf{x}}}{\partial t}$ are defined for fixed reference coordinates $\boldsymbol{\chi}$ and spatial coordinates $\mathbf{x}$, respectively. To keep the notation short, tensor notation has been used. In order to evaluate (2.19) and (2.20), derivatives of the potentially vector valued quantity $\mathbf{f}$ with respect to the coordinates $\boldsymbol{\chi}$ or $\mathbf{x}$ have to be determined. In index notation, the respective gradient operator reads

$$\left(\frac{\partial \mathbf{f}}{\partial \boldsymbol{\chi}}\right)_{ij} = (\boldsymbol{\nabla}_{\boldsymbol{\chi}} \mathbf{f})_{ij} = \frac{\partial f_i}{\partial \chi_j} \tag{2.21}$$

$$\left(\frac{\partial \mathbf{f}}{\partial \mathbf{x}}\right)_{ij} = (\boldsymbol{\nabla}_{\mathbf{x}} \mathbf{f})_{ij} = \frac{\partial f_i}{\partial x_j}. \tag{2.22}$$

In particular, the index notation of the last product in (2.20) is given as

$$\frac{\partial \mathbf{f}|_{\mathbf{x}}}{\partial \mathbf{x}} \cdot \frac{\partial \boldsymbol{\Phi}}{\partial \boldsymbol{\chi}} \cdot \mathbf{w}|_{\mathbf{X}} = \frac{\partial (\mathbf{f}|_{\mathbf{x}})_i}{\partial x_j} \frac{\partial \Phi_j}{\partial \chi_k} (\mathbf{w}|_{\mathbf{X}})_k, \tag{2.23}$$

where *Einstein summation convention* applies, i.e. when an index appears twice in a single term, summation over all its possible values is implied.

In order to find an alternative expression for the velocity $\mathbf{c}$, the general relation (2.19) is applied to the spatial coordinate $\mathbf{x}$, i.e. $\mathbf{f}|_{\mathbf{X}} = \boldsymbol{\varphi}$ and $\mathbf{f}|_{\boldsymbol{\chi}} = \boldsymbol{\Phi}$. Thus, the particle velocity can equivalently be expressed as

$$\underbrace{\frac{\mathrm{d}\boldsymbol{\varphi}}{\mathrm{d}t}}_{\mathbf{u}|_{\mathbf{X}}}(\mathbf{X}, t) = \underbrace{\frac{\partial \boldsymbol{\Phi}}{\partial t}}_{\mathbf{u}^{\mathcal{G}}|_{\boldsymbol{\chi}}}(\boldsymbol{\Psi}^{-1}(\mathbf{X}, t), t) + \frac{\partial \boldsymbol{\Phi}}{\partial \boldsymbol{\chi}} \left(\boldsymbol{\Psi}^{-1}(\mathbf{X}, t), t\right) \cdot \mathbf{w}|_{\mathbf{X}}(\mathbf{X}, t). \tag{2.24}$$

Comparing (2.17) and (2.24) immediately leads to

$$\mathbf{c}|_{\mathbf{X}}(\mathbf{X}, t) = \frac{\partial \boldsymbol{\Phi}}{\partial \boldsymbol{\chi}} \left(\boldsymbol{\Psi}^{-1}(\mathbf{X}, t), t\right) \cdot \mathbf{w}|_{\mathbf{X}}(\mathbf{X}, t) \tag{2.25}$$

and, finally, to a shortened version of the material time derivative (2.20)

$$\frac{\mathrm{d}\mathbf{f}|_{\mathbf{X}}(\mathbf{X}, t)}{\mathrm{d}t} = \frac{\partial \mathbf{f}|_{\boldsymbol{\chi}}}{\partial t} \left(\boldsymbol{\Psi}^{-1}(\mathbf{X}, t), t\right) + \frac{\partial \mathbf{f}|_{\mathbf{x}}}{\partial \mathbf{x}} (\boldsymbol{\varphi}(\mathbf{X}, t), t) \cdot \mathbf{c}|_{\mathbf{X}}(\mathbf{X}, t). \tag{2.26}$$

The next Remark 2.1 shows, how the Eulerian representation of the last equation can be obtained as a special case. Remark 2.2 presents the application of (2.26) to find an expression for material accelerations in referential coordinates.

Remark 2.1 (Eulerian representation) *The Eulerian representation for the material time derivative of a physical quantity* $\mathbf{f}$ *can be deduced as a special case of* (2.26)*. If the mapping* $\boldsymbol{\Phi}$ *is taken as identity mapping* $\mathbf{1}$ *on* $\Omega_{\boldsymbol{\chi}}(t)$*, grid velocities vanish, i.e.* $\mathbf{c}|_{\mathbf{X}} = \mathbf{u}|_{\mathbf{X}}$*. Thus,* (2.26) *reduces to*

$$\frac{\mathrm{d}\mathbf{f}|_{\mathbf{X}}(\mathbf{X}, t)}{\mathrm{d}t} = \frac{\partial \mathbf{f}|_{\mathbf{x}}}{\partial t} (\boldsymbol{\varphi}(\mathbf{X}, t), t) + \frac{\partial \mathbf{f}|_{\mathbf{x}}}{\partial \mathbf{x}} (\boldsymbol{\varphi}(\mathbf{X}, t), t) \cdot \mathbf{u}|_{\mathbf{X}}(\mathbf{X}, t). \tag{2.27}$$

Remark 2.2 (Accelerations) *The transformation* (2.26) *can also be employed to express the material accelerations* $\mathbf{a}|_{\mathbf{X}}(\mathbf{X}, t)$ *defined in* (2.14) *in the ALE framework:*

$$\mathbf{a}|_{\mathbf{X}}(\mathbf{X}, t) = \frac{\mathrm{d}\mathbf{u}|_{\mathbf{X}}(\mathbf{X}, t)}{\mathrm{d}t} = \frac{\partial \mathbf{u}|_{\boldsymbol{\chi}}}{\partial t} \left(\boldsymbol{\Psi}^{-1}(\mathbf{X}, t), t\right) + \frac{\partial \mathbf{u}|_{\mathbf{x}}}{\partial \mathbf{x}} (\boldsymbol{\varphi}(\mathbf{X}, t), t) \cdot \mathbf{c}|_{\mathbf{X}}(\mathbf{X}, t). \tag{2.28}$$

2.2 Balance equations

In this section, fundamental laws stating the conservation of mass and the balance of momentum are derived. A common property of these quantities is their definition by a volumetric integral. To state the balance equations, the material time derivative of these integrals is to be considered. To start with, the Reynolds' transport theorem is presented which yields a general expression for such a time derivative. The particular versions for mass and linear momentum will serve as a starting point for the governing equations of fluid and structure fields. The balance of momentum uses the kinetic relationship between motion and loads on the domain and its boundary as introduced by Newton's second law. Balance of angular momentum is also briefly addressed in the final subsection 2.2.4.

For details and proofs of the derivations, the reader is again referred to the textbooks by Gurtin [92] and Truesdell and Noll [187] or to the thesis by Gamnitzer [74].

2.2.1 Transport theorem

The *Reynolds' transport theorem* considers the material time derivative of a quantity $\mathbf{G}(t)$ that is defined as an integral of a physical quantify $\mathbf{f}$, i.e.

$$\mathbf{G}(t) = \int_{V^{\mathcal{G}}(t)} \mathbf{f}|_{\boldsymbol{\chi}}(\boldsymbol{\chi}, t)\, \mathrm{d}\boldsymbol{\chi}. \tag{2.29}$$

In order to obtain a general, i.e. ALE, version of the theorem, the balance volume $V^{\mathcal{G}}(t) \in \Omega_{\boldsymbol{\chi}}(t)$ has been chosen in the reference domain. The integral domain is, thus, transported in time by the mapping $V^{\mathcal{G}}(t) = \boldsymbol{\Psi}^{-1}(V(t_0), t)$, which brings about that the computation of the time derivative $\frac{\mathrm{d}\mathbf{G}}{\mathrm{d}t}$ is not straightforward. Two alternative ways have been presented in the theses of Wall [192] and Gamnitzer [74], both resulting in the ALE Reynolds' transport theorem in referential configuration

$$\begin{aligned}
\frac{\mathrm{d}\mathbf{G}(t)}{\mathrm{d}t} &= \int_{V^{\mathcal{G}}(t)} \left(\frac{\partial \mathbf{f}|_{\boldsymbol{\chi}}}{\partial t}(\boldsymbol{\chi}, t) + \sum_j \frac{\partial \left(\mathbf{f}|_{\boldsymbol{\chi}} \cdot (\mathbf{w}|_{\boldsymbol{\chi}})_j \right)}{\partial \chi_j}(\boldsymbol{\chi}, t) \right) \mathrm{d}\boldsymbol{\chi} \\
&= \int_{V^{\mathcal{G}}(t)} \left(\frac{\partial \mathbf{f}|_{\boldsymbol{\chi}}}{\partial t}(\boldsymbol{\chi}, t) + \frac{\partial \mathbf{f}|_{\boldsymbol{\chi}}}{\partial \boldsymbol{\chi}}(\boldsymbol{\chi}, t) \cdot \mathbf{w}|_{\boldsymbol{\chi}}(\boldsymbol{\chi}, t) + \right. \\
&\qquad \left. + \mathbf{f}|_{\boldsymbol{\chi}}(\boldsymbol{\chi}, t)\, \mathrm{div}|_{\boldsymbol{\chi}}(\mathbf{w}|_{\boldsymbol{\chi}})(\boldsymbol{\chi}, t)) \right) \mathrm{d}\boldsymbol{\chi}
\end{aligned} \tag{2.30}$$

where the divergence operator $\mathrm{div}|_{\boldsymbol{\chi}}$ for a quantity g with respect to the reference coordinates has been introduced as

$$\mathrm{div}|_{\boldsymbol{\chi}}(\mathbf{g}|_{\boldsymbol{\chi}}) = \sum_j \frac{\partial (\mathbf{g}|_{\boldsymbol{\chi}})_j}{\partial \chi_j}. \tag{2.31}$$

Again, the Lagrangean and Eulerian versions of the Reynolds' transport theorem can easily be deduced from the ALE version (2.30) as shown in Remark 2.3. It is sometimes

beneficial to express also the ALE version (2.30) in terms of spatial coordinates. The expression is shown in Remark 2.4 and is not to be confused with the Eulerian version of the transport theorem. For details, the reader is, for example, referred to the textbook of Donea and Huerta [50].

Remark 2.3 (Special cases of the transport theorem) *In case of a Lagrangean observer, the motion map $\boldsymbol{\Psi}^{-1}$ equals the identity map $\mathbf{1}$. Consequently, the velocity $\mathbf{w}$ vanishes and the transport theorem* (2.30) *reduces to*

$$\frac{\mathrm{d}\mathbf{G}(t)}{\mathrm{d}t} = \int_{V(t)} \frac{\partial \mathbf{f}|_{\mathbf{X}}}{\partial t}(\mathbf{X}, t)\,\mathrm{d}\mathbf{X}. \tag{2.32}$$

Alternatively, this equation can be easily derived from fact that, in a Lagrangean framework, the balance volume $V(t) = V(t_0)$ does not only have a constant shape but also contains the same particles at all times t. Thus, the order of integration and differentiation can be interchanged.

In classical fluid applications, the control or balance volume $V(t) = \boldsymbol{\varphi}(V(t_0), t)$ is fixed in space and the transport theorem in spatial configuration is to be employed. Here, with $\boldsymbol{\Phi} = \mathbf{1}$, $\boldsymbol{\Psi}^{-1} = \boldsymbol{\varphi}^{-1}$, and $\mathbf{w} = \mathbf{c} = \mathbf{u}$, the transport theorem emerges as

$$\begin{aligned}\frac{\mathrm{d}\mathbf{G}(t)}{\mathrm{d}t} &= \int_{V(t)} \left(\frac{\partial \mathbf{f}|_{\mathbf{x}}}{\partial t}(\mathbf{x}, t) + \sum_j \frac{\partial \left(\mathbf{f}|_{\mathbf{x}} \cdot (\mathbf{u}|_{\mathbf{x}})_j \right)}{\partial \mathbf{x}_j}(\mathbf{x}, t) \right) \mathrm{d}\mathbf{x} \\ &= \int_{V(t)} \left(\frac{\mathrm{d}\mathbf{f}|_{\mathbf{x}}}{\mathrm{d}t}(\boldsymbol{\varphi}^{-1}(\mathbf{x}, t), t) + \mathbf{f}|_{\mathbf{x}}(\mathbf{x}, t)\,\mathrm{div}|_{\mathbf{x}}(\mathbf{u}|_{\mathbf{x}})(\mathbf{x}, t) \right) \mathrm{d}\mathbf{x},\end{aligned} \tag{2.33}$$

with the spatial divergence operator $\mathrm{div}|_{\mathbf{x}}$ defined as

$$\mathrm{div}|_{\mathbf{x}}(\mathbf{f}) = \sum_j \frac{\partial (\mathbf{f}|_{\mathbf{x}})_j}{\partial x_j}. \tag{2.34}$$

Remark 2.4 (ALE transport theorem in spatial coordinates) *In case of two physical quantities $\mathbf{f}$ and $\tilde{\mathbf{f}}$ with*

$$\mathbf{G}(t) = \int_{V^{\mathcal{G}}(t)} \mathbf{f}|_{\boldsymbol{\chi}}(\boldsymbol{\chi}, t)\,\mathrm{d}\boldsymbol{\chi} = \int_{V(t)} \tilde{\mathbf{f}}|_{\mathbf{x}}(\mathbf{x}, t)\,\mathrm{d}\mathbf{x} \tag{2.35}$$

for control volumes $V^{\mathcal{G}}(t) \subset \Omega_{\boldsymbol{\chi}}(t)$ and $V(t) = \boldsymbol{\Phi}(V^{\mathcal{G}}(t)) \subset \Omega_{\mathbf{x}}(t)$, it can be shown that the ALE Reynolds' transport theorem (2.30) *can be equivalently expressed in terms of the spatial quantity $\tilde{\mathbf{f}}$:*

$$\begin{aligned}\frac{\mathrm{d}\mathbf{G}(t)}{\mathrm{d}t} = \int_{V(t)} \Bigg(&\frac{\partial \tilde{\mathbf{f}}|_{\mathbf{x}}}{\partial t}(\boldsymbol{\Phi}^{-1}(\mathbf{x}, t), t) + \frac{\partial \tilde{\mathbf{f}}|_{\mathbf{x}}}{\partial \mathbf{x}}(\mathbf{x}, t) \cdot \mathbf{c}|_{\mathbf{x}}(\mathbf{x}, t) + \\ &+ \tilde{\mathbf{f}}|_{\mathbf{x}}(\mathbf{x}, t)\,\mathrm{div}|_{\mathbf{x}}(\mathbf{u}|_{\mathbf{x}})(\mathbf{x}, t) \Bigg)\,\mathrm{d}\mathbf{x}.\end{aligned} \tag{2.36}$$

Details on the proof of equivalence can, for example, be found in the thesis of Gamnitzer [74, Appendix A].

It is important to note that, although spatial coordinates are used, equation (2.36) *still states the ALE Reynolds' transport theorem, as opposed to its spatial version* (2.33)*.*

2.2.2 Mass conservation

As first application of the transport theorem defined in the previous subsection, the mass $m(V(t))$ of a volume $V(t) \subset \Omega_{\mathbf{x}}(t)$ is considered. Introducing the *spatial density* ρ in every point $\mathbf{x}$ as the limit of the ratio between mass m and volume vol for vanishing V around $\mathbf{x}$, i.e.

$$\rho|_{\mathbf{x}}(\mathbf{x},t) = \lim_{\mathrm{vol}(V)\to 0} \frac{m(V)}{\mathrm{vol}(V)}, \quad \mathbf{x} \in V \subset \Omega_{\mathbf{x}}(t), \tag{2.37}$$

allows to compute the total mass $m(V(t))$ by the integral expression

$$m(V(t)) = \int_{V(t)} \rho|_{\mathbf{x}}(\mathbf{x},t)\ \mathrm{d}\mathbf{x}. \tag{2.38}$$

To evaluate the mass of $V(t)$ in terms of reference or material configurations, the *reference density* $\rho^{\mathcal{G}}$ and *material density* ρ^0 are defined such that

$$m(V(t)) = \int_{V(t)} \rho|_{\mathbf{x}}(\mathbf{x},t)\ \mathrm{d}\mathbf{x} = \int_{\mathbf{\Phi}^{-1}(V(t))} \rho^{\mathcal{G}}|_{\boldsymbol{\chi}}(\boldsymbol{\chi},t)\ \mathrm{d}\boldsymbol{\chi} = \int_{\boldsymbol{\varphi}^{-1}(V(t))} \rho^0|_{\mathbf{X}}(\mathbf{X},t)\ \mathrm{d}\mathbf{X}. \tag{2.39}$$

Thus, the mass has been expressed as an integral quantity as in (2.29). Moreover, the connection between the different density quantities can be identified as

$$\rho^{\mathcal{G}}|_{\boldsymbol{\chi}}(\boldsymbol{\chi},t) = \rho|_{\boldsymbol{\chi}}(\boldsymbol{\chi},t)\, J^{\mathcal{G}}|_{\boldsymbol{\chi}}(\boldsymbol{\chi},t) \quad \text{and} \tag{2.40}$$

$$\rho^0|_{\mathbf{X}}(\mathbf{X},t) = \rho|_{\mathbf{X}}(\mathbf{X},t)\, J|_{\mathbf{X}}(\mathbf{X},t), \tag{2.41}$$

where the determinants J and $J^{\mathcal{G}}$ have been defined in (2.4) and (2.5). The principle of mass conservation states that the mass contained in a transported volume does not change over time. Considering a balance volume $V^{\mathcal{G}}(t) = \mathbf{\Phi}^{-1}(V(t))$ in the reference configuration, the transport theorem (2.30) leads to the ALE mass conservation equation

$$\frac{\mathrm{d}V^{\mathcal{G}}(t)}{\mathrm{d}t} = \int_{V^{\mathcal{G}}(t)} \left(\frac{\partial \rho^{\mathcal{G}}|_{\boldsymbol{\chi}}}{\partial t}(\boldsymbol{\chi},t) + \sum_j \frac{\partial (\rho^{\mathcal{G}}|_{\boldsymbol{\chi}}(\mathbf{w}|_{\boldsymbol{\chi}})_j)}{\partial \chi_j}(\boldsymbol{\chi},t) \right) \mathrm{d}\boldsymbol{\chi} = 0. \tag{2.42}$$

Since the mass of any transported volume is to be preserved, (2.42) has to hold independently of the considered volume $V^{\mathcal{G}}(t)$. Consequently, the local ALE mass conservation equation is obtained as

$$\frac{\partial \rho^{\mathcal{G}}|_{\boldsymbol{\chi}}}{\partial t}(\boldsymbol{\chi},t) + \sum_j \frac{\partial (\rho^{\mathcal{G}}|_{\boldsymbol{\chi}}(\mathbf{w}|_{\boldsymbol{\chi}})_j)}{\partial \chi_j}(\boldsymbol{\chi},t) = 0, \tag{2.43}$$

which is also known as the ALE version of the continuity equation.

When it comes to incompressible behavior of fluids, it is useful to express the continuity equation in terms of spatial coordinates and the spatial density ρ. Following the same argumentation as before, but using the equivalent form of the ALE Reynolds' transport

theorem given in (2.36) instead of (2.30), the ALE version of the continuity equations in spatial representation is obtained for any point $\mathbf{x} = \mathbf{\Phi}(\boldsymbol{\chi}, t)$ as

$$\frac{\partial \rho|_{\boldsymbol{\chi}}}{\partial t}(\mathbf{\Phi}^{-1}(\mathbf{x},t),t) + \frac{\partial \rho|_{\mathbf{x}}}{\partial \mathbf{x}}(\mathbf{x},t) \cdot \mathbf{c}|_{\mathbf{x}}(\mathbf{x},t) + \rho|_{\mathbf{x}}(\mathbf{x},t)\mathrm{div}|_{\mathbf{x}}(\mathbf{u}|_{\mathbf{x}})(\mathbf{x},t) = 0. \tag{2.44}$$

Again, this relation is not to be mistaken for the spatial continuity equation, which is introduced in the following remark.

Remark 2.5 (Special cases of the continuity equation) *The local Lagrangean form of the continuity equation can easily be deduced using* (2.43) *and expressed in terms of the spatial density*

$$\frac{\partial \rho^0|_{\mathbf{X}}}{\partial t}(\mathbf{X},t) = \frac{\partial \left(\rho \cdot J\right)|_{\mathbf{X}}}{\partial t}(\mathbf{X},t) = 0. \tag{2.45}$$

The second special case of (2.43) *is the local Eulerian form*

$$\frac{\partial \rho|_{\mathbf{x}}}{\partial t}(\mathbf{x},t) + \sum_j \frac{\partial(\rho|_{\mathbf{x}}(\mathbf{u}|_{\mathbf{x}})_j)}{\partial x_j}(\mathbf{x},t) = 0. \tag{2.46}$$

2.2.3 Balance of linear momentum

So far, the motion of a fluid field or a structure body has been described without considering the cause of motion. In order to introduce the kinetics of fluid flow or structure motion, first the linear momentum $\mathbf{P}(V(t))$ associated with a transported balance volume $V(t) \subset \Omega_{\mathbf{x}}(t)$ with representation $V^{\mathcal{G}}(t) = \mathbf{\Phi}^{-1}(V(t),t)$ in the reference domain is defined by

$$\mathbf{P}(V(t)) = \int_{V^{\mathcal{G}}(t)} \rho^{\mathcal{G}}|_{\boldsymbol{\chi}}(\boldsymbol{\chi},t)\, \mathbf{u}|_{\boldsymbol{\chi}}(\boldsymbol{\chi},t)\, \mathrm{d}\boldsymbol{\chi} \tag{2.47}$$

$$= \int_{V(t)} \rho|_{\mathbf{x}}(\mathbf{x},t)\, \mathbf{u}|_{\mathbf{x}}(\mathbf{x},t)\, \mathrm{d}\mathbf{x}. \tag{2.48}$$

Its material time derivative will be focused on in the kinetic considerations to follow. Applying the ALE Reynolds theorem (2.30), the product rule, and the ALE version of the continuity equation (2.43), the time derivative of the linear momentum $\mathbf{P}$ emerges as

$$\frac{\mathrm{d}\mathbf{P}(V(t))}{\mathrm{d}t} = \int_{V^{\mathcal{G}}(t)} \rho^{\mathcal{G}}|_{\boldsymbol{\chi}}(\boldsymbol{\chi},t) \left(\frac{\partial \mathbf{u}|_{\boldsymbol{\chi}}}{\partial t}(\boldsymbol{\chi},t) + \frac{\partial \mathbf{u}|_{\boldsymbol{\chi}}}{\partial \boldsymbol{\chi}}(\boldsymbol{\chi},t) \cdot \mathbf{w}|_{\boldsymbol{\chi}}(\boldsymbol{\chi},t) \right) \mathrm{d}\boldsymbol{\chi} \tag{2.49}$$

in reference representation. A spatial representation of this equation can easily be derived from (2.48) using (2.36) and (2.44), i.e.

$$\frac{\mathrm{d}\mathbf{P}(V(t))}{\mathrm{d}t} = \int_{V(t)} \rho|_{\mathbf{x}}(\mathbf{x},t) \left(\frac{\partial \mathbf{u}|_{\boldsymbol{\chi}}}{\partial t}(\mathbf{\Phi}^{-1}(\mathbf{x},t),t) + \frac{\partial \mathbf{u}|_{\mathbf{x}}}{\partial \mathbf{x}}(\mathbf{x},t) \cdot \mathbf{c}|_{\mathbf{x}}(\mathbf{x},t) \right) \mathrm{d}\mathbf{x}. \tag{2.50}$$

The continuum mechanics extension of Newton's second law states that for every balance volume $V(t)$ the change of linear momentum equals the resulting force on this

balance volume. Two kinds of external forces are discussed in this work acting on the volume $V(t)$ and its boundary $\partial V(t)$. First, forces of volume type are expressed as body force per unit mass, the spatial representation of which is $\mathbf{b}|_{\mathbf{x}}$. Second, forces of surface type are considered. These are accounted for by the surface traction vector $\mathbf{t}|_{\mathbf{x}}$ associated with the current configuration. Given a resulting force $\mathbf{R}(a)$ on a surface a, the surface traction $\mathbf{t}$ is defined as limit value

$$\mathbf{t}|_{\mathbf{x}}(\mathbf{x}, t, \mathbf{n}|_{\mathbf{x}}) = \lim_{\mathrm{area}(a)\to 0} \frac{\mathbf{R}(a)}{\mathrm{area}(a)}, \quad \mathbf{x} \in a \subset \partial V(t), \tag{2.51}$$

where $\mathbf{n}|_{\mathbf{x}}$ denotes the spatial representation of the unit outward pointing normal vector on a. The latter has been introduced to indicate that for different balance volumes, which share a common point $\mathbf{x}$ on their respective boundaries, the limit (2.51) might result in different surface traction vectors if the respective surface normal vectors do not coincide. The extension of Newton's second law, finally, reads

$$\frac{\mathrm{d}\mathbf{P}(V(t))}{\mathrm{d}t} = \int_{V(t)} \rho|_{\mathbf{x}}(\mathbf{x}, t)\, \mathbf{b}|_{\mathbf{x}}(\mathbf{x}, t)\, \mathrm{d}\mathbf{x} + \int_{\partial V(t)} \mathbf{t}|_{\mathbf{x}}(\mathbf{x}, t, \mathbf{n}|_{\mathbf{x}})\, \mathrm{d}a. \tag{2.52}$$

The kinetic relation (2.52) cannot easily be put into relation with the kinematic equations introduced so far due to the boundary integral in (2.52). Therefore, Cauchy's fundamental lemma is used, which states the existence and uniqueness of a tensor field $\boldsymbol{\sigma}$, the so-called *Cauchy stress tensor* field, with

$$\mathbf{t}|_{\mathbf{x}}(\mathbf{x}, t, \mathbf{n}|_{\mathbf{x}}) = \boldsymbol{\sigma}|_{\mathbf{x}}(\mathbf{x}, t) \cdot \mathbf{n}|_{\mathbf{x}}. \tag{2.53}$$

The lemma holds for any point $\mathbf{x} \in \partial V(t)$ of any balance volume $V(t) \subset \Omega_{\mathbf{x}}(t)$ and, hence, for any point $\mathbf{x} \in \Omega_{\mathbf{x}}(t)$. It, thus, allows for the transformation of the boundary integral in (2.52) into a volume integral by applying Gauss' divergence theorem:

$$\frac{\mathrm{d}\mathbf{P}(V(t))}{\mathrm{d}t} = \int_{V(t)} \left(\rho|_{\mathbf{x}}(\mathbf{x}, t)\, \mathbf{b}|_{\mathbf{x}}(\mathbf{x}, t) + \mathbf{div}|_{\mathbf{x}}(\boldsymbol{\sigma}|_{\mathbf{x}})(\mathbf{x}, t)\right)\, \mathrm{d}\mathbf{x}, \tag{2.54}$$

where the vector valued divergence operator $\mathbf{div}$ of a tensor valued quantity $\mathbf{T}$ with respect to spatial coordinates is defined as

$$(\mathbf{div}|_{\mathbf{x}}(\mathbf{T}))_i = \frac{\partial T_{ij}}{\partial x_j}. \tag{2.55}$$

The identity of (2.50) and (2.54) holds for every balance Volume $V(t)$ and, thus, leads to the local form of the ALE linear momentum balance equation in spatial representation

$$\frac{\partial \mathbf{u}|_{\mathcal{X}}}{\partial t}(\boldsymbol{\Phi}^{-1}(\mathbf{x}, t), t) + \frac{\partial \mathbf{u}|_{\mathbf{x}}}{\partial \mathbf{x}}(\mathbf{x}, t) \cdot \mathbf{c}|_{\mathbf{x}}(\mathbf{x}, t) = \mathbf{b}|_{\mathbf{x}}(\mathbf{x}, t) + \frac{1}{\rho|_{\mathbf{x}}(\mathbf{x}, t)} \mathbf{div}|_{\mathbf{x}}(\boldsymbol{\sigma}|_{\mathbf{x}})(\mathbf{x}, t). \tag{2.56}$$

Remark 2.6 (Special cases of momentum conservation) *The Lagrangean linear momentum conservation equations in spatial representation can easily be deduced as*

$$\frac{\partial \mathbf{u}|_{\mathbf{X}}}{\partial t}(\boldsymbol{\varphi}^{-1}(\mathbf{x}, t), t) = \mathbf{b}|_{\mathbf{x}}(\mathbf{x}, t) + \frac{1}{\rho|_{\mathbf{x}}(\mathbf{x}, t)} \mathbf{div}|_{\mathbf{x}}(\boldsymbol{\sigma}|_{\mathbf{x}})(\mathbf{x}, t). \tag{2.57}$$

In order to describe the motion of a deformable structure subjected to external loads, the balance equation (2.57) *is usually transferred into material representation. When it comes to the derivation of the governing equations for the erythrocyte membrane in section 2.4, this transformation is presented in some detail and the appropriate stress tensor fields are introduced.*

The Eulerian version of the linear momentum balance in spatial representation

$$\frac{\mathrm{d}\mathbf{u}|_{\mathbf{x}}}{\mathrm{d}t}(\mathbf{x},t) + \frac{\partial \mathbf{u}|_{\mathbf{x}}}{\partial \mathbf{x}}(\mathbf{x},t) \cdot \mathbf{u}|_{\mathbf{x}}(\mathbf{x},t) = \mathbf{b}|_{\mathbf{x}}(\mathbf{x},t) + \frac{1}{\rho|_{\mathbf{x}}(\mathbf{x},t)} \mathbf{div}|_{\mathbf{x}}(\boldsymbol{\sigma}|_{\mathbf{x}})(\mathbf{x},t) \tag{2.58}$$

is the basis for the description of standard fluid flow on fixed domains.

2.2.4 Balance of angular momentum

Similarly to the linear momentum, the angular momentum $\mathbf{A}(V(t), \mathbf{x}_0)$ with respect to a fixed spatial point $\mathbf{x}_0 \in \Omega_{\mathbf{x}}(t)$ and a balance volume $V(t) \in \Omega_{\mathbf{x}}(t)$ in the spatial domain is defined as

$$\mathbf{A}(V(t)) = \int_{V(t)} \rho|_{\mathbf{x}}(\mathbf{x},t) \left((\mathbf{x} - \mathbf{x}_0) \times \mathbf{u}|_{\mathbf{x}}(\mathbf{x},t) \right) \mathrm{d}\mathbf{x}. \tag{2.59}$$

Its change over time can be calculated based on the transport theorem (2.36) and has to equal the resulting moments from body force $\mathbf{b}$ and from the surface traction $\mathbf{t}$. After some lengthy calculation, which is shown in Appendix A, this results in the symmetry of the Cauchy stress tensor

$$\boldsymbol{\sigma}|_{\mathbf{x}}(\mathbf{x},t) = \boldsymbol{\sigma}^{\mathsf{T}}|_{\mathbf{x}}(\mathbf{x},t). \tag{2.60}$$

2.3 Governing equations - Fluid

Throughout this thesis, the considered fluid fields represent either the blood plasma or the cytosol. From the continuum mechanical point of view, both fields can be described as incompressible flows of Newtonian fluids. The governing equations for such a fluid field are addressed in this section. Since only laminar flows have to be considered, the resulting flow description is rather standard. Therefore, the section can be kept relatively short.

First, incompressible fluid flow is discussed. Second, the constitutive relations for both Newtonian fluid fields are stated. Combining these to points, the initial boundary value problem for the incompressible Navier-Stokes equations on a deformable domain are presented in the third subsection.

For more details on the topic and possible extensions to more sophisticated flow descriptions and fluid constitutive equations, the reader is referred to textbooks on fluid mechanics for example by Batchelor [7], Donea and Huerta [50], and by Truesdell and Rajagopal [188].

Although an ALE formulation for the fluid will be used to account for the deformation of the control volume $V(t)$, the equations will be given in spatial coordinates. To ease the notation, the index $\cdot|_{\mathbf{x}}$ indicating an Eulerian observer and the point of observation $\mathbf{x}$ can, thus, be omitted, i.e. $\mathbf{f} = \mathbf{f}|_{\mathbf{x}}(\mathbf{x}, t)$.

2.3.1 Incompressibility

A fluid flow is said to be incompressible if the density of a fluid particle is not affected by the pressure within the fluid. Incompressibility is not a property of the fluid, but of the flow under consideration. For example, air flow in the lung can be assumed incompressible, whereas the air flowing around an aircraft has to be described as a compressible fluid problem.

For the application at hand, the flow of blood plasma and cytosol can be considered to exhibit a constant density in space and time, which is a sufficient but not necessary condition for incompressible fluid flows. Consequently, the ALE continuity equation in spatial representation (2.44) reduces to

$$\mathrm{div}(\mathbf{u}) = 0. \tag{2.61}$$

Thus, the continuity equation enforces a divergence-free fluid flow.

2.3.2 Constitutive equations

Constitutive equations state the relation between fluid motion and internal loads represented by the Cauchy stress tensor $\boldsymbol{\sigma}$. At static equilibrium, fluids are able to support only a hydrostatic stress state. It is expressed in terms of the fluid *pressure* p, which is defined as

$$p = -\mathrm{tr}(\boldsymbol{\sigma}). \tag{2.62}$$

This relation allows to separate the stress tensor $\boldsymbol{\sigma}$ into a hydrostatic stress state $p\,\mathbf{1}$, with $\mathbf{1}$ being the second order identity tensor, and the so-called *viscous stress tensor* $\boldsymbol{\tau}$ given as

$$\boldsymbol{\tau} = \boldsymbol{\sigma} + p \cdot \mathbf{1} \tag{2.63}$$

By definition, the tensor $\boldsymbol{\tau}$ represents the trace free, deviatoric part of the Cauchy stress tensor $\boldsymbol{\sigma}$.

When modeling an incompressible fluid flow, a constitutive equation can only be prescribed for the viscous stresses $\boldsymbol{\tau}$. The pressure p, on the other hand, can be interpreted as a Lagrange multiplier enforcing the incompressibility of the flow and a constitutive relation between pressure and fluid motion cannot be provided.

For all fluid formulations used in this thesis, *Newtonian fluids* are considered. In this case, a linear dependency is assumed between viscous stresses $\boldsymbol{\tau}$ and symmetric part $\boldsymbol{\varepsilon}$ of the velocity gradient, which is defined as

$$\boldsymbol{\varepsilon}(\mathbf{u}) = \frac{1}{2}\left(\boldsymbol{\nabla}\mathbf{u} + \boldsymbol{\nabla}\mathbf{u}^{\mathsf{T}}\right). \tag{2.64}$$

The symbolic gradient operator $\boldsymbol{\nabla} = \boldsymbol{\nabla}_{\mathbf{x}}$ is evaluated with respect to spatial coordinates and corresponds to the definition (2.22). Finally, the constitutive equation for a Newtonian fluid in an incompressible flow reads

$$\boldsymbol{\tau} = 2\mu \cdot \boldsymbol{\varepsilon}(\mathbf{u}) - \tfrac{2}{3}\mu \cdot \mathrm{tr}(\boldsymbol{\varepsilon}(\mathbf{u})) \cdot \mathbf{1} \overset{(2.61)}{=} 2\mu \cdot \boldsymbol{\varepsilon}(\mathbf{u}). \tag{2.65}$$

with one material parameter μ, the so-called *dynamic viscosity*.

The constitutive law presented in (2.65) is one of the simplest possible material models for fluids. As already mentioned in the introduction, from a macroscopic point of view, blood flow is characterized by shear-thinning and viscoelasticity. Naturally, such a behavior necessitates more sophisticated constitutive models than (2.65). However, blood plasma and cytosol, which are focused on in this thesis, are generally accepted to be Newtonian fluids.

2.3.3 Navier-Stokes equations

In this subsection, the resulting initial boundary value problem for the fluid fields will be stated. Indroducing the constitutive relations derived in the previous subsection into the ALE linear momentum equation (2.56) together with the continuity equation (2.61) results in the ALE version of the *Navier-Stokes equations*

$$\frac{\partial \mathbf{u}|_{\boldsymbol{\chi}}}{\partial t} \circ \boldsymbol{\Phi}^{-1} + (\mathbf{c} \cdot \boldsymbol{\nabla})\mathbf{u} + \frac{1}{\rho}\nabla p - 2\frac{\mu}{\rho}\boldsymbol{\nabla} \cdot \boldsymbol{\varepsilon}(\mathbf{u}) = \mathbf{b}, \tag{2.66}$$

$$\boldsymbol{\nabla} \cdot \mathbf{u} = 0. \tag{2.67}$$

For the symbolic notation of the momentum equation (2.66), the abbreviations

$$((\mathbf{c} \cdot \boldsymbol{\nabla})\mathbf{u})_i = \frac{\partial \mathbf{u}_i}{\partial x_j} \cdot \mathbf{c}_j \tag{2.68}$$

$$\boldsymbol{\nabla} \cdot \boldsymbol{\varepsilon}(\mathbf{u}) = \mathbf{div}(\boldsymbol{\varepsilon}(\mathbf{u})) \tag{2.69}$$

have been used, with the divergence operator $\mathbf{div}$ on tensor-valued quantities as defined in (2.55). In order to solve the system of differential algebraic equations (DAEs) (2.66) and (2.67), i.e. a set of partial differential equation (PDE) (2.66) and an algebraic boundary condition (2.67), for the pressure field p and the velocity field $\mathbf{u}$, appropriate initial and boundary values have to be prescribed. As initial velocity field, a divergence-free velocity field $\mathbf{u}^0$ is assumed to obtain a well posed problem.

In general, the definition of boundary conditions for the fluid flow is not straightforward. This is mainly due to the definition of control volumes $V(t)$ for the ALE and Eulerian formulations, which introduces artificial boundaries $\partial V(t)$. A detailed discussion of boundary conditions for fluid-flow problems is beyond the scope of this work. Here, we assume that the whole boundary $\partial V(t)$ is decomposed into two disjunct boundaries $\Gamma_D(t)$ and $\Gamma_N(t)$. On the *Dirichlet-boundary* $\Gamma_D(t)$, the velocity is prescribed, whereas on

the *Neumann-boundary* $\Gamma_N(t)$, a surface traction is applied. To summarize, initial and boundary values read

$$\mathbf{u}(\mathbf{x},0) = \mathbf{u}^0(\mathbf{x}) \quad \forall \mathbf{x} \in V(0), \tag{2.70}$$

$$\mathbf{u}(\mathbf{x},t) = \mathbf{u}_D(\mathbf{x},t) \quad \forall \mathbf{x} \in \Gamma_D, \tag{2.71}$$

$$\boldsymbol{\sigma}(\mathbf{x},t) \cdot \mathbf{n}(\mathbf{x},t) = \mathbf{t}_N(\mathbf{x},t) \quad \forall \mathbf{x} \in \Gamma_N \tag{2.72}$$

and close the Navier-Stokes equations.

Remark 2.7 (Eulerian formulation) *The Eulerian formulation of the Navier-Stokes equations can easily be deduced as special case of* (2.66) *and* (2.67)*. The ALE convective velocity* $\mathbf{c}$ *can be identified as the fluid velocity* $\mathbf{u}$ *yielding*

$$\frac{\partial \mathbf{u}}{\partial t} + (\mathbf{u} \cdot \boldsymbol{\nabla})\mathbf{u} + \frac{1}{\rho}\nabla p - 2\frac{\mu}{\rho}\boldsymbol{\nabla} \cdot (\boldsymbol{\varepsilon}(\mathbf{u})) = \mathbf{b}, \tag{2.73}$$

$$\boldsymbol{\nabla} \cdot \mathbf{u} = 0. \tag{2.74}$$

Remark 2.8 (Dirichlet bounded problems) *An important special case is given by a purely Dirichlet bounded problem, i.e.* $\Gamma_D(t) = \partial V(t)$*. For example, these are of particular interest when using partitioned coupling schemes for balloon-type fluid-structure interaction (FSI) problems, cf. discussion by Küttler et al. [124]. For the applications at hand, the cytosol enclosed by the erythrocyte membrane belongs to this class of problems.*

For Dirichlet bounded problems, the continuity equation can be expressed in terms of the prescribed values $\mathbf{u}_D$*:*

$$\int_{V(t)} \operatorname{div}(\mathbf{u})(\mathbf{x},t)\,\mathrm{d}\mathbf{x} = \int_{\Gamma_D(t)} \mathbf{u}_D(\mathbf{x},t) \cdot \mathbf{n}(\mathbf{x},t)\,\mathrm{d}a = 0. \tag{2.75}$$

This equation constrains the choice of applicable boundary values $\mathbf{u}_D$ *in order to obtain a well-posed problem. Furthermore, the pressure* p *is in this case only defined up to a constant value.*

Remark 2.9 (Comment on Reynolds numbers and simplified descriptions for RBC) *In some numerical studies, the fluid flow in and around erythrocytes was described as Stokes flow, which is a simplification of the Navier-Stokes equations. Neglecting inertia effects, the momentum equation* (2.66) *reduces to*

$$\frac{1}{\rho}\nabla p - 2\frac{\mu}{\rho}\boldsymbol{\nabla} \cdot (\boldsymbol{\varepsilon}(\mathbf{u})) = \mathbf{b}. \tag{2.76}$$

This corresponds to the low Reynolds number limit $\mathrm{Re} \to 0$*, defined by*

$$\mathrm{Re} = \frac{u\,L\,\rho}{\mu} \tag{2.77}$$

for a characteristic velocity u *and a characteristic length* L*. Within this thesis, the full Navier-Stokes equations are considered. The Reynolds numbers of the flows are indeed found to be relatively low, showing, first, that the assumption of Stokes flow can yield reasonable simulation results and, second, that laminar flow can be expected.*

2.4 Governing equations - Structure

A detailed and comprehensive description of the erythrocyte membrane is one of the key features of a realistic model of the whole erythrocyte. The discussion in chapter 1 showed that the behavior of the membrane is largely influenced by its two-layer nature and the properties of each individual membrane layer. Therefore, a comprehensive model has to consider shear elasticity with strain-hardening provided by the cytoskeleton. Moreover, viscoelasticity, bending resistance, and preservation of surface area, which all originate from the fluid-like lipid bilayer, have to be accounted for by the model as well.

In this section, appropriate strain and stress measures are defined to model the behavior of structures. Subsequently, incompressible and nearly-incompressible structure behavior is addressed in section 2.4.2. After some general remarks on constitutive modeling, particular equations for both layers of the RBC membrane are introduced in sections 2.4.4 and 2.4.5. Finally, the initial boundary value problem is stated.

As usual in structure mechanics, a Lagrangean description is employed in this section, which allows to omit the index $\cdot|_{\mathbf{X}}$ and the point of observation, i.e. $\mathbf{f} = \mathbf{f}|_{\mathbf{X}}(\mathbf{X}, t)$ if not stated otherwise. Consequently, there is no difference between the domain Ω and the control volume V.

It is important to note that this section only introduces concepts, measures, and material laws that are relevant for the ongoing of this thesis in order to keep it as brief and clear as possible. For a more general view on nonlinear solid mechanics including spatial or mixed strain measures and a variety of constitutive equations, the reader is referred to the monographs of Holzapfel [106], Marsden and Hughes [139], and Parisch [149].

2.4.1 Strain and stress measures

For the fluid description in section 2.3, a formulation with spatial coordinates and with the Cauchy stress tensor has been convenient. For the membrane, however, a description in a Lagrangean framework and in material coordinates is more suitable. Finite displacements and deformations of the membrane are expected. Therefore, strain and stress measures applicable in the nonlinear regime and defined in the material configuration will be introduced in this subsection.

Strain measures

The deformation of a structural body from the material to the spatial configuration is governed by the motion mapping $\boldsymbol{\varphi}$ defined in (2.1). In nonlinear continuum mechanics, its gradient $\mathbf{F}$ with respect to material points, i.e.

$$\mathbf{F}(\mathbf{X}, t) = \frac{\partial \boldsymbol{\varphi}(\mathbf{X}, t)}{\partial \mathbf{X}}, \tag{2.78}$$

is a crucial quantity called the *deformation gradient*. By definition, $\mathbf{F}$ is a two-point tensor involving points in two distinct configurations. The determinant of $\mathbf{F}$ has already been

defined in (2.4) as $J = \det(\mathbf{F})$. Considering an infinitesimal line element $\mathrm{d}\mathbf{X}$ in $\mathbf{X} \in \Omega_{\mathbf{X}}$, which is mapped to $\mathrm{d}\mathbf{x}$ in $\Omega_{\mathbf{x}}$, the deformation gradient can be identified as the linear mapping between these line elements:

$$\mathrm{d}\mathbf{x} = \mathbf{F}(\mathbf{X}, t)\,\mathrm{d}\mathbf{X}. \tag{2.79}$$

Furthermore, the deformation gradient $\mathbf{F}$ provides the ingredients to describe the motion of infinitesimal area elements. Let $\mathrm{d}\mathbf{A} = \mathbf{N}\,\mathrm{d}A$ define such an area element in the initial configuration with outward pointing normal $\mathbf{N}$, which is mapped to $\mathrm{d}\mathbf{a} = \mathbf{n}\,\mathrm{d}a$ in the current configuration with outward pointing normal $\mathbf{n}$. Then the linear mapping between $\mathrm{d}\mathbf{A}$ and $\mathrm{d}\mathbf{a}$ is given by

$$\mathrm{d}\mathbf{a} = \mathbf{n}\,\mathrm{d}a = J\mathbf{F}^{-\mathsf{T}}\mathbf{N}\,\mathrm{d}A = J\mathbf{F}^{-\mathsf{T}}\,\mathrm{d}\mathbf{A}. \tag{2.80}$$

This equation is called *Nanson's formula*. The existence of the inverse mapping $\mathbf{F}^{-\mathsf{T}}$ is ensured by the homeomorphism $\boldsymbol{\varphi}$, which, by definition, is invertible.

Finally, the Jacobi determinant J provides a mapping between associated infinitesimal volume elements $\mathrm{d}V \in \Omega_{\mathbf{X}}$ and $\mathrm{d}v \in \Omega_{\mathbf{x}}$:

$$\mathrm{d}v = J\,\mathrm{d}V. \tag{2.81}$$

Given a rigid body translation, the displacement field is independent of the material position $\mathbf{X}$ and, hence, the deformation gradient reduces to an identity matrix, i.e. $\mathbf{F} = \mathbf{1}$. The tensor $\mathbf{F}$ is, hence, said to be *invariant* with respect to rigid body translation. In contrast, $\mathbf{F}$ is not invariant with respect to rigid body rotations and can be decomposed into a rotation tensor $\mathbf{R}$ and the material stretch tensor $\mathbf{U}$ or, equivalently, into $\mathbf{R}$ and a spatial stretch tensor $\mathbf{v}$:

$$\begin{aligned} &\mathbf{F} = \mathbf{R}\,\mathbf{U} = \mathbf{v}\,\mathbf{R}, \\ &\text{with} \quad \mathbf{U} = \mathbf{U}^{\mathsf{T}},\ \mathbf{v} = \mathbf{v}^{\mathsf{T}},\ \mathbf{R}^{\mathsf{T}}\mathbf{R} = \mathbf{1}. \end{aligned} \tag{2.82}$$

The unique decomposition (2.82) is called *polar decomposition* and is a fundamental theorem in continuum mechanics.

A reasonable deformation measure should be invariant with respect to all rigid body motions and, hence, only depend on the stretch tensors $\mathbf{U}$ and $\mathbf{v}$. An important deformation measure in material coordinates is given by the symmetric *right Cauchy-Green tensor* $\mathbf{C}$, which is defined as

$$\mathbf{C} = \mathbf{F}^{\mathsf{T}}\mathbf{F} = (\mathbf{R}\,\mathbf{U})^{\mathsf{T}}(\mathbf{R}\,\mathbf{U}) = \mathbf{U}^{\mathsf{T}}\mathbf{U}. \tag{2.83}$$

When it comes to constitutive modeling of the erythrocyte membrane in sections 2.4.4 and 2.4.5, the relations between strain and energy (or consequently between strain and stresses) will be expressed in terms of this quantity $\mathbf{C}$. Physically, this tensor is closely related to the squared stretch of a material line element $\mathrm{d}\mathbf{X}$ under deformation $\boldsymbol{\varphi}$:

$$\mathrm{d}\mathbf{x} \cdot \mathrm{d}\mathbf{x} \overset{(2.79)}{=} \mathrm{d}\mathbf{X} \cdot \mathbf{F}^{\mathsf{T}}\mathbf{F}\mathrm{d}\mathbf{X} = \mathrm{d}\mathbf{X} \cdot \mathbf{C}\,\mathrm{d}\mathbf{X}. \tag{2.84}$$

Hence, the difference between the squared length of the two associated line elements $\mathrm{d}\mathbf{X}$ and $\mathrm{d}\mathbf{x}$ in material and spatial coordinates, respectively, is given by

$$\mathrm{d}\mathbf{x}\cdot\mathrm{d}\mathbf{x}-\mathrm{d}\mathbf{X}\cdot\mathrm{d}\mathbf{X}=\mathrm{d}\mathbf{X}\cdot\left(\mathbf{F}^{\mathsf{T}}\mathbf{F}-\mathbf{1}\right)\mathrm{d}\mathbf{X}=2\,\mathrm{d}\mathbf{X}\cdot\mathbf{E}\,\mathrm{d}\mathbf{X}, \tag{2.85}$$

where the commonly used symmetric *Green-Lagrange strain tensor* $\mathbf{E}$ with

$$\mathbf{E}=\frac{1}{2}\left(\mathbf{F}^{\mathsf{T}}\mathbf{F}-\mathbf{1}\right) \tag{2.86}$$

has been introduced. The strain measure $\mathbf{E}$ is invariant with respect to rigid body motion and vanishes for undeformed bodies.

For the applications in mind, it is beneficial to consider the material response to volumetric and isochoric deformation separately. A multiplicative decomposition of the deformation gradient $\mathbf{F}$ into a *dilatational* (volume-changing) and an *isochoric* (volume-preserving) part, the latter denoted by $\widehat{\mathbf{F}}$, is given by

$$\mathbf{F}=(J^{1/3}\mathbf{1})\widehat{\mathbf{F}}. \tag{2.87}$$

Due to the definition of the tensor $\mathbf{C}$, a multiplicative split of the deformation gradient $\mathbf{F}$ also provides a multiplicative decomposition of $\mathbf{C}$ into a dilatational part and an isochoric part $\widehat{\mathbf{C}}$, i.e.

$$\mathbf{C}=\mathbf{F}^{\mathsf{T}}\mathbf{F}=((J^{1/3}\mathbf{1})\widehat{\mathbf{F}})^{\mathsf{T}}((J^{1/3}\mathbf{1})\widehat{\mathbf{F}})=(J^{2/3}\mathbf{1})\widehat{\mathbf{C}}. \tag{2.88}$$

Stress measures

Cauchy's fundamental lemma has introduced the Cauchy stress tensor $\boldsymbol{\sigma}$ that is associated with the current configuration. This paragraph introduces a stress measure that is solely defined in the material configuration and is energy conjugate quantity of the material strain measure $\mathbf{E}$.

To begin with, the surface traction $\mathbf{t}|_{\mathbf{x}}(\mathbf{x},t,\mathbf{n}|_{\mathbf{x}})$ defined in (2.51) on the boundary $\partial\Omega_{\mathbf{x}}(t)$ of the current domain can be associated to a pseudo surface traction $\mathbf{T}|_{\mathbf{X}}(\mathbf{X},t,\mathbf{N}|_{\mathbf{X}})$ applied on the initial boundary $\partial\Omega_{\mathbf{X}}$ as

$$\int_{\partial\Omega_{\mathbf{x}}(t)}\mathbf{t}|_{\mathbf{x}}(\mathbf{x},t,\mathbf{n}|_{\mathbf{x}})\,\mathrm{d}a=\int_{\partial\Omega_{\mathbf{X}}}\mathbf{T}|_{\mathbf{X}}(\mathbf{X},t,\mathbf{N}|_{\mathbf{X}})\,\mathrm{d}A. \tag{2.89}$$

Note that $\mathbf{T}$ points in the same direction as the true surface traction $\mathbf{t}$. Using Cauchy's fundamental lemma (2.53) and Nanson's formula (2.80), it is easy to show that there exists a stress tensor $\mathbf{P}$ related to the Cauchy stress by

$$\mathbf{P}=J\boldsymbol{\sigma}\mathbf{F}^{-\mathsf{T}}, \tag{2.90}$$

such that the pseudo surface traction $\mathbf{T}$ can be rewritten as

$$\mathbf{T}(\mathbf{X},t,\mathbf{N})=\mathbf{P}(\mathbf{X},t)\cdot\mathbf{N}. \tag{2.91}$$

The second order tensor $\mathbf{P}$ is called *first Piola-Kirchhoff stress tensor*. Due to the nature of the pseudo traction $\mathbf{T}$, the stress $\mathbf{P}$ is a non-symmetric two-point tensor. In contrast, the commonly used *second Piola-Kirchhoff stress tensor* $\mathbf{S}$ defined by

$$\mathbf{S} = \mathbf{F}^{-1}\mathbf{P} = J\mathbf{F}^{-1}\boldsymbol{\sigma}\mathbf{F}^{-\mathsf{T}}, \tag{2.92}$$

is a symmetric tensor and is parametrized exclusively by material coordinates. It will be used for the membrane constitutive modeling in the following.

In the previous paragraph, the deformation gradient $\mathbf{F}$ and the right Cauchy-Green tensor $\mathbf{C}$ have been decomposed into dilatational and isochoric parts in order to consider the respective influences separately. This also makes a split of the stress measures reasonable. For fluid flow, such a split into an isochoric and a volumetric part has actually already been defined for the Cauchy stress $\boldsymbol{\sigma}$ in (2.63). The same split carries over to an additive split of the stress tensor $\mathbf{S}$ given by

$$\mathbf{S} = \mathbf{S}_{\text{iso}} - p\, J\mathbf{C}^{-1}. \tag{2.93}$$

2.4.2 Incompressibility and near-incompressibility

Due to the high water content in most biological materials, incompressibility plays an important role in many many biomechanical applications. In the framework of the erythrocyte membrane, incompressibility of the lipid-bilayer has to be considered and, consistent with incompressible fluid flow, a constant membrane density in space and time is assumed. The Lagrangean version of the continuity equation (2.45) then reduces to

$$\frac{\partial J}{\partial t}(\mathbf{X}, t) = 0. \tag{2.94}$$

Using $J(\mathbf{X}, 0) = \det(\mathbf{1}) = 1$, equation (2.94) is found to be equivalent to

$$J(\mathbf{X}, t) = 1. \tag{2.95}$$

Note that in order to numerically implement the algebraic constraint (2.95), several methods can be considered. The most widely used approaches are the Lagrange multiplier and the penalty approach. A general discussion on these approaches for arbitrary algebraic constraints can be found in the following section 2.5.

The first approach leads to a formulation that is similar to the fluid representation stated above. The Lagrange multiplier can be identified with a hydrostatic pressure p as introduced in (2.93), which can after a lengthy reformulation of (2.62) and (2.92) equivalently be expressed in terms of the second Piola-Kirchhoff stress $\mathbf{S}$ as

$$p = -\frac{1}{3} J^{-1}\mathbf{C} : \mathbf{S}. \tag{2.96}$$

The double contraction is defined as $\mathbf{A} : \mathbf{B} = \operatorname{tr}(\mathbf{A}^{\mathsf{T}}\mathbf{B})$ for two second order tensors $\mathbf{A}$ and $\mathbf{B}$. If the Lagrange multiplier method is chosen, the pressure values are independent variables and have to be solved for during the numerical procedure.

In contrast, a penalty method necessitates a constitutive equation that relates the pressure p with a change in volume. A volume dilatation, thus, results in a finite internal stress. This way, any deflection from the constraint (2.95) is not completely avoided but penalized and, in general, the constraint is not fulfilled exactly. In order to keep the deflection small, a problem specific, possibly large penalty parameter has to be chosen, which might result in numerical problems.

2.4.3 Constitutive modeling

As opposed to the linear relation between fluid Cauchy stress and strain rate, many structures in general and the erythrocyte membrane in particular exhibit a nonlinear relation between deformation and stress response. For this thesis, it is assumed that the membrane can adequately be described by either a *hyperelastic* material or by a viscoelastic material at constant temperature. As shown in the textbook by Holzapfel [106], in both cases, there exists a *Helmholtz free energy* $\Psi(t)$, which defines the total internal energy $W_{\text{int}}(t)$ of the structure by

$$W_{\text{int}}(t) = \int_{\Omega_{\mathbf{X}}} \Psi(t)\,\mathrm{d}V. \tag{2.97}$$

For all materials used here, it is further assumed that the free energy Ψ depends on the deformation (given by $\mathbf{F}$ or $\mathbf{C}$), on some collection of internal variables (denoted by $\mathcal{I}$) to account for viscoelasticity, and in case of anisotropic material behavior on a set of preferred directions (denoted by $\mathcal{M}$). The employed constitutive laws respect some fundamental principles, a detailed discussion of which would exceed the scope of this work. Only some important aspects are briefly addressed in the following paragraph.

In order to be well-defined, the energy density associated with a material point $\mathbf{X}$ at time t is determined by the history of motion of any arbitrarily small neighborhood of $\mathbf{X}$ (*principle of determinism* and *principle of local action*). The latter implies that the behavior is independent of higher-order gradients. The *principle of objectivity* states that the response has to be independent from the observer. In particular, superposition of a rigid body motion (translation or rotation) should not alter the energy of the structure. Being invariant under a rotation, the energy Ψ may conveniently be expressed in terms of the principal invariants of its arguments. This result is known as *representation theorem for invariants*, a proof of which can be found in Gurtin [92] or Truesdell and Noll [187].

For the most general case of the constitutive equations considered for the erythrocyte membrane, the free energy Ψ can be decomposed additively into three main parts:

$$\Psi = \Psi^{\text{bulk}} + \Psi^{\text{fbr}} + \Upsilon, \tag{2.98}$$

with an elastic bulk part Ψ^{bulk}, an anisotropic part Ψ^{fbr}, and a so-called *configurational free energy* Υ, which accounts for viscoelastic behavior.

The contribution Ψ^{bulk} is assumed to depend solely on the invariants of the right Cauchy-Green strain tensor $\mathbf{C}$ and (in case of incompressibility) on the pressure p. The principal

invariants of $\mathbf{C}$ are defined as

$$I_1 = \mathrm{tr}(\mathbf{C}) = \lambda_1^2 + \lambda_2^2 + \lambda_3^2, \tag{2.99}$$

$$I_2 = \frac{1}{2}\left((\mathrm{tr}\,\mathbf{C})^2 - \mathrm{tr}(\mathbf{C}^2)\right) = \lambda_1^2\lambda_2^2 + \lambda_2^2\lambda_3^2 + \lambda_3^2\lambda_1^2, \tag{2.100}$$

$$I_3 = \det(\mathbf{C}) = J^2 = \lambda_1^2\lambda_2^2\lambda_3^2, \tag{2.101}$$

where λ_i^2 denotes the i-th eigenvalue of $\mathbf{C}$. With regards to the split into isochoric and volumetric measures, an alternative, equivalent set of modified invariants $\{\widehat{I}_1, \widehat{I}_2, J, p\}$ can be defined as

$$\widehat{I}_1 = \mathrm{tr}(\widehat{\mathbf{C}}) = J^{-2/3} I_1, \tag{2.102}$$

$$\widehat{I}_2 = \frac{1}{2}\left((\mathrm{tr}\,\widehat{\mathbf{C}})^2 - \mathrm{tr}(\widehat{\mathbf{C}}^2)\right) = J^{-4/3} I_2. \tag{2.103}$$

The constitutive law for Ψ^{bulk} is further split into an isochoric contribution $\Psi^{\text{bulk}}_{\text{iso}}$ and a volumetric part $\Psi^{\text{bulk}}_{\text{vol}}$. It is additionally assumed that none of the materials used to describe the membrane depends on the second modified invariant $\widehat{I}_2$, such that the elastic bulk part reduces to

$$\Psi^{\text{bulk}}(\widehat{I}_1, J, p) = \Psi^{\text{bulk}}_{\text{iso}}(\widehat{I}_1) + \Psi^{\text{bulk}}_{\text{vol}}(J, p). \tag{2.104}$$

The anisotropic behavior results from an additional elastic contribution in one preferred direction $\mathbf{m}^0$, which only depends on the material position $\mathbf{X}$, i.e. $\mathcal{M} = \{\mathbf{m}^0\}$. Hence, the membrane can be thought of as a fiber-reinforced composite material, where one family of fibers is arranged continuously within a matrix material with initial fiber direction $\mathbf{m}^0$. For a normalized direction $|\mathbf{m}^0| = 1$, the stretch λ of the fiber is related to the right Cauchy-Green strain $\mathbf{C}$ by

$$\lambda^2 = \mathbf{m}^0 \cdot \mathbf{C}\mathbf{m}^0 = \mathrm{tr}(\mathbf{C}\mathbf{M}), \tag{2.105}$$

where the metric tensor $\mathbf{M}$ has been introduced as $\mathbf{M} = \mathbf{m}^0 \otimes \mathbf{m}^0$. Again, a modified invariant $\widehat{I}_4$ can be defined as

$$\widehat{I}_4 = \mathrm{tr}(\widehat{\mathbf{C}}\mathbf{M}) = J^{-2/3}\lambda^2. \tag{2.106}$$

For the constitutive modeling to come, it is assumed that the anisotropic energy exclusively depends on this invariant, i.e. $\Psi^{\text{fbr}} = \Psi^{\text{fbr}}(\widehat{I}_4)$.

Viscoelastic material behavior is related to a set of internal variables $\mathcal{I}$. The modeling approach taken here considers the simplest case with only one strain-like, internal, tensor-valued control variable $\mathbf{\Gamma}$. The configurational energy Υ depends on this internal variable and the isochoric deformation, i.e. $\Upsilon = \Upsilon(\widehat{I}_1, \mathbf{\Gamma})$.

Summing up the previous assumptions, the most general free energy function Ψ considered in this thesis is of the form

$$\Psi = \Psi(\widehat{I}_1, \widehat{I}_4, J, p, \mathbf{\Gamma}) = \Psi^{\text{bulk}}_{\text{iso}}(\widehat{I}_1) + \Psi^{\text{bulk}}_{\text{vol}}(J, p) + \Psi^{\text{fbr}}(\widehat{I}_4) + \Upsilon(\widehat{I}_1, \mathbf{\Gamma}). \tag{2.107}$$

To deduce a stress formulation, it is important that the energy Ψ belongs to a hyperelastic or viscoelastic material at constant temperature. In both cases, the second Piola-Kirchhoff stress $\mathbf{S}$ is defined as

$$\mathbf{S} = \frac{\partial \Psi}{\partial \mathbf{E}} = 2\frac{\partial \Psi}{\partial \mathbf{C}}. \tag{2.108}$$

Naturally, additive splitting of the free energy Ψ as given in (2.107) carries over to an additive split of the stress tensor, which reads

$$\mathbf{S} = \mathbf{S}_{\text{iso}}^{\text{bulk}} + \mathbf{S}_{\text{vol}}^{\text{bulk}} + \mathbf{S}^{\text{fbr}} + \mathbf{Q}. \tag{2.109}$$

Having defined the free energies in modified invariants, the evaluation of the stress tensor $\mathbf{S}$ necessitates repeated application of the chain rule. The resulting isochoric elastic contributions

$$\mathbf{S}_{\text{iso}}^{\text{bulk}} = 2\frac{\partial \Psi_{\text{iso}}^{\text{bulk}}(\widehat{I}_1)}{\partial \mathbf{C}} = 2\left(\frac{\partial \widehat{\mathbf{C}}}{\partial \mathbf{C}}\right)^{\mathsf{T}} : \frac{\partial \widehat{I}_1}{\partial \widehat{\mathbf{C}}}\,\frac{\partial \Psi_{\text{iso}}^{\text{bulk}}(\widehat{I}_1)}{\partial \widehat{I}_1} = 2J^{-2/3}\mathbb{P} : \mathbf{1}\,\frac{\partial \Psi_{\text{iso}}^{\text{bulk}}(\widehat{I}_1)}{\partial \widehat{I}_1}, \tag{2.110}$$

$$\mathbf{S}^{\text{fbr}} = 2\frac{\partial \Psi^{\text{fbr}}(\widehat{I}_1)}{\partial \mathbf{C}} = 2\left(\frac{\partial \widehat{\mathbf{C}}}{\partial \mathbf{C}}\right)^{\mathsf{T}} : \frac{\partial \widehat{I}_4}{\partial \widehat{\mathbf{C}}}\,\frac{\partial \Psi^{\text{fbr}}(\widehat{I}_4)}{\partial \widehat{I}_4} = 2J^{-2/3}\mathbb{P} : \mathbf{M}\,\frac{\partial \Psi^{\text{fbr}}(\widehat{I}_4)}{\partial \widehat{I}_4} \tag{2.111}$$

can be obtained, where the identities $\frac{\partial \widehat{I}_1}{\partial \widehat{\mathbf{C}}} = \mathbf{1}$ and $\frac{\partial \widehat{I}_4}{\partial \widehat{\mathbf{C}}} = \mathbf{M}$ have been used. As shown in the textbook of Holzapfel [106], defining the fourth order unit tensor $\mathbb{1}$ with $(\mathbb{1})_{ABCD} = (\delta_{AC}\delta_{BD} + \delta_{AD}\delta_{BC})/2$, allows to write the fourth order projection operator $\mathbb{P}$ as

$$\mathbb{P} = \mathbb{1} - \mathbf{C}^{-1} \otimes \mathbf{C}. \tag{2.112}$$

The internal non-equilibrium stress-like tensor $\mathbf{Q}$, introduced in (2.109), is formally introduced as

$$\mathbf{Q} = 2\frac{\partial \Upsilon(\widehat{I}_1, \boldsymbol{\Gamma})}{\partial \mathbf{C}}. \tag{2.113}$$

As will be shown in section 2.4.5, it is not necessary to explicitly specify the configurational energy Υ. Instead, an evolution equation for the tensor $\mathbf{Q}$ can be provided relating the time derivatives of tensor $\mathbf{Q}$ to the time derivatives of the stress tensor $\mathbf{S}$.

Finally, the volumetric stress has to be addressed. Formally, it can be written as

$$\mathbf{S}_{\text{vol}}^{\text{bulk}} = 2\frac{\partial \Psi_{\text{vol}}^{\text{bulk}}(J,p)}{\partial \mathbf{C}} = J\frac{\partial \Psi_{\text{vol}}^{\text{bulk}}(J,p)}{\partial J}\mathbf{C}^{-1}. \tag{2.114}$$

In case of true incompressibility ($J \equiv 1$), the pressure p serves as independent variable, leading to a so-called *mixed formulation*. The additive split in (2.93) establishes a free energy contribution $\Psi_{\text{vol}}^{\text{bulk}}(J,p) = p(1-J)$, such that the corresponding stress tensor emerges as

$$\mathbf{S}_{\text{vol}}^{\text{bulk}} = -Jp\mathbf{C}^{-1} = -p\mathbf{C}^{-1}. \tag{2.115}$$

In case of nearly-incompressible or compressible material behavior, the hydrostatic pressure p is not an independent variable, but it is to be related to the volumetric contribution $\Psi_{\text{vol}}^{\text{bulk}}$ by

$$p = \frac{\partial \Psi_{\text{vol}}^{\text{bulk}}(J)}{\partial J}. \tag{2.116}$$

In that case, a constitutive equation for the $\Psi_{\text{vol}}^{\text{bulk}}(J)$ is necessary for the material description.

The following sections 2.4.4 and 2.4.5 provide the particular strain-energy functions Ψ^{nw} for the network and Ψ^{bil} for the bilayer. They are chosen to realistically model the erythrocyte membrane. Note that corresponding second Piola-Kirchhoff stress tensors are not explicitly provided, since they can easily be computed based on above equations.

2.4.4 Constitutive equations for the cytoskeleton

To begin with, the properties of the cytoskeleton, which have been discussed in section 1.2.2, are briefly repeated. The cystoskeleton is an elastic protein network and provides shear elasticity to the erythrocyte membrane. In experimental studies, a strain-hardening behavior has been observed, which can be explained by the network topology. Bending elasticity and resistance against area and volume dilatation are generally thought to be one order of magnitude lower than the respective quantities of the lipid bilayer, cf. [65].

From these particular properties, it can be concluded that an isotropic, hyperelastic, strain-hardening, and compressible constitutive model is a suitable choice for the protein network. The implemented material law Ψ^{nw} for the cystoskeleton consists of two bulk parts $\Psi_{\text{iso}}^{\text{nw}}(\widehat{I}_1)$ and $\Psi_{\text{vol}}^{\text{nw}}(J)$.

The isochoric contribution $\Psi_{\text{iso}}^{\text{nw}}$ accounts for shear elasticity and includes the hardening behavior by using a third order *Yeoh* material, which is defined as

$$\Psi_{\text{iso}}^{\text{nw}}(\widehat{I}_1) = c_1 \left(\widehat{I}_1 - 3\right) + c_3 \left(\widehat{I}_1 - 3\right)^3, \tag{2.117}$$

with free material parameters c_1 and c_3. Note that the most general form of Yeoh materials, as first proposed by Yeoh [200], also includes a quadratic term of the form $c_2(\widehat{I}_1 - 3)^2$. The material model chosen here, which does not consider this term, is consistent with the formulation used in the study of Mills et al. [142].

For the volumetric contribution, a very simple quadratic formulation is used:

$$\Psi_{\text{vol}}^{\text{nw}}(J) = \kappa \left(J - 1\right)^2. \tag{2.118}$$

Here, the parameter κ denotes the dilatation modulus of the network. Li et al. [128] reported that a realistic dilatation modulus lies in the same order of magnitude as the linear bulk shear modulus $G^{\text{nw}} = 2c_1$ of the network.

In many experimental or numerical studies in literature, the linear or initial effective shear modulus of the membrane is deduced as the most important material parameter of the

membrane. For the Yeoh material, this quantity $G_{\text{eff}}^{\text{nw}}$ is defined as the product of the linear bulk shear modulus G^{nw} and the thickness t^{nw} of the membrane layer

$$G_{\text{eff}}^{\text{nw}} = G^{\text{nw}}\, t^{\text{nw}} = 2c_1\, t^{\text{nw}}. \tag{2.119}$$

Note that $G_{\text{eff}}^{\text{nw}}$ is only a meaningful measure for small deformations. In contrast, the response to large deformations is nonlinear and dominated by the c_3 term. Beside the shear modulus of the membrane, also its bending resistance B^{nw}, which is defined as

$$B^{\text{nw}} = \frac{2c_1(2c_1+\kappa)}{6(c_1+\kappa)}(t^{\text{nw}})^3, \tag{2.120}$$

is an important parameter of a thin structure. Its value is bounded by $\frac{2}{3}c_1(t^{\text{nw}})^3$ for $\kappa = 0$ and $\frac{1}{3}c_1(t^{\text{nw}})^3$ for $\kappa \to \infty$. For a realistic choice of material parameters, this bending modulus is orders of magnitude lower than the value reported for the bending elasticity of the erythrocyte membrane, which is in agreement with the assumption that bending elasticity is provided predominantly by the lipid bilayer, which is addressed in the following subsection.

2.4.5 Constitutive equations for the lipid bilayer

The lipid bilayer is a fluid-like membrane with very low shear elasticity but with significant shear viscosity and bending elasticity. Furthermore, it is reported to be incompressible (volume preserving) and almost inextensible (i.e. it shows a large resistance against changes of the total surface area). Since the molecules of the lipid bilayer are able to flow freely in this layer, they balance the molecular density within the layer as shown in the famous experiments by Discher et al. [47]. Therefore, it seems reasonable to employ a global area constraint, as will be introduced in section 2.5, on the outer surface area instead of including the inextensibility into the constitutive modeling, which, by definition, would result in a local property.

Incompressibility, however, is a local property of the membrane and is implemented by means of a mixed formulation. As discussed above, this leads to a volumetric strain energy function

$$\Psi_{\text{vol}}^{\text{bil}} = p(1-J)/2, \tag{2.121}$$

with independent hydrostatic scalar-valued pressure variable p.

The bulk elasticity of the lipid bilayer is relatively small and is accounted for by a simple first order neo-Hooke material defined as

$$\Psi_{\text{iso}}^{\text{bil}}(\widehat{I}_1) = \frac{1}{2}G^{\text{bil}}\left(\widehat{I}_1 - 3\right), \tag{2.122}$$

where the parameter G^{bil} denotes the shear modulus of the material. Given a thickness t^{bil} of the bilayer, the combined linear shear modulus $G_{\text{eff}}^{\text{mem}}$ of the erythrocyte membrane is, consequently, defined as

$$G_{\text{eff}}^{\text{mem}} = G_{\text{eff}}^{\text{nw}} + G_{\text{eff}}^{\text{bil}} = 2c_1\, t^{\text{nw}} + G^{\text{bil}}\, t^{\text{bil}}. \tag{2.123}$$

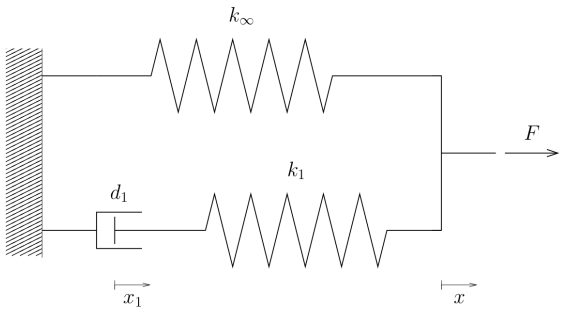

Figure 2.1: *Maxwell body*

For a thin bilayer ($t^{\text{bil}} \approx t^{\text{nw}}$) with low shear elasticity ($G^{\text{bil}} << c_1$), the effective modulus $G^{\text{mem}}_{\text{eff}}$ of the composite membrane is clearly governed by the cytoskeleton.

In order to describe the viscoelastic behavior of the lipid bilayer membrane, a rheological model is to be chosen. Following the approach proposed by Holzapfel and Gasser [107] for a viscoelastic fiber-reinforced material, a Maxwell model is employed. A schematic drawing is given in Figure 2.1. Since only one internal variable is considered, the model is fully described by means of two springs (k_1, k_∞) and one dashpot d_1.

In the framework of non-linear continuum mechanics, this rheological model is translated in a linear equation of evolution for the non-equilibrium stresses $\mathbf{Q}$ in terms of the isochoric elastic bulk stresses $\mathbf{S}^{\text{bil}}_{\text{iso}}$, which are defined in (2.110) and (2.122). Having defined a relaxation time τ and a non-dimensional free-energy factor β, the equation of evolution is given by

$$\dot{\mathbf{Q}} + \frac{\mathbf{Q}}{\tau} = \beta\, \dot{\mathbf{S}}^{\text{bil}}_{\text{iso}}. \tag{2.124}$$

For the 1D equivalent in Figure 2.1, the parameter β can be identified with the ratio of the spring constants k_1 and k_∞. The relaxation time τ defines the ratio between spring and dashpot, i.e. $\tau = \frac{d_1}{k_1}$. The effective membrane viscosity can be calculated from the above defined quantities:

$$\mu^{\text{bil}}_{\text{eff}} = \tau\, \beta\, G^{\text{bil}}\, t^{\text{bil}}. \tag{2.125}$$

It is important to note that due to the rheological model the non-equilibrium stresses can be calculated without explicitly defining the configurational free energy Υ.

Finally, the bending elasticity of the lipid bilayer membrane is addressed. Without further modification, the linear bending modulus B^{bil} would be given by

$$B^{\text{bil}} = \frac{1}{3} G^{\text{bil}}\, (t^{\text{bil}})^3. \tag{2.126}$$

For the very thin bilayer with a very low shear modulus, this value would be even less than the bending modulus B^{nw} of the cytoskeleton defined in (2.120).

The basic idea to generate a realistic, i.e. much higher, bending resistance of the bilayer is to include an additional stiffness in thickness direction of the membrane, represented by virtual fibers or rods. Since the outer surface area of the membrane is to be preserved, bending triggers a variation of the other surface area. Due to the incompressibility, this variation implies a corresponding change in membrane thickness. The combination of these changes of the geometry results in a stretch or a compression of the virtual fibers resulting in a finite stress state. Therefore, stiffness of the fibers adds the necessary bending elasticity to the bilayer formulation. Technically, the additional stiffness is expressed in the elastic anisotropic part $\Psi^{\text{bil,fbr}}$, which is assumed to depend solely on $\widehat{I}_4$ and is given by

$$\Psi^{\text{bil,fbr}}(\widehat{I}_4) = \frac{\kappa_1}{2\kappa_2} \exp\left(\kappa_2 \left(\widehat{I}_4 - 1\right)^2\right), \tag{2.127}$$

with the material parameters κ_1 and κ_2. This constitutive equation for the anisotropic part has also been proposed by Holzapfel and Gasser [107].

2.4.6 The initial boundary value problem

The initial boundary value problem is derived starting from the Lagrangean version of the balance of linear momentum. Instead of using spatial coordinates as in (2.57), the equation is transformed into the initial configuration and reads

$$\frac{\mathrm{d}^2\mathbf{d}}{\mathrm{d}t^2}(\mathbf{X},t) = \mathbf{b}(\mathbf{X},t) + \frac{1}{\rho^0(\mathbf{X})}\mathbf{Div}(\mathbf{F}\,\mathbf{S}(\mathbf{F},p))(\mathbf{X},t), \tag{2.128}$$

where the material divergence operator $\mathbf{Div}$ for tensor valued arguments is defined as

$$\mathbf{Div}(\mathbf{T}))_i = \frac{\partial T_{ij}}{\partial X_j}. \tag{2.129}$$

The explicit dependence on p of the momentum equation (2.128) is only to be considered for the lipid bilayer part of the membrane. In case of the cytoskeleton, the pressure p depends on the deformation $p = p(J)$.

In contrast to the governing equations of the fluid field, the momentum equation (2.128) is a second order PDE, since the structure stresses are related to strains and strain rates as derived in the previous subsections. Therefore, initial conditions do not only include an initial displacement field $\mathbf{d}^0$, but additionally an initial velocity field $\mathbf{v}^0$.

Furthermore, boundary conditions have to be applied. The boundary $\partial\Omega_{\mathbf{X}}$ of the structure body is split into a Dirichlet boundary Γ_D, where the displacement $\mathbf{d}_D$ is prescribed, and a Neumann boundary Γ_N, where a pseudo traction $\mathbf{T}$ is applied. As in the fluid field, these boundaries are disjunct and cover the whole boundary $\partial\Omega_{\mathbf{X}}$. Finally, the initial and boundary conditions read

$$\mathbf{d}(\mathbf{X},0) = \mathbf{d}^0(\mathbf{X}) \quad \forall \mathbf{X} \in \Omega_{\mathbf{X}}, \tag{2.130}$$

$$\dot{\mathbf{d}}(\mathbf{X},0) = \mathbf{v}^0(\mathbf{X}) \quad \forall \mathbf{X} \in \Omega_{\mathbf{X}}, \tag{2.131}$$

$$\mathbf{d}(\mathbf{X},t) = \mathbf{d}_D(\mathbf{X},t) \quad \forall \mathbf{X} \in \Gamma_D, \tag{2.132}$$

$$(\mathbf{FS})(\mathbf{X},t)\,\mathbf{N}(\mathbf{X},t) = \mathbf{T}_N(\mathbf{X},t) \quad \forall \mathbf{X} \in \Gamma_N. \tag{2.133}$$

In the domain of the cytoskeleton, the motion is completely governed by the above equations. They have to be solved for the unknown displacement d. In case of the lipid bilayer, however, the above equations are not sufficient to describe the mechanical behavior. Since an additional independent field p has been introduced in section 2.4.5, the system has to be closed by an additional equation. Here, the constraint

$$J - 1 = 0 \tag{2.134}$$

has to be fulfilled for all points of the bilayer to ensure an incompressible behavior.

2.5 Algebraic constraints

As already discussed before, some crucial properties of the erythrocyte are accounted for by algebraic constraints. The first subsection 2.5.1 lists the necessary constraint conditions for a realistic simulation of erythrocyte motion. The second subsection provides a mathematical interpretation and presents two commonly used strategies, i.e. the Lagrange multiplier formulation or the penalty approach.

2.5.1 Algebraic constraints for the human erythrocyte

To start with, the preservation of the membrane surface area under physiological conditions has to be accounted for. As mentioned above, this area conservation is a global property of the bilayer membrane. Given the current configuration $A(t)$ of the surface and the initial area $\bar{A}_0$, this constraint reads

$$\mathcal{B}_{\bar{A}_0}(t) = \int_{A(t)} 1 \, \mathrm{d}\mathbf{x} - \bar{A}_0 = 0. \tag{2.135}$$

In case of erythrocyte simulations, the outer surface of the erythrocyte membrane is chosen to be constrained.

The volume enclosed by the membrane is controlled by the incompressibility of the cytosol. Nevertheless, in order to impose a stress state for the biconcave shaped cell at rest or to improve the numerical performance in case of quasi-static simulations, it is advantageous to have an alternative measure to control the volume enclosed by the membrane. If the domain, denoted by V, is bounded by the closed surface Γ_V with positive orientation and its volume has to equal a prescribed value $\bar{V}(t)$ at time t, the condition can be expressed as

$$\mathcal{B}_{\bar{V}}(t) = \int_V 1 \, \mathrm{d}\mathbf{x} - \bar{V}(t) \tag{2.136}$$

$$= \tfrac{1}{3} \int_{\Gamma_V} (x_1 \, \mathrm{d}x_2 \, \mathrm{d}x_3 + x_2 \, \mathrm{d}x_1 \, \mathrm{d}x_3 + x_3 \, \mathrm{d}x_1 \, \mathrm{d}x_3) - \bar{V}(t) = 0. \tag{2.137}$$

For the numerical implementation, this volume constraint is evaluated based on the surface integral as given in (2.137).

Besides these constraints, which are both defined based on surface integrals, also so-called *multi-point constraints* are implemented controlling the motion of individual points of the membrane. They are, for example, used to represent realistic boundary conditions. Due to the rigidity of the beads attached to the cell in laser trap experiments, the part of the cell membrane in contact with the bead cannot deform, but is restricted to rigid body displacements. Given a set of points $\mathcal{J} \subset \Omega_{\mathbf{X}}$, a direction $\mathbf{n}$, and a particular point $\bar{\mathbf{X}} \in \Omega_{\mathbf{X}}$, the multi-point constraints for such rigid body translations read

$$\mathcal{B}_{\mathbf{d},\mathbf{n},\bar{\mathbf{X}},\mathcal{J}} = \big(\mathbf{d}(\mathbf{X},t) - \mathbf{d}(\bar{\mathbf{X}},t)\big) \cdot \mathbf{n} = 0, \quad \forall \mathbf{X} \in \mathcal{J}. \tag{2.138}$$

To simulate the attachment of the cell on a plain surface, it is useful not to control the relative displacement of a point with respect to a particular point $\bar{\mathbf{X}}$, but the relative position of the point with a constraint of the form

$$\begin{aligned} \mathcal{B}_{\mathbf{x},\mathbf{n},\bar{\mathbf{X}},\mathcal{J}} &= \big(\mathbf{x}(\mathbf{X},t) - \mathbf{x}(\bar{\mathbf{X}},t)\big) \cdot \mathbf{n} - \delta_{\bar{\mathbf{X}}}(t) = 0, \quad \forall \mathbf{X} \in \mathcal{J}, \\ &= \big(\mathbf{X} - \bar{\mathbf{X}} + \mathbf{d}(\mathbf{X},t) - \mathbf{d}(\bar{\mathbf{X}},t)\big) \cdot \mathbf{n} - \delta_{\bar{\mathbf{X}}}(t) = 0, \quad \forall \mathbf{X} \in \mathcal{J}. \end{aligned} \tag{2.139}$$

The scalar distance function $\delta_{\bar{\mathbf{X}}}(t)$ allows for the transition from a curved into a flat surface. Unlike the values on the Dirichlet boundaries, the absolute displacement values neither of $\bar{\mathbf{X}}$ nor of the points in $\mathcal{J}$ is prescribed, but rather the relative motion between the points in $\mathcal{J}$ with respect to $\bar{\mathbf{X}}$.

Of course some simulations require the use of multiple constraint conditions. To ease the notation, a number of $n^{\mathcal{B}}$ general constraints $\mathcal{B}_i = 0$ with $i = 1, \ldots, n^{\mathcal{B}}$ are introduced, which can take any form from (2.135) to (2.139).

2.5.2 Implementation strategies

The mathematical equivalent for the implementation of the algebraic conditions $\mathcal{B}_i = 0$ in the context of this thesis is *constrained optimization*, where the minimum of an objective function W subject to constraint conditions has to be found. This optimization problem reads

$$\begin{aligned} &\min W(\mathbf{d}, p) \\ &\text{s.t.} \quad \mathcal{B}_i(\mathbf{d}) = \mathbf{0} \quad \forall i \in \big\{1, \ldots, n^{\mathcal{B}}\big\} \end{aligned} \tag{2.140}$$

with unknown displacements and pressure functions $\mathbf{d}$ and p, respectively. In general, the solution of (2.140) is not trivial.

To be accessible by numerical approaches, the system can be reformulated based on additional *Lagrange multiplier* variables $\lambda_i^{\mathcal{S}}$, $i = 1, \ldots, n^{\mathcal{B}}$, which are merged into a vector $\boldsymbol{\lambda}^{\mathcal{S}}$ to shorten the notation. Instead of a minimum of W, a stationary point of the so-called Lagrange-functional $\tilde{W}$ is considered, i.e.

$$\operatorname{stat} \tilde{W}(\mathbf{d}, p, \boldsymbol{\lambda}^{\mathcal{S}}) = \operatorname{stat} \left(W(\mathbf{d}, p) + \sum_{i=1}^{n} \lambda_i^{\mathcal{S}} \, \mathcal{B}_i(\mathbf{d}) \right). \tag{2.141}$$

From a computational point of view, system (2.141) can be reduced to a variation problem, the solution of which is rather straightforward. One major advantage of this approach is that the solution of (2.141) fulfills the constraints exactly. Section 3.5.1 of the next chapter states the variational form and relates the approach to the mixed formulations used for incompressible structure, cf. section 2.4.2, and for incompressible fluid flow, cf. section 2.3.

An alternative to the Lagrange multiplier approach is the *penalty approach*, which does not introduce additional variables into the system. Instead, constant parameters $(\kappa_i^{\mathcal{S}})_{1\leq i\leq n}$ are defined and the solution process requires the minimization of the modified objective function $\tilde{W}$, in this case given by

$$\min \tilde{W}(\mathbf{d}, p) = \min \left(W(\mathbf{d}, p) + \sum_{i=1}^{n} \kappa_i^{\mathcal{S}} (\mathcal{B}_i(\mathbf{d}))^2 \right). \tag{2.142}$$

The minimization of system (2.142) is not equivalent to the minimization of the initial system (2.140) but is an approximation of it. In particular, the constraints are not fulfilled exactly. The quality of the solution rather depends on the values $\kappa_i^{\mathcal{S}}$, the optimal choice of which is problem specific. A too large penalty parameter has negative influence on the conditioning of the problem.

For some applications, the combination of the two approaches offers superior behavior compared to either of the standard methods. A discussion of this so-called class of *augmented Lagrange methods* exceeds to scope of this thesis, in particular, since different numerical algorithms can be derived. The reader is, thus, referred to the textbooks of Glowinski and Le Tallec [82] and Luenberger [136].

2.6 Fluid-Structure Interaction

The last section of this chapter addresses the coupling of the fluid and the structure equations introduced so far. The interface between fluid and structure fields is denoted by Γ_{FSI} and represents the third kind of boundary besides Dirichlet and Neumann boundaries. Let $V(t)$ denote the fluid control volume and $\Omega_{\mathbf{x}}(t)$ the structural body at time t, both in the spatial configuration. The interface is then defined as the common boundary $\Gamma_{\mathsf{FSI}} = V(t) \cap \Omega_{\mathbf{x}}(t) = \partial V(t) \cap \partial \Omega_{\mathbf{x}}(t)$.

At the FSI interface Γ_{FSI}, kinematic and dynamic constraints have to be enforced. In order to distinguish between quantities defined in the fluid and in the structure field, the superscripts $(\,\cdot\,)^{\mathcal{F}}$ and $(\,\cdot\,)^{\mathcal{S}}$ are introduced. To begin with, mass flow across Γ_{FSI} and any relative tangential movement of fluid and structure at Γ_{FSI} is to be prohibited. Therefore, the no-slip boundary condition

$$\frac{\partial \mathbf{d}^{\mathcal{S}}|_{\mathbf{X}}}{\partial t}(\boldsymbol{\varphi}^{-1}(\mathbf{x}, t), t) = \mathbf{u}^{\mathcal{F}}|_{\mathbf{x}}(\mathbf{x}, t), \quad \forall \mathbf{x} \in \Gamma_{\mathsf{FSI}} \tag{2.143}$$

is applied. The condition states a relation between primary variables of the respective single fields, i.e. displacements on the structure side and velocities on the fluid side.

Any numerical method, thus, has to consider that the implementation of (2.143) must be consistent with the overall time integration schemes of the single fields.

The coupling of two physical fields also brings about a surface traction, which results from constraining the quantities on the interface Γ_{FSI}. The interface traction is denoted by $\mathbf{h}$ and has to coincide on both sides of the interface:

$$\mathbf{h}^{\mathcal{S}}(\mathbf{x},t) = -\mathbf{h}^{\mathcal{F}}(\mathbf{x},t) \quad \forall \mathbf{x} \in \Gamma_{\mathsf{FSI}}. \tag{2.144}$$

From a mathematical point of view the interface traction can be interpreted as a Lagrange multiplier introduced to enforce the algebraic constraint (2.143). Hence, it is very similar to the constraints discussed in the previous section. The main difference is that, here, two different physical fields with possibly different discretizations in space have to be coupled. This will be accounted for by the discretization method of the Lagrange multiplier. Without loss of generality, it will be assumed that the multiplier equals the traction on the fluid side of the interface: $\boldsymbol{\lambda} = \mathbf{h}^{\mathcal{F}} = -\mathbf{h}^{\mathcal{S}}$.

Chapter 3

Finite Element model for the human red blood cell

This chapter introduces the numerical model of both the human RBC and the surrounding fluid as well as their mutual interaction. The governing equations presented in the previous chapter are PDEs or even DAEs with spatial and temporal components. In this thesis, the finite element method (FEM) is used for the spatial discretization of fluid, fluid grid, and structure, prior to the integration in time based on the generalized-α scheme. Finite element (FE) formulations and time integration schemes are the subject of many university lectures, textbooks, and publications. Therefore, the first section only briefly reviews the basics of the FEM and the time integration scheme.

The present numerical model of the erythrocyte was developed and implemented in the in-house research code BACI [193]. This C++ based software platform is jointly developed by the Institute of Computational Mechanics and provides, among others, a variety of fluid, fluid grid, and structure FE formulations. In particular, fluid and fluid grid element formulations have been used as implemented in BACI without further adaptation.

Thus, sections 3.2 and 3.3 contain relative short introductions on stabilized fluid finite elements and on the fluid grid motion, respectively. Additionally, a repositioning algorithm for the grid points at the FSI interface Γ_{FSI} is presented in order to realize large displacements and rotations of Γ_{FSI}. Section 3.4 addresses two kinds of solid shell finite elements used in this thesis: A stabilized equal-order hybrid solid shell formulation for the lipid bilayer and a more standard solid shell element implementation for the compressible cytoskeleton. Section 3.5 introduces the discretization schemes for the algebraic constraints put on the membrane. The subsequent section 3.6 discusses in more detail the development of a scaled thickness conditioning (STC) approach for solid shell finite elements. This method has been devised as part of this thesis to overcome the ill-conditioning problem of the thin erythrocyte membrane. The last section 3.7 introduces a computational FSI framework, which is developed to simulate the erythrocyte subjected to an exterior flow field. It is capable of coupling non-conforming interface meshes and can deal with structures undergoing large rotations.

3.1 The finite element method and the generalized-α scheme

This section briefly addresses the basics of the FEM for instationary problems and describes necessary steps to gain the discrete set of equations for a given PDE. Details on mathematical foundations and aspects of the FEM are skipped and can, for example, be found in the monographs of Braess [26], Hughes [112], Strang and Fix [178], or in the first volume of the series of textbooks of Zienkiewicz and Taylor [204].

In general, the FEM consists of two steps, which are presented in subsections 3.1.1 and 3.1.2. First, a weak form of the boundary value problem is derived by formulating the weighted residual and integrating by parts. The second step is the actual spatial discretization with finite elements, which results in a semi-discrete system of equations.

The final subsection 3.1.3 introduces the generalized-α time integration scheme used for the discretization of the semi-discrete systems in time. This sequential discretization approach is not the only feasible solution. It is also possible to start with the discretization in time, as for example described in the work of Rothe [169] or, more recently, in the thesis of Gamnitzer [74] for the fluid field. Alternatively, both discretizations can be performed at once using a space-time FE procedure. Details on this can, for example, be found in the work of Tezduyar et al. [182, 183] and in the thesis of Behr [12].

3.1.1 Weak form

To begin with, a PDE with differential operator $\boldsymbol{\mathcal{D}}$ and right hand side $\mathbf{f}$ is considered, which is to be solved for a function $\mathbf{y}$:

$$\boldsymbol{\mathcal{D}}(\mathbf{y}(\mathbf{x},t)) = \mathbf{f}(\mathbf{x},t) \quad \forall (\mathbf{x},t) \in \Omega_{\mathbf{x}} \times (0,T). \tag{3.1}$$

Boundary, initial, and constraint conditions have been dropped from the notation for the sake of clarity. Furthermore, it is assumed that the spatial domain $\Omega_{\mathbf{x}}$ implicitly contains information on the current time t, i.e. $\Omega_{\mathbf{x}} = \Omega_{\mathbf{x}}(t)$. Equivalently, the PDE can be expressed in terms of a residuum $\boldsymbol{\mathcal{R}}$ as

$$\boldsymbol{\mathcal{R}}(\mathbf{y}(\mathbf{x},t),\mathbf{x},t) = \boldsymbol{\mathcal{D}}(\mathbf{y}(\mathbf{x},t)) - \mathbf{f}(\mathbf{x},t) = \mathbf{0}. \tag{3.2}$$

The problems considered in chapter 2 allow for analytical and pointwise valid solutions in very special cases only. Therefore, the pointwise equality (3.2) is replaced by the so-called *weighted residual*: given an appropriate *test space* $\mathcal{T} \subset \mathcal{L}^2\left(\Omega_{\mathbf{x}} \times (0,T), \mathbb{R}^{n^{\text{dim}}}\right)$ the integral

$$\int_{\Omega_{\mathbf{x}}} \left(\boldsymbol{\mathcal{R}}(\mathbf{y}) \cdot \boldsymbol{\eta}\right)(\mathbf{x},t)\, \mathrm{d}\mathbf{x} = 0 \tag{3.3}$$

should vanish for all *test functions* (also-called *weighting functions*) $\boldsymbol{\eta} \in \mathcal{T}$. Here, the constant n^{dim} refers to the number of spatial dimensions and $\mathcal{L}^2$ to the space of square-integrable functions. At the Dirichlet boundary Γ_D, any test function $\boldsymbol{\eta} \in \mathcal{T}$ vanishes by definition, whereas the solution $\mathbf{y}$ has to coincide with the prescribed values.

The definition of the weighted residual (3.3) implies that a possible solution $\mathbf{y}$ is no longer restricted to be a continuously differentiable function, but can also be defined in a reasonable Sobolev space $\mathcal{S} \subset \mathcal{L}^2\left(\Omega_{\mathbf{x}} \times (0,T), \mathbb{R}^{n^{\mathsf{dim}}}\right)$, the so-called *trial space*. The weighted residual can be expressed in terms of the scalar product $(\,\cdot\,;\,\cdot\,)_{\Omega_{\mathbf{x}}}$ of the Hilbert space $\mathcal{L}^2\left(\Omega_{\mathbf{x}} \times (0,T), \mathbb{R}^{n^{\mathsf{dim}}}\right)$ as

$$(\boldsymbol{\mathcal{R}}(\mathbf{y})\,;\boldsymbol{\eta})_{\Omega_{\mathbf{x}}} = 0 \quad \forall \boldsymbol{\eta} \in \mathcal{T}. \tag{3.4}$$

In many cases, it is useful to apply integration by parts in order to further reduce the requirement put on the solution function $\mathbf{y}$ and, thus, to augment the solution space $\mathcal{S}$. This operation shifts some of the derivatives from trial to test function and adds a boundary integral term to the residual. Equivalently, the derivatives in (3.4) can be interpreted as weak derivatives defined in Sobolev spaces, which motivates the term *'weak form'*.

3.1.2 Discretization in space

To be solvable by computer systems, the infinite dimensional Sobolev spaces $\mathcal{S}$ and $\mathcal{T}$ have to be replaced by suitable finite dimensional vector spaces $\mathcal{S}^h$ and $\mathcal{T}^h$. To begin with, the discrete spatial approximation is considered, whereas the functions are assumed to remain continuous in time. For a so-called *Galerkin approximation*, sets of n^{nd} linearly independent functions $\mathbf{N}_i = \sum_{k=1}^{n^{\mathsf{dim}}} \mathbf{e}_k N_i$ with $\{\mathbf{N}_i\}_{1\le i\le n^{\mathsf{nd}}} \subset \mathcal{S}$ and $\bar{\mathbf{N}}_j = \sum_{k=1}^{n^{\mathsf{dim}}} \mathbf{e}_k \bar{N}_j$ with $\{\bar{\mathbf{N}}_j\}_{1\le j\le n^{\mathsf{nd}}} \subset \mathcal{T}$ are chosen, which depend only on the spatial variable $\mathbf{x}$. In these definitions, $\mathbf{e}_i$ denotes the i-th Cartesian basis vector of $\mathbb{R}^{n^{\mathsf{dim}}}$The discrete subspaces of $\mathcal{S}$ and $\mathcal{T}$

$$\mathcal{S}^h = \left\{ \mathbf{y}^h(\mathbf{x},t) \in \mathcal{S} : \mathbf{y}^h(\mathbf{x},t) = \sum_{k=1}^{n^{\mathsf{dim}}} \sum_{i=1}^{n^{\mathsf{nd}}} \mathbf{e}_k \alpha_{ik}(t)\, N_i(\mathbf{x}),\ \alpha_{ik} \in \mathbb{R},\ \mathbf{y}^h\big|_{\Gamma_D} = \mathbf{y}_D \right\} \tag{3.5}$$

$$\mathcal{T}^h = \left\{ \boldsymbol{\eta}^h(\mathbf{x},t) \in \mathcal{T} \colon \boldsymbol{\eta}^h(\mathbf{x},t) = \sum_{l=1}^{n^{\mathsf{dim}}} \sum_{j=1}^{n^{\mathsf{nd}}} \mathbf{e}_l \bar{\alpha}_{jl}(t)\, \bar{N}_j(\mathbf{x}), \bar{\alpha}_{jl} \in \mathbb{R},\ \boldsymbol{\eta}^h\big|_{\Gamma_D} = \mathbf{0} \right\} \tag{3.6}$$

are defined, where Γ_D denotes the Dirichlet boundary and $\mathbf{y}_D$ the prescribed Dirichlet values. In case of equal sets $\{N_i\}$ and $\{\bar{N}_j\}$ the approach is also-called *Bubnov-Galerkin method*, otherwise the term *Petrov-Galerkin method* is often used.

A function $\mathbf{y}^h \in \mathcal{S}^h$ is now said to solve the semi-discrete form of problem (3.4) if the weighted residual vanishes for all test functions $\boldsymbol{\eta}^h \in \mathcal{T}^h$, i.e. $\left(\boldsymbol{\mathcal{R}}(\mathbf{y}^h); \boldsymbol{\eta}^h\right) = 0$. Equivalently, this can be formulated as problem with $n^{\mathsf{dof}} = n^{\mathsf{nd}} \cdot n^{\mathsf{dim}}$ unknown real valued functions: Find functions $\alpha_{ik}(t)$, $1 \le i \le n^{\mathsf{nd}}$, $1 \le k \le n^{\mathsf{dim}}$, such that for all

$\bar{\alpha}_{jl}(t)$, $1 \leq j \leq n^{\mathsf{nd}}$, $1 \leq l \leq n^{\mathsf{dim}}$, the discrete form of the weighted residual

$$\begin{aligned} 0 &= \left(\boldsymbol{\mathcal{R}} \left(\sum_{k=1}^{n^{\mathsf{dim}}} \sum_{i=1}^{n^{\mathsf{nd}}} \mathbf{e}_k \, \alpha_{ik}(t) \, N_i(\mathbf{x}) \right) \; ; \left(\sum_{l=1}^{n^{\mathsf{dim}}} \sum_{j=1}^{n^{\mathsf{nd}}} \mathbf{e}_l \, \bar{\alpha}_{jl}(t) \, \bar{N}_j(\mathbf{x}) \right) \right)_{\Omega_{\mathbf{x}}} \\ &= \sum_{l=1}^{n^{\mathsf{dim}}} \sum_{j=1}^{n^{\mathsf{nd}}} \bar{\alpha}_{jl}(t) \left(\boldsymbol{\mathcal{R}} \left(\sum_{k=1}^{n^{\mathsf{dim}}} \sum_{i=1}^{n^{\mathsf{nd}}} \mathbf{e}_k \, \alpha_{ik}(t) \, N_i(\mathbf{x}) \right) \; ; \mathbf{e}_l \, \bar{N}_j(\mathbf{x}) \right)_{\Omega_{\mathbf{x}}} \end{aligned} \tag{3.7}$$

vanishes. Since (3.7) holds for arbitrary sets $\{\bar{\alpha}_{jl}\}$, the equation can be transformed into a system of n^{dof} independent equations given by

$$0 = \left(\boldsymbol{\mathcal{R}} \left(\sum_{k=1}^{n^{\mathsf{dim}}} \sum_{i=1}^{n^{\mathsf{nd}}} \mathbf{e}_k \, \alpha_{ik}(t) \, N_i(\mathbf{x}) \right) \; ; \mathbf{e}_l \, \bar{N}_j(\mathbf{x}) \right)_{\Omega_{\mathbf{x}}} \tag{3.8}$$

for $j = 1, \ldots, n^{\mathsf{nd}}$ and $l = 1, \ldots, n^{\mathsf{dim}}$. The unknown functions α_{ik} solely depend on the current time t, which means that all derivatives of the differential operator $\boldsymbol{\mathcal{D}}$ in $\boldsymbol{\mathcal{R}}$ with respect to spatial coordinates are carried out on the shape functions N_i alone. As already mentioned before, it is often beneficial to employ weak derivatives when applying the operator $\boldsymbol{\mathcal{R}}$ in order to lower the differentiability requirements on N_i.

The FEM is characterized by the particular choice of the *shape functions* N_i and $\bar{N}_j$. This brief general introduction is restricted to a Bubnov-Galerkin approach with continuous shape functions. The method requires a grid that discretizes the domain into n^{el} elements containing n^{nd} nodes with nodal positions $\mathbf{x}_i, i = 1, \ldots, n^{\mathsf{nd}}$. If the so-called *isoparametric concept* is employed, all physical and geometrical quantities are discretized with the same shape functions. A bijective function $\boldsymbol{\zeta}$ maps every element e from the spatial configuration into a parameter domain $\mathcal{Q}$, which exclusively depend on the element type, with a local coordinate system $\boldsymbol{\theta}$. Given the local coordinates of node j by $\boldsymbol{\theta}_j$, element shape functions $N_i^e = N_i^e(\boldsymbol{\theta})$ are defined in $\mathcal{Q}$ such that

$$N_i^e(\boldsymbol{\theta}_j) = \delta_{ij}, \quad N_i^e(\boldsymbol{\theta}) = 0 \; \forall \, \boldsymbol{\theta} \notin \mathcal{Q}, \quad \sum_i N_i^e(\boldsymbol{\theta}) = 1 \; \forall \, \boldsymbol{\theta} \in \mathcal{Q}. \tag{3.9}$$

This equation refers to the element local numbering of the nodes. Throughout this thesis, hexahedral elements with eight nodes and with tri-linear shape functions N_i^e are considered. In this case, the domain $\mathcal{Q}$ can be identified with the cube $\mathcal{Q} = [-1, 1]^{n^{\mathsf{dim}}}$ and the nodes of the element are mapped to its corners. The geometry of the element is approximated as

$$\mathbf{x}^h(\boldsymbol{\theta}) = \sum_{i=1}^{8} N_i^e(\boldsymbol{\theta}) \, \mathbf{x}_i. \tag{3.10}$$

Together with the mapping $\boldsymbol{\zeta}$, this approximation allows to (at least formally) define the global continuous shape function N_i with respect to the spatial coordinates and with $N_i(\mathbf{x}_j) = \delta_{ij}$. The compact support of N_i does not exceed the elements containing the

associated node i. These properties motivate the term 'finite elements'. Using these shape functions to discretize the unknown function $\mathbf{y}$ and denoting the discrete nodal values of $\mathbf{y}$ in node i as $\mathbf{y}_i^h$, it can easily be shown that

$$\mathbf{y}^h(\mathbf{x},t) = \sum_{i=1}^{n^{\text{nd}}} N_i(\mathbf{x})\,\mathbf{y}_i^h(t) = \underline{\mathbf{N}}(\mathbf{x})\underline{\mathbf{y}}(t), \tag{3.11}$$

$$\mathbf{y}^h(\boldsymbol{\theta},t) = \sum_{i=1}^{8} N_i^e(\boldsymbol{\theta})\,\mathbf{y}_i^h(t). \tag{3.12}$$

To shorten the notation, the vector of discrete nodal values $\underline{\mathbf{y}}(t)$ and a corresponding matrix $\underline{\mathbf{N}}(\mathbf{x})$ have been introduced. The definition of $\mathcal{S}^h$ in (3.5) brings about the restriction $\mathbf{y}_j^h(t) = \mathbf{y}_D(\mathbf{x}_j,t)$ for $\mathbf{x}_j \in \Gamma_D$. Definition (3.6) shows that the nodal values $\boldsymbol{\eta}_j^h(t)$ associated with a discrete test function $\boldsymbol{\eta}^h \in \mathcal{T}^h$ vanish on the Dirichlet boundary.

The major advantage of the FEM is that any integral over the domain $\Omega_{\mathbf{x}}$ can now be written as sum of element-wise integrals

$$(\,\cdot\,,\,\cdot\,)_{\Omega_{\mathbf{x}}} = \sum_{e=1}^{n^{\text{el}}} (\,\cdot\,,\,\cdot\,)_{\Omega_{\mathbf{x}}^e}, \tag{3.13}$$

showing that the integration only necessitates the knowledge of the element shape functions $N_i^e(\boldsymbol{\theta})$ and of the function $\boldsymbol{\zeta}$, but not of the global shape functions $N_i(\mathbf{x},t)$.

3.1.3 Discretization in time

The problems introduced in chapter 2 for the membrane and the fluid fields include dynamic deformations and instationary flow, implying derivatives with respect to the current time t in the differential operator $\boldsymbol{\mathcal{D}}$. Having defined a FE discretization in space, these time derivatives operate on the semi-discrete nodal values $\mathbf{y}_i^h(t)$ and lead to nonlinear ordinary differential equation (ODE) in time t. Since the differential equations at hand are linear in terms of the highest-order time derivative, the semi-discrete residual can be rewritten as

$$\underline{\mathbf{M}}\,\dot{\underline{\mathbf{y}}}(t) = \underline{\boldsymbol{f}}(\underline{\mathbf{y}}(t),t) \quad \text{or} \tag{3.14}$$

$$\underline{\mathbf{M}}\,\ddot{\underline{\mathbf{y}}}(t) = \underline{\boldsymbol{f}}(\dot{\underline{\mathbf{y}}}(t),\underline{\mathbf{y}}(t),t). \tag{3.15}$$

A problem like (3.15) can always be reformulated into an augmented system of ODEs having the form of (3.14). Hence, a system

$$\underline{\mathbf{M}}\,\dot{\tilde{\underline{\mathbf{y}}}}(t) = \underline{\boldsymbol{f}}(\tilde{\underline{\mathbf{y}}}(t),t) \tag{3.16}$$

is considered with either $\tilde{\underline{\mathbf{y}}} = \underline{\mathbf{y}}$ or $\tilde{\underline{\mathbf{y}}} = [\underline{\mathbf{y}}^{\mathsf{T}}, \dot{\underline{\mathbf{y}}}^{\mathsf{T}}]^{\mathsf{T}}$.

It is important to note that in case of incompressible flow or incompressible structures, the pressure is defined instantaneously. Therefore, to further ease the notation, it is assumed, that the vector $\tilde{\underline{\mathbf{y}}}$ either contains the fluid velocity or the structure displacement

degrees of freedom (DOFs). Possible pressure values or other internal variables are shifted to the functional $\underline{\boldsymbol{f}}$. The system is closed by additional algebraic constraints. The system is then called a system of *differential algebraic equations (DAEs)*.

For time discretization, the semi-discrete problem is evaluated at discrete time steps $t^0, t^1, \ldots, t^n, \ldots, T$ with a constant time step size $\Delta t = t^{n+1} - t^n$. The values of $\underline{\tilde{\mathbf{y}}}$ at time steps t^n are denoted by $\underline{\tilde{\mathbf{y}}}^n$. So-called *generalized-*α time integration schemes introduce generalized mid points $t^{n+1-\alpha_f}$ and $t^{n+1-\alpha_m}$ and interpolations

$$t^{n+1-\alpha_f} = (1-\alpha_f)t^{n+1} + \alpha_f t^n \tag{3.17}$$

$$t^{n+1-\alpha_m} = (1-\alpha_m)t^{n+1} + \alpha_m t^n \tag{3.18}$$

$$\underline{\dot{\tilde{\mathbf{y}}}}^{n+1-\alpha_m} = (1-\alpha_m)\underline{\dot{\tilde{\mathbf{y}}}}^{n+1} + \alpha_m \underline{\dot{\tilde{\mathbf{y}}}}^{n} \tag{3.19}$$

$$\underline{\tilde{\mathbf{y}}}^{n+1-\alpha_f} = (1-\alpha_f)\underline{\tilde{\mathbf{y}}}^{n+1} + \alpha_f \underline{\tilde{\mathbf{y}}}^{n}. \tag{3.20}$$

The discrete form of the problem (3.16) finally emerges as

$$\underline{\mathbf{M}}\underline{\dot{\tilde{\mathbf{y}}}}^{n+1-\alpha_m} = \underline{\boldsymbol{f}}(\underline{\tilde{\mathbf{y}}}^{n+1-\alpha_f}, t^{n+1-\alpha_f}). \tag{3.21}$$

Time derivatives $\underline{\dot{\tilde{\mathbf{y}}}}$ are to be related to $\underline{\tilde{\mathbf{y}}}$. In this thesis, finite difference schemes of the form

$$\frac{1}{\Delta t}\left(\underline{\tilde{\mathbf{y}}}^{n+1} - \underline{\tilde{\mathbf{y}}}^{n}\right) = \underline{\mathbf{D}} \begin{bmatrix} \underline{\dot{\tilde{\mathbf{y}}}}^{n+1} \\ \underline{\dot{\tilde{\mathbf{y}}}}^{n} \end{bmatrix} \tag{3.22}$$

are used with a constant rectangular matrix $\underline{\mathbf{D}}$.

The final system can be expressed in terms of $\underline{\tilde{\mathbf{y}}}^{n+1}$ and $\underline{\tilde{\mathbf{y}}}^{n}$ and has to be solved for the quantities at the end of the new time step t^{n+1}. In general, and for the problems considered in this work in particular, the discrete right hand side $\underline{\boldsymbol{f}}$ in (3.21) depends nonlinearly on the unknowns $\underline{\tilde{\mathbf{y}}}^{n+1}$. Therefore, the solution is computed iteratively with a Newton-type method, which requires the evaluation of derivatives of the system with respect to $\underline{\tilde{\mathbf{y}}}^{n+1}$ and possible other unknowns.

Of course, many alternative time integration schemes that do not fit into the scheme provided above can be thought of and have actually been proposed in literature. All integration schemes used in this work, however, can be derived with this approach. They only differ in the choice of generalized mid points $t^{n+1-\alpha_f}$ and $t^{n+1-\alpha_m}$ and in the finite difference schemes, i.e. in matrix $\underline{\mathbf{D}}$. Only implicit time integration schemes are considered, which are thought more suitable for the problems at hand, in particular for incompressible fluid flow and incompressible structure behavior. Details on solving ODEs and DAEs can, for example, be found in the books of Hairer et al. [94] and Hairer and Wanner [93].

3.2 Fluid discretization

This section introduces a FE formulation for the incompressible Navier-Stokes equations derived in section 2.3. As for the general case, it starts with the spatial discretization,

which here results in a system of DAEs. This part is followed by the time discretization with a one-step θ scheme. The last part of the section briefly discusses some of the numerical problems for the particular FE formulation and possible remedies.

More details on classical and alternative FE formulations for fluid flow problems can be found, for example, in the textbooks of Gresho and Sani [87] and Donea and Huerta [50] or the theses of Förster [69], Gravemeier [85], and Wall [192].

It is important to note that the influence of the FSI coupling on the fluid field is not considered in this section yet. It is addressed in section 3.7.3, after the special dual mortar discretization approach has been introduced in section 3.7.1.

3.2.1 Discretization in space

Starting point for the discretization is the ALE version of the Navier-Stokes equations as stated in (2.66) and (2.67). The same assumptions and conventions as introduced there also hold for this section. The weighted residual is the $\mathcal{L}^2$ scalar product of these equations and a test function $\boldsymbol{\eta} = (\mathbf{v}, q)$:

$$\left(\rho \mathring{\mathbf{u}} + \rho \left(\left(\mathbf{u} - \mathbf{u}^{\mathcal{G}}\right) \cdot \boldsymbol{\nabla}\right) \mathbf{u} + \nabla p - 2\mu \boldsymbol{\nabla} \cdot (\boldsymbol{\varepsilon}(\mathbf{u})) - \rho \mathbf{b} \,;\, \mathbf{v}\right)_{\Omega_{\mathbf{x}}} + \left(\boldsymbol{\nabla} \cdot \mathbf{u} \,, q\right)_{\Omega_{\mathbf{x}}} = 0. \tag{3.23}$$

In (3.23), the integration has to be performed on the current domain $\Omega_{\mathbf{x}}$, since the Navier-Stokes equations (2.66) and (2.67) have been formulated in spatial coordinates. To shorten the notation, the following abbreviation has been introduced:

$$\mathring{\mathbf{u}} = \frac{\partial \mathbf{u}|_{\boldsymbol{\chi}}}{\partial t} \circ \boldsymbol{\Phi}^{-1} = \frac{\partial (\mathbf{u} \circ \boldsymbol{\Phi})}{\partial t} \circ \boldsymbol{\Phi}^{-1}. \tag{3.24}$$

The weak form of the problem can now be obtained by integration by parts as follows: find $\mathbf{y} = (\mathbf{u}, p) \in \mathcal{S}_{\mathbf{u}} \times \mathcal{S}_p = \mathcal{S}$, such that for all test functions $\boldsymbol{\eta} = (\mathbf{v}, q) \in \mathcal{T}_{\mathbf{u}} \times \mathcal{T}_p = \mathcal{T}$ the scalar equation

$$\begin{aligned} &\rho \left(\mathring{\mathbf{u}} \,;\, \mathbf{v}\right)_{\Omega_{\mathbf{x}}} + \rho \left(\left(\left(\mathbf{u} - \mathbf{u}^{\mathcal{G}}\right) \cdot \boldsymbol{\nabla}\right) \mathbf{u} \,;\, \mathbf{v}\right)_{\Omega_{\mathbf{x}}} - \left(p \,, \boldsymbol{\nabla} \cdot \mathbf{v}\right)_{\Omega_{\mathbf{x}}} + 2\mu \left(\boldsymbol{\varepsilon}(\mathbf{u}) \,:\, \boldsymbol{\varepsilon}(\mathbf{v})\right)_{\Omega_{\mathbf{x}}} \\ &\quad + \left(\boldsymbol{\nabla} \cdot \mathbf{u} \,, q\right)_{\Omega_{\mathbf{x}}} = \rho \left(\mathbf{b} \,;\, \mathbf{v}\right)_{\Omega_{\mathbf{x}}} + \left(\mathbf{t}_N \,;\, \mathbf{v}\right)_{\Gamma_N} \end{aligned} \tag{3.25}$$

holds. In (3.25), integration by parts (or equivalently the use of weak derivatives) generates an additional boundary integral term. This term reduces to an integration on the Neumann boundary Γ_N, since the test functions vanish on the Dirichlet boundary Γ_D by definition.

From the fluid weak form (3.25), appropriate function spaces

$$\mathcal{S}_{\mathbf{u}} = \left\{ \mathbf{u} \in \mathcal{H}^1 \left(\Omega_{\mathbf{x}} \times (0,T), \mathbb{R}^{n_{\text{dim}}} \right) : \mathbf{u}|_{\Gamma_D} = \mathbf{u}_D \right\}, \tag{3.26}$$

$$\mathcal{T}_{\mathbf{u}} = \left\{ \mathbf{v} \in \mathcal{H}^1 \left(\Omega_{\mathbf{x}} \times (0,T), \mathbb{R}^{n_{\text{dim}}} \right) : \mathbf{v}|_{\Gamma_D} = \mathbf{0} \right\}, \tag{3.27}$$

$$\mathcal{S}_p = \mathcal{T}_p = \mathcal{L}^2 \left(\Omega_{\mathbf{x}} \times (0,T), \mathbb{R}^{n_{\text{dim}}} \right), \tag{3.28}$$

can be deduced. The velocity $\mathbf{u}_D$ prescribed on the Dirichlet boundary has to be a restriction of a function in $\mathcal{H}^1\left(\Omega_\mathbf{x} \times (0,T), \mathbb{R}^{n^{\text{dim}}}\right)$ onto the Dirichlet boundary Γ_D.

The spatial discretization of the fluid quantities follows a standard Galerkin scheme. As discussed above only eight noded, tri-linear, hexahedral finite elements are used. To discretize the fluid field, the same shape functions for velocity and pressure are utilized. This formulation leads to semi-discrete function spaces

$$\mathcal{S}_\mathbf{u}^h = \left\{ \mathbf{u}^h \in \mathcal{S}_\mathbf{u} : \mathbf{u}^h(\mathbf{x},t) = \sum_{i=1}^{n^{\text{nd}}} N_i(\mathbf{x})\, \mathbf{u}_i^h(t) = \underline{\mathbf{N}}_\mathbf{u}(\mathbf{x})\underline{\mathbf{u}}(t) \right\}, \tag{3.29}$$

$$\mathcal{S}_p^h = \left\{ p^h \in \mathcal{S}_p : p^h(\mathbf{x},t) = \sum_{i=1}^{n^{\text{nd}}} N_i(\mathbf{x})\, p_i^h(t) = \underline{\mathbf{N}}_p(\mathbf{x})\underline{\mathbf{p}}(t) \right\} \tag{3.30}$$

with nodal functions $\mathbf{u}_i(t)$ and $p_i(t)$ for fluid velocities and the pressure, respectively. The vectors of discrete nodal values are denoted by $\underline{\mathbf{u}}$ and $\underline{\mathbf{p}}$. The corresponding matrices $\underline{\mathbf{N}}_\mathbf{u}$ and $\underline{\mathbf{N}}_p$ contain the shape functions, but are of different size due to the definitions (3.29) and (3.30).

Using the same naming conventions for the test functions $\mathbf{v}$ and q, the semi-discrete test function spaces are given as

$$\mathcal{T}_\mathbf{u}^h = \left\{ \mathbf{v}^h \in \mathcal{T}_\mathbf{u} : \mathbf{v}^h(\mathbf{x},t) = \sum_{i=1}^{n^{\text{nd}}} N_i(\mathbf{x})\, \mathbf{v}_i^h(t) = \underline{\mathbf{N}}_\mathbf{u}(\mathbf{x})\underline{\mathbf{v}}(t) \right\}, \tag{3.31}$$

$$\mathcal{T}_p^h = \left\{ q^h \in \mathcal{T}_p : q^h(\mathbf{x},t) = \sum_{i=1}^{n^{\text{nd}}} N_i(\mathbf{x})\, q_i^h(t) = \underline{\mathbf{N}}_p(\mathbf{x})\underline{\mathbf{q}}(t) \right\}. \tag{3.32}$$

For a Dirichlet node j with position $\mathbf{x}_j$, values $\mathbf{u}_j^h(t) = \mathbf{u}_D(\mathbf{x}_j,t)$ and $\mathbf{v}_j^h(t) = \mathbf{0}$ are prescribed due to the definition of the semi-discrete spaces $\mathcal{S}_\mathbf{u}^h$ and $\mathcal{T}_\mathbf{u}^h$ as subspaces of $\mathcal{S}_\mathbf{u}$ and $\mathcal{T}_\mathbf{u}$, respectively.

So far, the grid velocity $\mathbf{u}^\mathcal{G}$ has been assumed to be given, but in the numerical scheme used in this thesis, it results from a mesh motion algorithm that is also based on a FE approach. Details on this approach will be provided in section 3.3 and its influence on the fluid system in section 3.7.3. For now and the remainder of this thesis, the discretization $\mathbf{u}^{\mathcal{G},h}$ of grid velocities is assumed to coincide with the discretization of the fluid velocity, i.e.

$$\mathbf{u}^{\mathcal{G},h}(\mathbf{x},t) = \underline{\mathbf{N}}_\mathbf{u}(\mathbf{x})\underline{\mathbf{u}}^\mathcal{G}(t). \tag{3.33}$$

Furthermore, the vector of nodal grid velocities $\underline{\mathbf{u}}^\mathcal{G}(t)$ is assumed to be known.

The semi-discrete representations (3.29) to (3.33) can now be applied to the weak form (3.25), resulting in

$$\begin{aligned}
&\rho\left(\underline{\mathbf{N}}_\mathbf{u}\,\mathring{\underline{\mathbf{u}}}(t)\,;\underline{\mathbf{N}}_\mathbf{u}\,\underline{\mathbf{v}}(t)\right)_{\Omega_\mathbf{x}} + \rho\left(\left(\left(\underline{\mathbf{N}}_\mathbf{u}\,\underline{\mathbf{u}}(t) - \underline{\mathbf{N}}_\mathbf{u}\,\underline{\mathbf{u}}^\mathcal{G}(t)\right)\cdot\boldsymbol{\nabla}\right)\underline{\mathbf{N}}_\mathbf{u}\,\underline{\mathbf{u}}(t)\,;\underline{\mathbf{N}}_\mathbf{u}\,\underline{\mathbf{v}}(t)\right)_{\Omega_\mathbf{x}} \\
&\quad - \left(\underline{\mathbf{N}}_p\,\underline{\mathbf{p}}(t)\,,\boldsymbol{\nabla}\cdot\left(\underline{\mathbf{N}}_\mathbf{u}\,\underline{\mathbf{v}}(t)\right)\right)_{\Omega_\mathbf{x}} + 2\mu\left(\boldsymbol{\varepsilon}(\underline{\mathbf{N}}_\mathbf{u}\underline{\mathbf{u}}(t)) : \boldsymbol{\varepsilon}(\underline{\mathbf{N}}_\mathbf{u}\,\underline{\mathbf{v}}(t))\right)_{\Omega_\mathbf{x}} \\
&\quad + \left(\boldsymbol{\nabla}\cdot\underline{\mathbf{N}}_\mathbf{u}\,\underline{\mathbf{u}}(t)\,,\underline{\mathbf{N}}_p\,\underline{\mathbf{q}}(t)\right)_{\Omega_\mathbf{x}} = \rho\left(\mathbf{b}\,;\underline{\mathbf{N}}_\mathbf{u}\,\underline{\mathbf{v}}(t)\right)_{\Omega_\mathbf{x}} + \left(\mathbf{t}_N\,;\underline{\mathbf{N}}_\mathbf{u}\,\underline{\mathbf{v}}(t)\right)_{\Gamma_N}.
\end{aligned} \tag{3.34}$$

Using the fact that the equations have to hold for arbitrary choices of $\underline{\mathbf{v}}$ and $\underline{\mathbf{q}}$, the matrix representation

$$\underline{\mathbf{M}}\,\mathring{\underline{\mathbf{u}}}(t) + \underline{\mathbf{C}}\left(\underline{\mathbf{u}}(t), \underline{\mathbf{u}}^{\mathcal{G}}(t)\right) + \underline{\mathbf{G}}\,\underline{\mathbf{p}}(t) = \underline{\mathbf{f}}(t) \tag{3.35}$$

$$\underline{\mathbf{G}}^{\mathsf{T}}\,\underline{\mathbf{u}}(t) = \underline{\mathbf{0}} \tag{3.36}$$

of the semi-discrete weak form (3.34) can easily be obtained. Of particular interest are those contributions to matrix $\underline{\mathbf{C}}$ that result from the convection terms. They depend on the velocities $\underline{\mathbf{u}}$ and yield, thus, a nonlinear expression in $\underline{\mathbf{u}}$. If these terms dominate the system, numerical problems arise as discussed briefly in section 3.2.3. In that section, the importance of the constraint matrix $\underline{\mathbf{G}}$ and further numerical issues attributed to it will also be discussed.

3.2.2 Discretization in time

The discrete time integration is applied to the semi-discrete momentum equation (3.35). This ODE can be rewritten in the form of the general equation (3.16), i.e.

$$\underline{\mathbf{M}}\,\mathring{\underline{\mathbf{u}}}(t) = \underline{\mathbf{f}}(t) - \underline{\mathbf{C}}\left(\underline{\mathbf{u}}(t), \underline{\mathbf{u}}^{\mathcal{G}}(t)\right) - \underline{\mathbf{G}}\,\underline{\mathbf{p}}(t) = \underline{\boldsymbol{f}}(\underline{\mathbf{u}}(t), p(t), t), \tag{3.37}$$

where $\dot{\underline{\mathbf{y}}}$ has been identified with $\mathring{\underline{\mathbf{u}}}$. For the definition of the vector $\underline{\boldsymbol{f}}$, the grid velocity $\underline{\mathbf{u}}^{\mathcal{G}}$ has been dropped from the notation.

For the time integration of the fluid problem, a *one-step-θ method* is used, which can be interpreted as a special case of the generalized-α scheme stated in section 3.1.3. The momentum equation is evaluated at the end point of the time step, i.e. $\alpha_f = \alpha_m = 0$. Therefore, equation (3.37) is evaluated at time t^{n+1} and the discrete system reads

$$\underline{\mathbf{M}}\,\mathring{\underline{\mathbf{u}}}^{n+1} = \underline{\boldsymbol{f}}(\underline{\mathbf{u}}^{n+1}, \underline{\mathbf{p}}^{n+1}, t^{n+1}). \tag{3.38}$$

Based on its definition in (3.24), the differential operator $\mathring{\underline{\mathbf{u}}}$ takes into consideration that all integrations leading to the previous equations are performed with respect to the spatial configuration $\Omega_{\mathbf{x}}$. Thus, this operator is associated with the motion map $\boldsymbol{\Phi}$ evaluated at time t^{n+1}:

$$\mathring{\underline{\mathbf{u}}}^{n+1} = \frac{\partial(\mathbf{u} \circ \boldsymbol{\Phi})}{\partial t}^{n+1} \circ \left(\boldsymbol{\Phi}^{-1}\right)^{n+1}. \tag{3.39}$$

The finite difference scheme has to be defined with respect to the current configuration of the control volume $V(t)$ as well. In case of the chosen one-step-θ method, the particular form of the scheme (3.22) reads

$$\begin{aligned}\frac{1}{\Delta t}\left(\underline{\mathbf{u}}^{n+1} - \underline{\mathbf{u}}^{n+}\right) &= \begin{bmatrix} \theta\,\underline{\mathbf{1}} & \underline{\mathbf{0}} \\ \underline{\mathbf{0}} & (1-\theta)\underline{\mathbf{1}} \end{bmatrix} \begin{bmatrix} \mathring{\underline{\mathbf{u}}}^{n+1} \\ \mathring{\underline{\mathbf{u}}}^{n+} \end{bmatrix} \\ &= \theta\,\mathring{\underline{\mathbf{u}}}^{n+1} + (1-\theta)\mathring{\underline{\mathbf{u}}}^{n+},\end{aligned} \tag{3.40}$$

with a parameter $\theta \in (0, 1]$. Being defined in $\Omega_{\mathbf{x}}$ and, hence, for the new time level t^{n+1}, the history values $\underline{\mathbf{u}}^{n+}$ and $\underline{\mathring{\mathbf{u}}}^{n+}$ have to be defined consistently. For any quantity $\underline{\mathbf{g}}$, the history value is given as

$$\underline{\mathbf{g}}^{n+} = (\underline{\mathbf{g}} \circ \boldsymbol{\Phi})^n \circ \left(\boldsymbol{\Phi}^{-1}\right)^{n+1}. \tag{3.41}$$

These values $\underline{\mathbf{g}}^{n+}$ can be identified with the history values of a fixed point in the reference configuration. In other words, for a fixed reference coordinate $\boldsymbol{\chi} \in \Omega_{\boldsymbol{\chi}}$ with $\boldsymbol{\Phi}^n(\boldsymbol{\chi}) = \mathbf{x}^n$ and $\boldsymbol{\Phi}^{n+1}(\boldsymbol{\chi}) = \mathbf{x}^{n+1}$, the following identity holds

$$\underline{\mathbf{g}}^{n+}(\mathbf{x}^{n+1}) = \underline{\mathbf{g}}^{n}(\mathbf{x}^{n}). \tag{3.42}$$

This fact is very convenient for a FE implementation. Due to the definition of the motion mapping $\boldsymbol{\Phi}$ as grid motion, finite element nodes represent points with fixed reference coordinates and, thus, history values stored at a node from the previous time step can be reused without further modification. This property is closely related with the *geometric conservation law*, details on which can, for example, be found in the work of Förster et al. [68].

The finite difference scheme (3.40) can be solved for the unknown accelerations $\underline{\mathring{\mathbf{u}}}^{n+1}$, which can then be substituted into the discrete form of the ODE (3.38). The result of this manipulation still contains accelerations from the previous time step n. These can be eliminated using the fact that the discrete balance of forces (3.38) also holds for time t^n.

The algebraic constraint (3.36) is consistently evaluated at time t^{n+1} and completes the nonlinear system of equations by the discrete form of the continuity equation

$$\underline{\mathbf{G}}^{\mathsf{T}}\underline{\mathbf{u}}^{n+1} = \underline{\mathbf{0}}. \tag{3.43}$$

The final system of equations is to be solved for the unknown quantities $\underline{\mathbf{u}}^{n+1}$ and $\underline{\mathbf{p}}^{n+1}$ as long as the grid motion is assumed to be given.

The solution of the nonlinear system is based on an iterative Newton-type solution scheme. This implies that the equations have to be linearized with respect to the unknown quantities and a set of linear equations is to be solved in every iteration step. In the particular case of a standard Galerkin approach for the Navier-Stokes equations, the linearization results in a block system of the form

$$\begin{bmatrix} \underline{\mathbf{K}} & \underline{\mathbf{G}} \\ \underline{\mathbf{G}}^{\mathsf{T}} & \underline{\mathbf{0}} \end{bmatrix}_i^{n+1} \begin{bmatrix} \Delta\underline{\mathbf{u}} \\ \Delta\underline{\mathbf{p}} \end{bmatrix}_{i+1}^{n+1} = - \begin{bmatrix} \underline{\mathbf{r}}_{\mathbf{u}} \\ \underline{\mathbf{0}} \end{bmatrix}_i^{n+1}, \tag{3.44}$$

where the linear stiffness matrix $\underline{\mathbf{K}}$ has been introduced containing entries resulting from the matrices $\underline{\mathbf{M}}$ and $\underline{\mathbf{C}}$. Given the residual vector $\underline{\mathbf{r}}_{\mathbf{u},i}^{n+1}$, system (3.44) is solved for the unknown velocity increments $\Delta\underline{\mathbf{u}}_{i+1}^{n+1}$ and pressure increments $\Delta\underline{\mathbf{p}}_{i+1}^{n+1}$. The velocity and pressure vectors for the new iteration step $i+1$ are obtained as

$$\underline{\mathbf{u}}_{i+1}^{n+1} = \underline{\mathbf{u}}^{n} + \sum_{j=1}^{i+1} \Delta\underline{\mathbf{u}}_{j}^{n+1} \tag{3.45}$$

$$\underline{\mathbf{p}}_{i+1}^{n+1} = \underline{\mathbf{p}}^{n} + \sum_{j=1}^{i+1} \Delta\underline{\mathbf{p}}_{j}^{n+1}. \tag{3.46}$$

The procedure is repeated until convergence is reached, i.e. until the norms of the residual vector $\underline{\mathbf{r}}_{\mathbf{u},i}^{n+1}$ and of the increments $\Delta\underline{\mathbf{u}}_{i+1}^{n+1}$ and $\Delta\underline{\mathbf{p}}_{i+1}^{n+1}$ are less than a certain given tolerance.

3.2.3 Numerical issues and remedies

The usage of equal shape functions for velocity and pressure DOFs and their corresponding test functions yield a non-injective constraint matrix $\underline{\mathbf{G}}$. Hence, there exists a non-zero vector $\underline{\mathbf{p}} \neq \underline{\mathbf{0}}$ with $\underline{\mathbf{G}}\underline{\mathbf{p}} = \underline{\mathbf{0}}$. For practical applications, large pressure oscillations will occur and a reasonable solution cannot be obtained. An obvious remedy would be a different choice of shape functions, such that a stable formulation is achieved. In literature, a couple of different stable combinations are proposed, a summary of which can be found in the book of Gresho and Sani [86, Table 3.13-1, Table 3.13-2].

These proposed combinations usually satisfy the so-called *Ladyzhenskaya-Babuska-Brezzi-condition (LBB-condition)* put on $\mathcal{T}_{\mathbf{u}}^h$ and $\mathcal{T}_p^h$, which guarantees stability of the solution (see, for example, Babuška [6], Brezzi [29], Brezzi and Fortin [30], Hughes [112], and Ladyzhenskaya [125]).

Instead of satisfying the LBB-condition, the fluid implementation in the software package BACI circumvents the condition using a stabilization technique. An additional term is introduced in the weighted residual (3.23) testing the momentum equation not only by $\mathbf{v}$ but also by $\tau_{mp}\nabla q$. Here, the scalar quantity τ_{mp} is a so-called stabilization parameter. This approach, which is known as *pressure stabilized Petrov-Galerkin (PSPG)* formulation, can be shown to result in numerically stable system with optimal convergence rate. Mathematical proofs and discussions can be found in the work of Brezzi and Douglas [31], Franca et al. [70], and Franca and Hughes [71]. The implications of circumventing the LBB-condition as compared to satisfying it have been discussed in the thesis of Wall [192] or in [71].

With regard to iterative linear solvers, one advantage of the PSPG formulation is found in the block structure of the linear system of equations. The saddle-point block structure of the system matrix as presented in (3.44) restricts the use of iterative solution schemes for the linear problem due to the zero diagonal block. In particular, so-called algebraic multigrid (AMG) preconditioner methods implemented in Trilinos are not able to deal with these block structures. The PSPG formulation adds a term $(\nabla p\,;\tau_{mp}\nabla q)_{\Omega_{\mathbf{x}}}$ to the weak form resulting in exclusively non-zero diagonal entries in the lower right block of the system matrix. As a consequence, AMG preconditioners become applicable.

As opposed to the pressure instabilities, which only depend on the choice of shape functions for velocity and pressure, large spurious velocity oscillations might emerge for convection dominated problems. These oscillations diminish with decreasing FE grid width. Since the stability of the numerical scheme should not be influenced by the chosen mesh size and the method should be applicable for a wide range of problems, more stabilization terms are added to the weighted residual (3.23) in order to obtain a stable formulation. The method chosen here is the *streamwise upwind Petrov-Galerkin (SUPG)* method. The approach is based on augmenting the test function of the

momentum equation by an additional term $\tau_m(\mathbf{c}\cdot\boldsymbol{\nabla})\mathbf{v}$ with stabilization parameter τ_m. Originally, the SUPG stabilization method has been developed based on mathematical investigations of the much simpler 1D convection-diffusion equation, which exhibits the same instabilities if convection dominates the problem. For this simplified problem, SUPG dates back to the work of Brooks and Hughes [32] and has some optimal numerical properties as shown by Hughes and Sangalli [111]. The combination of PSPG and SUPG for the Navier-Stokes equations was first proposed by Tezduyar et al. [184] and has been shown to improve the numerical behavior significantly.

In the formulation implemented in BACI, one further stabilization term is added modifying the test function for the residuum of the continuity equation. The term $q+\tau_c\boldsymbol{\nabla}\cdot\mathbf{v}$, which replaces q, is called *least-squares incompressibility constraint (LSIC)* stabilization. It is motivated by the stabilized formulation proposed by Hansbo and Szepessy [95] and is added to enhance the discrete mass conservation as shown by Linke [133].

The definition of the three stabilization parameters τ_{mp},τ_m, and τ_c is an ongoing field of research. Details on their definition and necessary limiting behavior with respect to mesh width and fluid properties can be found in the above mentioned publications or, as a summary, in the theses of Gamnitzer [74], Gravemeier [85], or Wall [192].

The final linear system of equations for the discretized, stabilized, and linearized fluid system can be written as

$$\left[\begin{array}{cc} \underline{\mathbf{K}}+\underline{\mathbf{S}}^{11}_{\mathsf{SUPG}}+\underline{\mathbf{S}}^{11}_{\mathsf{LSIC}} & \underline{\mathbf{G}}+\underline{\mathbf{S}}^{12}_{\mathsf{SUPG}} \\ \underline{\mathbf{G}}^{\mathsf{T}}+\underline{\mathbf{S}}^{21}_{\mathsf{PSPG}} & \underline{\mathbf{S}}^{22}_{\mathsf{PSPG}} \end{array}\right]^{n+1}_{i} \left[\begin{array}{c} \Delta\underline{\mathbf{u}} \\ \Delta\underline{\mathbf{p}} \end{array}\right]^{n+1}_{i+1} = -\left[\begin{array}{c} \underline{\mathbf{r}}_{\mathbf{u}} \\ \underline{\mathbf{r}}_{p} \end{array}\right]^{n+1}_{i}, \tag{3.47}$$

with stabilization matrices S.

For the development of the FSI method later in this thesis, a general notation for the fluid linear system is introduced as $\underline{\boldsymbol{\mathcal{F}}}^{n+1}_{i}\Delta\underline{\mathbf{x}}^{\mathcal{F},n+1}_{i+1}=-\underline{\mathbf{r}}^{\mathcal{F},n+1}_{i}$ with block structure

$$\left[\begin{array}{cc} \underline{\boldsymbol{\mathcal{F}}}_{\mathbf{uu}} & \underline{\boldsymbol{\mathcal{F}}}_{\mathbf{u}p} \\ \underline{\boldsymbol{\mathcal{F}}}_{p\mathbf{u}} & \underline{\boldsymbol{\mathcal{F}}}_{pp} \end{array}\right]^{n+1}_{i} \left[\begin{array}{c} \Delta\underline{\mathbf{u}}^{\mathcal{F}} \\ \Delta\underline{\mathbf{p}}^{\mathcal{F}} \end{array}\right]^{n+1}_{i+1} = -\left[\begin{array}{c} \underline{\mathbf{r}}^{\mathcal{F}}_{\mathbf{u}} \\ \underline{\mathbf{r}}^{\mathcal{F}}_{p} \end{array}\right]^{n+1}_{i}. \tag{3.48}$$

Any dependency on the grid motion has not been included in the fluid system yet, since this motion is still assumed to be given. In case of a FSI simulation, the grid displacements have to be introduced as additional variables. A mesh motion algorithm, which relates the grid displacements to the motion of the interface Γ_{FSI}, is given in the following subsection. The resulting modified system will be stated in section 3.7.3.

3.3 Fluid grid motion

The grid motion of the fluid field comes into play due the ALE approach used to account for deformable fluid domains. The requirements put on any mesh motion algorithm are, first, to respect the FSI interface motion and deformation and, second, to expand this motion to the whole fluid grid in a reasonable way.

There is not one unique way of describing and implementing the fluid grid motion, but a variety of different algorithms that have been proposed in the literature. For the problem at hand, algebraic approaches as, for example, proposed by Heil [98] are not suitable due to the rather complex geometry of the RBC. Algorithms that interpret the edges of the fluid grid as elastic linear springs and possibly add torsion springs into the nodes often yield reasonable fluid grid motions. Methods that belong to this class have been proposed by Batina [8], Degand and Farhat [45], and Farhat et al. [58]. In erythrocyte simulations, however, mesh motion resulting from this kind of approaches was found to be not satisfactory and often resulted in a break up of the calculation. Therefore, a quasi-static pseudo-structure approach is taken, which is described briefly in the first subsection.

Furthermore, due to large rotations and displacements of the FSI interface, the position of the fluid grid points at the interface are repositioned after each time-step to avoid distorted fluid meshes around the interface. Algorithms employed for the repositioning are discussed in subsection 3.3.2

3.3.1 Quasi-static pseudo structure approach

The motion of the fluid grid field, also referred to as ALE field, is to be constrained at the domain boundaries and has to follow the motion of the FSI interface. The governing equations in the domain Ω_{ALE} currently taken by the fluid grid are obtained by a simplified structure equation (2.128) transferred to spatial coordinates:

$$\boldsymbol{\nabla} \cdot \boldsymbol{\sigma} = \mathbf{0}, \quad \text{in } \Omega_{\mathsf{ALE}} \tag{3.49}$$

$$\mathbf{d}^{\mathcal{G}} = \bar{\mathbf{d}}^{\mathcal{G}} \quad \text{on } \Gamma_{\mathsf{ALE}} \tag{3.50}$$

with prescribed grid displacement values $\bar{\mathbf{d}}^{\mathcal{G}}$ on the boundary $\Gamma_{\mathsf{ALE}} = \Gamma_D \cup \Gamma_{\mathsf{FSI}}$. The divergence operator is to be evaluated with respect to the current grid positions.

The approach follows the method presented in detail in the thesis of Wall [192]. The governing equations are further simplified by assuming a linear strain measure $\boldsymbol{\varepsilon}^{\mathcal{G}}$ defined as

$$\boldsymbol{\varepsilon}^{\mathcal{G}}(\mathbf{d}^{\mathcal{G}}) = \tfrac{1}{2}\left(\left(\boldsymbol{\nabla}\, \mathbf{d}^{\mathcal{G}} \right)^{\mathsf{T}} + \boldsymbol{\nabla}\, \mathbf{d}^{\mathcal{G}} \right), \tag{3.51}$$

where the gradient operator is also defined with respect to the current mesh positions. For given Lamé constants $\lambda^{\mathcal{G}}$ and $\mu^{\mathcal{G}}$, the Cauchy stresses $\boldsymbol{\sigma}$ are calculated based on the simple Saint-Venant-Kirchhoff material

$$\boldsymbol{\sigma} = \lambda^{\mathcal{G}}\, \mathrm{tr}(\boldsymbol{\varepsilon}^{\mathcal{G}})\, \mathbf{I} + 2\mu^{\mathcal{G}} \boldsymbol{\varepsilon}^{\mathcal{G}} = \mathbb{C}\boldsymbol{\varepsilon}^{\mathcal{G}}. \tag{3.52}$$

The FE discretization of the ALE field is equivalent to the formulation for linear static structural problems. Since that procedure can be found in any textbook addressing linear finite elements, only a very short summary is given here. For details, the reader is,

for example, referred to Hughes [112] and Zienkiewicz and Taylor [205]. Introducing test functions $\delta\mathbf{d}^{\mathcal{G}}$, the weak form of (3.49) is given by

$$\left(\boldsymbol{\nabla}\cdot\boldsymbol{\sigma};\delta\mathbf{d}^{\mathcal{G}}\right)=\left(\boldsymbol{\sigma}\ :\delta\boldsymbol{\varepsilon}^{\mathcal{G}}\right)=\left(\mathbb{C}\boldsymbol{\varepsilon}^{\mathcal{G}}\ :\delta\boldsymbol{\varepsilon}^{\mathcal{G}}\right)=0 \tag{3.53}$$

Since the fluid elements introduced in section 3.2 are eight noded hexahedral elements, linear shape functions are also used for the discretization of the ALE field. The discretized displacements and virtual displacement can be written as

$$\mathbf{d}^{\mathcal{G},h}(\mathbf{x},t)=\underline{\mathbf{N}}_{\mathbf{d}^{\mathcal{G}}}(\mathbf{x})\underline{\mathbf{d}}^{\mathcal{G}}(t) \tag{3.54}$$

$$\delta\mathbf{d}^{\mathcal{G},h}(\mathbf{x},t)=\underline{\mathbf{N}}_{\mathbf{d}^{\mathcal{G}}}(\mathbf{x})\delta\underline{\mathbf{d}}^{\mathcal{G}}(t), \tag{3.55}$$

with linear shape functions $\underline{\mathbf{N}}_{\mathbf{d}^{\mathcal{G}}}(\mathbf{x})=\underline{\mathbf{N}}_{\mathbf{u}}(\mathbf{x})$ and vectors of semi-discrete nodal values $\underline{\mathbf{d}}^{\mathcal{G}}(t)$ and $\delta\underline{\mathbf{d}}^{\mathcal{G}}(t)$. This discretization is consistent with the discrete form of grid velocities $\mathbf{u}^{\mathcal{G},h}$ defined in (3.33).

Using the *Voigt notation*, the symmetric strain tensors $\boldsymbol{\varepsilon}^{\mathcal{G},h}$ and $\delta\boldsymbol{\varepsilon}^{\mathcal{G},h}$ can be regrouped into vectors

$$\underline{\boldsymbol{\varepsilon}}^{\mathcal{G},h}=\left[\begin{array}{cccccc}\underline{\boldsymbol{\varepsilon}}_{11}^{\mathcal{G},h} & \underline{\boldsymbol{\varepsilon}}_{22}^{\mathcal{G},h} & \underline{\boldsymbol{\varepsilon}}_{33}^{\mathcal{G},h} & 2\underline{\boldsymbol{\varepsilon}}_{12}^{\mathcal{G},h} & 2\underline{\boldsymbol{\varepsilon}}_{23}^{\mathcal{G},h} & 2\underline{\boldsymbol{\varepsilon}}_{31}^{\mathcal{G},h}\end{array}\right] \tag{3.56}$$

$$\delta\underline{\boldsymbol{\varepsilon}}^{\mathcal{G},h}=\left[\begin{array}{cccccc}\delta\underline{\boldsymbol{\varepsilon}}_{11}^{\mathcal{G},h} & \delta\underline{\boldsymbol{\varepsilon}}_{22}^{\mathcal{G},h} & \delta\underline{\boldsymbol{\varepsilon}}_{33}^{\mathcal{G},h} & 2\delta\underline{\boldsymbol{\varepsilon}}_{12}^{\mathcal{G},h} & 2\delta\underline{\boldsymbol{\varepsilon}}_{23}^{\mathcal{G},h} & 2\delta\underline{\boldsymbol{\varepsilon}}_{31}^{\mathcal{G},h}\end{array}\right]. \tag{3.57}$$

A linear B-operator $\underline{\mathbf{B}}^{\mathsf{lin}}$ can be defined such that the relation between strain and displacements in Voigt notation is given by

$$\underline{\boldsymbol{\varepsilon}}^{\mathcal{G}}=\underline{\mathbf{B}}^{\mathsf{lin}}\,\underline{\mathbf{d}}^{\mathcal{G}},\qquad\delta\underline{\boldsymbol{\varepsilon}}^{\mathcal{G}}=\underline{\mathbf{B}}^{\mathsf{lin}}\,\delta\underline{\mathbf{d}}^{\mathcal{G}}. \tag{3.58}$$

Applying the discretization to the weak form (3.53) and introducing a matrix form $\underline{\mathbb{C}}$ of the Saint-Venant-Kirchhoff constitutive tensor $\mathbb{C}$, a system of the form

$$(\delta\underline{\mathbf{d}}^{\mathcal{G}})^{\mathsf{T}}\,(\underline{\mathbf{B}}^{\mathsf{lin}})^{\mathsf{T}}\,\underline{\mathbb{C}}\,\underline{\mathbf{B}}^{\mathsf{lin}}\,\delta\underline{\mathbf{d}}^{\mathcal{G}} \tag{3.59}$$

is obtained, which has to hold for any vector $\delta\underline{\mathbf{d}}^{\mathcal{G}}$. The general form for the ALE system can, thus, be expressed with the general ALE stiffness matrix $\underline{\boldsymbol{\mathcal{A}}}$ as

$$\underline{\boldsymbol{\mathcal{A}}}\,\underline{\mathbf{d}}^{\mathcal{G}}=\underline{\mathbf{0}}. \tag{3.60}$$

Although the formulation is equivalent to linear structure finite elements, it is important to note that in case of the erythrocyte simulations, the FSI interface undergoes large displacements. For this application a recomputation of the ALE stiffness matrix $\underline{\boldsymbol{\mathcal{A}}}$ has been found to significantly improve the fluid grid quality throughout the course of the simulation.

The following subsection presents a novel repositioning algorithm for the grid points on the FSI interface Γ_{FSI}, which allows to simulate relatively large rotations of an embedded structure body.

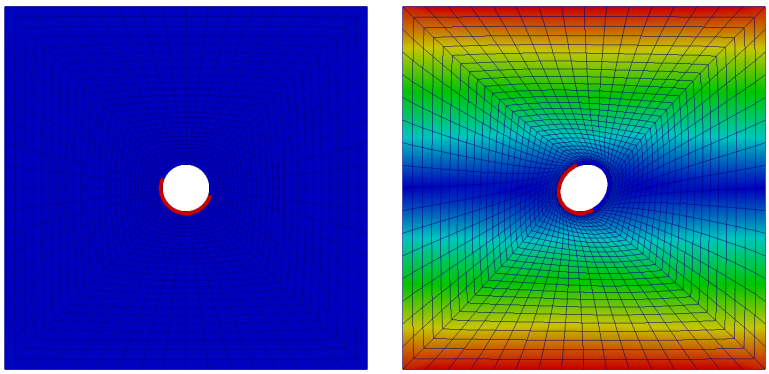

(a) initial configuration *(b) final configuration*

Figure 3.1: *Fluid mesh destruction due to a rotating structure, colour coding represents the fluid velocity*

3.3.2 Repositioning of the fluid interface grid

Subjected to shear flow, the erythrocyte membrane rotates. The particular motion depends on the viscosity of the surrounding fluid and the shear rate: a rigid body rotation of the whole cell can be observed for low viscosity and shear rates, whereas tank-treading with a stationary cell shape results from high viscosity and shear rates.

From a numerical point of view, this rotation adds complexity to the FSI simulation. In standard FSI approaches, fluid and fluid grid velocities are thought to coincide at the interface. Together with the no-slip condition (2.143), this assumption results in a grid motion that follows the interface movement, i.e. fluid grid and structure displacements match at Γ_{FSI}. In case of rotating structures, this approach often fails because of overly distorted fluid grids around the interface.

Exemplarily, Figure 3.1 shows a structure ring subjected to shear flow. The last configuration, just before the simulation breaks up, is depicted in Figure 3.1(b). Although the structure has rotated less than 45°, the fluid elements around the interface are severely sheared leading to negative Jacobian determinants in many elements.

The idea of the approach proposed in this thesis to allow for large structure rotations and displacements is a sliding of the fluid grid on the structure interface surface. This is realized by a fluid mesh motion that follows the structure interface during a time-step. Before continuing with the next time step, the resulting displacement $\underline{\mathbf{d}}_{\Gamma}^{\mathcal{G},n+1}$ is modified by $\widetilde{\Delta\underline{\mathbf{d}}}_{\Gamma}^{\mathcal{G},n+1}$, where the subscript $\cdot_{\Gamma}$ indicates that the considered quantity is restricted to the FSI interface Γ_{FSI}. Naturally, the corrected grid displacement

$$\widetilde{\underline{\mathbf{d}}}_{\Gamma}^{\mathcal{G},n+1} = \underline{\mathbf{d}}_{\Gamma}^{\mathcal{G},n+1} + \widetilde{\Delta\underline{\mathbf{d}}}_{\Gamma}^{\mathcal{G},n+1} \tag{3.61}$$

has still to account for the translation and deformation of the interface. For the calculation of $\widetilde{\Delta\underline{\mathbf{d}}}_{\Gamma}^{\mathcal{G},n+1}$, a distinction between the two FSI interfaces present in the erythrocyte simulation has to be made. In case of dealing with the interface $\Gamma_{\text{out}} \subset \Gamma_{\text{FSI}}$ between

Algorithm 3.1 Simple projection algorithm

$\Delta \mathbf{t}_\Gamma^{\mathcal{G},n+1} = 0,\ a = 0$
for all grid surface elements $e_i \in \Gamma$ **do**
$\Delta \mathbf{t}_\Gamma^{\mathcal{G},n+1} = \Delta \mathbf{t}_\Gamma^{\mathcal{G},n+1} + \int_{A_{e_i}} \Delta \mathbf{d}^{\mathcal{G},n+1}(\mathbf{x})\,\mathrm{d}\mathbf{x}$
$a = a + \int_{A_{e_i}} 1\,\mathrm{d}\mathbf{x}$
end for
$\bar{\Delta}\mathbf{t}_\Gamma^{\mathcal{G},n+1} = \Delta \mathbf{t}_\Gamma^{\mathcal{G},n+1}/a$
for all grid nodes i in Γ **do**
$\widetilde{\mathbf{x}}_i^{\mathcal{G},n+1/2} = \widetilde{\mathbf{x}}_i^{\mathcal{G},n} + \bar{\Delta}\mathbf{t}_\Gamma^{\mathcal{G},n+1}$
$\widetilde{\mathbf{x}}_i^{\mathcal{G},n+1} = \mathcal{P}(\widetilde{\mathbf{x}}_i^{\mathcal{G},n+1/2}, \underline{\mathbf{x}}_\Gamma^{\mathcal{S},n+1})$
end for
$\widetilde{\Delta \underline{\mathbf{d}}}_\Gamma^{\mathcal{G},n+1} = \widetilde{\underline{\mathbf{d}}}_\Gamma^{\mathcal{G},n+1} - \underline{\mathbf{d}}_\Gamma^{\mathcal{G},n+1} = \widetilde{\underline{\mathbf{x}}}_\Gamma^{\mathcal{G},n+1} - \underline{\mathbf{x}}_\Gamma^{\mathcal{G},n+1}$

plasma and membrane, modified grid displacements $\widetilde{\underline{\mathbf{d}}}_{\Gamma_{\text{out}}}^{\mathcal{G},n+1}$ should not follow any rotation of the interface. By contrast, the fluid grid enclosed by the membrane is able to cope with rigid body rotations of the membrane. Therefore, the modified motion $\widetilde{\underline{\mathbf{d}}}_{\Gamma_{\text{in}}}^{\mathcal{G},n+1}$ at the interface $\Gamma_{\text{in}} \subset \Gamma_{\text{FSI}}$ is to follow rigid body rotations but not the tank-treading motion of the membrane.

In the following, some approaches are introduced and it is discussed how these algorithms meet the requirements stated above.

Projection operation

One of the simplest methods that is able to suppress rotational movements of the interface is based on a projection method. To the modified positions $\widetilde{\underline{\mathbf{x}}}_\Gamma^{\mathcal{G},n}$ determined at the end of the previous time step n, the averaged translation $\bar{\Delta}\underline{\mathbf{t}}_\Gamma^{\mathcal{G},n+1}$ of the interface during the current time step $t^n \to t^{n+1}$ is added. Since, in general, the membrane has been deformed and rotated during the time step, the translated position $\widetilde{\underline{\mathbf{x}}}_\Gamma^{\mathcal{G},n+1/2} = \widetilde{\underline{\mathbf{x}}}_\Gamma^{\mathcal{G},n} + \bar{\Delta}\underline{\mathbf{t}}_\Gamma^{\mathcal{G},n+1}$ is to be projected onto the new position of structure membrane interface surface $\underline{\mathbf{x}}_\Gamma^{\mathcal{S},n+1}$ resulting in the final grid positions $\widetilde{\underline{\mathbf{x}}}_\Gamma^{\mathcal{G},n+1}$. The latter is done using a closest point projection $\mathcal{P}$. The complete approach is summarized in Algorithm 3.1.

Since the grid interface nodes are, consequently, moved based on translation and projection alone, tank-treading modes are effectively filtered out. Deformation and rigid body rotations are only accounted for by the projection $\mathcal{P}$. In case of large deformations and rotations, this may result in very poor mesh qualities of the fluid grid around the interface and, in particular, within the interface surface.

Determining rigid body rotations

The second procedure is only feasible for the grid motions within the enclosed cytosol domain, i.e. for Γ_{in}. The approach is closely related to the previous Algorithm 3.1. The position of the dimple of the cell is additionally tracked and a rigid body rotation

of the cell is approximated based on the movement of this distinguished point. The approximated rotation can be transferred into displacements of grid points, which are added of the auxiliary position $\underline{\widetilde{\mathbf{x}}}_{\Gamma}^{\mathcal{G},n+1/2}$.

The deformation is still accounted for by the projection $\mathcal{P}$, but since the preimage of the projection already includes the overall rotation of the cell, the resulting mesh quality can be significantly improved in comparison to the previously discussed simple projection approach.

Vanishing weighted average tangential displacements

The third and most involved algorithm has been designed to modify the position of the grid nodes on the outer interface Γ_{out} connecting plasma and membrane. The idea is to start from position $\underline{\mathbf{x}}_{\Gamma}^{\mathcal{G},n+1}$, which already accounts for the deformation of the interface within the time step $t^n \to t^{n+1}$ and to revert that part of the tangential component from the increment $\Delta\underline{\mathbf{d}}_{\Gamma}^{\mathcal{G},n+1}$ that results from rotation and tank-treading. The reason why the tangential displacement is not completely reverted is that also elongation of the cell results in locally tangential displacement components.

For the design of the algorithm, it is assumed that the cell rotates around the global z-axis. This is only a minor restriction since in case of the shear experiments considered in this thesis, the axis of rotation is known *a-priori*.

To motivate the method, a pure tank-treading motion of the cell membrane is considered. Given the circumferential length $l(z)$ for a cut through the membrane parallel to the xy-plane with offset z and the unit tangential vector $\boldsymbol{\vartheta}(\mathbf{x})$, which lies in the cutting plane and corresponds to a positive rotation with respect to the z-axis, the displacement increment of any point of the interface can be linearly approximated by

$$\Delta\mathbf{d}_{\Gamma}^{\mathcal{G},n+1}(\mathbf{x}) = \varsigma_{\Gamma}^{\mathcal{G},n+1}\, l(z)\, \boldsymbol{\vartheta}(\mathbf{x}), \tag{3.62}$$

for a constant scalar value $\varsigma_{\Gamma}^{\mathcal{G},n+1}$.

The circumferential length $l(z)$ can easily be approximated using the topological equivalence of the cell shape and a sphere. Let z_{max} denote the radius of the cell in z-direction and c a constant shape-dependent parameter, the approximation reads

$$l(z) = 2\pi c\sqrt{z_{\text{max}}^2 - z^2}. \tag{3.63}$$

As will be shown later, the constant c cancels out and its particular value is, thus, of no importance for the algorithm.

For a general movement of the membrane, the tangential component $\Delta\mathbf{d}_{\Gamma\|}^{\mathcal{G},n+1}$, which results from tank-treading motion, is to be reverted. There exists a constant scalar value $\varsigma_{\Gamma}^{\mathcal{G},n+1}$, such that this component of interest can be expressed based on (3.62) yielding

$$\Delta\mathbf{d}_{\Gamma\|}^{\mathcal{G},n+1}(\mathbf{x}) = \varsigma_{\Gamma}^{\mathcal{G},n+1}\, l(z)\, \boldsymbol{\vartheta}(\mathbf{x}). \tag{3.64}$$

Algorithm 3.2 Suppressing weighted average tangential displacement

$L = 0, \varsigma_\Gamma^{\mathcal{G},n+1} = 0$
for all grid surface elements $e_i \in \Gamma$ **do**
  compute unit tangents $\boldsymbol{\vartheta}(\mathbf{x})$
  $\varsigma_\Gamma^{\mathcal{G},n+1} = \varsigma_\Gamma^{\mathcal{G},n+1} + \int_\Gamma \left(\boldsymbol{\vartheta} \cdot \Delta \underline{\mathbf{d}}_\Gamma^{\mathcal{G},n+1} \right) \mathrm{d}\Gamma$
  $L = L + \int_\Gamma \sqrt{z_{\mathsf{max}}^2 - z^2}\, \mathrm{d}\Gamma$
end for
$\bar{\varsigma}_\Gamma^{\mathcal{G},n+1} = \varsigma_\Gamma^{\mathcal{G},n+1} / L$
for all grid nodes i in Γ **do**
  compute unit tangents $\boldsymbol{\vartheta}(\mathbf{x}_i)$
  $l = \sqrt{z_{\mathsf{max}}^2 - z^2}$
  $\widetilde{\mathbf{x}}_i^{\mathcal{G},n+1/2} = \mathbf{x}_{\Gamma,i}^{\mathcal{G},n+1} - \bar{\varsigma}_\Gamma^{\mathcal{G},n+1} l\, \boldsymbol{\vartheta}(\mathbf{x}_i)$
  $\widetilde{\mathbf{x}}_i^{\mathcal{G},n+1} = \mathcal{P}(\widetilde{\mathbf{x}}_i^{\mathcal{G},n+1/2}, \underline{\mathbf{x}}_\Gamma^{\mathcal{S},n+1})$
end for
$\widetilde{\Delta \underline{\mathbf{d}}}_\Gamma^{\mathcal{G},n+1} = \widetilde{\underline{\mathbf{d}}}_\Gamma^{\mathcal{G},n+1} - \underline{\mathbf{d}}_\Gamma^{\mathcal{G},n+1} = \widetilde{\underline{\mathbf{x}}}_\Gamma^{\mathcal{G},n+1} - \underline{\mathbf{x}}_\Gamma^{\mathcal{G},n+1}$

Using the identity $\boldsymbol{\vartheta} \cdot \boldsymbol{\vartheta} = 1$, results in an equivalent scalar equation

$$\Delta \mathbf{d}_{\Gamma\parallel}^{\mathcal{G},n+1}(\mathbf{x})\, \boldsymbol{\vartheta}(\mathbf{x}) = \varsigma_\Gamma^{\mathcal{G},n+1}\, l(z). \tag{3.65}$$

Subsequent integration over the interface of interest Γ results in

$$\int_\Gamma \Delta \mathbf{d}_{\Gamma\parallel}^{\mathcal{G},n+1}\, \boldsymbol{\vartheta}\, \mathrm{d}\Gamma = \int_\Gamma \varsigma_\Gamma^{\mathcal{G},n+1}\, l(z)\, \mathrm{d}\Gamma = \varsigma_\Gamma^{\mathcal{G},n+1} \int_\Gamma l(z)\, \mathrm{d}\Gamma, \tag{3.66}$$

which can easily be solved for $\varsigma_\Gamma^{\mathcal{G},n+1}$. Since tangential components of translation and deformation cancel out in an integral sense, the integral on the left hand side of (3.66) can equivalently be reformulated in terms of the displacement increment $\Delta \mathbf{d}_\Gamma^{\mathcal{G},n+1}$:

$$\int_\Gamma \Delta \mathbf{d}_{\Gamma\parallel}^{\mathcal{G},n+1} \cdot \boldsymbol{\vartheta}\, \mathrm{d}\Gamma = \int_\Gamma \Delta \mathbf{d}_\Gamma^{\mathcal{G},n+1} \cdot \boldsymbol{\vartheta}\, \mathrm{d}\Gamma. \tag{3.67}$$

Finally, equations (3.66) and (3.67) allow to calculate the value of $\varsigma_\Gamma^{\mathcal{G},n+1}$ and, consequently, the tangential displacement component of interest

$$\begin{aligned} \Delta \mathbf{d}_{\Gamma\parallel}^{\mathcal{G},n+1}(\mathbf{x}) = \varsigma_\Gamma^{\mathcal{G},n+1}\, l(z)\, \boldsymbol{\vartheta}(\mathbf{x}) &= \frac{\left(\int_\Gamma \Delta \mathbf{d}_\Gamma^{\mathcal{G},n+1} \cdot \boldsymbol{\vartheta}\, \mathrm{d}\Gamma \right) l(z)}{\int_\Gamma l(z)\, \mathrm{d}\Gamma}\, \boldsymbol{\vartheta}(\mathbf{x}) \\ &= \frac{\left(\int_\Gamma \Delta \mathbf{d}_\Gamma^{\mathcal{G},n+1} \cdot \boldsymbol{\vartheta}\, \mathrm{d}\Gamma \right) \not{2}\, \not{\pi}\, \not{c} \sqrt{z_{\mathsf{max}}^2 - z^2}}{\not{2}\, \not{\pi}\, \not{c} \int_\Gamma \sqrt{z_{\mathsf{max}}^2 - z^2}\, \mathrm{d}\Gamma}\, \boldsymbol{\vartheta}(\mathbf{x}). \end{aligned} \tag{3.68}$$

The complete approach is summarized in Algorithm 3.2.

The positive effect of the repositioning based on Algorithm 3.2 can be seen for the rotating ring depicted in Figure 3.2. Geometry and boundary conditions of the example coincide with the previously considered one at the beginning of this subsection (cf.

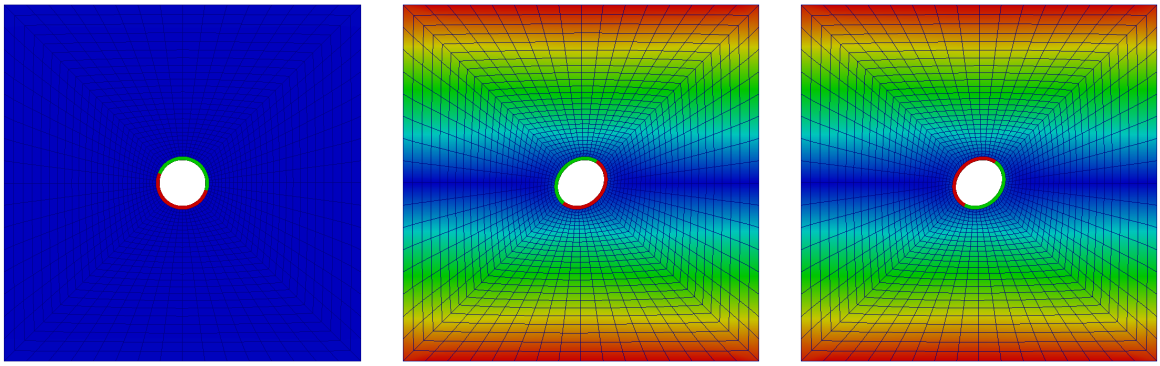

(a) initial configuration *(b) after $\approx 225°$ rotation* *(c) final $\approx 405°$ rotation*

Figure 3.2: *Sliding ALE approach for a rotating structure ring in shear flow*

Figure 3.1). Since it is a very simple pseudo 2D example and not a closed cell membrane, Algorithm 3.2 is slightly simplified by the assumption $l \equiv 1$. In contrast to the standard case, the presented approach preserves the mesh quality and arbitrary rotations of the structure can be realized.

Remark 3.1 (Alternative approaches for rotating structures) *The simulation of rotating structures within a fluid domain is of great interest for many applications in civil, mechanical, aerospace and biomechanical engineering. Very often, for example for the flow past a propeller, the structure displacements are very large, but the resulting deformations can be assumed to be relatively small. For such an application, the presented sliding ALE approach is not suitable, in particular for non-regular structure shapes. Instead of sliding along the FSI interface Γ_{FSI}, it would probably be beneficial to specify a fluid-fluid interface between a deformable and a fixed grid and let the deformable grid slide onto this surface. The coupling can again be realized by the dual mortar method, as proposed by Ehrl et al. [52] for fixed non-conforming fluid meshes.*

A similar method called shear-slip mesh update method was proposed by Behr and Arora [9] and Behr and Tezduyar [10]. This method is also based on a sliding along an interface within the fluid field, but instead of a continuous motion, the sliding is realized by a change in the connectivity of the mesh. In case of strained ALE elements, the whole interface of the deformable domain is rotated to the next element. Starting with conforming interface discretizations, the approach, thus, always produces conforming interfaces but relies on a regular discretization of this interface. Furthermore, changing the connectivity of the fluid mesh requires non-standard functionality within the FE code structure.

Alternatively, fixed grid FSI approaches do not necessitate special treatment of rotating structures. Methods developed at the Institute for Computational Mechanics are based on the extended finite element method (XFEM) to describe the fluid field. More details and a brief discussion on these approaches proposed by Gerstenberger and Wall [78, 79] and Shahmiri et al. [174] can be found in section 7.2.

3.4 Membrane discretization

This section presents the derivation of a FE formulation for the human RBC membrane, i.e. for the incompressible lipid bilayer and the compressible cytoskeleton. The weak form is derived in the first subsection based on an augmented system of equations. In this framework, the element technology necessary to avoid locking of the elements can be defined.

For the sake of readability, the element technologies used for each layer are addressed separately. Motivated by the fluid discretization, in case of the incompressible lipid bilayer, a stabilized equal-order mixed formulation with linear ansatz functions and an assumed natural strain (ANS) technology is employed. So far, this rather new formulation has only been described in a technical report by Bornemann and Wall [23]. Thus, it is introduced in some detail in section 3.4.2. In contrast, the formulation employed to discretize the cytoskeleton is based on the well-known solid shell element proposed by Tan and Vu-Quoc [181]. This formulation, which implements ANS and the enhanced assumed strain (EAS) method, is only briefly introduced in section 3.4.4. A more detailed discussion can be found in appendix B. This section is closed with the generalized-α time discretization scheme chosen for the structure field.

For further information on the FEM for linear and nonlinear structural mechanics, the reader is, for example, referred to the monographs of Belytschko et al. [13], Hughes [112], or Wriggers [198].

The coupling terms emerging from FSI are again omitted in this section. They require special discretization techniques that are introduced in section 3.7.1. The necessary modification of the structure system is the focus of section 3.7.2.

3.4.1 Weak form of the structure governing equations

The governing equations for structure motion are stated in (2.128) and (2.134). Using these equations for the finite element discretization without further modification would yield a formulation with various numerical defects. In particular, for thin elements and for nearly-incompressible material behavior, so-called *locking phenomena* would occur. Particular deformation modes trigger unwanted or ‘parasitic’ strains within the element, which cannot be counterbalanced by any other deformation mode of the element. The corresponding parasitic stresses spoil the response of the element and lead to a too stiff mechanical behavior, since one part of the outer load is balanced by the parasitic stresses. An overview on locking phenomena of continuum based elements and possible remedies can be found in the theses of Frenzel [72] and of Koschnick [122]. A short summary is given in appendix B at least for those effects that play an important role for the erythrocyte discretization.

All element technology used in this thesis is based on an augmented system of governing equations. In the continuous setting, the modified system is equivalent to the equations (2.128) and (2.134). As additional independent variables, an incompatible deformation

gradient $\bar{\mathbf{F}}$ and an incompatible stress field $\tilde{\mathbf{P}}$ are introduced, yielding

$$\rho^0(\mathbf{X})\frac{\mathrm{d}^2\mathbf{d}}{\mathrm{d}t^2}(\mathbf{X},t) - \rho^0(\mathbf{X})\mathbf{b}(\mathbf{X},t) - \mathbf{Div}(\tilde{\mathbf{P}})(\mathbf{X},t) = \mathbf{0}, \tag{3.69}$$

$$\det(\bar{\mathbf{F}}(\mathbf{X},t)) - 1 = 0, \tag{3.70}$$

$$\bar{\mathbf{F}}\,\mathbf{S}(\bar{\mathbf{F}},p) - \tilde{\mathbf{P}}(\mathbf{X},t) = \mathbf{0}, \tag{3.71}$$

$$\bar{\mathbf{F}}(\mathbf{X},t) - \mathbf{F}(\mathbf{X},t) = \mathbf{0}, \tag{3.72}$$

Of course, the constraint equation (3.70) and the explicit dependence of the stress tensor $\mathbf{S}$ on the pressure field p only apply for the lipid bilayer. Note that in this case, additional history values have to be considered to account for viscoelastic material behavior.

In order to obtain the weighted residual, the $\mathcal{L}^2$ scalar product of these equations with a test function $\boldsymbol{\eta} = (\delta\mathbf{d}, \delta p, \delta\bar{\mathbf{F}}, \delta\tilde{\mathbf{P}})$ is calculated:

$$\begin{aligned} 0 = &\left(\left(\rho^0\frac{\mathrm{d}^2\mathbf{d}}{\mathrm{d}t^2} - \rho^0\mathbf{b} - \mathbf{Div}(\tilde{\mathbf{P}})\right);\delta\mathbf{d}\right)_{\Omega_\mathbf{X}} + \left((\bar{J}-1),\delta p\right)_{\Omega_\mathbf{X}} + \\ &+ \left(\left(\bar{\mathbf{F}}\,\bar{\mathbf{S}} - \tilde{\mathbf{P}}\right) : \delta\bar{\mathbf{F}}\right)_{\Omega_\mathbf{X}} + \left(\left(\bar{\mathbf{F}} - \mathbf{F}\right) : \delta\tilde{\mathbf{P}}\right)_{\Omega_\mathbf{X}}, \end{aligned} \tag{3.73}$$

where the abbreviations $\bar{\mathbf{S}} = \mathbf{S}(\bar{\mathbf{F}},p)$ and $\bar{J} = \det(\bar{\mathbf{F}})$ have been introduced. For the cytoskeleton, the test function reduces to $\boldsymbol{\eta} = (\delta\mathbf{d}, \delta\bar{\mathbf{F}}, \delta\tilde{\mathbf{P}})$ and the corresponding terms in (3.73) vanish.

The choice of the additional variables is not completely free but has to fulfill the orthogonality condition

$$\left(\tilde{\mathbf{P}} : (\bar{\mathbf{F}} - \mathbf{F})\right)_{\Omega_\mathbf{X}} = 0, \tag{3.74}$$

which carries over to the corresponding weighting functions, i.e. $(\tilde{\mathbf{P}} : (\delta\bar{\mathbf{F}} - \delta\mathbf{F})) = 0$ and $(\delta\tilde{\mathbf{P}} : (\bar{\mathbf{F}} - \mathbf{F})) = 0$. These conditions and integration by parts transform the weighted residual into

$$0 = \left(\left(\rho^0\frac{\mathrm{d}^2\mathbf{d}}{\mathrm{d}t^2} - \rho^0\mathbf{b}\right);\delta\mathbf{d}\right)_{\Omega_\mathbf{X}} + \left((\bar{J}-1),\delta p\right)_{\Omega_\mathbf{X}} + \left((\bar{\mathbf{F}}\bar{\mathbf{S}}) : \delta\bar{\mathbf{F}}\right)_{\Omega_\mathbf{X}} - (\mathbf{T}_N;\delta\mathbf{d})_{\Gamma_N}. \tag{3.75}$$

Since the element technologies to come are based on particular choices of an incompatible Green-Lagrange strain $\bar{\mathbf{E}}$, it is beneficial to use $\bar{\mathbf{E}} = \frac{1}{2}(\bar{\mathbf{F}}^\mathsf{T}\bar{\mathbf{F}} - \mathbf{1})$ as independent parameter instead of $\bar{\mathbf{F}}$. Furthermore, the constitutive laws defined in sections 2.4.4 and 2.4.5 are split into isochoric and volumetric contributions. This split also applies to $\bar{\mathbf{S}}(\bar{\mathbf{E}},p) = \bar{\mathbf{S}}_{\mathsf{iso}}(\bar{\mathbf{E}}) + \bar{\mathbf{S}}_{\mathsf{vol}}(\bar{\mathbf{E}},p)$. Equivalence of the work conjugate pairs $\bar{\mathbf{P}} : \delta\bar{\mathbf{F}} = \bar{\mathbf{F}}\bar{\mathbf{S}} : \delta\bar{\mathbf{F}} = \bar{\mathbf{S}} : \delta\bar{\mathbf{E}}$ can be used to deduce

$$\begin{aligned} 0 = &\left(\rho^0\frac{\mathrm{d}^2\mathbf{d}}{\mathrm{d}t^2};\delta\mathbf{d}\right)_{\Omega_\mathbf{X}} + \left((\bar{J}-1),\delta p\right)_{\Omega_\mathbf{X}} + \left(\left(\bar{\mathbf{S}}_{\mathsf{iso}} + \bar{\mathbf{S}}_{\mathsf{vol}}\right) : \delta\bar{\mathbf{E}}\right)_{\Omega_\mathbf{X}} - \\ &- \left(\rho^0\mathbf{b};\delta\mathbf{d}\right)_{\Omega_\mathbf{X}} - (\mathbf{T}_N;\delta\mathbf{d})_{\Gamma_N}, \end{aligned} \tag{3.76}$$

which represents an equivalent formulation of the weighted residual (3.75).

Remark 3.2 (Interpretation of the weak form) *There are at least two alternative ways to interpret the weak form* (3.76)*:*

The derivation can be identified with the principle of virtual work. Therefore, the weighting functions $\delta\mathbf{d}, \delta p$, and $\delta\bar{\mathbf{E}}$ are often referred to as virtual displacements, virtual pressures, and virtual strains, respectively.

The weak form can also be derived from a Lagrange-Hu-Washizu work functional $W(\mathbf{d}, p, \bar{\mathbf{F}}, \tilde{\mathbf{P}})$ if such a potential exists. In that case, the contribution of the pressure can easily be related with a Lagrange multiplier potential $\int_{\Omega_\mathbf{X}} p(\bar{J}-1)\,\mathrm{d}\mathbf{X}$ used to enforce the incompressibility constraint condition $\bar{J}=1$. The solution minimizes the work W, i.e. it is the root of the variation δW of W with respect to the primary variables, which is identical to the weak form (3.76)*.*

Based on (3.76) and the constitutive equations defined in sections 2.4.4 and 2.4.5, the trial space $\mathcal{S}_\mathbf{y} = \mathcal{S}_\mathbf{d} \times \mathcal{S}_p \times \mathcal{S}_{\bar{\mathbf{E}}}$ for the solution function $\mathbf{y} = (\mathbf{d}, p, \bar{\mathbf{E}})$ and the test space $\mathcal{T}_\mathbf{y} = \mathcal{T}_\mathbf{d} \times \mathcal{T}_p \times \mathcal{T}_{\bar{\mathbf{E}}}$ for the weighting function $\boldsymbol{\eta} = (\delta\mathbf{d}, \delta p, \delta\bar{\mathbf{E}})$ can be defined as

$$\mathcal{S}_\mathbf{d} = \left\{ \mathbf{d} \in \mathcal{H}^1\left(\Omega_\mathbf{X} \times (0,T), \mathbb{R}^{n^{\mathsf{dim}}}\right) : \mathbf{d}|_{\Gamma_D} = \mathbf{d}_D \right\} \tag{3.77}$$

$$\mathcal{T}_\mathbf{d} = \left\{ \delta\mathbf{d} \in \mathcal{H}^1\left(\Omega_\mathbf{X} \times (0,T), \mathbb{R}^{n^{\mathsf{dim}}}\right) : \delta\mathbf{d}|_{\Gamma_D} = \mathbf{0} \right\} \tag{3.78}$$

$$\mathcal{S}_p = \mathcal{T}_p = \mathcal{L}^2\left(\Omega_\mathbf{X} \times (0,T), \mathbb{R}\right) \tag{3.79}$$

$$\mathcal{S}_{\bar{\mathbf{E}}} = \mathcal{T}_{\bar{\mathbf{E}}} = \mathcal{L}^2\left(\Omega_\mathbf{X} \times (0,T), \mathbb{R}^{n^{\mathsf{dim}}} \otimes \mathbb{R}^{n^{\mathsf{dim}}}\right). \tag{3.80}$$

The discrete versions of the weighted residual are derived separately for both membrane layers in the following subsections, since they differ in the primary variables as well as in the particular element technologies. Nevertheless, both formulations agree in the discretization of displacements and geometry. Again, eight noded tri-linear hexahedral finite elements are used. Hence, the following element local interpolations can be defined

$$\mathbf{X}^h(\boldsymbol{\theta}) = \sum_{i=1}^{8} N_i^e(\boldsymbol{\theta})\mathbf{X}_i, \tag{3.81}$$

$$\mathbf{d}^h(\boldsymbol{\theta}, t) = \sum_{i=1}^{8} N_i^e(\boldsymbol{\theta})\mathbf{d}_i(t), \tag{3.82}$$

$$\delta\mathbf{d}^h(\boldsymbol{\theta}, t) = \sum_{i=1}^{8} N_i^e(\boldsymbol{\theta})\delta\mathbf{d}_i(t), \tag{3.83}$$

with initial nodal positions $\mathbf{X}_i$, displacements $\mathbf{d}_i$, virtual displacements $\delta\mathbf{d}_i$, and local coordinates $\boldsymbol{\theta} = (\theta^1, \theta^2, \theta^3)$. In equations (3.81) to (3.83), the subscript $\cdot_i$ refers to element local node numbers.

Globally, semi-discrete trial space $\mathcal{S}_{\mathbf{d}}^h$ and test space $\mathcal{T}_{\mathbf{d}}^h$ can be formally defined as

$$\mathcal{S}_{\mathbf{d}}^h = \left\{ \mathbf{d}^h \in \mathcal{S}_{\mathbf{d}} : \mathbf{d}^h(\mathbf{X},t) = \sum_{i=1}^{n^{\text{nd}}} N_i(\mathbf{X})\, \mathbf{d}_i^h(t) = \underline{\mathbf{N}}_{\mathbf{d}}(\mathbf{X})\underline{\mathbf{d}}(t) \right\} \tag{3.84}$$

$$\mathcal{T}_{\mathbf{d}}^h = \left\{ \delta\mathbf{d}^h \in \mathcal{T}_{\mathbf{d}} : \delta\mathbf{d}^h(\mathbf{X},t) = \sum_{i=1}^{n^{\text{nd}}} N_i(\mathbf{X})\, \delta\mathbf{d}_i^h(t) = \underline{\mathbf{N}}_{\mathbf{d}}(\mathbf{X})\delta\underline{\mathbf{d}}(t) \right\} \tag{3.85}$$

with global matrices $\underline{\mathbf{N}}_{\mathbf{d}}(\mathbf{X})$. Being subspaces of $\mathcal{S}_{\mathbf{d}}$ and $\mathcal{T}_{\mathbf{d}}$ by definition, the finite vector spaces $\mathcal{S}_{\mathbf{d}}^h$ and $\mathcal{T}_{\mathbf{d}}^h$ also have to respect the Dirichlet boundaries. For a Dirichlet node j with initial position $\mathbf{X}_j$, the displacement $\mathbf{d}_j^h(t) = \mathbf{d}_D(\mathbf{X}_j,t)$ and the value of the discrete test function $\delta\mathbf{d}_j^h(t) = \mathbf{0}$ are prescribed.

As discussed above, one advantage of the FEM is that neither trial nor test functions have to be defined explicitly on the global scale. Instead, it is sufficient to have an explicit representation on the element level. For the following derivation of FE formulations, all quantities and relations are given with respect to the element level, i.e. $\underline{\mathbf{d}} = \underline{\mathbf{d}}^e$ and $\delta\underline{\mathbf{d}} = \delta\underline{\mathbf{d}}^e$ are vectors of discrete nodal values on the element level.

To further ease the notation, the Voigt notation is used, which represents the symmetric tensors $\mathbf{S}$, $\mathbf{E}$, and $\bar{\mathbf{E}}$ by vectors of reduced size:

$$\underline{\mathbf{S}} = \begin{bmatrix} \bar{\mathbf{S}}_{11} & \bar{\mathbf{S}}_{22} & \bar{\mathbf{S}}_{33} & \bar{\mathbf{S}}_{12} & \bar{\mathbf{S}}_{23} & \bar{\mathbf{S}}_{31} \end{bmatrix} \tag{3.86}$$

$$\underline{\bar{\mathbf{E}}} = \begin{bmatrix} \bar{\mathbf{E}}_{11}^h & \bar{\mathbf{E}}_{22}^h & \bar{\mathbf{E}}_{33}^h & 2\bar{\mathbf{E}}_{12}^h & 2\bar{\mathbf{E}}_{23}^h & 2\bar{\mathbf{E}}_{31}^h \end{bmatrix} \tag{3.87}$$

$$\delta\underline{\bar{\mathbf{E}}} = \begin{bmatrix} \delta\bar{\mathbf{E}}_{11}^h & \delta\bar{\mathbf{E}}_{22}^h & \delta\bar{\mathbf{E}}_{33}^h & 2\delta\bar{\mathbf{E}}_{12}^h & 2\delta\bar{\mathbf{E}}_{23}^h & 2\delta\bar{\mathbf{E}}_{31}^h \end{bmatrix}. \tag{3.88}$$

3.4.2 Lipid bilayer discretization - a stabilized, mixed solid shell

The element formulation used to discretize the weak form (3.76) in case of the lipid bilayer is characterized by the numerical handling of the pressure DOFs and the particular choice of the incompatible Green-Lagrange strains $\bar{\mathbf{E}}$.

For a purely displacement-based FE formulation, the incompatible strains $\bar{\mathbf{E}}$ are set to the compatible strains $\mathbf{E}$ and the virtual strains $\delta\bar{\mathbf{E}}$ are consequently approximated by the compatible virtual strains. In Voigt notation, this can be written as

$$\delta\underline{\mathbf{E}}(\boldsymbol{\theta},t) = \underline{\mathbf{B}}(\boldsymbol{\theta})\delta\underline{\mathbf{d}}(t), \tag{3.89}$$

where the nonlinear B-operator $\underline{\mathbf{B}}$ has been introduced. The definition of the B-operator can be found in any textbook on nonlinear finite elements for structures, cf. the monographs by Belytschko et al. [13] or by Wriggers [198].

Since the lipid bilayer is a very thin membrane, the performance of the element in case of high aspect ratios is crucial for a realistic simulation with a reasonable mesh size. In the following, it is assumed that the thickness direction of the element can easily be

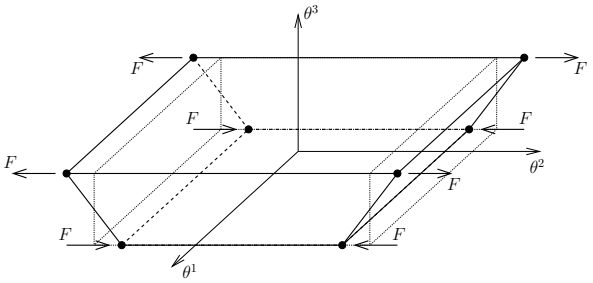

Figure 3.3:
Sketch of a bending mode of a tri-linear element

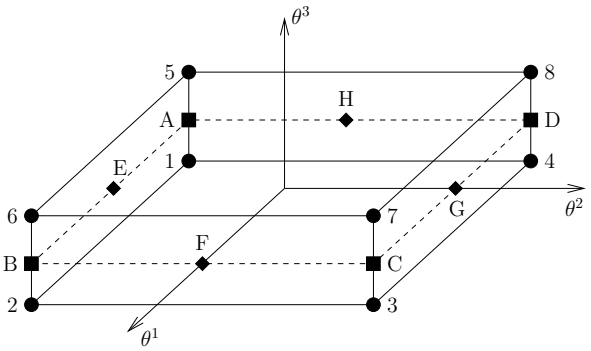

Figure 3.4:
Local node numbering for a thin element and ANS sampling points $A - H$

singled out and that the bijective function ζ maps this distinguished direction onto the third local coordinate direction θ^3.

Unfortunately, especially for this kind of slender elements, a displacement-based formulation exhibits two major geometric locking phenomena. Both effects are associated with a shortcoming of linear elements in modeling pure bending. In Figure 3.3, one bending mode is sketched exemplarily for a thin element of thickness t. This mode introduces artificial shear strains and stresses resulting in *shear locking*, since they cannot be compensated for by any other mode of a linear element. For discretizations of curved structures, bending also leads to parasitic normal stresses in thickness direction, causing the so-called *trapezoidal locking* effect. Both effects are discussed in more detail in appendix B.1.

Shear and trapezoidal locking can be reduced by the so-called assumed natural strain (ANS) method, the basic idea of which is to choose a new interpolation of the critical strain components instead of using the compatible strain values derived directly from the displacements, cf. (3.89). The new interpolation is based on values evaluated in particular points. The position of these sample points A to H in local coordinates is sketched in Figure 3.4. The particular interpolation and further details on the ANS method are provided in appendix B.2.

Introducing the modified B-operator $\bar{\underline{\mathbf{B}}}$ that accounts for the ANS interpolations, the virtual incompatible strains can be computed based on the vector of nodal virtual displacements by

$$\delta\bar{\underline{\mathbf{E}}}(\boldsymbol{\theta}) = \bar{\underline{\mathbf{B}}}(\boldsymbol{\theta})\delta\underline{\mathbf{d}}. \tag{3.90}$$

The complete modification in the element formulation introduced by the ANS approach is contained in this modified operator $\bar{\underline{\mathbf{B}}}$. The ANS method, thus, belongs to the class of *B-bar methods*, which are characterized by the usage of a modified B-operator.

The ANS formulation provides a remedy for the locking phenomena, but poses one additional challenge to the FE formulation at hand. Since an incompressible formulation is

used for this layer, some of the terms in (3.76) still explicitly depend on the incompatible deformation gradient $\bar{\mathbf{F}}$, which has to be chosen such that $\bar{\mathbf{E}} = \frac{1}{2}(\bar{\mathbf{F}}^{\mathsf{T}}\bar{\mathbf{F}} - \mathbf{1})$, for consistency. Numerically, the gradient $\bar{\mathbf{F}}$ is recovered from the incompatible Green-Lagrange strain $\bar{\mathbf{E}}$ based on a polar decomposition. The recovery and especially the linearization of $\bar{\mathbf{F}}$ with respect to the displacements is numerically very expensive. Details on this approach can be found in the report of Bornemann and Wall [23].

The discretization chosen for the structure does not satisfy the LBB-condition. Instead, pressure and the corresponding test function are discretized by the same tri-linear shape functions as the displacement variables

$$p^h(\boldsymbol{\theta}) = \sum_{i=1}^{8} N_i^e(\boldsymbol{\theta}) p_i = \underline{\mathbf{N}}_p^e(\boldsymbol{\theta})\underline{\mathbf{p}}(t), \tag{3.91}$$

$$\delta p^h(\boldsymbol{\theta}) = \sum_{i=1}^{8} N_i^e(\boldsymbol{\theta}) \delta p_i(t) = \underline{\mathbf{N}}_p^e(\boldsymbol{\theta})\, \delta\underline{\mathbf{p}}(t). \tag{3.92}$$

The DAEs describing an incompressible structure are closely related to the system of incompressible fluid flow and lead to the same stability issues as discussed in section 3.2.3. Without additional stabilization terms, a singular saddle-point type system matrix would emerge at the end of the discretization process. The stabilization technique used for the structure is adopted from the stabilization approach for the Stokes problem as proposed by Dohrmann and Bochev [49] and further elaborated by Bochev et al. [21]. The method is motivated by the fact that a discretization with a discontinuous element-wise constant pressure would yield a stable formulation, given the tri-linear discretization of the displacements.

The stabilization procedure consists of two steps: first, a discontinuous pressure $\bar{p}$ is formally defined by a projection Π of the continuous pressure p and, second, the difference between both pressure values is minimized. A least-squares formulation leads to the following additional stabilization term in the weak form (3.76)

$$\tfrac{1}{\tau}\left((p - \Pi(p))\ , (\delta p - \Pi(\delta p))\right)_{\Omega_{\mathbf{X}}}, \tag{3.93}$$

where the stabilization factor τ is usually taken as the shear modulus of the material. Since the value of $\bar{p} = \Pi(p)$ is to be constant within an element and the mapping Π is a linear operation, the projection is consequently carried out on the element level based on the discrete nodal pressure values:

$$\bar{p}^h(\boldsymbol{\theta}) = \underline{\boldsymbol{\Pi}}(\boldsymbol{\theta})\underline{\mathbf{p}}(t). \tag{3.94}$$

Denoting the element stabilization matrix by $\underline{\mathbf{P}}^e$, the element contribution to the stabilization (3.93) can be written in the form of the following integral:

$$\int_e \delta\underline{\mathbf{p}}^{\mathsf{T}} \left(N_p^e(\boldsymbol{\theta}) - \underline{\boldsymbol{\Pi}}(\boldsymbol{\theta})\right)^{\mathsf{T}} \left(N_p^e(\boldsymbol{\theta}) - \underline{\boldsymbol{\Pi}}(\boldsymbol{\theta})\right) \underline{\mathbf{p}}(t)\, \mathrm{d}\boldsymbol{\theta} = \delta\underline{\mathbf{p}}^{\mathsf{T}}\underline{\mathbf{P}}^e\underline{\mathbf{p}}. \tag{3.95}$$

The semi-discrete system of (3.76) can now be formulated in terms of the *global* semi-discrete vectors $\underline{\mathbf{d}}(t)$ and $\underline{\mathbf{p}}(t)$ as

$$\underline{\mathbf{M}}\,\underline{\ddot{\mathbf{d}}}(t) + \underline{\mathbf{f}}_{\text{int}}(\underline{\mathbf{d}}(t)) + \underline{\mathbf{G}}(\underline{\mathbf{d}}(t))\underline{\mathbf{p}}(t) = \underline{\mathbf{f}}(t), \tag{3.96}$$

$$\underline{\mathbf{f}}_{\text{vol}}(\underline{\mathbf{d}}(t)) + \underline{\mathbf{P}}\underline{\mathbf{p}}(t) = \underline{\mathbf{0}}. \tag{3.97}$$

Here, the vector $\underline{\mathbf{f}}_{\text{int}}$ emerges from the isochoric stresses alone. Its evaluation requires a discrete time integration on the material level to account for the viscoelastic properties, i.e. to solve the evolution equation (2.124). For the implementation at hand, a one-step-θ scheme with $\theta = 0.5$ is employed for its discretization. The residual force $\underline{\mathbf{f}}_{\text{vol}}$ results from the incompressibility constraint and, finally, the right hand side vector $\underline{\mathbf{f}}(t)$ accounts for external loading.

Similarly to the PSPG stabilization for the fluid system, which has been discussed in section 3.2, only terms emerging from the stabilization depend on both pressure and pressure test function. These contributions lead to stable equal-order mixed FE formulations and, additionally, avoid zero diagonal blocks in the final system matrix.

3.4.3 Cytoskeleton discretization - a solid shell with ANS and EAS

The cytoskeleton is modeled as a thin but compressible structure membrane. Therefore, the weak form (3.76) reduces to

$$0 = \left(\left(\rho^0 \frac{\mathrm{d}^2 \mathbf{d}}{\mathrm{d}t^2} - \rho^0 \mathbf{b} \right) ; \delta \mathbf{d} \right)_{\Omega_{\mathbf{X}}} + \left(\bar{\mathbf{S}}_{\text{iso}} + \bar{\mathbf{S}}_{\text{vol}} \, : \delta \bar{\mathbf{E}} \right)_{\Omega_{\mathbf{X}}} - \left(\mathbf{T}_N \, ; \delta \mathbf{d} \right)_{\Gamma_N} = 0, \tag{3.98}$$

where the stress tensor $\bar{\mathbf{S}}$ now solely depends on the incompatible right Cauchy-Green strain $\bar{\mathbf{E}}$. Due to the thinness of the membrane, a large aspect ratio of the employed elements and, thus, shear and trapezoidal locking have to be considered. Again, the ANS method is employed to account for these defects. The incompatible strains and the corresponding test functions are split up as

$$\underline{\bar{\mathbf{E}}}(\boldsymbol{\theta}, t) = \underline{\mathbf{E}}^{\text{ANS}}(\boldsymbol{\theta}, t) + \underline{\tilde{\mathbf{E}}}(\boldsymbol{\theta}, t), \tag{3.99}$$

$$\delta \underline{\bar{\mathbf{E}}}(\boldsymbol{\theta}) = \underline{\bar{\mathbf{B}}}(\boldsymbol{\theta}) \delta \underline{\mathbf{d}} + \delta \underline{\tilde{\mathbf{E}}}(\boldsymbol{\theta}). \tag{3.100}$$

The additional contributions denoted with $\tilde{\cdot}$ are necessary since, besides the geometric locking types, also a *volumetric locking* may occur that depends on the employed material. The key parameter in this case is the dilatation modulus κ of the network introduced in (2.118) or, more generally speaking, the Poisson's ratio of the material in use. It results from the fact that for linear shape functions bending as depicted in Figure 3.3 always goes along with an artificial local volume change, which introduces parasitic volumetric strains and stresses as discussed in appendix B.1.

The enhanced assumed strain (EAS) method provides a remedy for the volumetric locking. The basic idea is that strain components that are necessary for a locking free element, but that are not provided by the standard element formulation, are locally

added as enhancements $\underline{\tilde{\mathbf{E}}}$. For every element, a vector of additional unknowns $\underline{\boldsymbol{\alpha}}$, corresponding test functions $\delta\underline{\boldsymbol{\alpha}}$, and a matrix $\underline{\mathbf{M}}^{\alpha}$ are introduced, defining

$$\underline{\tilde{\mathbf{E}}}(\boldsymbol{\theta}, t) = \underline{\mathbf{M}}^{\alpha}(\boldsymbol{\theta})\underline{\boldsymbol{\alpha}}(t) \tag{3.101}$$

$$\delta\underline{\tilde{\mathbf{E}}}(\boldsymbol{\theta}) = \underline{\mathbf{M}}^{\alpha}(\boldsymbol{\theta})\delta\underline{\boldsymbol{\alpha}}. \tag{3.102}$$

For the solid shell element employed here, seven additional EAS parameters are used to improve the element behavior. The particular element formulation utilized for the cytoskeleton has been proposed by Vu-Quoc and Tan [190, 191]. A short summary can be found in appendix B.3. A detailed discussion of accurateness, efficiency, and robustness of the implementation at hand can be found in the thesis of Frenzel [72].

Finally, the semi-discrete system of equations of (3.98) can be written as follows

$$\underline{\mathbf{M}}\,\underline{\ddot{\mathbf{d}}}(t) + \underline{\mathbf{f}}_{\text{int}}(\underline{\mathbf{d}}(t), \underline{\boldsymbol{\alpha}}(t)) = \underline{\mathbf{f}}(t) \tag{3.103}$$

$$\underline{\mathbf{f}}_{\text{EAS}}(\underline{\mathbf{d}}(t), \underline{\boldsymbol{\alpha}}(t)) = \underline{\mathbf{0}}. \tag{3.104}$$

In contrast to the definition of the bilayer in (3.96), here, the vector $\underline{\mathbf{f}}_{\text{int}}$ includes both isochoric and volumetric stresses. The forces due to the EAS enhancements are denoted by $\underline{\mathbf{f}}_{\text{EAS}}$.

3.4.4 Discretization in time

In order to apply the time integration scheme defined in the general framework of section 3.1.3, the ODEs (3.96) and (3.103) have to be identified with (3.21). Choosing $\underline{\tilde{\mathbf{y}}}(t) = [\underline{\dot{\mathbf{d}}}(t), \underline{\mathbf{d}}(t)]^{\mathsf{T}}$, both structure equations can be rewritten as

$$\underline{\tilde{\mathbf{M}}}\,\underline{\dot{\tilde{\mathbf{y}}}}(t) = \begin{bmatrix} \underline{\mathbf{M}}\,\underline{\ddot{\mathbf{d}}}(t) \\ \underline{\dot{\mathbf{d}}}(t) \end{bmatrix} = \begin{bmatrix} \underline{\boldsymbol{f}}(\underline{\mathbf{d}}(t), t) \\ \underline{\dot{\mathbf{d}}}(t) \end{bmatrix} = \underline{\tilde{\boldsymbol{f}}}(\underline{\tilde{\mathbf{y}}}(t), t). \tag{3.105}$$

Of course, only the non-trivial first line of the block system is of practical interest. The function $\underline{\boldsymbol{f}}$ depends on the membrane layer considered. For the lipid bilayer it depends on the pressure and can be written as

$$\underline{\boldsymbol{f}}(\underline{\mathbf{d}}(t), \underline{\mathbf{p}}(t), t) = \underline{\mathbf{f}}(t) - \underline{\mathbf{f}}_{\text{int}}(\underline{\mathbf{d}}(t)) - \underline{\mathbf{G}}(\underline{\mathbf{d}}(t))\underline{\mathbf{p}}(t). \tag{3.106}$$

Since the pressure itself has no evolution equation, it serves as an instantaneous parameter in the last equation. For the cytoskeleton, the EAS parameters contribute to the right hand side $\underline{\boldsymbol{f}}$, i.e.

$$\underline{\boldsymbol{f}}(\underline{\mathbf{d}}(t), \underline{\boldsymbol{\alpha}}(t), t) = \underline{\mathbf{f}}(t) - \underline{\mathbf{f}}_{\text{int}}(\underline{\mathbf{d}}(t), \underline{\boldsymbol{\alpha}}(t)). \tag{3.107}$$

As for the pressure, there is no evolution equation for the EAS parameter. Therefore, it is reasonable to drop the hydrostatic pressure $\underline{\mathbf{p}}(t)$ and the EAS parameters $\underline{\boldsymbol{\alpha}}(t)$ from the notation and to derive the time integration scheme considering the general form

$$\underline{\mathbf{M}}\,\underline{\ddot{\mathbf{d}}}(t) = \underline{\boldsymbol{f}}(\underline{\mathbf{d}}(t), t), \tag{3.108}$$

as ODE of interest.

Following the generalized-α scheme (3.21), which has first been introduced for structure dynamics by Chung and Hulbert [40], the discrete balance of forces is given by

$$\underline{\mathbf{M}}\,\ddot{\underline{\mathbf{d}}}^{n+1-\alpha_m} = \underline{\boldsymbol{f}}(\underline{\mathbf{d}}^{n+1-\alpha_f}, t^{n+1-\alpha_f}). \tag{3.109}$$

In order to obtain displacements, accelerations, pressure values, or values of the internal EAS parameters at the generalized midpoints $t^{n+1-\alpha_f}$ and $t^{n+1-\alpha_m}$, their respective values at times t^n and t^{n+1} are linearly interpolated as shown in (3.19) to (3.20) for the abstract quantity $\tilde{\mathbf{y}}$. The finite difference scheme which relates the different derivatives with respect to time is set as

$$\frac{1}{\Delta t}\begin{bmatrix} \dot{\underline{\mathbf{d}}}^{n+1} - \dot{\underline{\mathbf{d}}}^{n} \\ \underline{\mathbf{d}}^{n+1} - \underline{\mathbf{d}}^{n} \end{bmatrix} = \begin{bmatrix} \gamma\,\underline{\mathbf{1}} & (1-\gamma)\,\underline{\mathbf{1}} & \underline{\mathbf{0}} & \underline{\mathbf{0}} \\ \beta\,\Delta t\,\underline{\mathbf{1}} & \frac{\Delta t}{2}(1-2\beta)\,\underline{\mathbf{1}} & \underline{\mathbf{0}} & \underline{\mathbf{1}} \end{bmatrix} \begin{bmatrix} \ddot{\underline{\mathbf{d}}}^{n+1} \\ \ddot{\underline{\mathbf{d}}}^{n} \\ \dot{\underline{\mathbf{d}}}^{n+1} \\ \dot{\underline{\mathbf{d}}}^{n} \end{bmatrix}, \tag{3.110}$$

where two adjustable parameters $\gamma \in [0,1]$ and $\beta \in [0, \frac{1}{2}]$ have been introduced. This finite different scheme is known as Newmark scheme.

The advantage of the generalized-α approach is the flexibility gained by the four parameters α_m, α_f, β, and γ. Different parameter combinations allow to adjust the amount of numerical damping introduced to the system and, for the same set of parameters, to obtain a second order accurate, unconditionally stable time integrator. For many applications, an adjustable numerical dissipation is important to stabilize the simulation.

Using the finite difference scheme (3.110), the accelerations $\ddot{\underline{\mathbf{d}}}^{n+1}$ and velocities $\dot{\underline{\mathbf{d}}}^{n+1}$ can easily be expressed in terms of the unknown displacements $\underline{\mathbf{d}}^{n+1}$. Applying this expression to the midpoint interpolation, an expression for $\ddot{\underline{\mathbf{d}}}^{n+1-\alpha_m}$ in terms of $\underline{\mathbf{d}}^{n+1}$ can be obtained. Therefore, problem (3.109) can be generally be thought of a problem formulated in the unknown quantities $\underline{\mathbf{d}}^{n+1}$, $\underline{\mathbf{p}}^{n+1}$, and $\underline{\boldsymbol{\alpha}}^{n+1}$.

To close the system, either the additional constraint equation (3.97) (in case of the lipid bilayer) or the EAS expression (3.104) (in case of the cytoskeleton) have to be considered. For an easy implementation, (3.97) and (3.104) are both evaluated at the generalized mid point $t^{n+1-\alpha_f}$. This way, the time integration scheme does not have to distinguish between displacement and pressure DOFs of the structure field and the additional EAS parameters con conveniently be eliminated for the system.

3.4.5 Linearization

The nonlinear systems are solved based on a Newton-type method, i.e. they have to be linearized with respect to the unknown displacements $\underline{\mathbf{d}}^{n+1}$, pressure values $\underline{\mathbf{p}}^{n+1}$, and EAS parameters $\underline{\boldsymbol{\alpha}}^{n+1}$. To begin with, the final linear systems of equations are derived for both membrane layers separately. In the end of this subsection, a general form of the linearized structure system is then given for the erythrocyte composite membrane.

Considering the lipid bilayer first, the vector of internal forces $\underline{\mathbf{f}}_{\text{int}}$ is given in terms of the isochoric stresses $\bar{\mathbf{S}}_{\text{iso}}$ and of the incompatible right Cauchy-Green strain tensor $\bar{\mathbf{E}}$. The linearization with respect to discrete nodal displacement values $\underline{\mathbf{d}}^{n+1}$ can be easily calculated using the chain rule:

$$\operatorname{Lin} \underline{\mathbf{f}}_{\text{int}} = \frac{\partial \underline{\mathbf{f}}_{\text{int}}}{\partial \underline{\bar{\mathbf{E}}}} \Delta \underline{\bar{\mathbf{E}}} = \frac{\partial \underline{\mathbf{f}}_{\text{int}}}{\partial \underline{\bar{\mathbf{E}}}} \frac{\partial \underline{\bar{\mathbf{E}}}}{\partial \underline{\mathbf{d}}} \Delta \underline{\mathbf{d}} = \frac{\partial \underline{\mathbf{f}}_{\text{int}}}{\partial \underline{\bar{\mathbf{E}}}} \underline{\bar{\mathbf{B}}} \, \Delta \underline{\mathbf{d}}, \tag{3.111}$$

with the ANS-modified B-operator $\underline{\bar{\mathbf{B}}}$ defined in section 3.4.2. The derivative of the vector $\underline{\mathbf{f}}_{\text{vol}}$ with respect to the displacements can be identified with the transpose of the matrix $\underline{\mathbf{G}}$ used in (3.96) as can be expected for a Lagrange multiplier formulation, cf. the following section 3.5. The final linear system to be solved in every iteration step i of the Newton algorithm is given as

$$\left[\begin{array}{cc} \underline{\mathbf{K}} & \underline{\mathbf{G}} \\ \underline{\mathbf{G}}^{\mathsf{T}} & \underline{\mathbf{P}} \end{array} \right]_i^{n+1} \left[\begin{array}{c} \Delta \underline{\mathbf{d}} \\ \Delta \underline{\mathbf{p}} \end{array} \right]_{i+1}^{n+1} = - \left[\begin{array}{c} \underline{\mathbf{r}}_{\mathbf{d}} \\ \underline{\mathbf{r}}_p \end{array} \right]_i^{n+1}, \tag{3.112}$$

with iterative residuals $\underline{\mathbf{r}}_{\mathbf{d},i}^{n+1}$ and $\underline{\mathbf{r}}_{p,i}^{n+1}$ of (3.96) and (3.97), respectively.

In case of the cytoskeleton, the incompatible strain $\bar{\mathbf{E}}$ is constructed based on ANS modifications and EAS enhancements. The linearization of the vector of internal forces $\underline{\mathbf{f}}_{\text{int}}$, which again is a function of $\bar{\mathbf{E}}$ can be calculated as

$$\operatorname{Lin} \underline{\mathbf{f}}_{\text{int}} = \frac{\partial \underline{\mathbf{f}}_{\text{int}}}{\partial \underline{\bar{\mathbf{E}}}} \Delta \underline{\bar{\mathbf{E}}} = \frac{\partial \underline{\mathbf{f}}_{\text{int}}}{\partial \underline{\bar{\mathbf{E}}}} \left(\frac{\partial \underline{\bar{\mathbf{E}}}}{\partial \underline{\mathbf{d}}} \Delta \underline{\mathbf{d}} + \frac{\partial \underline{\bar{\mathbf{E}}}}{\partial \underline{\boldsymbol{\alpha}}} \Delta \underline{\boldsymbol{\alpha}} \right) = \frac{\partial \underline{\mathbf{f}}_{\text{int}}}{\partial \underline{\bar{\mathbf{E}}}} \left(\underline{\bar{\mathbf{B}}} \, \Delta \underline{\mathbf{d}} + \underline{\mathbf{M}}^{\alpha} \, \Delta \underline{\boldsymbol{\alpha}} \right). \tag{3.113}$$

The linearization of the vector $\underline{\mathbf{f}}_{\text{EAS}}$ can be decomposed into a sum $\underline{\mathbf{K}}_{\mathbf{d}\alpha} \Delta \underline{\mathbf{d}} + \underline{\mathbf{K}}_{\alpha\alpha} \Delta \underline{\boldsymbol{\alpha}}$. Due to a local definition of the EAS parameters, which are discontinuous across element boundaries, the single element matrices $\underline{\mathbf{K}}_{\alpha\alpha}^{e}$ are decoupled in the global matrix $\underline{\mathbf{K}}_{\alpha\alpha}$. Consequently, the increments $\Delta \underline{\boldsymbol{\alpha}}^{e}$ of one element e only depend on the displacements increments $\Delta \underline{\mathbf{d}}^{e}$ of this element. This allows for a relatively easy local static condensation that eliminates the internal variables $\Delta \underline{\boldsymbol{\alpha}}$ on the global level. The final system matrix, thus, reduces to

$$\underline{\mathbf{K}}_i^{n+1} \Delta \underline{\mathbf{d}}_{i+1}^{n+1} = - \underline{\mathbf{r}}_{\mathbf{d},i}^{n+1}. \tag{3.114}$$

The linearized system for the composite, two-layer erythrocyte membrane is denoted by $\underline{\mathbb{S}}_i^{n+1} \Delta \underline{\mathbf{x}}_{i+1}^{\mathcal{S},n+1} = - \underline{\mathbf{r}}_i^{\mathcal{S},n+1}$. The vector of unknowns $\Delta \underline{\mathbf{x}}^{\mathcal{S}}$ is grouped into displacement and pressure DOFs with a corresponding split of matrix and right hand side vector

$$\left[\begin{array}{cc} \underline{\mathbb{S}}_{\mathbf{dd}} & \underline{\mathbb{S}}_{\mathbf{d}p} \\ \underline{\mathbb{S}}_{p\mathbf{d}} & \underline{\mathbb{S}}_{pp} \end{array} \right]_i^{n+1} \left[\begin{array}{c} \Delta \underline{\mathbf{d}}^{\mathcal{S}} \\ \Delta \underline{\mathbf{p}}^{\mathcal{S}} \end{array} \right]_{i+1}^{n+1} = - \left[\begin{array}{c} \underline{\mathbf{r}}_{\mathbf{d}}^{\mathcal{S}} \\ \underline{\mathbf{r}}_p^{\mathcal{S}} \end{array} \right]_i^{n+1}. \tag{3.115}$$

Common nodes at the interface between the layers share displacement DOFs, but, due to the different discretizations, only the nodes of the bilayer carry pressure DOFs.

3.5 Algebraic constraints on the erythrocyte membrane

This section presents how the algebraic constraints defined in section 2.5 can be implemented in the FE framework. The Lagrange multiplier and the penalty approach are addressed in section 3.5.1 and 3.5.2, respectively, and related modifications of the structure system are discussed. Since the approaches have been introduced starting from a minimization problem, both subsections start with variational problems, relate the result to the structure weak form, and finally state how the additional contributions are discretized in space and time.

Although it has not been used for the derivation of the FE formulation of unconstrained structures in section 3.4, for the investigation in this section, the existence of a *Lagrange-Hu-Washizu work functional* $W(\mathbf{d}, p, \bar{\mathbf{F}}, \tilde{\mathbf{P}})$ is assumed. The equivalence between the weak form and a variational form has been commented on in Remark 3.2. The work functional serves as the objective function W defining the constrained minimization problem (2.140).

3.5.1 Lagrange multiplier formulation

Starting point for this numerical realization of a constrained structure is the modified objective function $\tilde{W}(\mathbf{d}, p, \bar{\mathbf{F}}, \tilde{\mathbf{P}}, \boldsymbol{\lambda}^{\mathcal{S}}) = W(\mathbf{d}, p, \bar{\mathbf{F}}, \tilde{\mathbf{P}}) + \sum_{i=1}^{n^{\mathcal{B}}} \lambda_i^{\mathcal{S}} \mathcal{B}_i(\mathbf{d})$, cf. general notation in (2.141). Although the evaluation of some of the constraints $\mathcal{B}_i$ necessitates the evaluation of an integral, all conditions introduced in section 2.5 are global constraints and scalar-valued. Thus, also the Lagrange multipliers associated with them are globally defined scalar values. To find a stationary point of $\tilde{W}$, the variation with respect to the independent variables has to be computed

$$\delta\tilde{W}(\mathbf{d}, p, \bar{\mathbf{F}}, \tilde{\mathbf{P}}, \boldsymbol{\lambda}^{\mathcal{S}}) = \delta W(\mathbf{d}, p, \bar{\mathbf{F}}, \tilde{\mathbf{P}}) + \sum_{i=1}^{n^{\mathcal{B}}} \left(\lambda_i^{\mathcal{S}} \frac{\partial \mathcal{B}_i}{\partial \mathbf{d}} \delta\mathbf{d} \right) + \sum_{i=1}^{n^{\mathcal{B}}} \left(\delta\lambda_i^{\mathcal{S}}\, \mathcal{B}_i(\mathbf{d}) \right) = 0. \quad (3.116)$$

The term $\delta W(\mathbf{d}, p, \bar{\mathbf{F}}, \tilde{\mathbf{P}})$ agrees with the variation of the unconstrained structure system and is equivalent to the weak form (3.73) as already discussed in Remark 3.2. Using the orthogonality condition (3.74), the variation $\delta\tilde{W}(\mathbf{d}, p, \bar{\mathbf{F}}, \tilde{\mathbf{P}}, \boldsymbol{\lambda}^{\mathcal{S}})$ can be reduced to

$$\begin{aligned} 0 =& \delta W(\mathbf{d}, p, \bar{\mathbf{E}}, \boldsymbol{\lambda}^{\mathcal{S}}) \\ =& \left(\rho^0 \frac{\mathrm{d}^2\mathbf{d}}{\mathrm{d}t^2} \,;\, \delta\mathbf{d} \right)_{\Omega_{\mathbf{X}}} + \left((\bar{J} - 1) \,,\, \delta p \right)_{\Omega_{\mathbf{X}}} + \left(\bar{\mathbf{S}}_{\text{iso}} + \bar{\mathbf{S}}_{\text{vol}} \,:\, \delta\bar{\mathbf{E}} \right)_{\Omega_{\mathbf{X}}} - \\ & - \left(\rho^0 \mathbf{b} \,;\, \delta\mathbf{d} \right)_{\Omega_{\mathbf{X}}} - \left(\mathbf{T}_N \,;\, \delta\mathbf{d} \right)_{\Gamma_N} + \sum_{i=1}^{n^{\mathcal{B}}} \left(\lambda_i^{\mathcal{S}} \frac{\partial \mathcal{B}_i}{\partial \mathbf{d}} \delta\mathbf{d} \right) + \sum_{i=1}^{n^{\mathcal{B}}} \left(\delta\lambda_i^{\mathcal{S}}\, \mathcal{B}_i(\mathbf{d}) \right). \end{aligned} \quad (3.117)$$

Remark 3.3 (Interpretation of hydrostatic pressure values) *In the following, the contribution of the structure hydrostatic pressure* $\left(\bar{\mathbf{S}}_{\text{vol}} : \delta\bar{\mathbf{E}} \right)$ *and of its virtual counterpart* $\left((\bar{J} - 1), \delta p \right)$ *to the weak form are revisited. Using* $\bar{\mathbf{S}}_{\text{vol}} = p\bar{J}\bar{\mathbf{C}}^{-1}$*, the scalar product can*

be rewritten as

$$\left(\bar{\mathbf{S}}_{\text{vol}} : \delta\bar{\mathbf{E}}\right)_{\Omega_{\mathbf{X}}} = \left(p\bar{J}\bar{\mathbf{C}}^{-1} : \delta\bar{\mathbf{E}}\right)_{\Omega_{\mathbf{X}}} = \left(p\frac{\partial\bar{J}}{\partial\bar{\mathbf{E}}} : \delta\bar{\mathbf{E}}\right)_{\Omega_{\mathbf{X}}}. \tag{3.118}$$

A comparison of the pressure terms with the Lagrange multiplier entries in (3.117) *directly shows that the pressure* p *is a Lagrange multiplier enforcing of the algebraic constraint* $\mathcal{B}(\bar{J}) = \bar{J} - 1 = 0$*. In contrast to the algebraic constraints* $\mathcal{B}_i$*, the incompressibility is a local property. Consequently, the pressure is a field variable and the resulting entries to the weak form have to be given in an integral form.*

Similarly, it is easy to show that the fluid hydrostatic pressure can be identified with a Lagrange multiplier that enforces a locally divergence-free fluid flow $\mathcal{B}(\mathbf{u}) = \text{div}\mathbf{u} = 0$*, which implies the incompressibility of the flow.*

The next step towards a numerical realization is the spatial discretization of the modified weak form. Since the Lagrange multipliers merged into $\boldsymbol{\lambda}^{\mathcal{S}}$ are globally defined scalar values, they are already discrete values. Moreover, the discretization of the unconstrained structure field has already been given in the previous section. With this discretization at hand, the evaluation of the constraints $\mathcal{B}_i$ can follow standard FE procedures. Defining a rectangular constraint matrix $\underline{\mathcal{B}}$ by

$$\underline{\mathcal{B}}_{ij} = \frac{\partial\mathcal{B}_i}{\partial\underline{\mathbf{d}}_j}, \tag{3.119}$$

where $\underline{\mathbf{d}}$, again, denotes the global vector of discrete nodal displacements, the semi-discrete system can be stated as a system of ODEs

$$\underline{\mathbf{M}}\,\ddot{\underline{\mathbf{d}}}(t) = \underline{\boldsymbol{f}}(\underline{\mathbf{d}}(t), t) + \left(\underline{\mathcal{B}}(t)\right)^{\mathsf{T}}\boldsymbol{\lambda}^{\mathcal{S}}(t). \tag{3.120}$$

The right hand side vector $\underline{\boldsymbol{f}}(\underline{\mathbf{d}}(t), t)$ resulting from the unconstrained structure is defined in (3.108) and possibly contains pressure or EAS entries. In addition, the following equations need to be fulfilled:

$$\underline{\mathbf{f}}_{\text{EAS}}(\underline{\mathbf{d}}(t), \underline{\boldsymbol{\alpha}}(t)) = \underline{\mathbf{0}} \tag{3.121}$$

$$\underline{\mathbf{f}}_{\text{vol}}(\underline{\mathbf{d}}(t)) + \underline{\mathbf{P}}\underline{\mathbf{p}}(t) = \underline{\mathbf{0}} \tag{3.122}$$

$$\mathcal{B}_i(\underline{\mathbf{d}}(t)) = 0 \quad \forall i. \tag{3.123}$$

For the generalized-α scheme, the ODE (3.120) is evaluated at the generalized mid points, i.e.

$$\underline{\mathbf{M}}\,\ddot{\underline{\mathbf{d}}}^{n+1-\alpha_m} = \underline{\boldsymbol{f}}(\underline{\mathbf{d}}^{n+1-\alpha_f}, t^{n+1-\alpha_f}) + \left(\underline{\mathcal{B}}^{n+1-\alpha_f}\right)^{\mathsf{T}}\boldsymbol{\lambda}^{\mathcal{S},n+1-\alpha_f}, \tag{3.124}$$

leading to a discrete balance of forces. As discussed in section 3.4.4, the equations (3.121) and (3.122) are evaluated at the generalized mid point $t^{n+1-\alpha_f}$. This would also be a valid choice for the evaluation of (3.123). However, for the sake of post-processing,

it is always assumed that the constraint condition is to be satisfied at the end of a time step t^{n+1}, i.e.

$$\mathcal{B}_i^{n+1} = 0 \quad \forall i. \tag{3.125}$$

For efficiency, the constraint matrix $\underline{\mathcal{B}}$ should only be evaluated with respect to one time step when evaluating the residual of the system. Choosing the end point t^{n+1} for evaluation, a linear interpolation

$$\underline{\mathcal{B}}^{n+1-\alpha_f} = (1-\alpha_f)\underline{\mathcal{B}}^{n+1} + \alpha_f \underline{\mathcal{B}}^{n} \tag{3.126}$$

is used in the discrete balance of forces (3.124).

Some of the constraints $\mathcal{B}_i$ are non-linear with respect to the displacements $\underline{\mathbf{d}}$.Thus, the matrix $\underline{\mathcal{B}}$ depends on the displacement values as well and its linearization has to be considered within the Newton-Raphson iteration. Defining the matrix $\underline{\mathfrak{S}}^{\lambda}_{\mathbf{dd}}$ as

$$\left(\underline{\mathfrak{S}}^{\lambda}_{\mathbf{dd}}\right)_i^{n+1} = (1-\alpha_f) \sum_{j=1}^{n^{\mathcal{B}}} \left(\frac{\partial^2 \mathcal{B}_j}{\partial \underline{\mathbf{d}}^2} \lambda_j^{\mathcal{S}} \right)_i^{n+1} \tag{3.127}$$

and the off-diagonal blocks $\underline{\mathfrak{S}}_{\mathbf{d}\mathcal{B}}$ and $\underline{\mathfrak{S}}_{\mathcal{B}\mathbf{d}}$ as

$$\left(\underline{\mathfrak{S}}_{\mathbf{d}\mathcal{B}}\right)_i^{n+1} = \left(\underline{\mathcal{B}}^{n+1-\alpha_f}\right)^{\mathsf{T}} = (1-\alpha_f)\left(\underline{\mathcal{B}}_i^{n+1}\right)^{\mathsf{T}} + \alpha_f \left(\underline{\mathcal{B}}^{n}\right)^{\mathsf{T}} \tag{3.128}$$

$$\left(\underline{\mathfrak{S}}_{\mathcal{B}\mathbf{d}}\right)_i^{n+1} = \underline{\mathcal{B}}_i^{n+1}, \tag{3.129}$$

the extended structure system can be written as

$$\left[\begin{array}{ccc} \underline{\mathfrak{S}}_{\mathbf{dd}} + \underline{\mathfrak{S}}^{\lambda}_{\mathbf{dd}} & \underline{\mathfrak{S}}_{\mathbf{d}p} & \underline{\mathfrak{S}}_{\mathbf{d}\mathcal{B}} \\ \underline{\mathfrak{S}}_{p\mathbf{d}} & \underline{\mathfrak{S}}_{pp} & 0 \\ \underline{\mathfrak{S}}_{\mathcal{B}\mathbf{d}} & 0 & 0 \end{array} \right]_i^{n+1} \left[\begin{array}{c} \Delta \underline{\mathbf{d}}^{\mathcal{S}} \\ \Delta \underline{\mathbf{p}}^{\mathcal{S}} \\ \underline{\boldsymbol{\lambda}}^{\mathcal{S}} \end{array} \right]_{i+1}^{n+1} = - \left[\begin{array}{c} \underline{\mathbf{r}}^{\mathcal{S}}_{\mathbf{d}} \\ \underline{\mathbf{r}}^{\mathcal{S}}_{p} \\ \underline{\boldsymbol{\mathcal{B}}} \end{array} \right]_i^{n+1} . \tag{3.130}$$

The right hand side vector $\underline{\boldsymbol{\mathcal{B}}}_i^{n+1}$ contains the current status of the constraints. Of course, the system could equivalently be formulated in terms of increments $\Delta\underline{\boldsymbol{\lambda}}$. In that case, the residual $\underline{\mathbf{r}}^{\mathcal{S}}_{\mathbf{d}}$ would need to be modified to account for the history of the Lagrange multiplier.

One disadvantage of the above stated Lagrange multiplier formulation is the block structure of the linear system of equations as has already been discussed for unstabilized equal-order mixed formulations. The saddle-point type of system with its characteristic zero diagonal block is incompatible with many preconditioners usually used to accelerate the convergence behavior of iterative linear solvers. A static condensation, however, is not a reasonable option due to the non-locality of the constraints, which would lead to a significantly increased bandwidth of the matrix.

3.5.2 Penalty formulation

In contrast to the former method, the modification of the objective function resulting from the penalty formulation, i.e. $\tilde{W}(\mathbf{d}, p, \bar{\mathbf{F}}, \tilde{\mathbf{P}}) = W(\mathbf{d}, p, \bar{\mathbf{F}}, \tilde{\mathbf{P}}) + \sum_{i=1}^{n^{\mathcal{B}}} \kappa_i^{\mathcal{S}} (\mathcal{B}_i(\mathbf{d}))^2$, does not necessitate any additional variables, but constant parameters $\kappa_i^{\mathcal{S}} > 0$. A stationary point is the root of the variation, which is given by

$$\delta\tilde{W}(\mathbf{d}, p, \bar{\mathbf{F}}, \tilde{\mathbf{P}}) = \delta W(\mathbf{d}, p, \bar{\mathbf{F}}, \tilde{\mathbf{P}}) + 2 \sum_{i=1}^{n^{\mathcal{B}}} \left(\kappa_i^{\mathcal{S}} \mathcal{B}_i \frac{\partial \mathcal{B}_i}{\partial \mathbf{d}} \delta\mathbf{d} \right) = 0 \tag{3.131}$$

where the chain rule has been used. The standard variation $\delta W(\mathbf{d}, p, \bar{\mathbf{F}}, \tilde{\mathbf{P}})$ is of course again equivalent to the weak form of the unconstrained structure given in (3.73). The orthogonality condition (3.74) allows to rewrite (3.131) as

$$\begin{aligned} 0 =& \delta W(\mathbf{d}, p, \bar{\mathbf{E}}) \\ =& \left(\rho^0 \frac{\mathrm{d}^2 \mathbf{d}}{\mathrm{d}t^2} \,;\, \delta\mathbf{d} \right)_{\Omega_{\mathbf{X}}} + \left((\bar{J} - 1) \,,\, \delta p \right)_{\Omega_{\mathbf{X}}} + \left(\bar{\mathbf{S}}_{\mathsf{iso}} + \bar{\mathbf{S}}_{\mathsf{vol}} \,:\, \delta\bar{\mathbf{E}} \right)_{\Omega_{\mathbf{X}}} - \\ & - \left(\rho^0 \mathbf{b} \,;\, \delta\mathbf{d} \right)_{\Omega_{\mathbf{X}}} - \left(\mathbf{T}_N \,;\, \delta\mathbf{d} \right)_{\Gamma_N} + 2 \sum_{i=1}^{n^{\mathcal{B}}} \left(\kappa_i^{\mathcal{S}} \mathcal{B}_i \frac{\partial \mathcal{B}_i}{\partial \mathbf{d}} \delta\mathbf{d} \right). \end{aligned} \tag{3.132}$$

Let $\underline{\mathcal{B}}_{i\,\cdot}$ denote the i-th row of the constraint matrix $\underline{\mathcal{B}}$ defined in (3.119), i.e. it corresponds to the derivative of constraint $\mathcal{B}_i$ with respect to the discrete nodal displacement values $\underline{\mathbf{d}}$. The semi-discrete system can then be stated as follows

$$\underline{\mathbf{M}}\, \ddot{\underline{\mathbf{d}}}(t) = \underline{\boldsymbol{f}}(\underline{\mathbf{d}}(t), t) + 2 \sum_{i=1}^{n^{\mathcal{B}}} \left(\kappa_i^{\mathcal{S}} \mathcal{B}_i(t) \left(\underline{\mathcal{B}}_{i\,\cdot}(t) \right)^{\mathsf{T}} \right) \tag{3.133}$$

$$\underline{\mathbf{0}} = \underline{\mathbf{f}}_{\mathsf{EAS}}(\underline{\mathbf{d}}(t), \underline{\boldsymbol{\alpha}}(t)) \tag{3.134}$$

$$\underline{\mathbf{0}} = \underline{\mathbf{f}}_{\mathsf{vol}}(\underline{\mathbf{d}}(t)) + \underline{\mathbf{P}}\underline{\mathbf{p}}(t). \tag{3.135}$$

Since there are no additional variables, the method does not require additional constraint equations to close the system.

In the final systems for the human RBC it should be possible to enforce some of the constraints with the penalty method, while others are implemented using the Lagrange multiplier approach. Therefore, it is beneficial to evaluate the forces resulting from the penalty formulation also at time t^{n+1}, which leads to

$$\begin{aligned} \underline{\mathbf{M}}\, \ddot{\underline{\mathbf{d}}}^{n+1-\alpha_m} =& \underline{\boldsymbol{f}}(\underline{\mathbf{d}}^{n+1-\alpha_f}, t^{n+1-\alpha_f}) + \\ & + 2 \sum_{i=1}^{n^{\mathcal{B}}} \kappa_i^{\mathcal{S}} \left((1 - \alpha_f) \mathcal{B}_i^{n+1} \left(\underline{\mathcal{B}}_{i\,\cdot}^{n+1} \right)^{\mathsf{T}} + \alpha_f \mathcal{B}_i^n \left(\underline{\mathcal{B}}_{i\,\cdot}^{n} \right)^{\mathsf{T}} \right). \end{aligned} \tag{3.136}$$

When deriving the linearization of the previous equation, the nonlinearity of some of the constraints used for the erythrocyte membrane has to be accounted for. The linear structure system is finally given by

$$\begin{bmatrix} \underline{\mathbf{S}}_{\mathbf{dd}} + \underline{\mathbf{S}}_{\mathbf{dd}}^{\kappa} & \underline{\mathbf{S}}_{\mathbf{d}p} \\ \underline{\mathbf{S}}_{p\mathbf{d}} & \underline{\mathbf{S}}_{pp} \end{bmatrix}_i^{n+1} \begin{bmatrix} \Delta\underline{\mathbf{d}}^{\mathcal{S}} \\ \Delta\underline{\mathbf{p}}^{\mathcal{S}} \end{bmatrix}_{i+1}^{n+1} = - \begin{bmatrix} \underline{\mathbf{r}}_{\mathbf{d}}^{\mathcal{S}} + \alpha_f \underline{\mathbf{r}}_{\mathbf{d}}^{\mathcal{S},\kappa} \\ \underline{\mathbf{r}}_{p}^{\mathcal{S}} \end{bmatrix}_i^{n+1} \tag{3.137}$$

with the residual vector $\underline{\mathbf{r}}_{\mathbf{d}}^{\mathcal{S},\kappa}$ and matrix $\underline{\mathfrak{S}}_{\mathbf{dd}}^{\kappa}$ defined as

$$\underline{\mathbf{r}}_{\mathbf{d}}^{\mathcal{S},\kappa} = 2\sum_{j=1}^{n^{\mathcal{B}}} \kappa_j^{\mathcal{S}} \left(\alpha_f \mathcal{B}_j^n \left(\underline{\mathcal{B}}_j^n . \right)^{\mathsf{T}} \right) \tag{3.138}$$

$$(\underline{\mathfrak{S}}_{\mathbf{dd}}^{\kappa})_{kl} = \sum_{j=1}^{n^{\mathcal{B}}} \kappa_j^{\mathcal{S}} \underline{\mathcal{B}}_{jk} \underline{\mathcal{B}}_{jl} + \mathcal{B}_j \frac{\partial^2 \mathcal{B}_j}{\partial \underline{\mathbf{d}}_k \partial \underline{\mathbf{d}}_l}. \tag{3.139}$$

Since the block structure of the system matrix does not change, standard structure solvers can be used to solve the linear system (3.130). Nevertheless, also the penalty method has some major disadvantages. The optimal choice of the parameters κ_i depends on the example. If chosen too small, the formulation fails to enforce the constraint properly. A large parameter, however, increases the condition number of the system, which may also lead to poor convergence of linear iterative solvers.

3.5.3 Constrained structure equations

For some of the simulations of the human erythrocyte in this work, both Lagrange multiplier and penalty formulations are employed. For example, the high resistance of the bilayer against dilatation of the membrane surface can realistically be accounted for by a penalty formulation. The volume constraint, on the other hand, which is used to imprint the pre-stressing into the membrane, is enforced with Lagrange multipliers.

Therefore, let $\mathcal{B}_i^{\lambda}$ denote the constraints implemented using Lagrange multipliers $\lambda_i^{\mathcal{S}}$ and $\mathcal{B}_j^{\kappa}$ the ones associated with penalty parameters $\kappa_j^{\mathcal{S}}$. The linear system

$$\begin{bmatrix} \underline{\mathfrak{S}}_{\mathbf{dd}}^{\lambda,\kappa} & \underline{\mathfrak{S}}_{\mathbf{d}p} & \underline{\mathfrak{S}}_{\mathbf{d}\mathcal{B}} \\ \underline{\mathfrak{S}}_{p\mathbf{d}} & \underline{\mathfrak{S}}_{pp} & \underline{\mathbf{0}} \\ \underline{\mathfrak{S}}_{\mathcal{B}\mathbf{d}} & \underline{\mathbf{0}} & \underline{\mathbf{0}} \end{bmatrix}_i^{n+1} \begin{bmatrix} \Delta\underline{\mathbf{d}}^{\mathcal{S}} \\ \Delta\underline{\mathbf{p}}^{\mathcal{S}} \\ \underline{\boldsymbol{\lambda}}^{\mathcal{S}} \end{bmatrix}_{i+1}^{n+1} = - \begin{bmatrix} \underline{\mathbf{r}}_{\mathbf{d}}^{\mathcal{S}} + \alpha_f \underline{\mathbf{r}}_{\mathbf{d}}^{\mathcal{S},\kappa} \\ \underline{\mathbf{r}}_p^{\mathcal{S}} \\ \underline{\boldsymbol{\mathcal{B}}} \end{bmatrix}_i^{n+1}, \tag{3.140}$$

thus, represents the general form of a constrained structure considered in this thesis, where the abbreviation $\underline{\mathfrak{S}}_{\mathbf{dd}}^{\lambda,\kappa} = \underline{\mathfrak{S}}_{\mathbf{dd}} + \underline{\mathfrak{S}}_{\mathbf{dd}}^{\lambda} + \underline{\mathfrak{S}}_{\mathbf{dd}}^{\kappa}$ has been introduced.

3.6 A scaled thickness conditioning approach for thin walled structures

In section 3.4, element formulations have been presented that are tailored for the simulation of thin-walled structures. Nevertheless, it is well known that the final linearized systems of equations for such structures are ill-conditioned in case of a parametrization depending on the shell thickness. For example, relative-displacement based shells, 3D bricks, and also the solid-shell formulations introduced in sections 3.4.2 and 3.4.3 belong to this class of parametrizations. The ill-conditioning, which is independent of the particular element technology employed, is characterized in the first subsection.

For the so-called *7-parameter relative displacement shell*, which was presented by Bischoff and Ramm [17, 18] and Büchter et al. [33], the problems associated with this

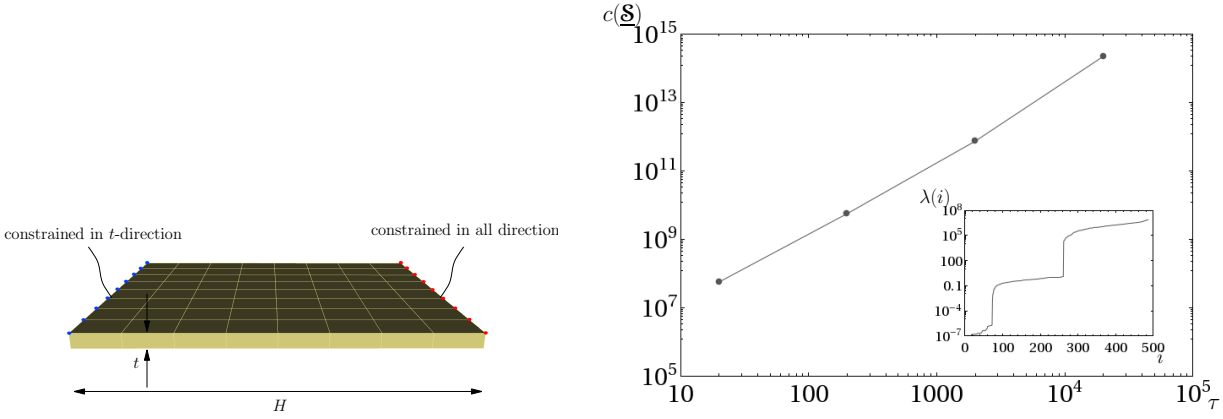

(a) Example geometry with boundary conditions

(b) Conditioning number $c(\underline{\mathbb{S}})$ for varying aspect ratios $\tau = H/t$. Inset shows eigenvalue spectrum for $\tau = 2000$.

Figure 3.5: *Example of the ill-conditioning of thin-walled structures*

ill-conditioning of the linear system were discussed in the thesis of Gee [75] and in the publication by Gee et al. [76]. In those contributions, a *scaled director conditioning (SDC)* approach was proposed to overcome the numerical issues. The SDC method is based on a scaling of the parametrization in order to balance the length scales of slender elements and has to be consistently introduced into the shell element formulation.

From the problem statement of the erythrocyte membrane, it is evident that a severe ill-conditioning of the system will occur due the expected aspect ratios of the elements. Moreover, anisotropic material behavior of the lipid bilayer, which adds stiffness in direction of the element thickness, will additionally contribute to the ill-conditioning. A suitable solution strategy has to be able to deal with at least two shell layers, which are discretized with different FE formulations. Furthermore, algebraic constraints, various boundary conditions, and coupling to a fluid field have to be considered.

As part of this thesis, therefore, a conditioning approach for continuum based finite elements has been developed that meets these requirements, cf. the recent publication by Klöppel et al. [120]. This so-called *scaled thickness conditioning (STC)* approach, which can be related to the SDC algorithm, is formulated as an algebraic preconditioning operator for the effective stiffness matrix $\underline{\mathbb{S}}$. The STC method is described in section 3.6.2, where the focus lies on multi layer membranes discretized with solid shell finite elements. Finally, the effect of the method on the conditioning of a thin walled structure is exemplarily demonstrated in section 3.6.3.

3.6.1 Problem characterization

To demonstrate the effect of varying aspect ratio τ on the ill-conditioning problem, a plane, square, thin plate as depicted in Figure 3.5(a) is considered. The structure is discretized with 8×8 solid shell finite elements employing ANS and EAS technology as

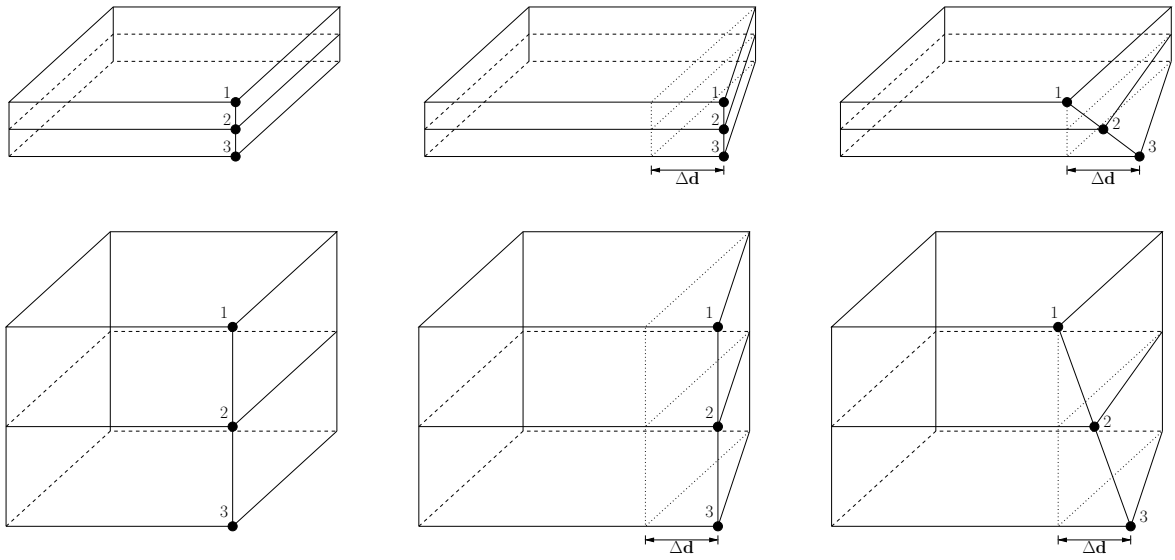

Figure 3.6: *Example of the ill-conditioning of thin-walled structures for in-plane deformation*

introduced in section 3.4.3.

The condition number $c(\underline{\mathbf{S}})$ is defined as the ratio between the largest and the smallest eigenvalue of the structure effective stiffness matrix $\underline{\mathbf{S}}$. Figure 3.5(b) shows that the conditioning c increases exponentially with increasing aspect ratio τ. One exemplified eigenvalue spectrum for $\tau = 2000$ is given in the inset of Figure 3.5(b). Similar trends and spectra with two characteristic jumps can also be observed for the incompressible shell formulation and are related to the properties of the matrix $\underline{\mathbf{S}}_{\mathbf{dd}}$ of (3.115). The first jump separates eigenvalues corresponding to bending modes on the left from ones corresponding from shear modes on the right. Thus, this jump results from a mechanical property of the structure.

The second jump, however, results from the parametrization of the structure. Gee et al. [76] found this jump also in the eigenvalue spectrum of the 7-parameter shell and identified the eigenvalues after the jump with transverse shear and thickness change modes. By contrast, a shell parametrization with rotational DOFs, which would be unsuitable for coupled simulations, did not show such a jump.

To motivate the STC approach and gain some insight into the problem, a two-layer membrane is considered. The behavior of two different configurations and two different deformation patterns is analyzed. The problem under consideration is restricted to two elements and it is sufficient to displace three nodes that share a common edge ℓ aligned in thickness direction of the membrane. The considered problem is depicted in Figure 3.6, where the upper row shows a thin membrane and the lower row a thicker one. The initial configurations of the elements is given in the leftmost column.

As a first scenario, all three nodes are moved in-plane with the same displacement $\Delta\mathbf{d}$ as shown in the middle column of Figure 3.6. The deformation results in very similar

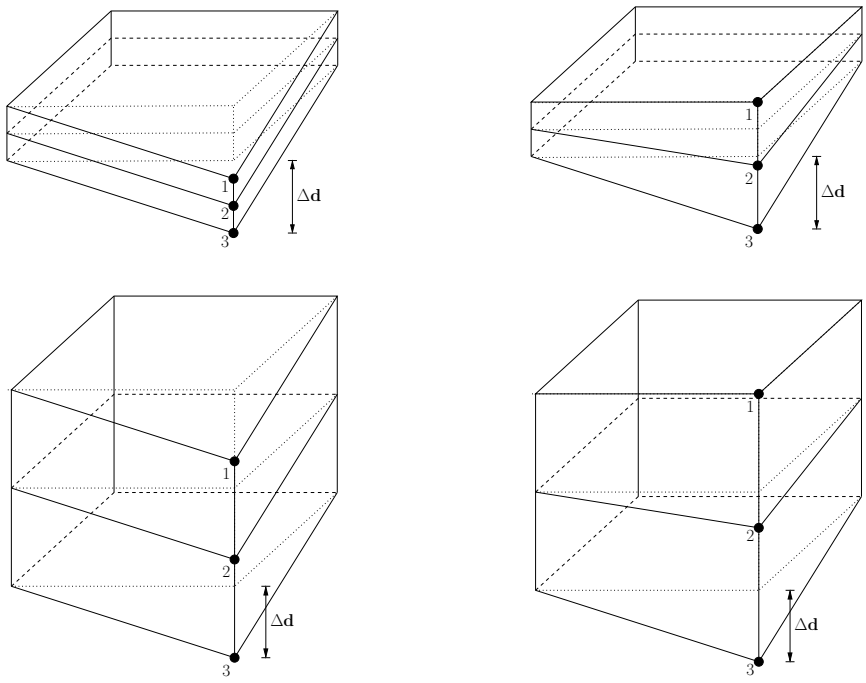

Figure 3.7: *Example of the ill-conditioning of thin-walled structures for out-of-plane deformation*

in-plane strain states within both element configurations and the responses can also be expected to be comparable. If the displacement vector $\Delta\mathbf{d}$ points in thickness-direction of the elements as shown on the left hand side in Figure 3.7, again similar strain states evolve in the elements. This observation corresponds well to the fact that these modes correspond to eigenvalues found between the jumps in the eigenvalue spectrum.

Second, a deformation is considered in which node 1 does not move and node 3 is displaced by $\Delta\mathbf{d}$. For the in-plane displacement depicted in the rightmost column of Figure 3.6, the displacement of node 2 is chosen such that the nodes stay on a straight edge. Although the nodal displacements are the same for both configurations, the thin element is considerably more strained, as can be deduced easily from the increased rotation of the edge as it is apparent in the sketch. This is consistent with the high eigenvalues obtained for transverse shear modes as observed in [76]. If the displacement $\Delta\mathbf{d}$ has a component in thickness direction of the shell, this deformation leads to a thickness change. The right column of Figure 3.7 shows the increase in thickness associated with such a deformation. The relative volume changes associated with this deformation is considerably larger for the thin shell, corresponding with the extreme high eigenvalues of thickness change modes for slender elements. The difference will be even more pronounced for the anisotropic material model used for the lipid bilayer with additional resistance against thickness changes.

3.6.2 STC for single and multi layer shells

For the derivation, again only one edge ℓ in thickness direction is considered. It can be concluded from the little survey in the previous subsection, that the displacement difference $\boldsymbol{\delta}_i^\ell$ of the node i, i.e.

$$\boldsymbol{\delta}_i^\ell = \mathbf{d}^\ell - \mathbf{d}_i, \tag{3.141}$$

with respect to a given average displacement $\mathbf{d}^\ell$ of the whole edge ℓ, is a crucial quantity for the ill-conditioning of thin-walled structures. As long as the nodes on the edge undergo the same displacement, i.e. $\boldsymbol{\delta}_i^\ell = 0$, the response of thin and thick elements is comparable. By contrast, the strains and stresses associated with a fixed relative displacement $\boldsymbol{\delta}_i^\ell \neq \mathbf{0}$ increases, however, with increasing element thinness.

Differently put, in order to obtain the same strain state in a cubic element e^1 as in a thin element e^2, the displacement differences along the edge have to be much larger for element e^1. Thus, there exist a scaling factor $\mathcal{C} >> 1$ with

$$\boldsymbol{\delta}^{\ell,e^1} = \mathcal{C}\boldsymbol{\delta}^{\ell,e^2}, \tag{3.142}$$

such that the responses of the elements e^1 and e^2 are comparable. This indicates a much higher sensitivity of the element stiffness with respect to relative displacements for the thin element. In terms of the effective stiffness matrix, it is equivalent to larger eigenvalues associated with the modes characterized by non-zero relative displacements $\boldsymbol{\delta}_i^\ell \neq \mathbf{0}$.

Motivated by (3.142), the basic idea of the STC approach is to use scaled relative displacement quantities $\boldsymbol{\delta}^{\ell,\mathcal{C}} = \mathcal{C}\boldsymbol{\delta}^\ell$ for thin elements, such that the scaled displacement values $\mathbf{d}^\mathcal{C}$ can be defined as

$$\mathbf{d}^\mathcal{C} = \mathbf{d}^\ell + \boldsymbol{\delta}^{\ell,\mathcal{C}} = \mathbf{d}^\ell + \mathcal{C}\boldsymbol{\delta}^\ell. \tag{3.143}$$

As opposed to most shell formulations, continuum-based formulations do not readily provide a displacement value $\mathbf{d}^\ell$ that can be thought of representative for the whole edge ℓ. Furthermore, in case of multiple shell layers, no element does contain information about all nodal displacements across an edge. However, in order to ensure an efficient implementation of the STC method within the software package BACI, the conditioning should only rely on information available on the element level.

One possible solution for this dilemma is a staggered approach, which is derived here for one edge ℓ. The scaling procedure starts with an initial element layer a, of which the edge ℓ is assumed to contain the nodes 1 and 2, cf. Figure 3.6. The edge displacements $\mathbf{d}_a^\ell$ can now be defined as any affine combination of the nodal values $\mathbf{d}_1$ and $\mathbf{d}_2$

$$\mathbf{d}_a^\ell = \theta_a \mathbf{d}_1 + (1-\theta_a)\mathbf{d}_2, \quad \theta_a \in [0,1]. \tag{3.144}$$

The particular choice of parameter θ_a does not influence the effectiveness of the approach. The general scaling (3.143) can be expressed for element layer a as

$$\mathbf{d}_1^\mathcal{C} = \mathbf{d}_a^\ell + \mathcal{C}\,\boldsymbol{\delta}_1^\ell = (\theta_a + \mathcal{C}(1-\theta_a))\mathbf{d}_1 + (1-\theta_a)(1-\mathcal{C})\mathbf{d}_2, \tag{3.145}$$

$$\mathbf{d}_2^\mathcal{C} = \mathbf{d}_a^\ell + \mathcal{C}\,\boldsymbol{\delta}_2^\ell = (1-\theta_a)(1-\mathcal{C})\mathbf{d}_1 + (\theta_a + \mathcal{C}(1-\theta_a))\mathbf{d}_2. \tag{3.146}$$

Scaling of the adjacent element layer b now uses the fact that for one of the nodes (here node 2, cf. definition given in Figure 3.6 and Figure 3.7) the scaling has already been performed. Displacements of the residual node 3 on ℓ can, hence, be scaled as

$$\mathbf{d}_b^\ell = \theta_b \mathbf{d}_3 + (1-\theta_b)\mathbf{d}_2^{\mathcal{C}}, \quad \theta_b \in [0,1) \tag{3.147}$$

$$\mathbf{d}_3^{\mathcal{C}} = \mathbf{d}_b^\ell + \mathcal{C}\,\boldsymbol{\delta}_3^\ell = (\theta_b + \mathcal{C}(1-\theta_b))\mathbf{d}_3 + (1-\theta_b)(1-\mathcal{C})\mathbf{d}_2^{\mathcal{C}}. \tag{3.148}$$

More general, the scaled displacement $\mathbf{d}_i^{\mathcal{C}}$ of the i-th node on the edge ℓ can be defined recursively as

$$\mathbf{d}_i^{\mathcal{C}} = (\theta + \mathcal{C}(1-\theta))\mathbf{d}_i + (1-\theta)(1-\mathcal{C})\mathbf{d}_{i-1}^{\mathcal{C}}, \quad \theta \in [0,1). \tag{3.149}$$

For the remainder of this work, only the two-layer composite erythrocyte membrane is considered. Moreover, the parameters $\theta_a = 0.5$ and $\theta_b = 0$ are chosen. Since the scaling operations (3.145), (3.146), and (3.148) are linear operations, they can be rewritten as a matrix vector product

$$\begin{bmatrix} \mathbf{d}_1^{\mathcal{C}} \\ \mathbf{d}_2^{\mathcal{C}} \\ \mathbf{d}_3^{\mathcal{C}} \end{bmatrix} = \begin{bmatrix} \underline{\mathbf{1}} & \underline{\mathbf{0}} & \underline{\mathbf{0}} \\ \underline{\mathbf{0}} & \underline{\mathbf{1}} & \underline{\mathbf{0}} \\ \underline{\mathbf{0}} & (1-\mathcal{C})\underline{\mathbf{1}} & \mathcal{C}\,\underline{\mathbf{1}} \end{bmatrix} \begin{bmatrix} \frac{1+\mathcal{C}}{2}\underline{\mathbf{1}} & \frac{1-\mathcal{C}}{2}\underline{\mathbf{1}} & \underline{\mathbf{0}} \\ \frac{1-\mathcal{C}}{2}\underline{\mathbf{1}} & \frac{1+\mathcal{C}}{2}\underline{\mathbf{1}} & \underline{\mathbf{0}} \\ \underline{\mathbf{0}} & \underline{\mathbf{0}} & \underline{\mathbf{1}} \end{bmatrix} \begin{bmatrix} \mathbf{d}_1 \\ \mathbf{d}_2 \\ \mathbf{d}_3 \end{bmatrix} \tag{3.150}$$

$$= \begin{bmatrix} \frac{1+\mathcal{C}}{2}\underline{\mathbf{1}} & \frac{1-\mathcal{C}}{2}\underline{\mathbf{1}} & \underline{\mathbf{0}} \\ \frac{1-\mathcal{C}}{2}\underline{\mathbf{1}} & \frac{1+\mathcal{C}}{2}\underline{\mathbf{1}} & \underline{\mathbf{0}} \\ (1-\mathcal{C})(\frac{1-\mathcal{C}}{2})\underline{\mathbf{1}} & (1-\mathcal{C})(\frac{1+\mathcal{C}}{2})\underline{\mathbf{1}} & \mathcal{C}\,\underline{\mathbf{1}} \end{bmatrix} \begin{bmatrix} \mathbf{d}_1 \\ \mathbf{d}_2 \\ \mathbf{d}_3 \end{bmatrix} \tag{3.151}$$

The final scaling matrix (3.151) cannot be assembled from element matrices directly, since the scaling of $\mathbf{d}_3$ depends on $\mathbf{d}_1$ although nodes 1 and 3 are not contained in the same element. Nevertheless, both matrices necessary for the matrix-vector product (3.150) can be assembled from element matrices alone (for all choices of θ_a, θ_b, θ and also for an arbitrary number of membrane layers), which shows the main advantage of the staggered approach.

The relation of this approach to the SDC method and the earlier STC version as presented in [120] is commented on the following remarks.

Remark 3.4 (SDC vs. STC) *The SDC approach is restricted to single layer shells, but the basic idea of the scaling is very similar. For that method, the shell has to be formulated in terms of the mid surface displacement $\mathbf{v}$ and the relative displacement field $\mathbf{w}$ between the upper and mid surfaces. Having identified $\mathbf{d}^\ell := \mathbf{v}$ and $\boldsymbol{\delta}^\ell = \mathbf{w}$, the STC agrees with the scaling introduced by Gee et al. [76], i.e. $\mathbf{v}^{\mathcal{C}} = \mathbf{v}$ and $\mathbf{w}^{\mathcal{C}} = \mathcal{C}\,\mathbf{w}$. After the consistent modification of the FE formulation including modified stiffness and mass matrices, Gee et al. [76] could show that the characteristic jump in the eigenvalue spectrum, cf. Figure 3.5(b), vanishes and the conditioning of the system is significantly improved.*

Remark 3.5 (Earlier STC version) *The multi layer version presented in [120] was based on an edge displacement $\mathbf{d}^\ell$ defined as average of all nodal values on the edge. Its*

effectiveness could be shown for a plain square thin plate, where the nodes sharing an edge can easily be grouped together. But it is clear that this particular version of STC is not suitable for the simulation of the human erythrocyte. In this sense, the STC approach presented in this thesis is a generalization of the earlier work shown in [120].

For the particular case of two membrane layers, the STC version in [120] used a global edge displacement $\mathbf{d}^\ell = \mathbf{d}_a^\ell = \mathbf{d}_b^\ell = \mathbf{d}_2$*, which can be interpreted as a special case of the scaling approach presented in this thesis for* $\theta_a = \theta_b = 0$*.*

The global system (3.140) is solved for scaled displacement increments in order to benefit from the improved conditioning. The update in the Newton iteration, however, requires unscaled quantities. The necessary transition of scaled quantities to unscaled ones can easily be obtained by inversion of (3.150):

$$\begin{aligned}\begin{bmatrix}\Delta\mathbf{d}_1\\ \Delta\mathbf{d}_2\\ \Delta\mathbf{d}_3\end{bmatrix} &= \begin{bmatrix}\frac{\mathfrak{C}+1}{2\mathfrak{C}}\underline{\mathbf{1}} & \frac{\mathfrak{C}-1}{2\mathfrak{C}}\underline{\mathbf{1}} & \underline{\mathbf{0}}\\ \frac{\mathfrak{C}-1}{2\mathfrak{C}}\underline{\mathbf{1}} & \frac{\mathfrak{C}+1}{2\mathfrak{C}}\underline{\mathbf{1}} & \underline{\mathbf{0}}\\ \underline{\mathbf{0}} & \underline{\mathbf{0}} & \underline{\mathbf{1}}\end{bmatrix}\begin{bmatrix}\underline{\mathbf{1}} & \underline{\mathbf{0}} & \underline{\mathbf{0}}\\ \underline{\mathbf{0}} & \underline{\mathbf{1}} & \underline{\mathbf{0}}\\ \underline{\mathbf{0}} & \frac{\mathfrak{C}}{1-\mathfrak{C}}\underline{\mathbf{1}} & \frac{1}{\mathfrak{C}}\underline{\mathbf{1}}\end{bmatrix}\begin{bmatrix}\Delta\mathbf{d}_1^{\mathfrak{C}}\\ \Delta\mathbf{d}_2^{\mathfrak{C}}\\ \Delta\mathbf{d}_3^{\mathfrak{C}}\end{bmatrix}\\ &= \begin{bmatrix}\frac{\mathfrak{C}+1}{2\mathfrak{C}}\underline{\mathbf{1}} & \frac{\mathfrak{C}-1}{2\mathfrak{C}}\underline{\mathbf{1}} & \underline{\mathbf{0}}\\ \frac{\mathfrak{C}-1}{2\mathfrak{C}}\underline{\mathbf{1}} & \frac{\mathfrak{C}+1}{2\mathfrak{C}}\underline{\mathbf{1}} & \underline{\mathbf{0}}\\ \underline{\mathbf{0}} & \frac{\mathfrak{C}}{1-\mathfrak{C}}\underline{\mathbf{1}} & \frac{1}{\mathfrak{C}}\underline{\mathbf{1}}\end{bmatrix}\begin{bmatrix}\Delta\mathbf{d}_1^{\mathfrak{C}}\\ \Delta\mathbf{d}_2^{\mathfrak{C}}\\ \Delta\mathbf{d}_3^{\mathfrak{C}}\end{bmatrix}.\end{aligned} \tag{3.152}$$

For this unscaling operation, the final matrix can be assembled from element matrices directly and does not necessitate a matrix-matrix multiplication due to the particular choice of parameters θ_a and θ_b.

The mapping (3.152) relates quantities of the nodes sharing an edge in thickness direction. This direction corresponds for eight noded hexahedral elements introduced in section 3.4 with the θ^3 parameter direction. The element local node numbering depicted in Figure 3.4 implies that the numbers of the nodes on a common edge of interest always differ by four. Hence, it is rather straightforward to deduce the element scaling matrices $\underline{\boldsymbol{\mathcal{C}}}^e$. For the initial layer a, this matrix is given by

$$\underline{\boldsymbol{\mathcal{C}}}_a^e = \begin{bmatrix}\frac{\mathfrak{C}+1}{2\mathfrak{C}}\underline{\mathbf{1}} & \underline{\mathbf{0}} & \underline{\mathbf{0}} & \underline{\mathbf{0}} & \frac{\mathfrak{C}-1}{2\mathfrak{C}}\underline{\mathbf{1}} & \underline{\mathbf{0}} & \underline{\mathbf{0}} & \underline{\mathbf{0}}\\ \underline{\mathbf{0}} & \frac{\mathfrak{C}+1}{2\mathfrak{C}}\underline{\mathbf{1}} & \underline{\mathbf{0}} & \underline{\mathbf{0}} & \underline{\mathbf{0}} & \frac{\mathfrak{C}-1}{2\mathfrak{C}}\underline{\mathbf{1}} & \underline{\mathbf{0}} & \underline{\mathbf{0}}\\ \underline{\mathbf{0}} & \underline{\mathbf{0}} & \frac{\mathfrak{C}+1}{2\mathfrak{C}}\underline{\mathbf{1}} & \underline{\mathbf{0}} & \underline{\mathbf{0}} & \underline{\mathbf{0}} & \frac{\mathfrak{C}-1}{2\mathfrak{C}}\underline{\mathbf{1}} & \underline{\mathbf{0}}\\ \underline{\mathbf{0}} & \underline{\mathbf{0}} & \underline{\mathbf{0}} & \frac{\mathfrak{C}+1}{2\mathfrak{C}}\underline{\mathbf{1}} & \underline{\mathbf{0}} & \underline{\mathbf{0}} & \underline{\mathbf{0}} & \frac{\mathfrak{C}-1}{2\mathfrak{C}}\underline{\mathbf{1}}\\ \frac{\mathfrak{C}-1}{2\mathfrak{C}}\underline{\mathbf{1}} & \underline{\mathbf{0}} & \underline{\mathbf{0}} & \underline{\mathbf{0}} & \frac{\mathfrak{C}+1}{2\mathfrak{C}}\underline{\mathbf{1}} & \underline{\mathbf{0}} & \underline{\mathbf{0}} & \underline{\mathbf{0}}\\ \underline{\mathbf{0}} & \frac{\mathfrak{C}-1}{2\mathfrak{C}}\underline{\mathbf{1}} & \underline{\mathbf{0}} & \underline{\mathbf{0}} & \underline{\mathbf{0}} & \frac{\mathfrak{C}+1}{2\mathfrak{C}}\underline{\mathbf{1}} & \underline{\mathbf{0}} & \underline{\mathbf{0}}\\ \underline{\mathbf{0}} & \underline{\mathbf{0}} & \frac{\mathfrak{C}-1}{2\mathfrak{C}}\underline{\mathbf{1}} & \underline{\mathbf{0}} & \underline{\mathbf{0}} & \underline{\mathbf{0}} & \frac{\mathfrak{C}+1}{2\mathfrak{C}}\underline{\mathbf{1}} & \underline{\mathbf{0}}\\ \underline{\mathbf{0}} & \underline{\mathbf{0}} & \underline{\mathbf{0}} & \frac{\mathfrak{C}-1}{2\mathfrak{C}}\underline{\mathbf{1}} & \underline{\mathbf{0}} & \underline{\mathbf{0}} & \underline{\mathbf{0}} & \frac{\mathfrak{C}+1}{2\mathfrak{C}}\underline{\mathbf{1}}\end{bmatrix}. \tag{3.153}$$

For the second layer b, it is assumed that without loss of generality the nodes connecting to the lipid bilayer have the local numbering $1, 2, 3, 4$. Consequently, the corresponding

element matrix reads

$$\underline{\boldsymbol{\mathcal{C}}}_b^e = \begin{bmatrix} \underline{\mathbf{0}} & \underline{\mathbf{0}} & \underline{\mathbf{0}} & \underline{\mathbf{0}} & \underline{\mathbf{0}} & \underline{\mathbf{0}} & \underline{\mathbf{0}} & \underline{\mathbf{0}} \\ \underline{\mathbf{0}} & \underline{\mathbf{0}} & \underline{\mathbf{0}} & \underline{\mathbf{0}} & \underline{\mathbf{0}} & \underline{\mathbf{0}} & \underline{\mathbf{0}} & \underline{\mathbf{0}} \\ \underline{\mathbf{0}} & \underline{\mathbf{0}} & \underline{\mathbf{0}} & \underline{\mathbf{0}} & \underline{\mathbf{0}} & \underline{\mathbf{0}} & \underline{\mathbf{0}} & \underline{\mathbf{0}} \\ \underline{\mathbf{0}} & \underline{\mathbf{0}} & \underline{\mathbf{0}} & \underline{\mathbf{0}} & \underline{\mathbf{0}} & \underline{\mathbf{0}} & \underline{\mathbf{0}} & \underline{\mathbf{0}} \\ \frac{\mathcal{C}}{1-\mathcal{C}}\underline{\mathbf{1}} & \underline{\mathbf{0}} & \underline{\mathbf{0}} & \underline{\mathbf{0}} & \frac{1}{\mathcal{C}}\underline{\mathbf{1}} & \underline{\mathbf{0}} & \underline{\mathbf{0}} & \underline{\mathbf{0}} \\ \underline{\mathbf{0}} & \frac{\mathcal{C}}{1-\mathcal{C}}\underline{\mathbf{1}} & \underline{\mathbf{0}} & \underline{\mathbf{0}} & \underline{\mathbf{0}} & \frac{1}{\mathcal{C}}\underline{\mathbf{1}} & \underline{\mathbf{0}} & \underline{\mathbf{0}} \\ \underline{\mathbf{0}} & \underline{\mathbf{0}} & \frac{\mathcal{C}}{1-\mathcal{C}}\underline{\mathbf{1}} & \underline{\mathbf{0}} & \underline{\mathbf{0}} & \underline{\mathbf{0}} & \frac{1}{\mathcal{C}}\underline{\mathbf{1}} & \underline{\mathbf{0}} \\ \underline{\mathbf{0}} & \underline{\mathbf{0}} & \underline{\mathbf{0}} & \frac{\mathcal{C}}{1-\mathcal{C}}\underline{\mathbf{1}} & \underline{\mathbf{0}} & \underline{\mathbf{0}} & \underline{\mathbf{0}} & \frac{1}{\mathcal{C}}\underline{\mathbf{1}} \end{bmatrix} \tag{3.154}$$

Subsequently, these element matrices $\underline{\boldsymbol{\mathcal{C}}}_a^e$ and $\underline{\boldsymbol{\mathcal{C}}}_b^e$ can be assembled into a global scaling matrix $\underline{\boldsymbol{\mathcal{C}}}$. Note that all n_ℓ^{adj} elements adjacent to the edge ℓ deliver the same entries. Therefore, in order to use the standard assembly process, the rows of the matrix $\underline{\boldsymbol{\mathcal{C}}}^e$ associated with ℓ have to be scaled with $1/n_\ell^{\text{adj}}$. Details on this and the whole assembly process can be found in [120].

Finally, the mapping to be performed in each Newton update step can be expressed in form of the global matrix vector product

$$\Delta\underline{\mathbf{d}} = \underline{\boldsymbol{\mathcal{C}}}\,\Delta\underline{\mathbf{d}}^{\mathcal{C}}. \tag{3.155}$$

This identity can now be applied to the linear system for the constrained structure problem (3.140). Additional scaling of the first row of the system by $\underline{\boldsymbol{\mathcal{C}}}^{\mathsf{T}}$ results in the block system

$$\begin{bmatrix} \underline{\boldsymbol{\mathcal{C}}}^{\mathsf{T}}\underline{\mathbf{S}}_{\mathbf{dd}}^{\lambda,\kappa}\underline{\boldsymbol{\mathcal{C}}} & \underline{\boldsymbol{\mathcal{C}}}^{\mathsf{T}}\underline{\mathbf{S}}_{\mathbf{d}p} & \underline{\boldsymbol{\mathcal{C}}}^{\mathsf{T}}\underline{\mathbf{S}}_{\mathbf{d}\mathcal{B}} \\ \underline{\mathbf{S}}_{p\mathbf{d}}\underline{\boldsymbol{\mathcal{C}}} & \underline{\mathbf{S}}_{pp} & 0 \\ \underline{\mathbf{S}}_{\mathcal{B}\mathbf{d}}\underline{\boldsymbol{\mathcal{C}}} & 0 & 0 \end{bmatrix}_i^{n+1} \begin{bmatrix} \Delta\underline{\mathbf{d}}^{\mathcal{S},\mathcal{C}} \\ \Delta\underline{\mathbf{p}}^{\mathcal{S}} \\ \underline{\boldsymbol{\lambda}}^{\mathcal{S}} \end{bmatrix}_{i+1}^{n+1} = -\begin{bmatrix} \underline{\boldsymbol{\mathcal{C}}}^{\mathsf{T}}\left(\underline{\mathbf{r}}_{\mathbf{d}}^{\mathcal{S}} + \alpha_f\underline{\mathbf{r}}_{\mathbf{d}}^{\mathcal{S},\kappa}\right) \\ \underline{\mathbf{r}}_p^{\mathcal{S}} \\ \underline{\boldsymbol{\mathcal{B}}} \end{bmatrix}_i^{n+1} \tag{3.156}$$

This modified linear system can be equivalently expressed using the block matrix $\underline{\mathbf{S}}_i^{n+1}$ of the unscaled structure system as given in (3.140). The relation reads

$$\underbrace{\begin{bmatrix} \underline{\boldsymbol{\mathcal{C}}} & \underline{\mathbf{0}} & \underline{\mathbf{0}} \\ \underline{\mathbf{0}} & \underline{\mathbf{1}} & \underline{\mathbf{0}} \\ \underline{\mathbf{0}} & \underline{\mathbf{0}} & \underline{\mathbf{1}} \end{bmatrix}^{\mathsf{T}}}_{\hat{\underline{\boldsymbol{\mathcal{C}}}}^{\mathsf{T}}} \underbrace{\begin{bmatrix} \underline{\mathbf{S}}_{\mathbf{dd}}^{\lambda,\kappa} & \underline{\mathbf{S}}_{\mathbf{d}p} & \underline{\mathbf{S}}_{\mathbf{d}\mathcal{B}} \\ \underline{\mathbf{S}}_{p\mathbf{d}} & \underline{\mathbf{S}}_{pp} & 0 \\ \underline{\mathbf{S}}_{\mathcal{B}\mathbf{d}} & 0 & 0 \end{bmatrix}_i^{n+1}}_{\underline{\mathbf{S}}_i^{n+1}} \underbrace{\begin{bmatrix} \underline{\boldsymbol{\mathcal{C}}} & \underline{\mathbf{0}} & \underline{\mathbf{0}} \\ \underline{\mathbf{0}} & \underline{\mathbf{1}} & \underline{\mathbf{0}} \\ \underline{\mathbf{0}} & \underline{\mathbf{0}} & \underline{\mathbf{1}} \end{bmatrix}}_{\hat{\underline{\boldsymbol{\mathcal{C}}}}} \underbrace{\begin{bmatrix} \Delta\underline{\mathbf{d}}^{\mathcal{S},\mathcal{C}} \\ \Delta\underline{\mathbf{p}}^{\mathcal{S}} \\ \underline{\boldsymbol{\lambda}}^{\mathcal{S}} \end{bmatrix}_{i+1}^{n+1}}_{\Delta\underline{\mathbf{x}}_{i+1}^{\mathcal{S},\mathcal{C},n+1}} =$$

$$= -\underbrace{\begin{bmatrix} \underline{\boldsymbol{\mathcal{C}}} & \underline{\mathbf{0}} & \underline{\mathbf{0}} \\ \underline{\mathbf{0}} & \underline{\mathbf{1}} & \underline{\mathbf{0}} \\ \underline{\mathbf{0}} & \underline{\mathbf{0}} & \underline{\mathbf{1}} \end{bmatrix}^{\mathsf{T}}}_{\hat{\underline{\boldsymbol{\mathcal{C}}}}^{\mathsf{T}}} \underbrace{\begin{bmatrix} \underline{\mathbf{r}}_{\mathbf{d}}^{\mathcal{S}} + \alpha_f\underline{\mathbf{r}}_{\mathbf{d}}^{\mathcal{S},\kappa} \\ \underline{\mathbf{r}}_p^{\mathcal{S}} \\ \underline{\boldsymbol{\mathcal{B}}} \end{bmatrix}_i^{n+1}}_{\underline{\mathbf{r}}_i^{\mathcal{S},n+1}}. \tag{3.157}$$

The double matrix-matrix product can be interpreted as left and right preconditioning operation with the preconditioning matrix $\hat{\underline{\boldsymbol{\mathcal{C}}}}$. The result of the computation is unaffected of the STC approach.

As shown in the earlier publication [120], a right preconditioner would suffice to improve the conditioning of the matrix. Nevertheless, for the later application of AMG preconditioners in the framework of an iterative linear solver scheme, the additional left preconditioner in (3.157) (or equivalently the scaling of the first row in (3.156)) has proven superior. It leads to the symmetric system of equations given that the original structure system is symmetric.

Remark 3.6 (Higher-order kinematics) *The STC approach presented here for multiple layers of linear solid shell finite elements can be extended to higher-order kinematics in a straightforward manner by performing the scaling recursively for the nodal layers. From a preconditioning point of view, a linear scaling is sufficient even though the element kinematics are of higher-order. In practice, the STC could be shown to effectively improve the conditioning of thin walled structures discretized with iso-geometric, second order, displacement based elements, which employ non-uniform rational B-splines (NURBS) basis functions. Details on this discretization can for example be found in the thesis of Gamnitzer [74].*

3.6.3 Effectiveness of the STC approach

To conclude this section, the example of a thin square plate presented in section 3.6.1 is revisited, cf. Figure 3.5. The effect of STC for a single layer plate with the same discretization as in section 3.6.1 and a plate discretized with two element layers is considered here. Figure 3.8(a) shows an almost constant condition number $c(\underline{\boldsymbol{S}})$ for the considered range of aspect ratios τ in both cases. The inset of the plot furthermore shows that the second jump in the eigenvalue spectrum (here exemplarily for $\tau = 2000$) has vanished. Figure 3.8(b) addresses the conditioning with respect to the parameter $\mathcal{C}$. The graph is again given for $\tau = 2000$. Best conditioning of the system is found for a parameter given by $\mathcal{C} \approx \sqrt{\tau^e}$. The square root can be explained with the fact that the preconditioning operator $\underline{\boldsymbol{\mathcal{C}}}$ is applied from the left and the right.

As already mentioned above, the anisotropy of the bilayer membrane does add to the ill-conditioning of the system due to increased resistance against thickness changes. Therefore, for the simulation of the human erythrocyte membrane, especially for the bilayer, a scaling factor $\mathcal{C}$ larger than $\sqrt{\tau^e}$ is often used. In many cases, it was found that the STC preconditioning operation was indispensable in order to enable the solution of the linear system.

3.7 Sliding ALE monolithic FSI

Up to this point, the two physical fields, structure and fluid, as well as the artificial ALE, i.e. fluid grid, field have been considered separately. The discretization of the coupling between the fields, the continuum representation of which is stated in section 2.6, is addressed in this section. The discretization method for the additional DOFs and the additional constraint equations is presented in the first subsection 3.7.1. In this work, a

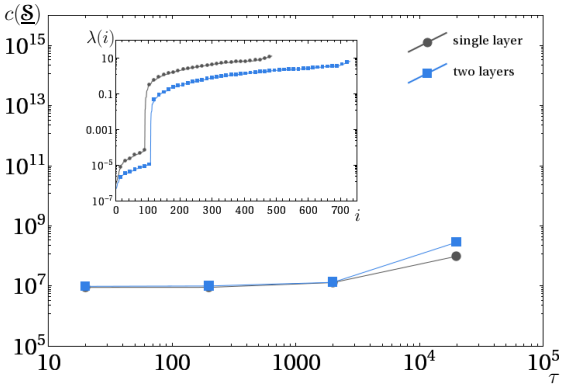

(a) Condition number $c(\underline{\mathbf{S}})$ for varying aspect ratios $\tau = H/t$. Inset shows eigenvalue spectrum for $\tau = 2000$.

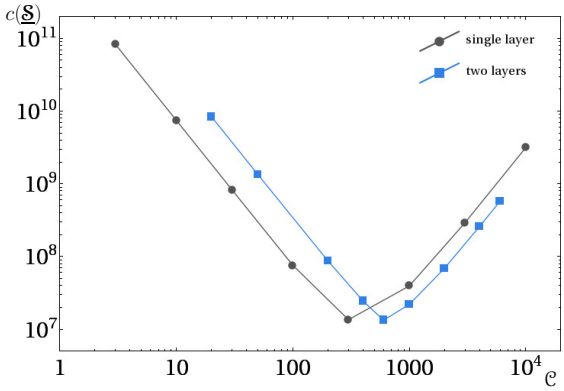

(b) Condition number $c(\underline{\mathbf{S}})$ for varying scaling parameter $\mathcal{C}$ and fixed aspect ratio $\tau = 2000$

Figure 3.8: *Effect of STC preconditioning for the example of a thin plate, cf. Figure 3.5(a)*

dual mortar approach is utilized, which does not require matching discretizations of the interface on both sides. The constraint equations are enforced by a Lagrange multiplier approach. The particular choice of shape functions for the multiplier field allows for the Lagrange multiplier DOFs and the coupling terms on one side of the interface to be eliminated from the system by static condensation at relatively low numerical cost.

The second subsection briefly shows how the interface traction is implemented within the structure field. Its discretization and incorporation into the structure formulation coincide with the mortar-based, FSI approach presented in the recent publication [121]. Subsequently, section 3.7.3 addresses the coupling of the fluid and the fluid grid systems and introduces the modification due to the interaction with the structure field. In contrast to the version shown in [121], not only the interface traction, but also the repositioning of the grid nodes around the interface (cf. section 3.3.1) are considered.

As apparent from the morphology of the erythrocyte, which is discussed in the section 1.1.2, the incompressible fluid domain of the cytosol is completely enclosed by the cell membrane. Küttler et al. [124] showed that this balloon-type scenario causes severe numerical issues for the prominent and widely used class of partitioned FSI coupling approaches. Therefore, all field and coupling equations are solved simultaneously in one monolithic system, which is stated in the last subsection. Monolithic coupling schemes do not suffer the same shortcomings as partitioned approaches for balloon-type problems. Static condensation allows to reformulate the system into a systems that has the same block structure as the standard monolithic FSI system. Thus, it can be solved with state-of-the-art FSI preconditioners developed for conforming discretizations, cf. the work of Gee et al. [77], in a straightforward manner.

3.7.1 Dual mortar discretization of FSI constraint and interface traction

Starting point of the discretization is the no slip condition (2.143), that can be written in short as

$$\dot{\mathbf{d}}_{\Gamma}^{\mathcal{S}} = \mathbf{u}_{\Gamma}^{\mathcal{F}}. \tag{3.158}$$

In this equation and the remainder of this thesis, the subscript $\cdot_{\Gamma}$ indicates that the considered quantity is restricted to the FSI interface Γ_{FSI}.

In order to be, on the one hand, consistent with the FE formulations of the individual fields and, on the other hand, flexible enough for non-matching interface discretizations, the no-slip condition is to be fulfilled in an integral sense. With an appropriate test function $\delta\boldsymbol{\lambda}$, the weighted residual (here equivalent to the weak form) is given by

$$\left(\delta\boldsymbol{\lambda}\,;\dot{\mathbf{d}}_{\Gamma}^{\mathcal{S}} - \mathbf{u}_{\Gamma}^{\mathcal{F}}\right)_{\Gamma_{\text{FSI}}}. \tag{3.159}$$

The test function $\delta\boldsymbol{\lambda}$ is associated with a Lagrange multiplier $\boldsymbol{\lambda}$, which has been defined in section 2.6 to equal the interface traction with respect to the fluid side $\boldsymbol{\lambda} = \mathbf{h}^{\mathcal{F}} = -\mathbf{h}^{\mathcal{S}}$.

The discretization of velocity values on the fluid and the structure side of the interface is straightforward given the discretizations of the individual fields discussed in sections 3.2.1, 3.4.2, and 3.4.3, respectively. With shape functions $N_k^{\mathcal{F}}$ and $N_l^{\mathcal{S}}$ at hand, the discrete velocities on the interface can be expressed as

$$\mathbf{u}_{\Gamma}^{\mathcal{F}} = \sum_{k=1}^{n_{\Gamma}^{\text{nd},\mathcal{F}}} N_k^{\mathcal{F}}\mathbf{u}_k^{\mathcal{F}} \qquad \dot{\mathbf{d}}_{\Gamma}^{\mathcal{S}} = \sum_{l=1}^{n_{\Gamma}^{\text{nd},\mathcal{S}}} N_l^{\mathcal{S}}\dot{\mathbf{d}}_l^{\mathcal{S}}, \tag{3.160}$$

where the sums have been restricted to shape functions that do not vanish on the interface Γ_{FSI}. It is important to note that in case of non-conforming discretizations, the fluid side $\Gamma_{\text{FSI}}^{\mathcal{F}}$ and the structure side $\Gamma_{\text{FSI}}^{\mathcal{S}}$ do not coincide in the discrete setting. Within the *dual mortar method*, the Lagrange multiplier $\boldsymbol{\lambda}$ and the test functions $\delta\boldsymbol{\lambda}$ are discretized on one side of the interface (called *slave side*) with *dual shape functions* Φ_j. In this thesis, the fluid side of the interface $\Gamma_{\text{FSI}}^{\mathcal{F}}$ is chosen to be the slave part of the coupling, which leads to discretizations

$$\boldsymbol{\lambda} = \sum_{j=1}^{n_{\Gamma}^{\text{nd},\mathcal{F}}} \Phi_j\,\boldsymbol{\lambda}_j, \qquad \delta\boldsymbol{\lambda} = \sum_{j=1}^{n_{\Gamma}^{\text{nd},\mathcal{F}}} \Phi_j\,\delta\boldsymbol{\lambda}_j, \tag{3.161}$$

with discrete nodal Lagrange multiplier values $\boldsymbol{\lambda}_j$ and test function values $\delta\boldsymbol{\lambda}_j$. In contrast to the standard mortar methods, dual shape functions are constructed such that the *biorthogonality* condition

$$\left(\Phi_j\,,N_k^{\mathcal{F}}\right)_{\Gamma_{\text{FSI}}^{\mathcal{F}}} = \delta_{jk}\left(1\,,N_k^{\mathcal{F}}\right)_{\Gamma_{\text{FSI}}^{\mathcal{F}}} = \delta_{jk}\int_{\Gamma_{\text{FSI}}^{\mathcal{F}}} N_k^{\mathcal{F}}\,\mathrm{d}\Gamma \tag{3.162}$$

holds. Details on the construction as well as on the properties of these special shape functions is beyond the scope of this thesis. A brief overview on the literature on this

topics is given in the following Remark 3.7. In this work, only eight noded, hexahedral elements are used. Therefore, the interface both on the fluid and the structure side is discretized with four noded quadrilateral elements.

Remark 3.7 (Dual shape functions) *The dual mortar method has initially been introduced by Hüeber and Wohlmuth [109] and Wohlmuth [196, 197]. Due to their definition, dual shape functions cannot be constructed a priori in general, but depend on the possibly distorted shape of the specific element in the spatial configuration. Details on the construction and properties of dual shape functions can be found in the publications by Flemisch and Wohlmuth [67], Hartmann et al. [97], and Popp et al. [154].*

Applications to structure meshtying and contact problems can be found in the work by Flemisch and Wohlmuth [67], Gitterle et al. [81], Popp et al. [153, 154], Puso and Laursen [164], and Wohlmuth [196].

Applying discretizations (3.160) and (3.161) into the weak form (3.159), the semi discrete form of the constraint condition can be obtained as

$$\begin{aligned}
\left(\delta\boldsymbol{\lambda}\,;\dot{\mathbf{d}}_{\Gamma}^{\mathcal{S}}-\mathbf{u}_{\Gamma}^{\mathcal{F}}\right)_{\Gamma_{\mathsf{FSI}}} &= \left(\sum_{j=1}^{n_{\Gamma}^{\mathsf{nd},\mathcal{F}}}\Phi_j\,\delta\boldsymbol{\lambda}_j\,;\sum_{k=1}^{n_{\Gamma}^{\mathsf{nd},\mathcal{S}}}N_k^{\mathcal{S}}\dot{\mathbf{d}}_k^{\mathcal{S}}-\sum_{l=1}^{n_{\Gamma}^{\mathsf{nd},\mathcal{F}}}N_l^{\mathcal{F}}\mathbf{u}_l^{\mathcal{F}}\right)_{\Gamma_{\mathsf{FSI}}^{\mathcal{F}}} \\
&= \sum_{j=1}^{n_{\Gamma}^{\mathsf{nd},\mathcal{F}}}\sum_{k=1}^{n_{\Gamma}^{\mathsf{nd},\mathcal{S}}}\delta\boldsymbol{\lambda}_j^{\mathsf{T}}\left(\Phi_j\,,N_k^{\mathcal{S}}\right)_{\Gamma_{\mathsf{FSI}}^{\mathcal{F}}}\dot{\mathbf{d}}_k^{\mathcal{S}}-\sum_{j=1}^{n_{\Gamma}^{\mathsf{nd},\mathcal{F}}}\sum_{l=1}^{n_{\Gamma}^{\mathsf{nd},\mathcal{F}}}\delta\boldsymbol{\lambda}_j^{\mathsf{T}}\left(\Phi_j\,,N_l^{\mathcal{F}}\right)_{\Gamma_{\mathsf{FSI}}^{\mathcal{F}}}\mathbf{u}_l^{\mathcal{F}} \\
&= \sum_{j=1}^{n_{\Gamma}^{\mathsf{nd},\mathcal{F}}}\sum_{k=1}^{n_{\Gamma}^{\mathsf{nd},\mathcal{S}}}\delta\boldsymbol{\lambda}_j^{\mathsf{T}}M_{jk}\dot{\mathbf{d}}_k^{\mathcal{S}}-\sum_{j=1}^{n_{\Gamma}^{\mathsf{nd},\mathcal{F}}}\sum_{l=1}^{n_{\Gamma}^{\mathsf{nd},\mathcal{F}}}\delta\boldsymbol{\lambda}_j^{\mathsf{T}}D_{jl}\mathbf{u}_l^{\mathcal{F}}=0. \qquad (3.163)
\end{aligned}$$

The last equation provides the nodal blocks for global mortar matrices $\underline{\mathfrak{M}}$ and $\underline{\mathfrak{D}}$, respectively, which are given as

$$\underline{\mathfrak{M}}[j,k]=M_{jk}\,\underline{\mathbf{1}}=\left(\Phi_j\,,N_k^{\mathcal{S}}\right)_{\Gamma_{\mathsf{FSI}}^{\mathcal{F}}}\underline{\mathbf{1}}\in\mathbb{R}^{n^{\mathsf{dim}}\times n^{\mathsf{dim}}} \qquad (3.164)$$

$$\underline{\mathfrak{D}}[j,l]=D_{jl}\,\underline{\mathbf{1}}=\left(\Phi_j\,,N_l^{\mathcal{F}}\right)_{\Gamma_{\mathsf{FSI}}^{\mathcal{F}}}\underline{\mathbf{1}}=\delta_{jk}\left(1\,,N_k^{\mathcal{F}}\right)_{\Gamma_{\mathsf{FSI}}^{\mathcal{F}}}\underline{\mathbf{1}}\in\mathbb{R}^{n^{\mathsf{dim}}\times n^{\mathsf{dim}}}. \qquad (3.165)$$

Keeping in mind that (3.163) has to hold for all values of $\delta\boldsymbol{\lambda}_j$, the matrix form of the constraint equation can finally be introduced as

$$\underline{\mathfrak{M}}\,\underline{\dot{\mathbf{d}}}_{\Gamma}^{\mathcal{S}}(t)-\underline{\mathfrak{D}}\,\underline{\mathbf{u}}_{\Gamma}^{\mathcal{F}}(t)=\underline{\mathbf{0}}, \qquad (3.166)$$

where the global vectors of discrete nodal velocity values restricted on the respective FSI interface are denoted by $\underline{\dot{\mathbf{d}}}_{\Gamma}^{\mathcal{S}}$ and $\underline{\mathbf{u}}_{\Gamma}^{\mathcal{F}}$.

Since the Lagrange multiplier field is defined on the fluid side, the matrix $\underline{\mathfrak{D}}$ is a square matrix. More importantly, due to the biorthogonality condition (3.162), the matrix $\underline{\mathfrak{D}}$ is even diagonal. This feature distinguishes the dual mortar method from standard mortar

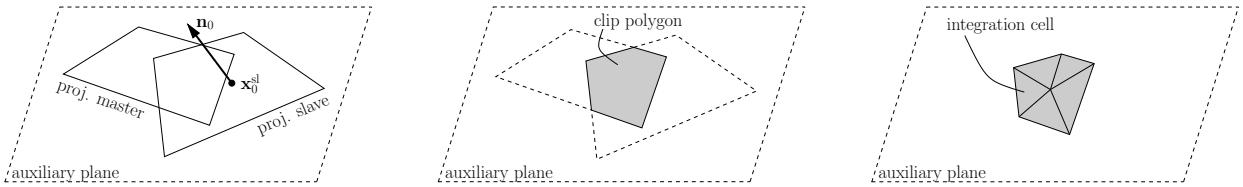

Figure 3.9: *Basic steps to evaluate the mortar matrix $\underline{\mathfrak{M}}$ for a 3D mortar coupling: Projection on auxiliary plane (left), polygon clipping (middle), and triangulation (right)*

methods. The inversion of $\underline{\mathfrak{D}}$ is trivial and, thus, a discrete projection operator $\underline{\mathbf{P}}$ from fluid to structure DOFs is naturally given by

$$\underline{\mathbf{u}}_{\Gamma}^{\mathcal{F}}(t) = \underline{\mathfrak{D}}^{-1}\,\underline{\mathfrak{M}}\,\dot{\underline{\mathbf{d}}}_{\Gamma}^{\mathcal{S}}(t) = \underline{\mathcal{P}}\,\dot{\underline{\mathbf{d}}}_{\Gamma}^{\mathcal{S}}(t). \tag{3.167}$$

As it is true for all mortar-based methods, the matrix $\underline{\mathfrak{M}}$ is in general a rectangular matrix and its constructions requires the evaluation of a mortar integral $\left(\Phi_j\,, N_k^{\mathcal{S}}\right)_{\Gamma_{\text{FSI}}^{\mathcal{F}}}$. The integration is not straightforward since the integral domain is defined on the fluid side, whereas the structure shape functions are defined on the structure side. More generally speaking, the master shape functions have to be integrated on the slave side of the interface. There are several ways to numerically approximate this integral. A rough idea of the approach taken here can be gained from Figure 3.9. First, master and slave facets are projected onto an auxiliary plane. Second, the intersection (called clipping polygon) is constructed. Third, the clipping polygon in triangulated into so-called mortar segments.

Mortar segments constructed in such a way ensure that the integrand (here the structure shape function $N_k^{\mathcal{S}}$) is continuous on these integration cells and does not exhibit kinks. Consequently, a consistent Gauss quadrature on each segment is possible. Details on the algorithm can be found in the original work by Puso [163], Puso and Laursen [164, 165], or, with a focus on dual mortar methods, in Popp et al. [153, 154].

The discrete no-slip condition (3.166) cannot be applied directly as additional equation to the monolithic FSI system, since it is formulated in structure velocities $\dot{\underline{\mathbf{d}}}^{\mathcal{S}}$, as opposed to the membrane description itself that is based on structure displacements $\underline{\mathbf{d}}^{\mathcal{S}}$. In the thesis of Förster [69], the second order time integration scheme

$$\tfrac{1}{\Delta t}\left(\underline{\mathbf{d}}_{\Gamma}^{\mathcal{S},n+1} - \underline{\mathbf{d}}_{\Gamma}^{\mathcal{S},n}\right) = \tfrac{1}{2}\left(\dot{\underline{\mathbf{d}}}_{\Gamma}^{\mathcal{S},n+1} + \dot{\underline{\mathbf{d}}}_{\Gamma}^{\mathcal{S},n}\right) \tag{3.168}$$

was proposed for the interface values and will be used throughout this thesis as well. It corresponds to a one-step θ time integration with $\theta = \frac{1}{2}$. In terms of displacement and velocity increments for iteration step i, the time integration (3.168) reads

$$\Delta\underline{\mathbf{d}}_{\Gamma,i+1}^{\mathcal{S},n+1} = \tfrac{\Delta t}{2}\,\Delta\dot{\underline{\mathbf{d}}}_{\Gamma,i+1}^{\mathcal{S},n+1} + \delta_{i0}\Delta t\,\dot{\underline{\mathbf{d}}}_{\Gamma}^{\mathcal{S},n}, \tag{3.169}$$

where δ_{i0} denotes the Kronecker-δ, which ensures that the old velocity values $\dot{\underline{\mathbf{d}}}_{\Gamma}^{\mathcal{S},n}$ are accounted for only in the first iteration step, i.e. $i = 0$. Enforcing the weak identity of

structure and fluid velocities (3.166) at t^{n+1} and t^n finally leads to the discrete form of the no-slip condition

$$\underline{\mathfrak{M}}\,\Delta\underline{\mathbf{d}}^{\mathcal{S},n+1}_{\Gamma,i+1} = \tfrac{\Delta t}{2}\,\underline{\mathfrak{D}}\,\Delta\underline{\mathbf{u}}^{\mathcal{F},n+1}_{\Gamma,i+1} + \delta_{i0}\Delta t\,\underline{\mathfrak{D}}\,\underline{\mathbf{u}}^{\mathcal{F},n}_{\Gamma}. \tag{3.170}$$

Condition (3.170) will be added as an additional equation to the combined system of structure, fluid, and ALE. The equation represents the discrete linearized kinematic constraint condition. Furthermore, the following subsections show how the interface tractions resulting from the coupling are accounted for in the structure and fluid fields, respectively.

3.7.2 The modified structure field

As introduced in section 2.6, the traction on the structure side $\mathbf{h}^{\mathcal{S}}$ corresponds to the Lagrange multiplier $\boldsymbol{\lambda} = -\mathbf{h}^{\mathcal{S}}$, the spatial discretization of which has just been introduced in the previous subsection. Since the kinematic constraint is fulfilled at the end of the time interval, it is reasonable to consider the multiplier as an external force at time $t = t^{n+1}$. The numerical treatment is equivalent to the surface loads $\mathbf{T}_N$ on the Neumann boundary. The weak form of the uncoupled and (to ease the notation) unconstrained structure field given in (3.76) is to be extended by a boundary term on the interface Γ_{FSI}:

$$\begin{aligned} 0 =& \delta W(\mathbf{d}^{\mathcal{S}}, p^{\mathcal{S}}, \bar{\mathbf{E}}, \boldsymbol{\lambda}) \\ =& \left(\rho^0 \frac{\mathrm{d}^2\mathbf{d}^{\mathcal{S}}}{\mathrm{d}t^2}\,;\delta\mathbf{d}^{\mathcal{S}}\right)_{\Omega_{\mathbf{X}}} + \left((\bar{J}-1)\,,\delta p^{\mathcal{S}}\right)_{\Omega_{\mathbf{X}}} + \left(\bar{\mathbf{S}}_{\mathsf{iso}} + \bar{\mathbf{S}}_{\mathsf{vol}}\,:\delta\bar{\mathbf{E}}\right)_{\Omega_{\mathbf{X}}} - \\ & - \left(\rho^0\mathbf{b}\,;\delta\mathbf{d}^{\mathcal{S}}\right)_{\Omega_{\mathbf{X}}} - \left(\mathbf{T}_N\,;\delta\mathbf{d}^{\mathcal{S}}\right)_{\Gamma_N} + \left(\boldsymbol{\lambda}\,;\delta\mathbf{d}^{\mathcal{S}}\right)_{\Gamma_{\mathsf{FSI}}}. \end{aligned} \tag{3.171}$$

Using the already known discretizations for virtual displacements $\delta\mathbf{d}^{\mathcal{S}}$ and Lagrange multiplier $\boldsymbol{\lambda}$ from (3.160) and (3.161), the additional integral can be rewritten as

$$\left(\boldsymbol{\lambda}\,;\delta\mathbf{d}^{\mathcal{S}}\right)_{\Gamma_{\mathsf{FSI}}} = \sum_{j=1}^{n_\Gamma^{\mathsf{nd},\mathcal{F}}}\sum_{k=1}^{n_\Gamma^{\mathsf{nd},\mathcal{S}}} \left(\delta\mathbf{d}^{\mathcal{S}}\right)^{\mathsf{T}} M_{jk}\boldsymbol{\lambda}_k = \left(\delta\underline{\mathbf{d}}^{\mathcal{S}}\right)^{\mathsf{T}}\underline{\mathfrak{M}}^{\mathsf{T}}\underline{\boldsymbol{\lambda}}, \tag{3.172}$$

with the global mortar matrix $\underline{\mathfrak{M}}$ defined in the previous subsection and the global vector of discrete nodal multiplier values $\underline{\boldsymbol{\lambda}}$.

As a consequence of the generalized-α time integration scheme used for the structure discretization, the discrete balance of forces is to be evaluated at the generalized midpoints $t^{n+1-\alpha_f}$ and $t^{n+1-\alpha_m}$. Therefore, a linear interpolation for the Lagrange multiplier values is employed such that system (3.109) has to be extended by two linear terms:

$$\underline{\mathbf{M}}\,\ddot{\underline{\mathbf{d}}}^{n+1-\alpha_m} = \underline{\boldsymbol{f}}(\underline{\mathbf{d}}^{n+1-\alpha_f}, t^{n+1-\alpha_f}) + (1-\alpha_f)\left(\underline{\mathfrak{M}}^{n+1}\right)^{\mathsf{T}}\underline{\boldsymbol{\lambda}}^{n+1} + \alpha_f\left(\underline{\mathfrak{M}}^{n}\right)^{\mathsf{T}}\underline{\boldsymbol{\lambda}}^{n}. \tag{3.173}$$

For convenience, the displacement DOFs $\underline{\mathbf{d}}^{\mathcal{S}}$ of the membrane are further split into displacements $\underline{\mathbf{d}}^{\mathcal{S}}_\Gamma$ defined on the interface Γ_{FSI} and displacements $\underline{\mathbf{d}}^{\mathcal{S}}_{\mathrm{I}}$ defined on the interior $\mathrm{I} = \Omega^{\mathcal{S}}\backslash\Gamma_{\mathsf{FSI}}$. The same split can be performed on the residual vector $\underline{\mathbf{r}}^{\mathcal{S}}_{\mathbf{d}}$, resulting

in a split of the matrix blocks of the structure matrix $\underline{\mathfrak{S}}$ in (3.140). Finally, the constrained standard structure problem $\underline{\mathfrak{S}}_i^{n+1}\,\Delta\underline{\mathbf{x}}_i^{\mathcal{S},n+1} = -\underline{\mathbf{r}}_i^{\mathcal{S},n+1}$ emerges as

$$\begin{bmatrix} \underline{\mathfrak{S}}_{\mathrm{II}}^{\lambda,\kappa} & \underline{\mathfrak{S}}_{\mathrm{I}\Gamma}^{\lambda,\kappa} & \underline{\mathfrak{S}}_{\mathrm{I}p} & \underline{\mathfrak{S}}_{\mathrm{I}\mathcal{B}} \\ \underline{\mathfrak{S}}_{\Gamma\mathrm{I}}^{\lambda,\kappa} & \underline{\mathfrak{S}}_{\Gamma\Gamma}^{\lambda,\kappa} & \underline{\mathfrak{S}}_{\Gamma p} & \underline{\mathfrak{S}}_{\Gamma\mathcal{B}} \\ \underline{\mathfrak{S}}_{p\mathrm{I}} & \underline{\mathfrak{S}}_{p\Gamma} & \underline{\mathfrak{S}}_{pp} & \underline{\mathbf{0}} \\ \underline{\mathfrak{S}}_{\mathcal{B}\mathrm{I}} & \underline{\mathfrak{S}}_{\mathcal{B}\Gamma} & \underline{\mathbf{0}} & \underline{\mathbf{0}} \end{bmatrix}_i^{n+1} \begin{bmatrix} \Delta\underline{\mathbf{d}}_{\mathrm{I}}^{\mathcal{S}} \\ \Delta\underline{\mathbf{d}}_{\Gamma}^{\mathcal{S}} \\ \Delta\underline{\mathbf{p}}^{\mathcal{S}} \\ \underline{\boldsymbol{\lambda}}^{\mathcal{S}} \end{bmatrix}_{i+1}^{n+1} = - \begin{bmatrix} \underline{\mathbf{r}}_{\mathrm{I}}^{\mathcal{S}} + \alpha_f \underline{\mathbf{r}}_{\mathrm{I}}^{\mathcal{S},\kappa} \\ \underline{\mathbf{r}}_{\Gamma}^{\mathcal{S}} + \alpha_f \underline{\mathbf{r}}_{\Gamma}^{\mathcal{S},\kappa} \\ \underline{\mathbf{r}}_{p}^{\mathcal{S}} \\ \underline{\boldsymbol{\mathcal{B}}} \end{bmatrix}_i^{n+1} . \tag{3.174}$$

Considering the balance equation (3.173), the vector of discrete Lagrange multiplier values $\underline{\boldsymbol{\lambda}}^{n+1}$ is included in the vector of unknown increments $\Delta\underline{\mathbf{x}}_{i+1}^{\mathcal{S},n+1}$. This new contribution only affects the balance of forces at the interface Γ_{FSI}, i.e. the second row of system (3.174). Since the relation of the discrete interface forces and the discrete Lagrange multipliers is linear, the system is directly formulated in terms of the new Lagrange multiplier $\underline{\boldsymbol{\lambda}}_i^{n+1}$ rather than its increment. The modified structure system, thus, reads

$$\begin{bmatrix} \underline{\mathfrak{S}}_{\mathrm{II}}^{\lambda,\kappa} & \underline{\mathfrak{S}}_{\mathrm{I}\Gamma}^{\lambda,\kappa} & \underline{\mathfrak{S}}_{\mathrm{I}p} & \underline{\mathfrak{S}}_{\mathrm{I}\mathcal{B}} & \underline{\mathbf{0}} \\ \underline{\mathfrak{S}}_{\Gamma\mathrm{I}}^{\lambda,\kappa} & \underline{\mathfrak{S}}_{\Gamma\Gamma}^{\lambda,\kappa} & \underline{\mathfrak{S}}_{\Gamma p} & \underline{\mathfrak{S}}_{\Gamma\mathcal{B}} & (1-\alpha_f)\underline{\mathfrak{M}}^{\mathsf{T}} \\ \underline{\mathfrak{S}}_{p\mathrm{I}} & \underline{\mathfrak{S}}_{p\Gamma} & \underline{\mathfrak{S}}_{pp} & \underline{\mathbf{0}} & \underline{\mathbf{0}} \\ \underline{\mathfrak{S}}_{\mathcal{B}\mathrm{I}} & \underline{\mathfrak{S}}_{\mathcal{B}\Gamma} & \underline{\mathbf{0}} & \underline{\mathbf{0}} & \underline{\mathbf{0}} \end{bmatrix}_i^{n+1} \begin{bmatrix} \Delta\underline{\mathbf{d}}_{\mathrm{I}}^{\mathcal{S}} \\ \Delta\underline{\mathbf{d}}_{\Gamma}^{\mathcal{S}} \\ \Delta\underline{\mathbf{p}}^{\mathcal{S}} \\ \underline{\boldsymbol{\lambda}}^{\mathcal{S}} \\ \underline{\boldsymbol{\lambda}} \end{bmatrix}_{i+1}^{n+1} =$$

$$= - \begin{bmatrix} \underline{\mathbf{r}}_{\mathrm{I}}^{\mathcal{S}} + \alpha_f \underline{\mathbf{r}}_{\mathrm{I}}^{\mathcal{S},\kappa} \\ \underline{\mathbf{r}}_{\Gamma}^{\mathcal{S}} + \alpha_f \underline{\mathbf{r}}_{\Gamma}^{\mathcal{S},\kappa} \\ \underline{\mathbf{r}}_{p}^{\mathcal{S}} \\ \underline{\boldsymbol{\mathcal{B}}} \end{bmatrix}_i^{n+1} - \begin{bmatrix} \underline{\mathbf{0}} \\ \alpha_f \underline{\mathfrak{M}}^{\mathsf{T}} \underline{\boldsymbol{\lambda}} \\ \underline{\mathbf{0}} \\ \underline{\mathbf{0}} \end{bmatrix}^{n} . \tag{3.175}$$

3.7.3 The modified fluid and fluid grid field

Before considering the modification necessary due to the interface tractions $\mathbf{h}^{\mathcal{F}}$, the coupling of the fluid and the ALE fields is addressed. The fluid grid positions have to be included as additional unknowns in the fluid system and can no longer be assumed to be given as in the derivation of the standard fluid system (3.48) presented in section 3.2. One possible algorithm to compute the motion of the fluid grid based on the interface motion is proposed in section 3.3. Here, the fluid grid field is formulated in terms of grid displacements $\mathbf{d}^{\mathcal{G}}$. Since also the fluid flow solution depends on these displacements, the linear system (3.48) has to be extended by the so-called *shape derivatives* $\underline{\mathfrak{F}}^{\mathcal{G}}$. These matrices represent the derivatives of the fluid residual forces $\underline{\mathbf{r}}^{\mathcal{F}}$ with respect to the grid displacements $\underline{\mathbf{d}}^{\mathcal{G}}$. They have been discussed in detail by Braess and Wriggers [27] and Fernández and Moubachir [63].

Similar to what has been discussed for the structure in section 3.7.2, the fluid velocities and grid displacements are further split into quantities on the interface, denoted again by a subscript $\cdot_{\Gamma}$, and quantities defined in the interior fluid domain, denoted by a subscript $\cdot_{\mathrm{I}}$. Considering only the fluid residuals, the fluid system emerges as a

rectangular 3×5 block system

$$\left[\begin{array}{ccccc} \underline{\mathcal{F}}_{\mathrm{II}} & \underline{\mathcal{F}}_{\mathrm{I}\Gamma} & \underline{\mathcal{F}}_{\mathrm{I}p} & \underline{\mathcal{F}}^{\mathcal{G}}_{\mathrm{II}} & \underline{\mathcal{F}}^{\mathcal{G}}_{\mathrm{I}\Gamma} \\ \underline{\mathcal{F}}_{\Gamma\mathrm{I}} & \underline{\mathcal{F}}_{\Gamma\Gamma} & \underline{\mathcal{F}}_{\Gamma p} & \underline{\mathcal{F}}^{\mathcal{G}}_{\Gamma\mathrm{I}} & \underline{\mathcal{F}}^{\mathcal{G}}_{\Gamma\Gamma} \\ \underline{\mathcal{F}}_{p\mathrm{I}} & \underline{\mathcal{F}}_{p\Gamma} & \underline{\mathcal{F}}_{pp} & \underline{\mathcal{F}}^{\mathcal{G}}_{p\mathrm{I}} & \underline{\mathcal{F}}^{\mathcal{G}}_{p\Gamma} \end{array}\right]^{n+1}_{i} \left[\begin{array}{c} \Delta\underline{\mathbf{u}}^{\mathcal{F}}_{\mathrm{I}} \\ \Delta\underline{\mathbf{u}}^{\mathcal{F}}_{\Gamma} \\ \Delta\underline{\mathbf{p}}^{\mathcal{F}} \\ \Delta\underline{\mathbf{d}}^{\mathcal{G}}_{\mathrm{I}} \\ \Delta\underline{\mathbf{d}}^{\mathcal{G}}_{\Gamma} \end{array}\right]^{n+1}_{i+1} = - \left[\begin{array}{c} \underline{\mathbf{r}}^{\mathcal{F}}_{\mathrm{I}} \\ \underline{\mathbf{r}}^{\mathcal{F}}_{\Gamma} \\ \underline{\mathbf{r}}^{\mathcal{F}}_{p} \end{array}\right]^{n+1}_{i} . \tag{3.176}$$

Although the fluid grid at the interface Γ_{FSI} is repositioned after every time step to avoid mesh destruction for large structure rotations, fluid and structure meshes undergo the same deformation within a time step. Therefore, the time integration to relate fluid velocities and grid displacements is chosen to be consistent with integration scheme (3.170) for iteration steps $i > 0$. For the initial step $i = 0$, however, the reposition $\widetilde{\Delta\underline{\mathbf{d}}}^{\mathcal{G},n}_{\Gamma}$ has additionally to be accounted for. The consistent time integration, hence, reads

$$\Delta\underline{\mathbf{d}}^{\mathcal{G},n+1}_{\Gamma,i} = \tfrac{\Delta t}{2}\,\Delta\underline{\mathbf{u}}^{\mathcal{F},n+1}_{\Gamma,i} + \delta_{i0}\left(\Delta t\,\underline{\mathbf{u}}^{\mathcal{F},n}_{\Gamma} + \widetilde{\Delta\underline{\mathbf{d}}}^{\mathcal{G},n}_{\Gamma}\right). \tag{3.177}$$

This identity can be used to eliminate the grid displacement DOFs at the interface of system (3.176). The modified system

$$\begin{aligned} &\left[\begin{array}{cccc} \underline{\mathcal{F}}_{\mathrm{II}} & \underline{\mathcal{F}}_{\mathrm{I}\Gamma} + \frac{\Delta t}{2}\underline{\mathcal{F}}^{\mathcal{G}}_{\mathrm{I}\Gamma} & \underline{\mathcal{F}}_{\mathrm{I}p} & \underline{\mathcal{F}}^{\mathcal{G}}_{\mathrm{II}} \\ \underline{\mathcal{F}}_{\Gamma\mathrm{I}} & \underline{\mathcal{F}}_{\Gamma\Gamma} + \frac{\Delta t}{2}\underline{\mathcal{F}}^{\mathcal{G}}_{\Gamma\Gamma} & \underline{\mathcal{F}}_{\Gamma p} & \underline{\mathcal{F}}^{\mathcal{G}}_{\Gamma\mathrm{I}} \\ \underline{\mathcal{F}}_{p\mathrm{I}} & \underline{\mathcal{F}}_{p\Gamma} + \frac{\Delta t}{2}\underline{\mathcal{F}}^{\mathcal{G}}_{p\Gamma} & \underline{\mathcal{F}}_{pp} & \underline{\mathcal{F}}^{\mathcal{G}}_{p\mathrm{I}} \end{array}\right]^{n+1}_{i} \left[\begin{array}{c} \Delta\underline{\mathbf{u}}^{\mathcal{F}}_{\mathrm{I}} \\ \Delta\underline{\mathbf{u}}^{\mathcal{F}}_{\Gamma} \\ \Delta\underline{\mathbf{p}}^{\mathcal{F}} \\ \Delta\underline{\mathbf{d}}^{\mathcal{G}}_{\mathrm{I}} \end{array}\right]^{n+1}_{i+1} = \\ &= - \left[\begin{array}{c} \underline{\mathbf{r}}^{\mathcal{F}}_{\mathrm{I}} \\ \underline{\mathbf{r}}^{\mathcal{F}}_{\Gamma} \\ \underline{\mathbf{r}}^{\mathcal{F}}_{p} \end{array}\right]^{n+1}_{i} - \delta_{i0}\left(\Delta t \left[\begin{array}{c} \underline{\mathcal{F}}^{\mathcal{G}}_{\mathrm{I}\Gamma}\,\underline{\mathbf{u}}^{\mathcal{F}}_{\Gamma} \\ \underline{\mathcal{F}}^{\mathcal{G}}_{\Gamma\Gamma}\,\underline{\mathbf{u}}^{\mathcal{F}}_{\Gamma} \\ \underline{\mathcal{F}}^{\mathcal{G}}_{p\Gamma}\,\underline{\mathbf{u}}^{\mathcal{F}}_{\Gamma} \end{array}\right]^{n} + \left[\begin{array}{c} \underline{\mathcal{F}}^{\mathcal{G}}_{\mathrm{I}\Gamma}\,\widetilde{\Delta\underline{\mathbf{d}}}^{\mathcal{G}}_{\Gamma} \\ \underline{\mathcal{F}}^{\mathcal{G}}_{\Gamma\Gamma}\,\widetilde{\Delta\underline{\mathbf{d}}}^{\mathcal{G}}_{\Gamma} \\ \underline{\mathcal{F}}^{\mathcal{G}}_{p\Gamma}\,\widetilde{\Delta\underline{\mathbf{d}}}^{\mathcal{G}}_{\Gamma} \end{array}\right]^{n}\right) \end{aligned} \tag{3.178}$$

is of reduced size and has to be closed by the equations of fluid grid motion discussed in section 3.3. Since the ALE field does not represent a physical field, it is not supposed to influence the motion of the interface Γ_{FSI}. Thus, forces acting on the interface are to be neglected and the system (3.60) reduces to

$$\begin{aligned} \underline{\mathbf{0}} &= \left[\begin{array}{cc} \underline{\mathcal{A}}_{\mathrm{II}} & \underline{\mathcal{A}}_{\mathrm{I}\Gamma} \end{array}\right]^{n+1}_{i} \left[\begin{array}{c} \Delta\underline{\mathbf{d}}^{\mathcal{G}}_{\mathrm{I}} \\ \Delta\underline{\mathbf{d}}^{\mathcal{G}}_{\Gamma} \end{array}\right]^{n+1}_{i+1} \\ &= \left[\begin{array}{cc} \underline{\mathcal{A}}_{\mathrm{II}} & \frac{\Delta t}{2}\underline{\mathcal{A}}_{\mathrm{I}\Gamma} \end{array}\right]^{n+1}_{i} \left[\begin{array}{c} \Delta\underline{\mathbf{d}}^{\mathcal{G}}_{\mathrm{I}} \\ \Delta\underline{\mathbf{u}}^{\mathcal{F}}_{\Gamma} \end{array}\right]^{n+1}_{i+1} + \delta_{i0}\left[\Delta t\,\underline{\mathcal{A}}_{\mathrm{I}\Gamma}\underline{\mathbf{u}}^{\mathcal{F}}_{\Gamma} + \underline{\mathcal{A}}_{\mathrm{I}\Gamma}\,\widetilde{\Delta\underline{\mathbf{d}}}^{\mathcal{G}}_{\Gamma}\right]^{n}. \end{aligned} \tag{3.179}$$

In (3.179), the displacement DOFs $\underline{\mathbf{d}}^{\mathcal{G}}_{\Gamma}$ have been eliminated from the system by applying (3.177). Equations (3.178) and (3.179) state the linearized 4×4 block system of equations for the fluid motion on a deformable domain.

Nevertheless, the interface traction given by the Lagrange multiplier $\boldsymbol{\lambda}$ has not yet been considered. For a consistent integration into the system, the weak form of the fluid

problem (3.25) is reconsidered and modified. As for the structure part, the interface traction $\mathbf{h}^{\mathcal{F}} = \boldsymbol{\lambda}$ is added to the system as an external surface boundary load yielding the modified weak form

$$\begin{aligned} 0 =& \rho^{\mathcal{F}} \left(\mathring{\mathbf{u}}^{\mathcal{F}} ; \mathbf{v} \right)_{\Omega_{\mathbf{x}}} + \rho^{\mathcal{F}} \left(\left(\left(\mathbf{u}^{\mathcal{F}} - \mathbf{u}^{\mathcal{G}} \right) \cdot \boldsymbol{\nabla} \right) \mathbf{u}^{\mathcal{F}} ; \mathbf{v} \right)_{\Omega_{\mathbf{x}}} + 2\mu \left(\boldsymbol{\varepsilon}(\mathbf{u}^{\mathcal{F}}) ; \boldsymbol{\varepsilon}(\mathbf{v}) \right)_{\Omega_{\mathbf{x}}} - \\ & - \left(p^{\mathcal{F}} , \boldsymbol{\nabla} \cdot \mathbf{v} \right)_{\Omega_{\mathbf{x}}} + \left(\boldsymbol{\nabla} \cdot \mathbf{u}^{\mathcal{F}} , q \right)_{\Omega_{\mathbf{x}}} - \rho^{\mathcal{F}} \left(\mathbf{b} ; \mathbf{v} \right)_{\Omega_{\mathbf{x}}} - \left(\mathbf{t}_N ; \mathbf{v} \right)_{\Gamma_N} - \left(\boldsymbol{\lambda} ; \mathbf{v} \right)_{\Gamma_{\mathsf{FSI}}} . \end{aligned} \tag{3.180}$$

The discretization of the additional term is rather straightforward given the already defined discretizations (3.160) and (3.161) and results in

$$\left(\boldsymbol{\lambda} ; \mathbf{v} \right)_{\Gamma_{\mathsf{FSI}}} = \sum_{j=1}^{n_{\Gamma}^{\mathsf{nd},\mathcal{F}}} \sum_{k=1}^{n_{\Gamma}^{\mathsf{nd},\mathcal{F}}} \mathbf{v}^{\mathsf{T}} D_{jk} \boldsymbol{\lambda}_k = \underline{\mathbf{v}}^{\mathsf{T}} \underline{\mathcal{D}}^{\mathsf{T}} \underline{\boldsymbol{\lambda}}. \tag{3.181}$$

The diagonal global mortar matrix $\underline{\mathcal{D}}$ has been introduced in section 3.7.1. The global vector of discrete nodal Lagrange multiplier values $\underline{\boldsymbol{\lambda}}$ coincides with the vector defined in section 3.7.2 considered for the structure field.

The discretization in time is chosen to be consistent with the one-step-θ method introduced in section 3.2.2, i.e. with the balance of forces stated in (3.38). The additional traction has to be evaluated at the end of the time step t^{n+1}, such that the discrete balance of forces reads

$$\underline{\mathbf{M}}\, \underline{\mathring{\mathbf{u}}}^{n+1} = \underline{\boldsymbol{f}}(\underline{\mathbf{u}}^{\mathcal{F},n+1}, \underline{\mathbf{u}}^{\mathcal{G},n+1}, \underline{\mathbf{p}}^{\mathcal{F},n+1}, t^{n+1}) - \underline{\mathcal{D}}^{\mathsf{T}} \underline{\boldsymbol{\lambda}}^{n+1}. \tag{3.182}$$

The function $\underline{\boldsymbol{f}}$ has been defined in (3.37), but the grid velocity is now formally added as an unknown quantity.

Due to the particular choice of the time integration scheme, the Lagrange multiplier from the previous time step t^n is not needed to derive the fluid system. However, if a generalized-α method is employed for the fluid field as well, a similar interpolation as in (3.173) is needed.

The matrix form of (3.182) can be obtained as an extension of the combined system of (3.178) and (3.179). The Lagrange multiplier contributes to the interface forces of the fluid, i.e. to the the second row of (3.178). Using the abbreviation $\widehat{\underline{\boldsymbol{\mathcal{F}}}} = \underline{\boldsymbol{\mathcal{F}}} + \frac{\Delta t}{2} \underline{\boldsymbol{\mathcal{F}}}^{\mathcal{G}}$, the final fluid system is given as

$$\begin{aligned} & \begin{bmatrix} \underline{\boldsymbol{\mathcal{F}}}_{\mathrm{II}} & \widehat{\underline{\boldsymbol{\mathcal{F}}}}_{\mathrm{I}\Gamma} & \underline{\boldsymbol{\mathcal{F}}}_{\mathrm{I}p} & \underline{\boldsymbol{\mathcal{F}}}^{\mathcal{G}}_{\mathrm{II}} & \underline{\mathbf{0}} \\ \underline{\boldsymbol{\mathcal{F}}}_{\Gamma\mathrm{I}} & \widehat{\underline{\boldsymbol{\mathcal{F}}}}_{\Gamma\Gamma} & \underline{\boldsymbol{\mathcal{F}}}_{\Gamma p} & \underline{\boldsymbol{\mathcal{F}}}^{\mathcal{G}}_{\Gamma\mathrm{I}} & -\underline{\mathcal{D}} \\ \underline{\boldsymbol{\mathcal{F}}}_{p\mathrm{I}} & \widehat{\underline{\boldsymbol{\mathcal{F}}}}_{p\Gamma} & \underline{\boldsymbol{\mathcal{F}}}_{pp} & \underline{\boldsymbol{\mathcal{F}}}^{\mathcal{G}}_{p\mathrm{I}} & \underline{\mathbf{0}} \\ \underline{\mathbf{0}} & \frac{\Delta t}{2} \underline{\boldsymbol{\mathcal{A}}}_{\mathrm{I}\Gamma} & \underline{\mathbf{0}} & \underline{\boldsymbol{\mathcal{A}}}_{\mathrm{II}} & \underline{\mathbf{0}} \end{bmatrix}^{n+1}_{i} \begin{bmatrix} \Delta \underline{\mathbf{u}}^{\mathcal{F}}_{\mathrm{I}} \\ \Delta \underline{\mathbf{u}}^{\mathcal{F}}_{\Gamma} \\ \Delta \underline{\mathbf{p}}^{\mathcal{F}} \\ \Delta \underline{\mathbf{d}}^{\mathcal{G}}_{\mathrm{I}} \\ \underline{\boldsymbol{\lambda}} \end{bmatrix}^{n+1}_{i+1} = \\ & = - \begin{bmatrix} \underline{\mathbf{r}}^{\mathcal{F}}_{\mathrm{I}} \\ \underline{\mathbf{r}}^{\mathcal{F}}_{\Gamma} \\ \underline{\mathbf{r}}^{\mathcal{F}}_{p} \\ \underline{\mathbf{0}} \end{bmatrix}^{n+1}_{i} - \delta_{i0} \left(\Delta t \begin{bmatrix} \underline{\boldsymbol{\mathcal{F}}}^{\mathcal{G}}_{\mathrm{I}\Gamma}\, \underline{\mathbf{u}}^{\mathcal{F}}_{\Gamma} \\ \underline{\boldsymbol{\mathcal{F}}}^{\mathcal{G}}_{\Gamma\Gamma}\, \underline{\mathbf{u}}^{\mathcal{F}}_{\Gamma} \\ \underline{\boldsymbol{\mathcal{F}}}^{\mathcal{G}}_{\Gamma\Gamma}\, \underline{\mathbf{u}}^{\mathcal{F}}_{\Gamma} \\ \underline{\boldsymbol{\mathcal{A}}}_{\mathrm{I}\Gamma}\, \underline{\mathbf{u}}^{\mathcal{F}}_{\Gamma} \end{bmatrix}^{n} + \begin{bmatrix} \underline{\boldsymbol{\mathcal{F}}}^{\mathcal{G}}_{\mathrm{I}\Gamma}\, \widetilde{\Delta \underline{\mathbf{d}}}^{\mathcal{G}}_{\Gamma} \\ \underline{\boldsymbol{\mathcal{F}}}^{\mathcal{G}}_{\Gamma\Gamma}\, \widetilde{\Delta \underline{\mathbf{d}}}^{\mathcal{G}}_{\Gamma} \\ \underline{\boldsymbol{\mathcal{F}}}^{\mathcal{G}}_{\Gamma\Gamma}\, \widetilde{\Delta \underline{\mathbf{d}}}^{\mathcal{G}}_{\Gamma} \\ \underline{\boldsymbol{\mathcal{A}}}_{\mathrm{I}\Gamma}\, \widetilde{\Delta \underline{\mathbf{d}}}^{\mathcal{G}}_{\Gamma} \end{bmatrix}^{n} \right) . \end{aligned} \tag{3.183}$$

3.7.4 Final monolithic system and solution strategies

With the structure system (3.175), the fluid system (3.183), and the coupling (3.170), the necessary building blocks for a monolithic FSI system are at hand. To begin with, a three-field problem is stated considering structure (including algebraic constraints), fluid (including grid motion), and the Lagrange multiplier DOFs. The linear system to be solved in each iteration step i of the Newton-type algorithm is denoted by

$$\underline{\mathcal{J}}_i^{3,n+1} \, \Delta \underline{\mathbf{x}}_{i+1}^{3,n+1} = -\underline{\mathbf{r}}_i^{3,n+1}, \tag{3.184}$$

where the superscript $\cdot^3$ refers to the three fields involved.

The number of fields naturally determines the block structure of the system. The vector of unknowns $\Delta \underline{\mathbf{x}}_{i+1}^{3,n+1}$ includes the DOFs of all fields:

$$\Delta \underline{\mathbf{x}}_{i+1}^{3,n+1} = \begin{bmatrix} \Delta \underline{\mathbf{d}}_{\Gamma}^{\mathcal{S}} \\ \Delta \underline{\mathbf{d}}_{\mathrm{I}}^{\mathcal{S}} \\ \Delta \underline{\mathbf{p}}^{\mathcal{S}} \\ \underline{\boldsymbol{\lambda}}^{\mathcal{S}} \\ \Delta \underline{\mathbf{u}}_{\mathrm{I}}^{\mathcal{F}} \\ \Delta \underline{\mathbf{u}}_{\Gamma}^{\mathcal{F}} \\ \Delta \underline{\mathbf{p}}^{\mathcal{F}} \\ \Delta \underline{\mathbf{d}}_{\mathrm{I}}^{\mathcal{G}} \\ \underline{\boldsymbol{\lambda}} \end{bmatrix}_{i+1}^{n+1} . \tag{3.185}$$

Beside the number of fields, the entries in the right hand side vector of the system $\underline{\mathbf{r}}_i^{3,n+1}$ also depend on the iteration step i. Because of the time integration schemes (3.170) and (3.177), history values of the previous time step have to be considered for $i = 0$,

which reads

$$\underline{\mathbf{r}}_i^{3,n+1} = \begin{bmatrix} \underline{\mathbf{r}}_{\mathrm{I}}^{\mathcal{S}} + \alpha_f \underline{\mathbf{r}}_{\mathrm{I}}^{\mathcal{S},\kappa} \\ \underline{\mathbf{r}}_{\Gamma}^{\mathcal{S}} + \alpha_f \underline{\mathbf{r}}_{\Gamma}^{\mathcal{S},\kappa} \\ \underline{\mathbf{r}}_{p}^{\mathcal{S}} \\ \underline{\boldsymbol{\mathcal{B}}} \\ \underline{\mathbf{r}}_{\mathrm{I}}^{\mathcal{F}} \\ \underline{\mathbf{r}}_{\Gamma}^{\mathcal{F}} \\ \underline{\mathbf{r}}_{p}^{\mathcal{F}} \\ \underline{\mathbf{0}} \\ \underline{\mathbf{0}} \end{bmatrix}_i^{n+1} + \begin{bmatrix} \underline{\mathbf{0}} \\ \alpha_f \underline{\mathfrak{M}}^{\mathsf{T}} \boldsymbol{\lambda} \\ \underline{\mathbf{0}} \\ \underline{\mathbf{0}} \\ \underline{\mathbf{0}} \\ \underline{\mathbf{0}} \\ \underline{\mathbf{0}} \\ \underline{\mathbf{0}} \\ \underline{\mathbf{0}} \end{bmatrix}^{n} + \\ + \delta_{i0} \left(\Delta t \begin{bmatrix} \underline{\mathbf{0}} \\ \underline{\mathbf{0}} \\ \underline{\mathbf{0}} \\ \underline{\mathbf{0}} \\ \underline{\mathfrak{F}}_{\mathrm{I}\Gamma}^{\mathcal{G}} \, \underline{\mathbf{u}}_{\Gamma}^{\mathcal{F}} \\ \underline{\mathfrak{F}}_{\Gamma\Gamma}^{\mathcal{G}} \, \underline{\mathbf{u}}_{\Gamma}^{\mathcal{F}} \\ \underline{\mathfrak{F}}_{p\Gamma}^{\mathcal{G}} \, \underline{\mathbf{u}}_{\Gamma}^{\mathcal{F}} \\ \underline{\mathcal{A}}_{\mathrm{I}\Gamma} \, \underline{\mathbf{u}}_{\Gamma}^{\mathcal{F}} \\ \underline{\mathfrak{D}} \, \underline{\mathbf{u}}_{\Gamma}^{\mathcal{F}} \end{bmatrix}^{n} + \begin{bmatrix} \underline{\mathbf{0}} \\ \underline{\mathbf{0}} \\ \underline{\mathbf{0}} \\ \underline{\mathbf{0}} \\ \underline{\mathfrak{F}}_{\mathrm{I}\Gamma}^{\mathcal{G}} \, \widetilde{\Delta \mathbf{d}}_{\Gamma}^{\mathcal{G}} \\ \underline{\mathfrak{F}}_{\Gamma\Gamma}^{\mathcal{G}} \, \widetilde{\Delta \mathbf{d}}_{\Gamma}^{\mathcal{G}} \\ \underline{\mathfrak{F}}_{p\Gamma}^{\mathcal{G}} \, \widetilde{\Delta \mathbf{d}}_{\Gamma}^{\mathcal{G}} \\ \underline{\mathcal{A}}_{\mathrm{I}\Gamma} \, \widetilde{\Delta \mathbf{d}}_{\Gamma}^{\mathcal{G}} \\ \underline{\mathbf{0}} \end{bmatrix}^{n} \right). \tag{3.186}$$

The monolithic system matrix $\underline{\mathfrak{J}}_i^{3,n+1}$, which is given by

$$\underline{\mathfrak{J}}_i^{3,n+1} = \begin{bmatrix} \underline{\mathfrak{S}}_{\mathrm{II}}^{\lambda,\kappa} & \underline{\mathfrak{S}}_{\mathrm{I}\Gamma}^{\lambda,\kappa} & \underline{\mathfrak{S}}_{\mathrm{I}p} & \underline{\mathfrak{S}}_{\mathrm{I}\mathcal{B}} & & & & & \\ \underline{\mathfrak{S}}_{\Gamma\mathrm{I}}^{\lambda,\kappa} & \underline{\mathfrak{S}}_{\Gamma\Gamma}^{\lambda,\kappa} & \underline{\mathfrak{S}}_{\Gamma p} & \underline{\mathfrak{S}}_{\Gamma\mathcal{B}} & & & & & (1-\alpha_f)\underline{\mathfrak{M}}^{\mathsf{T}} \\ \underline{\mathfrak{S}}_{p\mathrm{I}} & \underline{\mathfrak{S}}_{p\Gamma} & \underline{\mathfrak{S}}_{pp} & \underline{\mathbf{0}} & & & & & \\ \underline{\mathfrak{S}}_{\mathcal{B}\mathrm{I}} & \underline{\mathfrak{S}}_{\mathcal{B}\Gamma} & \underline{\mathbf{0}} & \underline{\mathbf{0}} & & & & & \\ & & & & \underline{\mathfrak{F}}_{\mathrm{II}} & \underline{\widehat{\mathfrak{F}}}_{\mathrm{I}\Gamma} & \underline{\mathfrak{F}}_{\mathrm{I}p} & \underline{\mathfrak{F}}_{\mathrm{II}}^{\mathcal{G}} & \\ & & & & \underline{\mathfrak{F}}_{\Gamma\mathrm{I}} & \underline{\widehat{\mathfrak{F}}}_{\Gamma\Gamma} & \underline{\mathfrak{F}}_{\Gamma p} & \underline{\mathfrak{F}}_{\Gamma\mathrm{I}}^{\mathcal{G}} & -\underline{\mathfrak{D}} \\ & & & & \underline{\mathfrak{F}}_{p\mathrm{I}} & \underline{\widehat{\mathfrak{F}}}_{p\Gamma} & \underline{\mathfrak{F}}_{pp} & \underline{\mathfrak{F}}_{p\mathrm{I}}^{\mathcal{G}} & \\ & & & & \underline{\mathbf{0}} & \frac{\Delta t}{2}\underline{\mathcal{A}}_{\mathrm{I}\Gamma} & \underline{\mathbf{0}} & \underline{\mathcal{A}}_{\mathrm{II}} & \\ & \underline{\mathfrak{M}} & & & & -\frac{\Delta t}{2}\underline{\mathfrak{D}} & & & \end{bmatrix}_i^{n+1}, \tag{3.187}$$

has a saddle-point type structure, which is known to cause numerical problems with many iterative linear solvers.

It is interesting to note that in case of conforming interface meshes, both mortar matrices $\underline{\mathfrak{M}}$ and $\underline{\mathfrak{D}}$ reduce to diagonal matrices and the projection $\underline{\mathfrak{P}}$ to the identity operation. For this case and $\alpha_f = 1$, it can easily be shown that the linear system derived here matches with the starting point of the standard monolithic FSI approach for conforming meshes as derived in the thesis by Küttler [123]. To avoid the saddle-point structure, this standard approach eliminated the Lagrange multiplier and the fluid velocity DOFs at the interface by a static condensation. For the condensed system, Gee et al. [77] proposed AMG based FSI preconditioners, which have been shown to significantly improve the convergence behavior.

A very similar approach can be taken for the system of nonconforming interfaces. A static condensation is possible due to the dual mortar method used here. To begin with, the sixth row of (3.184) allows to express the Lagrange multiplier $\underline{\boldsymbol{\lambda}}_{i+1}^{n+1}$ in terms of fluid quantities as follows

$$\begin{aligned}\underline{\boldsymbol{\lambda}}_{i+1}^{n+1} =& \underline{\mathfrak{D}}^{-1} \left(\underline{\mathfrak{F}}_{\Gamma\mathrm{I}} \, \Delta \underline{\mathbf{u}}_{\mathrm{I},i+1}^{\mathcal{F},n+1} + \widehat{\underline{\mathfrak{F}}}_{\Gamma\Gamma} \Delta \underline{\mathbf{u}}_{\Gamma,i+1}^{\mathcal{F},n+1} + \underline{\mathfrak{F}}_{\Gamma p} \, \Delta \underline{\mathbf{p}}_{i+1}^{\mathcal{F},n+1} + \underline{\mathfrak{F}}_{\Gamma\mathrm{I}}^{\mathcal{G}} \Delta \underline{\mathbf{d}}_{\mathrm{I},i+1}^{\mathcal{G},n+1} \right) \\ & + \underline{\mathfrak{D}}^{-1} \left(\underline{\mathbf{r}}_{\Gamma,i}^{\mathcal{F},n+1} + \delta_{i0} \Delta t \, \underline{\mathfrak{F}}_{\Gamma\Gamma}^{\mathcal{G}} \underline{\mathbf{u}}_{\Gamma}^{\mathcal{F},n} + \delta_{i0} \, \underline{\mathfrak{F}}_{\Gamma\Gamma}^{\mathcal{G}} \, \widetilde{\Delta \underline{\mathbf{d}}}_{\Gamma}^{\mathcal{G},n} \right) . \end{aligned} \tag{3.188}$$

Since the global mortar matrix $\underline{\mathfrak{D}}$ is a diagonal matrix, its inversion is a trivial operation. Expression (3.188) can be introduces in the second row of (3.184). This procedure eliminates the Lagrange multiplier DOFs $\underline{\boldsymbol{\lambda}}$ from the system and the sixth row can be neglected.

As a next step, the discrete no-slip condition (3.170) or equivalently the last row of (3.184) can be solved for the fluid velocity increments $\Delta \underline{\mathbf{u}}_{\Gamma,i}^{\mathcal{F},n+1}$ at the interface

$$\Delta \underline{\mathbf{u}}_{\Gamma,i}^{\mathcal{F},n+1} = \tfrac{2}{\Delta t} \underline{\mathfrak{P}} \Delta \underline{\mathbf{d}}_{\Gamma,i}^{\mathcal{S},n+1} - 2\delta_{i0} \, \underline{\mathbf{u}}_{\Gamma}^{\mathcal{F},n}, \tag{3.189}$$

with mortar projection matrix $\underline{\mathfrak{P}} = \underline{\mathfrak{D}}^{-1} \underline{\mathfrak{M}}$. Subsequently, this solution can be used to reduce the system size further, i.e. it allows to eliminate the last row of the system and the fluid velocity DOFs at the interface.

The condensed, fully coupled, monolithic FSI system finally reads

$$\underline{\mathfrak{J}}_{i}^{2,n+1} \, \Delta \underline{\mathbf{x}}_{i+1}^{2,n+1} = - \underline{\mathbf{r}}_{i}^{2,n+1}. \tag{3.190}$$

The superscript $\cdot^{2}$ indicates the fact that only two physical fields remain, since the Lagrange multiplier DOFs $\underline{\boldsymbol{\lambda}}$ have been eliminated form the system.

Consistent with the naming convention introduced in the thesis of Küttler [123], the previous publication [121] referred to this system as *fluid-split*, since the vector of unknowns $\Delta \underline{\mathbf{x}}_{i+1}^{2,n+1}$ contains only fluid velocity DOFs in the interior domain I:

$$\Delta \underline{\mathbf{x}}_{i+1}^{2,n+1} = \begin{bmatrix} \Delta \underline{\mathbf{d}}_{\mathrm{I}}^{\mathcal{S}} \\ \Delta \underline{\mathbf{d}}_{\Gamma}^{\mathcal{S}} \\ \Delta \underline{\mathbf{p}}^{\mathcal{S}} \\ \underline{\boldsymbol{\lambda}}^{\mathcal{S}} \\ \Delta \underline{\mathbf{u}}_{\mathrm{I}}^{\mathcal{F}} \\ \Delta \underline{\mathbf{p}}^{\mathcal{F}} \\ \Delta \underline{\mathbf{d}}_{\mathrm{I}}^{\mathcal{G}} \end{bmatrix}_{i+1}^{n+1} . \tag{3.191}$$

The right hand side vector $\underline{\mathbf{r}}_{i}^{2,n+1}$ is also of reduced size. As for the vector of unknowns,

two blocks can be eliminated, such that the block structure of the right hand side reads

$$\underline{\mathbf{r}}_i^{2,n+1} = \begin{bmatrix} \underline{\mathbf{r}}_{\mathrm{I}}^{\mathcal{S}} + \alpha_f \underline{\mathbf{r}}_{\mathrm{I}}^{\mathcal{S},\kappa} \\ \underline{\mathbf{r}}_{\Gamma}^{\mathcal{S}} + \alpha_f \underline{\mathbf{r}}_{\Gamma}^{\mathcal{S},\kappa} + (1-\alpha_f)\underline{\boldsymbol{\mathcal{P}}}^{\mathsf{T}} \underline{\mathbf{r}}_{\Gamma}^{\mathcal{F}} \\ \underline{\mathbf{r}}_{p}^{\mathcal{S}} \\ \underline{\boldsymbol{\mathcal{B}}} \\ \underline{\mathbf{r}}_{\mathrm{I}}^{\mathcal{F}} \\ \underline{\mathbf{r}}_{p}^{\mathcal{F}} \\ \underline{\mathbf{0}} \end{bmatrix}_i^{n+1} + \begin{bmatrix} \underline{\mathbf{0}} \\ \alpha_f \underline{\mathcal{M}}^{\mathsf{T}} \boldsymbol{\lambda} \\ \underline{\mathbf{0}} \\ \underline{\mathbf{0}} \\ \underline{\mathbf{0}} \\ \underline{\mathbf{0}} \\ \underline{\mathbf{0}} \end{bmatrix}^{n} + \tag{3.192}$$

$$+ \delta_{i0} \left(\begin{bmatrix} \underline{\mathbf{0}} \\ 2(1-\alpha_f)\underline{\boldsymbol{\mathcal{P}}}^{\mathsf{T}} \underline{\boldsymbol{\mathcal{F}}}_{\Gamma\Gamma} \underline{\mathbf{u}}_{\Gamma}^{\mathcal{F}} \\ \underline{\mathbf{0}} \\ \underline{\mathbf{0}} \\ 2\underline{\boldsymbol{\mathcal{F}}}_{\mathrm{I}\Gamma}\, \underline{\mathbf{u}}_{\Gamma}^{\mathcal{F}} \\ 2\underline{\boldsymbol{\mathcal{F}}}_{p\Gamma}^{\mathcal{G}}\, \underline{\mathbf{u}}_{\Gamma}^{\mathcal{F}} \\ \underline{\mathbf{0}} \end{bmatrix}^{n} + \begin{bmatrix} \underline{\mathbf{0}} \\ (1-\alpha_f)\underline{\boldsymbol{\mathcal{P}}}^{\mathsf{T}} \underline{\boldsymbol{\mathcal{F}}}_{\Gamma\Gamma}^{\mathcal{G}}\, \widetilde{\Delta \mathbf{d}}_{\Gamma}^{\mathcal{G}} \\ \underline{\mathbf{0}} \\ \underline{\mathbf{0}} \\ \underline{\boldsymbol{\mathcal{F}}}_{\mathrm{I}\Gamma}^{\mathcal{G}}\, \widetilde{\Delta \mathbf{d}}_{\Gamma}^{\mathcal{G}} \\ \underline{\boldsymbol{\mathcal{F}}}_{p\Gamma}^{\mathcal{G}}\, \widetilde{\Delta \mathbf{d}}_{\Gamma}^{\mathcal{G}} \\ \underline{\boldsymbol{\mathcal{A}}}_{\mathrm{I}\Gamma}\, \widetilde{\Delta \mathbf{d}}_{\Gamma}^{\mathcal{G}} \end{bmatrix}^{n} \right) \tag{3.193}$$

The static condensation yields a 7×7 block matrix $\underline{\mathcal{J}}_i^{2,n+1}$. Defining $\alpha_f^- = (1-\alpha_f)$, it can be written as

$$\underline{\mathcal{J}}_i^{2,n+1} = \begin{bmatrix} \underline{\mathbb{S}}_{\mathrm{II}} & \underline{\mathbb{S}}_{\mathrm{I}\Gamma} & \underline{\mathbb{S}}_{\mathrm{I}p} & \underline{\mathbb{S}}_{\mathrm{I}\mathcal{B}} & & & \\ \underline{\mathbb{S}}_{\Gamma\mathrm{I}} & \underline{\mathbb{S}}_{\Gamma\Gamma} + \alpha_f^- \underline{\boldsymbol{\mathcal{P}}}^{\mathsf{T}} \widehat{\underline{\boldsymbol{\mathcal{F}}}}_{\Gamma\Gamma} \underline{\boldsymbol{\mathcal{P}}} & \underline{\mathbb{S}}_{\Gamma p} & \underline{\mathbb{S}}_{\Gamma\mathcal{B}} & \alpha_f^- \underline{\boldsymbol{\mathcal{P}}}^{\mathsf{T}} \underline{\boldsymbol{\mathcal{F}}}_{\Gamma\mathrm{I}} & \alpha_f^- \underline{\boldsymbol{\mathcal{P}}}^{\mathsf{T}} \underline{\boldsymbol{\mathcal{F}}}_{\Gamma p} & \alpha_f^- \underline{\boldsymbol{\mathcal{P}}}^{\mathsf{T}} \underline{\boldsymbol{\mathcal{F}}}_{\Gamma\mathrm{I}}^{\mathcal{G}} \\ \underline{\mathbb{S}}_{p\mathrm{I}} & \underline{\mathbb{S}}_{p\Gamma} & \underline{\mathbb{S}}_{pp} & \underline{\mathbf{0}} & & & \\ \underline{\mathbb{S}}_{\mathcal{B}\mathrm{I}} & \underline{\mathbb{S}}_{\mathcal{B}\Gamma} & \underline{\mathbf{0}} & \underline{\mathbf{0}} & & & \\ & \frac{2}{\Delta t} \widehat{\underline{\boldsymbol{\mathcal{F}}}}_{\mathrm{I}\Gamma} \underline{\boldsymbol{\mathcal{P}}} & & & \underline{\boldsymbol{\mathcal{F}}}_{\mathrm{II}} & \underline{\boldsymbol{\mathcal{F}}}_{\mathrm{I}p} & \underline{\boldsymbol{\mathcal{F}}}_{\mathrm{II}}^{\mathcal{G}} \\ & \frac{2}{\Delta t} \widehat{\underline{\boldsymbol{\mathcal{F}}}}_{p\Gamma} \underline{\boldsymbol{\mathcal{P}}} & & & \underline{\boldsymbol{\mathcal{F}}}_{p\mathrm{I}} & \underline{\boldsymbol{\mathcal{F}}}_{pp} & \underline{\boldsymbol{\mathcal{F}}}_{p\mathrm{I}}^{\mathcal{G}} \\ & \underline{\boldsymbol{\mathcal{A}}}_{\mathrm{I}\Gamma} \underline{\boldsymbol{\mathcal{P}}} & & & \underline{\mathbf{0}} & \underline{\mathbf{0}} & \underline{\boldsymbol{\mathcal{A}}}_{\mathrm{II}} \end{bmatrix}_i^{n+1} . \tag{3.194}$$

The chosen fluid-split approach considers the full set of structure DOFs and, thus, allows for the return to the standard grouping of the structure DOFs as in (3.140), which only distinguishes between structure displacements $\underline{\mathbf{d}}^{\mathcal{S}}$, pressure $\underline{\mathbf{p}}^{\mathcal{S}}$, and possibly Lagrange multipliers $\underline{\boldsymbol{\lambda}}^{\mathcal{S}}$ for the algebraic constraints. The resulting block structure of the Jacobian $\underline{\mathcal{J}}_i^{2,n+1}$ is then simplified to a 6×6 block matrix

$$\underline{\mathcal{J}}_i^{2,n+1} = \begin{bmatrix} \widehat{\underline{\mathbb{S}}}_{\mathbf{dd}} & \underline{\mathbb{S}}_{\mathbf{d}p} & \underline{\mathbb{S}}_{\mathbf{d}\mathcal{B}} & \alpha_f^- \underline{\boldsymbol{\mathcal{F}}}_{\mathbf{d}^{\mathcal{S}}\mathrm{I}} & \alpha_f^- \underline{\boldsymbol{\mathcal{F}}}_{\mathbf{d}^{\mathcal{S}}p} & \alpha_f^- \underline{\boldsymbol{\mathcal{F}}}_{\mathbf{d}^{\mathcal{S}}\mathrm{I}}^{\mathcal{G}} \\ \underline{\mathbb{S}}_{p\mathbf{d}} & \underline{\mathbb{S}}_{pp} & \underline{\mathbf{0}} & & & \\ \underline{\mathbb{S}}_{\mathcal{B}\mathbf{d}} & \underline{\mathbf{0}} & \underline{\mathbf{0}} & & & \\ \frac{2}{\Delta t} \widehat{\underline{\boldsymbol{\mathcal{F}}}}_{\mathrm{I}\mathbf{d}^{\mathcal{S}}} & & & \underline{\boldsymbol{\mathcal{F}}}_{\mathrm{II}} & \underline{\boldsymbol{\mathcal{F}}}_{\mathrm{I}p} & \underline{\boldsymbol{\mathcal{F}}}_{\mathrm{II}}^{\mathcal{G}} \\ \frac{2}{\Delta t} \widehat{\underline{\boldsymbol{\mathcal{F}}}}_{p\mathbf{d}^{\mathcal{S}}} & & & \underline{\boldsymbol{\mathcal{F}}}_{p\mathrm{I}} & \underline{\boldsymbol{\mathcal{F}}}_{pp} & \underline{\boldsymbol{\mathcal{F}}}_{p\mathrm{I}}^{\mathcal{G}} \\ \underline{\boldsymbol{\mathcal{A}}}_{\mathrm{I}\mathbf{d}^{\mathcal{S}}} & & & \underline{\mathbf{0}} & \underline{\mathbf{0}} & \underline{\boldsymbol{\mathcal{A}}}_{\mathrm{II}} \end{bmatrix}_i^{n+1} , \tag{3.195}$$

which is convenient to start with for the application of the scaled thickness approach as derived in section 3.6. The definition of the matrix blocks $\widehat{\underline{\mathbb{S}}}_{\mathbf{dd}}$, $\widehat{\underline{\boldsymbol{\mathcal{F}}}}_{\mathrm{I}\mathbf{d}^{\mathcal{S}}}$, $\underline{\boldsymbol{\mathcal{F}}}_{p\mathbf{d}^{\mathcal{S}}}$, and $\underline{\boldsymbol{\mathcal{A}}}_{\mathrm{I}\mathbf{d}^{\mathcal{S}}}$ newly

introduced in (3.195) can easily be deduced by comparison with (3.194). The scaled thickness approach can now be consistently applied to the coupled system resulting in a left hand side

$$\begin{bmatrix} \underline{\boldsymbol{\mathcal{C}}}^{\mathsf{T}}\widehat{\underline{\mathbf{S}}}_{\mathbf{dd}}\underline{\boldsymbol{\mathcal{C}}} & \underline{\boldsymbol{\mathcal{C}}}^{\mathsf{T}}\underline{\mathbf{S}}_{\mathbf{d}p} & \underline{\boldsymbol{\mathcal{C}}}^{\mathsf{T}}\underline{\mathbf{S}}_{\mathbf{d}\mathcal{B}} & \underline{\boldsymbol{\mathcal{C}}}^{\mathsf{T}}\alpha_f^-\underline{\boldsymbol{\mathcal{F}}}_{\mathbf{d}^{\mathcal{S}}\mathrm{I}} & \underline{\boldsymbol{\mathcal{C}}}^{\mathsf{T}}\alpha_f^-\underline{\boldsymbol{\mathcal{F}}}_{\mathbf{d}^{\mathcal{S}}p} & \underline{\boldsymbol{\mathcal{C}}}^{\mathsf{T}}\alpha_f^-\underline{\boldsymbol{\mathcal{F}}}^{\mathcal{G}}_{\mathbf{d}^{\mathcal{S}}\mathrm{I}} \\ \underline{\mathbf{S}}_{p\mathbf{d}}\underline{\boldsymbol{\mathcal{C}}} & \underline{\mathbf{S}}_{pp} & \underline{\mathbf{0}} & & & \\ \underline{\mathbf{S}}_{\mathcal{B}\mathbf{d}}\underline{\boldsymbol{\mathcal{C}}} & \underline{\mathbf{0}} & \underline{\mathbf{0}} & & & \\ \frac{2}{\Delta t}\widehat{\underline{\boldsymbol{\mathcal{F}}}}_{|\mathbf{d}^{\mathcal{S}}}\underline{\boldsymbol{\mathcal{C}}} & & & \underline{\boldsymbol{\mathcal{F}}}_{\mathrm{II}} & \underline{\boldsymbol{\mathcal{F}}}_{\mathrm{I}p} & \underline{\boldsymbol{\mathcal{F}}}^{\mathcal{G}}_{\mathrm{II}} \\ \frac{2}{\Delta t}\widehat{\underline{\boldsymbol{\mathcal{F}}}}_{p\mathbf{d}^{\mathcal{S}}}\underline{\boldsymbol{\mathcal{C}}} & & & \underline{\boldsymbol{\mathcal{F}}}_{p\mathrm{I}} & \underline{\boldsymbol{\mathcal{F}}}_{pp} & \underline{\boldsymbol{\mathcal{F}}}^{\mathcal{G}}_{p\mathrm{I}} \\ \underline{\boldsymbol{\mathcal{A}}}_{\mathrm{I}\mathbf{d}^{\mathcal{S}}}\underline{\boldsymbol{\mathcal{C}}} & & & \underline{\mathbf{0}} & \underline{\mathbf{0}} & \underline{\boldsymbol{\mathcal{A}}}_{\mathrm{II}} \end{bmatrix}^{n+1}_{i} \begin{bmatrix} \Delta\underline{\mathbf{d}}^{\mathcal{S},\mathcal{C}} \\ \Delta\underline{\mathbf{p}}^{\mathcal{S}} \\ \underline{\boldsymbol{\lambda}}^{\mathcal{S}} \\ \Delta\underline{\mathbf{u}}^{\mathcal{F}}_{\mathrm{I}} \\ \Delta\underline{\mathbf{p}}^{\mathcal{F}} \\ \Delta\underline{\mathbf{d}}^{\mathcal{G}}_{\mathrm{I}} \end{bmatrix}^{n+1}_{i+1}. \tag{3.196}$$

The implementation of the STC according to this system can easily be interpreted as a left and right preconditioning of the condensed system. Of course, the standard structure displacements have to be recovered from the scaled quantities in order to update the structure state within the Newton iteration. Equivalent to the discussion in section 3.6, this only requires the application of the STC matrix $\underline{\boldsymbol{\mathcal{C}}}$.

The left preconditioning operation leads to the scaled right hand side

$$\begin{aligned} &- \begin{bmatrix} \underline{\boldsymbol{\mathcal{C}}}^{\mathsf{T}}\widehat{\underline{\mathbf{r}}}^{\mathcal{S}}_{\mathbf{d}} \\ \underline{\mathbf{r}}^{\mathcal{S}}_{p} \\ \underline{\boldsymbol{\mathcal{B}}} \\ \underline{\mathbf{r}}^{\mathcal{F}}_{\mathrm{I}} \\ \underline{\mathbf{r}}^{\mathcal{F}}_{p} \\ \underline{\mathbf{0}} \end{bmatrix}^{n+1}_{i} - \begin{bmatrix} \underline{\boldsymbol{\mathcal{C}}}^{\mathsf{T}}\alpha_f\underline{\boldsymbol{\mathcal{M}}}^{\mathsf{T}}_{\mathbf{d}^{\mathcal{S}}\Gamma}\boldsymbol{\lambda} \\ \underline{\mathbf{0}} \\ \underline{\mathbf{0}} \\ \underline{\mathbf{0}} \\ \underline{\mathbf{0}} \\ \underline{\mathbf{0}} \end{bmatrix}^{n} - \\ &- \delta_{i0}\left(\Delta t \begin{bmatrix} 2(1-\alpha_f)\underline{\boldsymbol{\mathcal{C}}}^{\mathsf{T}}\underline{\boldsymbol{\mathcal{F}}}_{\mathbf{d}^{\mathcal{S}}\Gamma}\underline{\mathbf{u}}^{\mathcal{F}}_{\Gamma} \\ \underline{\mathbf{0}} \\ \underline{\mathbf{0}} \\ 2\underline{\boldsymbol{\mathcal{F}}}_{\mathrm{II}\Gamma}\,\underline{\mathbf{u}}^{\mathcal{F}}_{\Gamma} \\ 2\underline{\boldsymbol{\mathcal{F}}}^{\mathcal{G}}_{p\Gamma}\,\underline{\mathbf{u}}^{\mathcal{F}}_{\Gamma} \\ \underline{\mathbf{0}} \end{bmatrix}^{n} + \begin{bmatrix} (1-\alpha_f)\underline{\boldsymbol{\mathcal{C}}}^{\mathsf{T}}\underline{\boldsymbol{\mathcal{F}}}_{\mathbf{d}^{\mathcal{S}}\Gamma}\,\widetilde{\Delta\underline{\mathbf{d}}}^{\mathcal{G}}_{\Gamma} \\ \underline{\mathbf{0}} \\ \underline{\mathbf{0}} \\ \underline{\boldsymbol{\mathcal{F}}}_{\mathrm{II}\Gamma}\,\widetilde{\Delta\underline{\mathbf{d}}}^{\mathcal{G}}_{\Gamma} \\ \underline{\boldsymbol{\mathcal{F}}}^{\mathcal{G}}_{p\Gamma}\,\widetilde{\Delta\underline{\mathbf{d}}}^{\mathcal{G}}_{\Gamma} \\ \underline{\boldsymbol{\mathcal{A}}}_{\mathrm{II}\Gamma}\,\widetilde{\Delta\underline{\mathbf{d}}}^{\mathcal{G}}_{\Gamma} \end{bmatrix}^{n} \right), \end{aligned} \tag{3.197}$$

where a modified block $\widehat{\underline{\mathbf{r}}}^{\mathcal{S}}_{\mathbf{d}}$ has been introduced as

$$\widehat{\underline{\mathbf{r}}}^{\mathcal{S}}_{\mathbf{d}} = \begin{bmatrix} \underline{\mathbf{r}}^{\mathcal{S}}_{\mathrm{I}} + \alpha_f\underline{\mathbf{r}}^{\mathcal{S},\kappa}_{\mathrm{I}} \\ \underline{\mathbf{r}}^{\mathcal{S}}_{\Gamma} + \alpha_f\underline{\mathbf{r}}^{\mathcal{S},\kappa}_{\Gamma} + (1-\alpha_f)\underline{\boldsymbol{\mathcal{P}}}^{\mathsf{T}}\underline{\mathbf{r}}^{\mathcal{F}}_{\Gamma} \end{bmatrix}. \tag{3.198}$$

Remark 3.8 (structure split) *It is also possible to chose the structure as the slave side of the interface, which results in a three field FSI matrix* (3.184) *with interchanged mortar matrices* $\underline{\mathfrak{M}}$ *and* $\underline{\mathfrak{D}}$*. The approach is called structure split and beside the Lagrange multiplier the structure displacements at the interface are eliminated from the system. The reader is referred to the previous publication [121] for details.*

It is important to note that the block structure of the final condensed system coincides with the standard FSI system derived by Küttler [123]. The STC preconditioning does not change this matrix block structure. Therefore, the preconditioners proposed by Gee et al. [77] can also be used for the STC modified monolithic FSI system in a straightforward manner.

For all FSI simulations in this thesis, a block Gauss-Seidel algorithm as discussed in [121] is used. The algorithm has been proposed for the conforming case in the thesis of Küttler [123] and in the publication by Gee et al. [77]. The algorithm, which is referred to as BGS(AMG) in [77], does not invert the blocks, but uses the preconditioners chosen for the single fields to approximates the inverse of the blocks.

Chapter 4
Shape of the red blood cell

This chapter addresses the shape of an undeformed human erythrocyte at rest. In this work, simulations do not start with a biconcave and stress-free shape, which is based on experimental measurements, as it was done by most numerical studies in literature. Instead, the initial cell shapes used in the following chapters are results of a computational procedure, which allows for starting with different ellipsoidal shapes. The stress-state emerging during the transition from an ellipsoid to a biconcave disk can be considered as residual stresses of the membrane.

The chapter begins with a section on experimentally determined RBC shapes, which are important for validation. In section 4.2, a mechanical interpretation of the biconcave shape and some numerical implementations are briefly discussed. Subsequently, the form-finding process used in this thesis is stated and resulting shapes are presented. The last section 4.4 discusses the open question of the stress-free state of the erythrocyte membrane and shows how the present approach can help to answer this question.

4.1 Measurements of the shape for a red cell at rest

Pioneering quantitative measurements of the unloaded shape of the human erythrocyte have been performed by Canham [34] and Evans and Fung [53]. The latter study provided a closed formula to describe the thickness D of the cell with respect of the radius r. For the expression

$$D(r) = \sqrt{1 - \left(\frac{r}{R_0}\right)^2} \left(C_0 + C_2 \left(\frac{r}{R_0}\right)^2 + C_4 \left(\frac{r}{R_0}\right)^4 \right). \tag{4.1}$$

an optimal parameter set was determined:

$$R_0 = 3.91\ \mu\text{m}, \quad C_0 = 0.1035805, \quad C_2 = 1.001279, \quad C_4 = -0.561381. \tag{4.2}$$

Formula (4.1) has been used to generate the initial (and stress-free) geometry in almost all numerical studies on human erythrocytes. In contrast, it is widely accepted that, *in vivo*, the shape of the cell at rest is not stress-free. Consequently, most numerical studies share a common shortcoming in neglecting the residual stress state of the unloaded erythrocyte membrane. However, a thorough study on the effect of this modeling assumption is still missing.

4.2 Mechanical interpretation of the biconcave shape

The biconcave shape of the erythrocyte represents the state of minimal mechanical energy stored in the lipid bilayer/membrane skeleton composite for given surface area and given cell volume. Summarizing the pioneering work of Helfrich [100], Helfrich and Deuling [101], and Svetina and Zeks [180], an expression for the energy stored in the membrane has been proposed by Khairy et al. [118] as

$$E = \frac{\kappa_B}{2} \oint_{\text{Surf}} (2H - C_0)^2 \, dA + \frac{\kappa_A \pi}{2AD^2} (\Delta A - \Delta A_0)^2 + E_{\text{nw}}. \tag{4.3}$$

The first term corresponds to the bending energy that is associated with the mean curvature H. The necessary scalar parameters are the bending elastic modulus κ_B and the preferred or spontaneous curvature C_0. The second term, which also represents a type of bending energy, originates from the lipid bilayer morphology and accounts for the resistance of this layer against area differences ΔA between outer and inner leaflet. The energy associated with this resistance is determined by the area-difference elastic modulus κ_A and, geometrically, by the total area A, the separation D, and the initial difference ΔA_0. This contribution explains the relatively high bending resistance of the erythrocyte membrane despite its thinness. Finally, the energy E_{nw} represents the contribution of the cytoskeleton network and can, thus, be identified with an energy resulting from shear deformations.

As already mentioned, the minimization of energy expression (4.3) is subjected to surface and volume constraints put on the membrane. Thus, the solution of the minimization problem is, in general, not accessible by analytical methods, but requires numerical approaches.

The FEM for the membrane has been derived in section 3.4 by means of the weak form of the governing equations. Alternatively, it can be deduced from the optimization process of an energy functional, as briefly discussed in Remark 3.2. The equivalence between the FEM and an optimization process was used by Feng and Klug [62], who discretized an initially spherical cell with shell elements, which exclusively accounted for bending stiffness, and obtained a biconcave cell by adjusting the cell volume-to-surface ratio. Due to the spherical reference shape and the simplistic membrane model, poor convergence behavior of the numerical method and the occurrence of spurious stresses in the membrane were observed. Moreover, the model could only be used for shape optimization, but the response of the cell to external loading could not be investigated.

An alternative to the FEM was proposed by Li et al. [128]. In that work, a coarse grained molecular dynamics simulation started from the analytically given shape (4.1) and the cytoskeleton was allowed to deviate from this shape. The relaxed shapes were characterized by a less pronounced dimple and lower curvatures. However, the results of the form-finding process stayed unused in the simulations of laser trap experiments, which started again with the stress-free biconcave shape determined by (4.1).

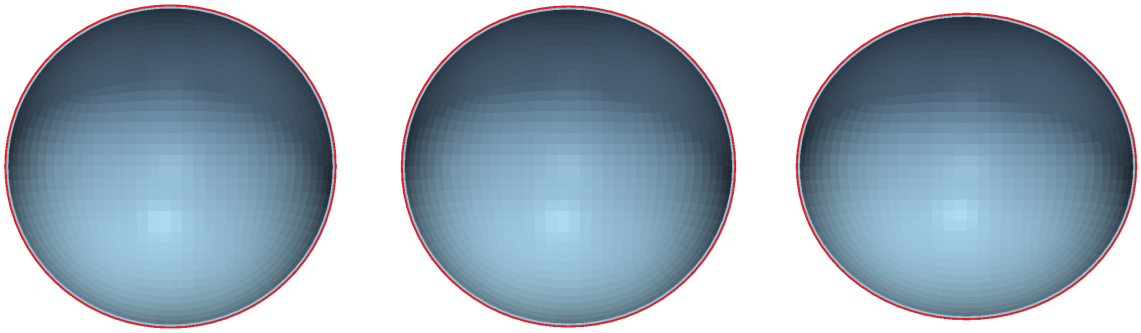

(a) configuration RBC975 *(b) configuration* RBC960 *(c) configuration* RBC900

Figure 4.1: *Initial states for the form-finding process*

4.3 Form finding process and resulting shapes

In the previous chapters a comprehensive FE based model for the human erythrocyte has been derived. It accounts realistically for the bending elasticity of the bilayer and the shear elasticity of the cytoskeleton. Therefore, it is reasonable to use this novel model in order to find the biconcave shape of an erythrocyte at rest. The idea is to start with a problem independent initial state, such as a flat disc, an oblate ellipsoid, or an almost spherical state. The experimental results (4.1) and (4.2) serve as validation of the form-finding process.

A perfectly spherical reference shape would contradict the shape memory of erythrocytes observed in the experiments by Fischer [65]. Since the dimple of the cell is always formed by the same parts of the cell membrane, also the stress-free state has to provide one distinguished direction. Even in terms of the form-finding process, a spherical initial state is unsuitable, as indicated by the numerical problems found by Feng and Klug [62]. Moreover, Li et al. [128] pointed out that in case of a spherical stress-free state, the biconcave shape has to be stabilized against a cup-shape by an unphysiologically high bending modulus of the membrane. Both, shape memory and stability of the erythrocyte, will be discussed in more detail in section 6.3.

The discussion in the literature seems to converge towards an almost spherical stress-free shape, but the particular form is still an open question. Therefore, the form-finding process presented in this thesis does not start with the relatively oblate ellipsoid used in the earlier contribution [119], which employed an initial diameter ratio 0.6:1.0:1.0. Instead, three different initial states for the form-finding process are considered. All three are still oblate ellipsoids and have the same surface area of about $135\,\mu m^2$, which corresponds to expression (4.1). The first membrane configuration, referred to as RBC975, is almost spherical (diameter ratio 0.975:1.0:1.0) and is depicted in Figure 4.1(a). The slightly more oblate second configuration RBC960 with a diameter ratio of 0.96:1.0:1.0 is drawn in Figure 4.1(b). Finally, the most oblate configuration RBC900 (0.9:1.0:1.0) is depicted in Figure 4.1(c).

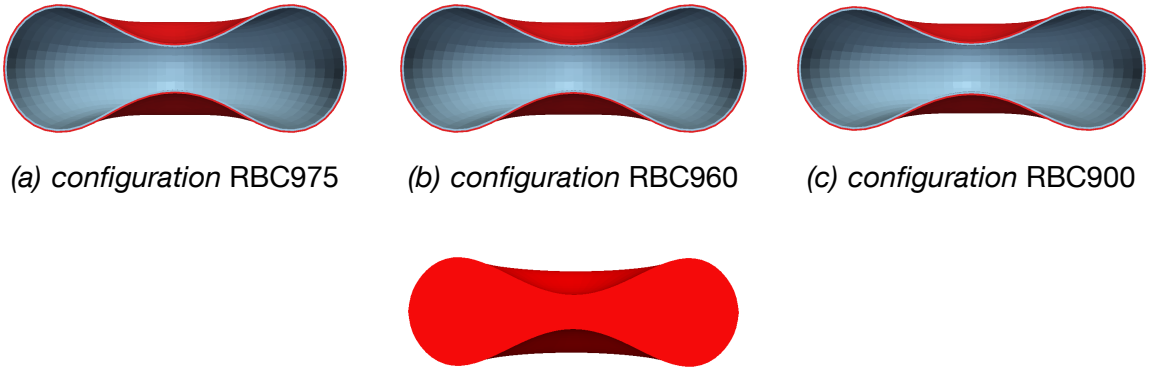

(a) configuration RBC975 *(b) configuration* RBC960 *(c) configuration* RBC900

(d) reference shape taken from Evans and Fung [53], cf. (4.1)

Figure 4.2: *Final states of the form-finding process*

Since Figure 4.1 shows only half of the membranes, the two-layer set-up of the membrane FE model becomes visible, where the bilayer is colored in red, the cytoskeleton in turquoise.

In order to obtain a biconcave cell, the volume enclosed by the membrane is reduced to about 100 μm^3, i.e. to a physiological volume to area ratio. This shrinking simulation is controlled by surface and volume constraints that have been introduced in section 2.5. The resulting shapes are shown in Figure 4.2. All computed shapes agree very well with each other and, more importantly, with the experimentally determined shape, which is given for comparison in Figure 4.2(d). Small deviations arise for example around the dimple of the cell, which is more pronounced for the analytically generated shape. This observation is consistent with the numerical results reported by Li et al. [128].

The particular discretization of the ellipsoidal initial shapes and, thus, of the resulting biconcave shapes is chosen depending on the experimental set-up considered. The employed meshes will be discussed at the beginning of the respective chapters. Numerical results showed that the different discretizations did not have a significant influence on the obtained biconcave shape. The shapes shown here in Figure 4.1 and Figure 4.2 are obtained with a relatively coarse discretization used to model the behavior of erythrocyte in fluid flow, cf. chapter 6.

During the form-finding process, the fluid volume enclosed by the membrane is controlled by a volume constraint. On the other hand, dynamical simulations necessitate to take the influence of the incompressible fluid field into account. Numerically, the solution of this conflict is found in the separation of the form-finding process from the simulation of the respective experiment. In this first phase, the enclosed volume is reduced and only the fluid grid motion is considered. The fluid equations, which describe an incompressible flow, are not solved for.

4.4 Undeformed vs. stress-free state

Having completed the calculation of a biconcave shape, there exists two alternative ways to proceed the simulation. The first possibility takes the biconcave shape cell as new initial configuration, i.e. the displacements of structure and fluid field are added to the old initial configuration in order to obtain a new one. This approach results in a stress-free biconcave cell shape and is, thus, very similar to the available numerical approaches proposed in the literature, which start from an initial shape defined by the analytical expression (4.1). If the cytosol contribution is considered for the following simulation, the algebraic volume constraint put on the membrane is no longer necessary, since the incompressibility is ensured by the fluid formulation. Due to the similarity of the deformed shapes obtained from the ellipsoidal configurations, cf. Figure 4.2, it is sufficient to consider one these biconcave shapes as stress-free initial state. For the remainder of this thesis, the shape depicted in Figure 4.2(a) is employed. The corresponding erythrocyte model is referred to as RBC975SF.

Alternatively, it is also possible to restart the simulation after the form-finding process has been completed. This approach implies that the reference state of the membrane model is unchanged. The stresses resulting from the transition from an ellipsoidal to a biconcave shape are, thus, accounted for the rest of the simulation. Technically, for the restart, the initial fluid velocity in the whole domain is assumed to vanish, i.e. $\mathbf{u}^{\mathcal{F}} \equiv \mathbf{0}$. It is important to note that the incompressibility of the fluid is expressed in terms of the fluid velocity, cf. the continuity equations (2.61). Since the zero restart velocity field of course is divergence-free, the change from an ellipsoidal to a biconcave state, if completed, does not interfere with the fluid governing equations. For the further course of the simulation, the algebraic volume constraint on the structure can be omitted. The value of the corresponding Lagrange multiplier values is recovered by the fluid hydrostatic pressure p at the beginning of the restart.

The advantages of the presented approach is, hence, twofold: First, shapes for the human RBC at rest are obtained, which adopt a realistic shear-to-bending ratio of the cell membrane and are comparable with experimentally determined shapes. Second, the approach allows to investigate the influence of the residual stresses present in the membrane of the cell at rest on the outcome of the simulations. It may be possible to draw conclusions from these results regarding the open question of the stress-free state of a human erythrocyte. At least, it is possible to predict the sensitivity of an experiment with respect to the residual stresses in the membrane. Such investigations are beyond the scope of any other numerical method found in literature, since none of them considers a stress-free state other than the biconcave disk.

Chapter 5

Simulations of healthy erythrocytes in laser traps

In the previous chapters, a FE model for the human erythrocyte has been derived. As already mentioned before, it is an extension of the erythrocyte model presented by the author in [119] with regard to the employed FSI approach. A detailed validation of the model based on static and dynamic laser trap experiments is already given in that contribution for different stress-free initial shapes. Thus, the validation of the RBC model based on results from laser trap experiments is kept relatively short in this chapter. Important results from the parameter studies presented in [119] are reviewed and discussed.

The first section addresses simulations of static laser trap experiments as performed by Mills et al. [142]. Those are of particular importance, since they have been used for the validation of many numerical erythrocyte models in literature. Thus, the elastic behavior of the present FE model is also validated with those experimental results. Furthermore, the results are checked against other numerical studies. The comparison demonstrates the importance of correct modeling assumptions and realistic boundary conditions. Section 5.2 discusses the problems of deducing realistic dynamic material parameters from the recovery behavior recorded for cells escaping the laser trap.

For validation of the dynamic response of the cell, thus, the dynamic experiments performed by Yoon et al. [201] are considered, which are characterized by fast moving laser traps. Simulation results and their sensitivity to certain material parameters are discussed in section 5.3. Finally, the chapter is completed by a general discussion on the simulation of laser trap experiments and the uncertainties with respect to realistic boundary conditions.

5.1 Quasi-static experiments

The numerical simulation of static laser trap experiments follows the procedure described by Mills et al. [142]. Experimentally, two silica beads were attached to diametrically opposite ends of the cell. One bead was trapped by the laser, whereas the other

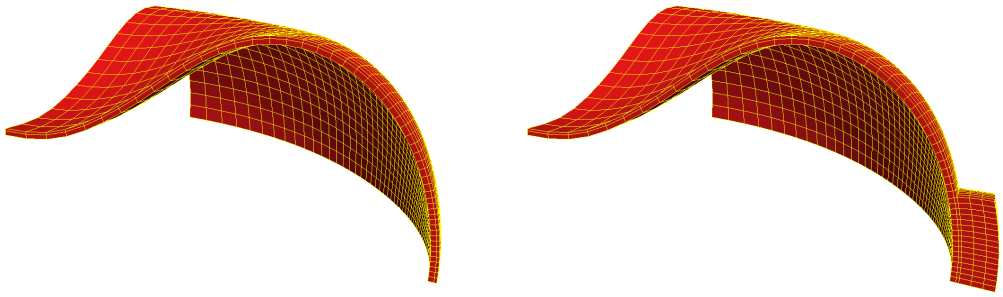

(a) erythrocyte membrane

(b) erythrocyte membrane with additional elastic block

Figure 5.1: *Finite element mesh for static laser trap experiments*

was adhered to a slowly moving glass slide. As result, the trap force could be related to the elongation of the cell just before the cell escaped the trap.

5.1.1 Finite element discretization and boundary conditions

For the sake efficiency, the symmetry of the quasi-static loading is used, such that only an eighth of the cell is to be considered in the numerical simulation. Furthermore, the contribution of the fluid fields reduces to the incompressibility of the cytosol, which can equivalently be realized by an algebraic constraint put on the membrane. Thus, accounting for FSI is not necessary in this example.

The FE mesh for the not necessarily stress-free biconcave cell membrane can be seen in Figure 5.1(a), where each membrane layer is discretized with the 1104 hexahedral elements. The lipid bilayer is modeled with a thickness $t^{\text{bil}} = 20\,\text{nm}$, resulting in thin element geometries everywhere in this layer. The cytoskeleton thickness is assumed twice as thick, i.e. $t^{\text{nw}} = 40\,\text{nm}$. In total, the structure model contains 4676 nodes and leads to a system with 17,535 DOFs.

Subjected to high stretching forces, the trap rigidity leads to high bending deformations of the elements around the contact surface and eventually to a failure of the numerical simulation. A remedy is provided by an additional elastic block appended to the contact surface and application of the algebraic constraint to the outermost surface of this block.

The motivation for this block is not entirely numerical. From a modeling point of view, it accounts for a local separation of the cell from the bead for high stresses. The additional block is discretized with 720 elements and increases the number of DOFs to 19,956. The complete mesh is depicted in Figure 5.1(b), where again the biconcave cell shape is shown. In this section, all results are obtained with this elastic loading condition if not explicitly stated otherwise.

5.1.2 Sensitivity with respect to residual stresses

The form-finding process described in the previous chapter is dominated by the bending behavior of the cell. Consequently, the bending stresses are predominant in the stress state of the cell at rest in the configurations RBC975, RBC960, and RBC900. By contrast, the response of the cell to static laser trap experiments, in particular for large tensile forces, is governed by the shear elasticity of the cytoskeleton. The residual stresses are, therefore, expected to play only a minor role for the simulations considered in this chapter. This assumption is supported by the numerical results presented in the earlier publication [119], in which the quasi-static response of the cell was found to be insensitive with respect to residual stresses.

Although the stress-free shapes of the configurations RBC975, RBC960, and RBC900 are closer to a sphere than the one of the model considered in [119], the observation presented there are still valid for the present cell models. For pres-stressed and stress-free biconcave cells, the courses of the axial and transverse diameter are found to be almost indistinguishable. Thus, the numerical simulations for the static laser trap experiments presented in the following subsections always start with a stress-free biconcave cell shape.

5.1.3 Validation with experimental results

Application of forces up to 200 pN leads to a severely deformed cells, which are stretched by more than 100%. Exemplarily, Figure 5.2 shows the deformation for four different stretching forces. Due to the loading, the dimple of the cell vanishes completely and the cell adopts a convex shape. Moreover, Figure 5.2 clearly demonstrates the effect of the elastic block. On the one hand, this loading condition prevents too sharp gradients at the contact surface, but, on the other hand, the rigidity of the trap is still accounted for.

With a shear modulus $G_{\text{eff}}^{\text{mem}} = 4.4\,\text{pN}/\mu\text{m}$, which is defined according to (2.123), and a third order parameter of the Yeoh material with $c_3 t^{\text{nw}} = 0.72\,\text{pN}/\mu\text{m}$, the numerically computed course of axial and transverse diameters with increasing stretching force is shown in Figure 5.3. This graph shows an excellent agreement of the simulation with the experimental reference of Mills et al. [142].

This close match between simulation and experiments demonstrates the ability of the model to accurately predict the response of the cell to stretching forces. Furthermore, the effective linear shear modulus agrees reasonably well with literature, where a range of $4\,\text{pN}/\mu\text{m}$ to $9\,\text{pN}/\mu\text{m}$ is reported for this parameter.

A thoroughly validation of the model, however, additionally requires to compare the results and, particularly, the deduced material parameters with other numerical studies as shown in the following subsection.

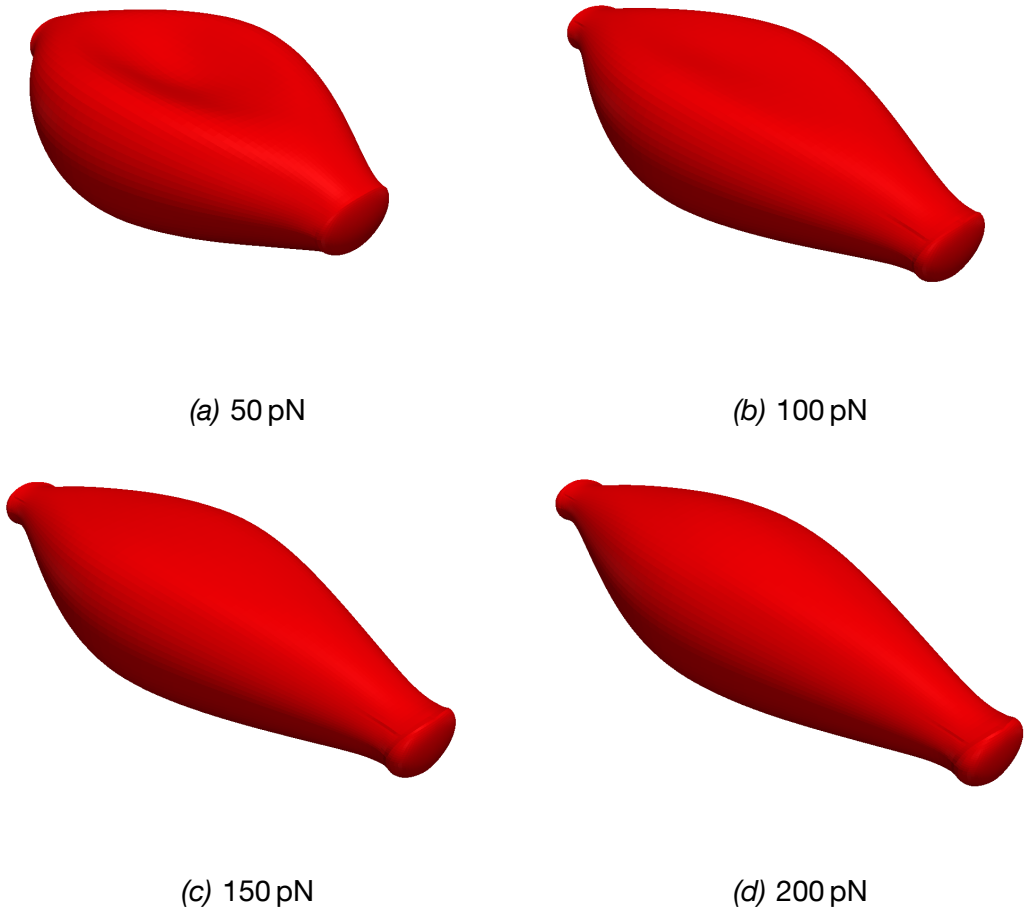

(a) 50 pN *(b)* 100 pN

(c) 150 pN *(d)* 200 pN

Figure 5.2: *Deformed geometries obtained with an elastic block boundary condition*

5.1.4 Validation with available numerical studies in literature

Despite the fact that the numerical study presented by Li et al. [128] was based on a coarse grained molecular dynamics approach, the model assumptions of that study coincide with the quasi-static properties accounted for in the present model, i.e. shear elasticity, area conservation, and bending rigidity of the membrane were considered. However, Li et al. [128] deduced a significantly larger material parameter $G_{\text{eff}}^{\text{mem}} = 8.3\,\text{pN}/\mu\text{m}$.

The reason for this discrepancy can easily be identified by comparison of the boundary conditions applied. The numerical approach employed in [128] was not able to realistically account for the rigidity of the laser trap. Instead, a time dependent stretching force was directly applied to 5% of the nodes. In terms of the present model, this is equivalent to a Neumann-type boundary load acting on the contact surface or an extremely low shear modulus of the elastic block. As a result, a loaded erythrocyte adopts a different shape with very pointed tips as shown in Figure 5.4, which is in good agreement with the results shown in [128].

Quantitatively, such an altered boundary condition leads to a softer response of the

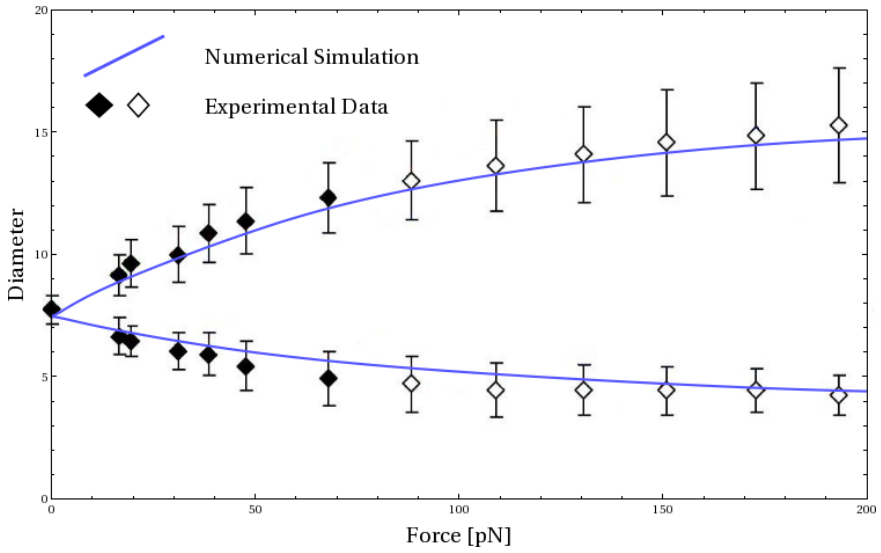

Figure 5.3: *Comparison of numerical results for axial (top) and transverse (bottom) diameter over force with experiments from [142]*

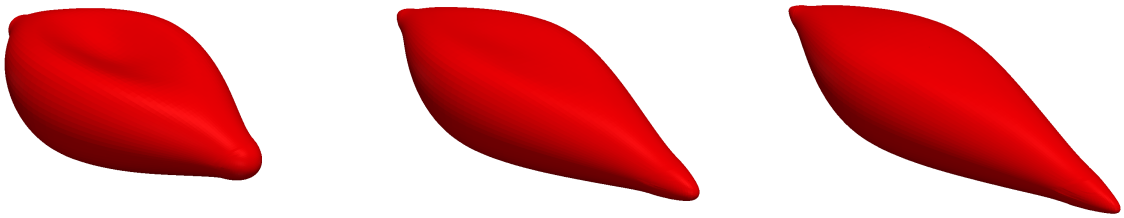

(a) trap force 50 pN *(b) trap force* 100 pN *(c) trap force* 150 pN

Figure 5.4: *Deformed geometries for a model neglecting the rigidity of the laser trap*

cell, which has to be balanced for by a significantly higher shear stiffness in order to obtain acceptable diameter over force diagrams, in particular for the axial diameter. For the present model, $G_{\text{eff}}^{\text{mem}}$ has to be increased to about 7.6 pN/µm, a choice in good agreement with [128]. It is important to note that the transverse diameter is hardly affected by the chance of boundary conditions. Therefore, the increased shear modulus leads to a course of transverse diameter that lies well above the experimentally determined range. Such a behavior can also be found in the simulation results presented in [128].

Besides experimental data, the contribution of Mills et al. [142] contained a FE study that focused on the properties of cytoskeleton network. The model was based on a single-layer membrane discretization, utilized a Yeoh material, and assumed a rigid contact surface. However, the deduced shear parameter $G_{\text{eff}}^{\text{mem}} = 7.3\,\text{pN}/\mu\text{m}$ for the membrane is closer to the results of Li et al. [128] than to the respective value deduced

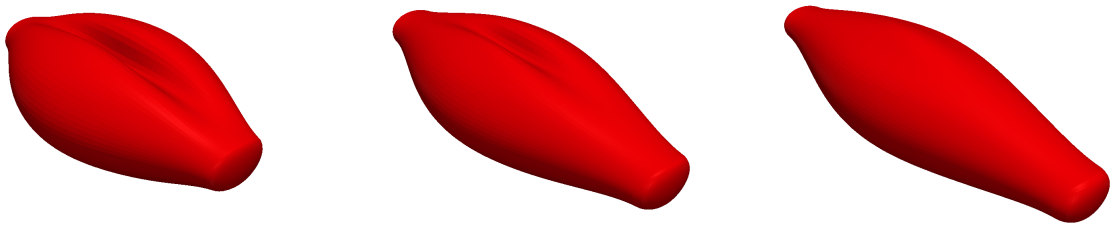

(a) trap force 50 pN *(b) trap force* 100 pN *(c) trap force* 150 pN

Figure 5.5: *Deformed geometries for a model, which accounts for the cytoskeleton and the area conservation.*

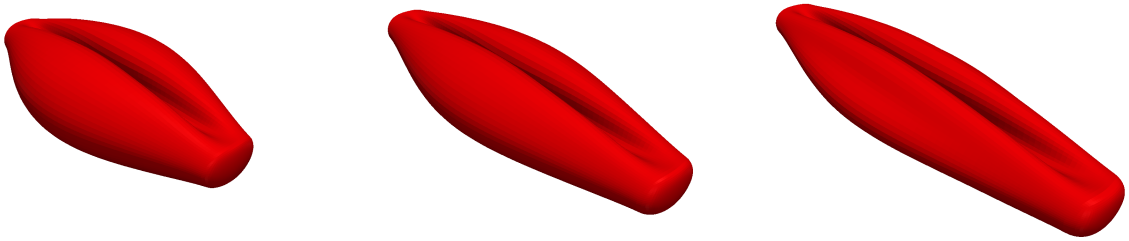

(a) trap force 50 pN *(b) trap force* 100 pN *(c) trap force* 150 pN

Figure 5.6: *Deformed geometries for a model accounting for the cytoskeleton alone.*

in the previous subsection.

Although the constitutive law and the boundary conditions coincide with the present model, area conservation was not accounted for in [142]. Dao et al. [44] analytically estimated a decrease in the shear modulus $G_{\text{eff}}^{\text{mem}}$ by 25% in case of such an algebraic constraint. Numerically, the effect of the neglected area preservation is tested here with a modified FE model that only accounts for the properties of the cytoskeleton. If the lipid bilayer behavior would be accounted for, the isolated effect of the area constraint could not be considered. Its removal has wide implication on the overall behavior of the lipid layer, particularly on its bending resistance.

The results of a modified model that accounts for the cytoskeleton contribution and the area conservation are presented in Figure 5.5. Comparing these resulting shapes with the ones shown in Figure 5.2 clearly indicates the lack of bending resistance of the membrane at least for trapping forces up to 100 pN. More importantly, Figure 5.6 shows that the absence of the area preservation leads to a qualitatively different response of the modified cell model. Instead of forming a convex shape for high tensile forces, the resulting cell shapes are characterized by a deep folding, which can also be found in [142]. The quantitative response of the cell is found to be much softer. In order to balance the effect of neglected area conservation, an increased shear modulus of $G_{\text{eff}}^{\text{mem}} \approx 8\,\text{pN}/\mu\text{m}$ is found to be necessary.

These discussions conclusively show the importance of correct modeling assumptions

and realistic boundary conditions when deducing material parameters from laser trap experiments. Furthermore, they demonstrate the validity of the present model. It is not only able to predict the experimental data presented in [142], but can also recover the results of other numerical studies if the modelling assumptions and conditions are adapted to match the set-up that is (although sometimes unphysiological) utilized in those studies.

The sensitivity of the results with respect to boundary conditions indicates one drawback of the experimental set-up, which does not allow for an exact measurement of the contact area.

5.2 Creeping behavior of escaping cells

In the previous section, material parameters for the membrane have been derived based on static laser trap experiments. Consequently, the derivation is restricted to shear and bending stiffness moduli of the membrane. However, quasi-static laser trap experiments were also used to investigate dynamic properties of the cell by recording the recovery behavior of the cell escaping from the cells. The progression of the axial diameter or, in order to be consistent with an earlier experimental study by Hochmuth et al. [105], of the principal stretch was fitted to an exponential decay with a characteristic recovery time t_c. The values estimated by Henon et al. [102] ($t_c = 206\,\text{ms}$) and Mills et al. [142] ($t_c = 190\,\text{ms}$) represent average values computed based on the creeping of many cells.

Naturally, the individual cell escapes started from different deformed membrane states. Simulations of the recovering behavior of erythrocytes with different stressed states were performed in the previous study by Klöppel and Wall [119]. It could be concluded that the value t_c characterizes the initial condition of the recovery phase rather than the properties of the cell. For an equal set of material parameters but different stressed configurations, the deduced relaxation time t_c varied by more than 30%. Furthermore, its sensitivity regarding fluid and membrane viscosity changed as well. For small deformations, the fluid viscosity has a bigger influence on the results as for larger deformations, cf. the more detailed parameter study given in [119].

Within this thesis, the recovery behavior of the cell is, thus, not used for validation of the model. Instead, the response of the cell to dynamic deformations induced by fast moving laser traps is considered in the following section.

5.3 Fast moving laser traps

Based on the discussion of the previous section, dynamic experiments have to be considered in order to determine dynamic cell parameters associated with the viscosity of the membrane and the cytosol. In the laser trap experiments by Yoon et al. [201], both beads were controlled with the laser beam. One trap was held fixed, while the translation of the other one followed a triangle wave pattern. In all experiments, the magnitude of the pattern was $3.5\,\mu\text{m}$, but the frequency was varied. The experiments showed an

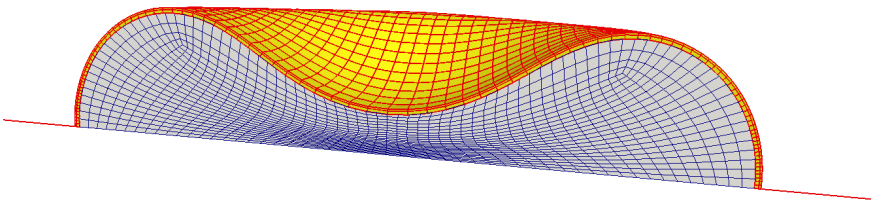

Figure 5.7: *Finite element mesh for dynamic laser trap experiments*

elasticity of the trap itself, which was described as a harmonic spring. This elasticity does not change the contact between the cell and the bead, but is characterized by a difference between bead position and the focus of the laser beam.

There are no direct measurements of the membrane viscosity available. Based on tank-treading experiments Tran-Son-Tay et al. [186] estimated $\mu_{\text{eff}}^{\text{bil}} = 0.1\,\text{pN}\,\text{s}/\mu\text{m}$. Evaluation of micropipette aspiration, on the other hand, suggested a value between $0.6\,\text{pN}\,\text{s}/\mu\text{m}$ and $1.2\,\text{pN}\,\text{s}/\mu\text{m}$ as reported by Hochmuth [104]. The viscosity of the hemoglobin solutions was determined by McClain et al. [141], who proposed a value for the cytosol of the RBCs of $\mu_{\text{cyt}}^{\mathcal{F}} = 46 \pm 6\,\text{mPa}\,\text{s}$. However, earlier measurements estimated the value of $\mu_{\text{cyt}}^{\mathcal{F}}$ to range between $10\,\text{mPa}\,\text{s}$ and $18\,\text{mPa}\,\text{s}$. The latter range is still widely used in the literature.

5.3.1 Discretization, boundary conditions and material parameters

In terms of the numerical model, the boundary conditions at the contact surfaces have to be slightly adapted. Since the maximum displacement of the bead is relatively small, an elastic block is not necessary and the multi-point constraint is directly applied on the contact surface. A harmonic spring, the end of which is controlled by a Dirichlet boundary condition to follow the triangle wave pattern, is attached to the contact surface. Furthermore, the contribution of the cytosol can no longer be reduced to the incompressibility. Consequently, the proposed monolithic FSI approach is used for the dynamic simulations and the coupling between the fields relies on the dual mortar method as introduced in section 3.7.

For the sake of efficiency, a quarter of the cell is discretized and symmetry boundary conditions are applied. The thicknesses of the membrane layers and their discretization are chosen as for the quasi-static simulations. Consequently, the membrane mesh contains 4416 hexahedral elements and 6939 nodes. The cytosol domain is discretized independently, i.e. membrane and fluid mesh do not match at the interface. The employed fluid mesh consists of $30,400$ elements and $32,967$ nodes. Additionally, two truss elements implementing harmonic springs have to be added accounting for the elasticity of the trap. The final discretization, which is shown in Figure 5.7 for the biconcave cell, results in $256,218$ DOFs.

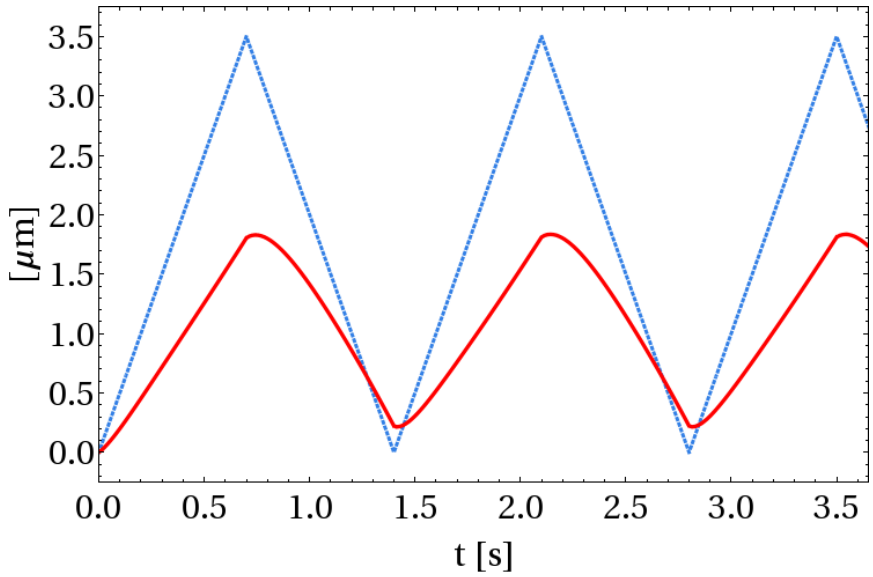

Figure 5.8: *Distance change d_{laser} between the laser beams (blue, dashed curve) and elongation ΔL of the cell (red, solid curve) over time for a trap speed of* 5 μm/s

Besides material parameters determined from quasi-static simulations, the viscosities of the cytosol and the lipid bilayer membrane are to be chosen for the dynamic simulations. The results presented in this thesis are obtained with a cytosol viscosity $\mu^{\mathcal{F}}_{\text{cyt}}$ of 15 mPa s. The visoelastic behavior of the membrane is determined by the already known elastic material parameters, the dimensionless parameter β, and the relaxation time τ, which have been introduced in section 2.4.5. The effective membrane viscosity $\mu^{\text{bil}}_{\text{eff}}$ is defined as their product according to (2.125). For the present simulation, it is assumed to be $\mu^{\text{bil}}_{\text{eff}} = 1.2\,\text{pN s}/\mu\text{m}$, where material parameters β =100 and $\tau = 30$ ms are used. Due to symmetry, the stiffness of the springs is given by a quarter of the reported laser trap elastic modulus of $\kappa_{\text{trap}} = 44\,\text{pN}/\mu\text{m}$, cf. [201].

After the cell is transformed into its biconcave shape, the course of the simulation is controlled by Dirichlet boundary conditions put on both end points of the trusses. The distance change d_{laser} between these points corresponds to the distance change between the two laser beams and is to follow a triangle wave pattern with a maximal displacement of 3.5 μm. The pattern is exemplarily shown in Figure 5.8 for a trap speed of 5 μm/s.

Although the trapping forces generated in the dynamic experiments are considerably smaller than the loads used in section 5.1, the residual (bending) stresses in the membrane are still found to have a very small effect on the dynamic response of the cell. Consequently, the biconcave cell can be assumed stress-free for the simulations in this section. Moreover, inertia effects are found to be negligible.

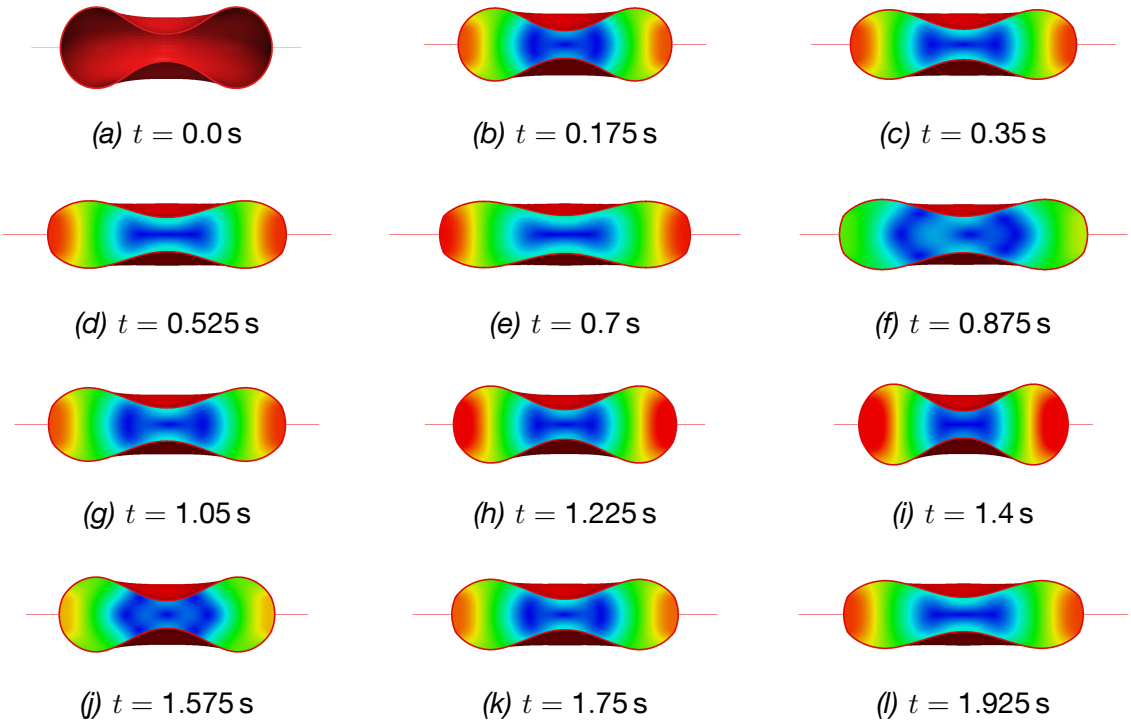

(a) $t = 0.0\,\mathrm{s}$ *(b)* $t = 0.175\,\mathrm{s}$ *(c)* $t = 0.35\,\mathrm{s}$

(d) $t = 0.525\,\mathrm{s}$ *(e)* $t = 0.7\,\mathrm{s}$ *(f)* $t = 0.875\,\mathrm{s}$

(g) $t = 1.05\,\mathrm{s}$ *(h)* $t = 1.225\,\mathrm{s}$ *(i)* $t = 1.4\,\mathrm{s}$

(j) $t = 1.575\,\mathrm{s}$ *(k)* $t = 1.75\,\mathrm{s}$ *(l)* $t = 1.925\,\mathrm{s}$

Figure 5.9: *Flow fields inside the deformed erythrocyte for a trap speed of* $5\,\mu\mathrm{m/s}$*. Fluid field is color-coded by velocity magnitude*

5.3.2 Hysteresis curves

Applying the prescribed motion d_{laser} as Dirichlet boundary condition for the trap results in significant deformation of the cell, as can be seen in Figure 5.9. In this figure, which shows the deformed states of the cell at different points in time during the second cycle of the loading, the cytosol domain is color-coded by the fluid velocity.

The graph in Figure 5.8 does not only show the described distance d_{laser} between the laser beams, but also the elongation ΔL of the RBC. This quantity roughly follows the triangle wave. Naturally, due to viscous fluid flow and viscoelastic membrane behavior, energy is dissipated from the system during the simulation. Thus, a slight phase shift between the curves can be seen and the cell elongation does not recover the triangle pattern exactly. The difference can easily be related to Δx, which denotes the elongation or compression of the springs:

$$\Delta x = \frac{d_{\text{laser}} - \Delta L}{2}. \tag{5.1}$$

Thus, the data provided by Figure 5.8 allows to compute the current trapping force as $F = \kappa_{\text{trap}} \Delta x$.

This force is used to generate hysteresis curves showing the course of trapping force F over the elongation ΔL of the cell. In Figure 5.10 the simulated hysteresis behavior for a trap speed of $5\,\mu\mathrm{m/s}$ is graphically compared with experimental results of Yoon et al.

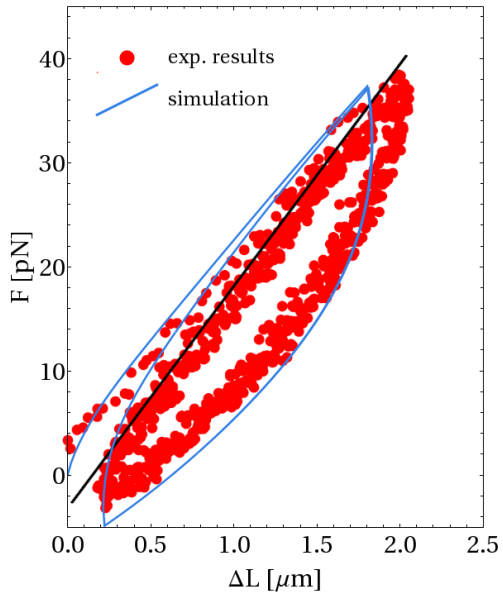

Figure 5.10: *Numerically determined hysteresis curve compared with experimental results taken from [201].*

[201]. The numerical model is able to accurately recover the experimental measurements. The form of the curve as well as the predicted ranges for force and displacement values demonstrate a good agreement between experiment and simulation.

The hysteresis recordings provide a measure of the dissipated energy E_{diss}, which can be identified by the area enclosed by the curve. Yoon et al. [201] normalized this energy by the square of the strain amplitude γ^2_{max}. The corresponding values calculated from Figure 5.10 are found to be $E_{\text{diss}} = 22.9\,10^{-18}$J and $E_{\text{diss}}/\gamma^2_{\text{max}} = 404.4\,10^{-18}$J and are, thus, higher than the experimentally determined average values.

Beside the hysteresis behavior, Figure 5.10 allows to define an apparent linear stiffness κ_{lin} by a linear fit during extension of the cell. Graphically, it represents the gradient of the black line shown in Figure 5.10, which was fitted for the experimental data. The graph demonstrates, that numerical and experimental results for the apparent stiffness agree very well.

5.3.3 Dependence on trap speed

One major focus of the study by Yoon et al. [201] was put on the strain rate dependence of the energy dissipation and apparent cell stiffness. For that purpose, the results for four different trap speeds between 0.2 μm/s and 20 μm/s were considered. Both, the energy dissipation and apparent linear stiffness, were reported to follow power law functions with respect to the strain rate.

The experiments demonstrate that the apparent stiffness κ_{lin}, as defined in the previous subsection, is not an intrinsic property of the cell, but increases with increasing strain

rate. Such a behavior can, of course, be expected for a viscoelastic object. For the considered range of strain rates, measurements found an increase by a factor of 3. The best power law fit was obtained with an exponent of 0.25. The numerical simulations recover these measurements very well. Fitting a power law as a function of shear rate, an exponent of about 0.3 is obtained, which also shows the close match between simulation and experiment at least for the elongation phases.

Experimentally, normalized energy dissipation was found to have a similar dependence on strain rate as the linear stiffness. The variation in absolute values as well as the exponent of the power law fit were found to be very close to the results for the linear stiffness. In the numerical simulations, the energy dissipation is underestimated for lower and is overestimated for higher shear rates. Nevertheless, the obtained values lie within the experimentally determined range given in [201].

5.3.4 Sensitivities with respect to membrane and fluid viscosities

Although it considered a different initial configuration of the form-finding process, the sensitivities found in the detailed parameter study in the previous contribution [119] also hold for the present model. In this subsection, the most important observations and trends are, thus, briefly reviewed and discussed.

The membrane viscoelasticity is identified as the most predominant parameter with regards to the viscoelastic response of the whole cell in laser traps. Whereas an increase in fluid viscosity by a factor of 4 has no noticeable influence on the stiffness and adds only 14% to the overall energy dissipation, a relatively moderate increase of the structure viscosity by 50% results in a significantly stiffer response of the cell model and rises the normalized energy dissipation by about 40%.

Due to this sensitivity, the actual realization of the membrane viscosity $\mu_{\text{eff}}^{\text{bil}}$, which has been defined in (2.125) as product $\tau\beta G^{\text{bil}} t^{\text{bil}}$, becomes important. The shear modulus G^{bil} and the thickness t^{bil} are fixed, but relaxation time τ and parameter β can be chosen freely, as long as the product yields the desired viscosity $\mu_{\text{eff}}^{\text{bil}}$. As already mentioned, the above shown results are obtained with $\tau = 30\,\text{ms}$ and $\beta =$100. Rising the dimensionless parameter β can be interpreted as a transition from a Maxwell to a Kelvin-Voigt model for the viscoelasticity. Although such a Kelvin-Voigt rheological model was proposed in the literature for the RBC membrane, cf. the early publications of Chien et al. [36] and Evans and Hochmuth [54], higher values of parameter β lead to an increasingly poor agreement of the hysteresis behavior and to increasing energy dissipation values, as was shown in the earlier contribution [119].

5.4 Discussion on laser trap experiments and the simulations

This chapter has shown that the numerical model is able to accurately predict the outcome of different laser trap experiments. Based on quasi-static deformations, realistic material parameter can be deduced and the obtained displacement over force curves are in excellent agreement with measurements.

Differences to other numerical studies that address the same experimental set-up can be explained by different boundary conditions and modeling assumptions. Corresponding modifications of the presented model allow to reproduce the results reported in literature, which demonstrates the validity of the developed RBC model as well as the the deduced elastic material parameters.

Unfortunately, there are no other numerical studies available for the dynamic laser trap experiments to compare the results of the presented model with. Comparison with experimental data shows a good agreement for the hysteresis behavior. However, the model overestimates the sensitivity of the energy dissipation on the strain rate. Probably, it would be possible to obtain a closer match for a more sophisticated rheological model of the membrane viscoelasticity. By contrast, earlier publications proposed an even simpler Kelvin-Voigt model, which results in less accurate hysteresis predictions.

Beside a validation of the model, this chapter has also brought forward some of the shortcomings and uncertainties of the experimental set-up under consideration. The results show a strong sensitivity with respect to boundary conditions, i.e. the size and the numerical handling of the contact zone between cell and trap. Experimentally, neither the geometry nor the surface area of the contact zone can be determined precisely. Furthermore, it is not completely clear, if the adhesion between bead and membrane is strong enough to guarantee a constant contact area during the elongation of the cell. The description of the trap stiffness as harmonic spring might also be a simplistic assumption. Thus, a further modification of the model, in particular of the membrane description, based on the results presented in the previous section does not seem very promising.

The next chapter presents the numerical results for the erythrocyte motion in shear flow. These experiments do not suffer the shortcommings of the laser traps and realistic boundary conditions can easily be determined.

Chapter 6
Erythrocytes in shear flow

The proposed erythrocyte model has been shown to accurately predict the response of the cell in laser traps. However, the results also demonstrate a sensitivity with respect to the boundary conditions accounting for the trap. This chapter addresses the simulation of human erythrocytes in shear flow, in which the boundary conditions can easily determined and realized by the numerical model.

The first section presents the geometry, the FE discretization and the boundary conditions applied. Section 6.2 shows the cell response to steady shear flow in different shear stress regimes, in which qualitatively different cell motions can be expected. Using a reasonable initial stress-free membrane state, all experimentally observed motions (tumbling, tank-treading, and swinging) are accurately predicted. The results allow for a rating of the configurations under consideration. The focus of section 6.3 lies on the shape memory of the cell, which can be deduced from the response to a sudden stop of the flow. Consistent with experimental observations, the considered numerical models show a tank-treading motion, such that the rim of the cell at rest are always formed by the same parts of the membrane. The last section of this chapter concludes the findings with regards to steady shear flow and shape memory. The different stress-free configurations are rated, also taken into consideration that some configurations suffer from a reduced stability of the biconcave shape.

6.1 Finite element discretization and boundary conditions

For all simulations performed in this chapter the material parameters of the cell are fixed to the values deduced in the previous chapter. Both, bilayer and cytoskeleton, are modeled as layers with a thickness of $t^{\text{bil}} = t^{\text{nw}} = 40\,\text{nm}$ and discretized with one layer of thin hexahedral elements each. The FE mesh (3888 elements, 5838 nodes) can be seen in Figure 6.1. The difference in thickness of the bilayer is balanced by the material parameter employed, in order to obtain the same properties as for the model in the previous chapter.

The erythrocyte model is embedded in a $100\,\mu\text{m} \times 50\,\mu\text{m} \times 50\,\mu\text{m}$ fluid channel. Velocities are prescribed on the top and bottom surface to generate a shear flow with vanishing

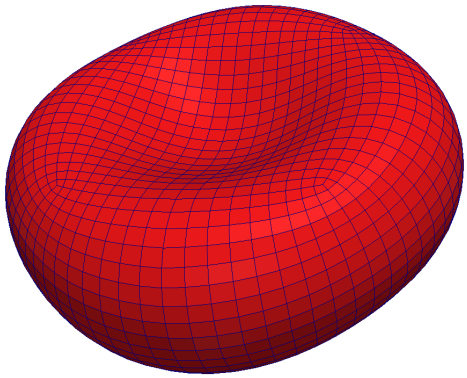

Figure 6.1: *Mesh of the membrane*

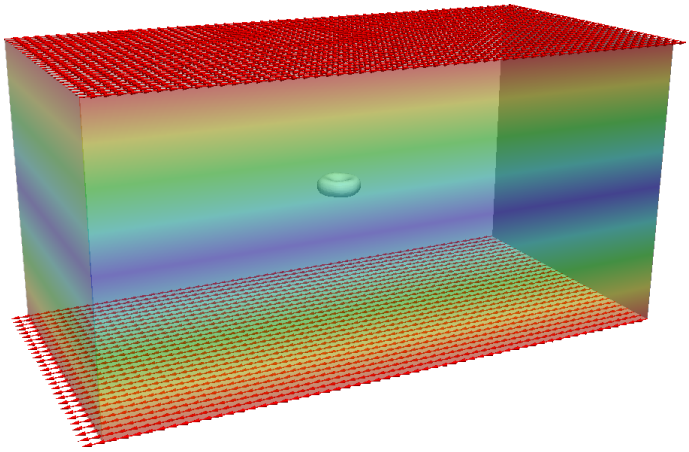

Figure 6.2: *Schematic drawing of channel geometry*

average velocity. Free-slip boundary conditions are applied at front and rear wall of the channel. A schematic drawing for the channel and the embedded RBC is given in Figure 6.2. Discretization of the fluid domains contains 63,334 elements and 69,343 nodes. Consequently, the whole coupled system has to be solved for 506,807 unknowns. Simulations with finer discretizations did not yield significantly different results.

6.2 Steady shear flow

It has long been known that the motion of a human RBC in steady shear flow changes qualitatively with the strength of the fluid shear stresses. These stresses are defined as the product of shear rate $\dot{\gamma}$ and viscosity of the outer fluid $\mu_{\text{out}}^{\mathcal{F}}$. For very low stresses, the cell rotates in a solid-like fashion. This behavior is called *tumbling* and was, for example, reported for erythrocytes and artificial vesicles by Goldsmith and Marlow [83] and by Kantsler and Steinberg [116]. In the high shear stress regime, the cell deforms into an ellipsoid, which aligns with the flow, and the membrane rotates around an otherwise steady cell shape. This so-called *tank-treading*, which is similar to the behavior of a liquid droplet, was first reported by Schmid-Schönbein and Wells [170] and was the subject of many experimental and theoretical studies, e.g. the of the contributions of Fischer et al. [66] and Tran-Son-Tay et al. [186].

Whereas tumbling and tank-treading have been well-understood for decades, it is the transition between these limiting motions that recent scientific studies focus on. Abkarian et al. [1] showed that erythrocytes undergo a *swinging* motion, which is characterized by a tank-treading of the membrane around an almost undeformed biconcave cell with an oscillating inclination angle. Using a mesoscopic numerical method as well as a theoretical approach, Noguchi and Gompper [147] reported a similar swinging motion for fluid vesicles, which are characterized by much simpler membrane mechanics and a different geometry.

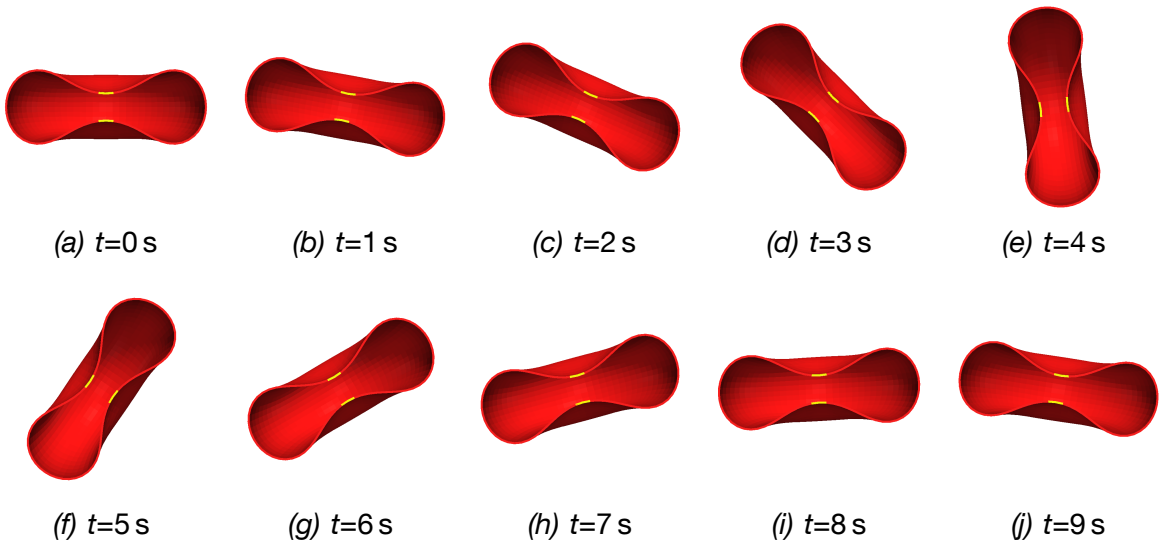

(a) t=0 s (b) t=1 s (c) t=2 s (d) t=3 s (e) t=4 s

(f) t=5 s (g) t=6 s (h) t=7 s (i) t=8 s (j) t=9 s

Figure 6.3: *Motion of* RBC975SF *in slow shear flow with shear rate* $\dot{\gamma} = 1\,\mathrm{s}^{-1}$ *and fluid viscosity* $\mu^{\mathcal{F}}_{\text{out}} = 10\,\mathrm{mPa\,s}$

The first two subsections present numerical results for low and high shear forces, respectively. These sections demonstrate a minor influence of the stress-free state on tumbling for low and on tank-treading for high shear forces. For all configurations considered, the results deviate only slightly from each other. The situation changes dramatically in case of moderate shear stress $\dot{\gamma}\mu^{\mathcal{F}}_{\text{out}}$ between 0.225 Pa and 0.45 Pa, which is considered in the third subsection. Here, the stress-free reference state is the predominant parameter controlling the qualitative behavior. Finally, the results are discussed and interpreted in the last subsection.

6.2.1 Results for the low shear stress regime

In order to qualify and quantify the effect of the initial configuration on the tumbling behavior of cell, the cell is subjected to a steady shear flow with a shear rate of $\dot{\gamma} = 1\,\mathrm{s}^{-1}$. Assuming a viscosity $\mu^{\mathcal{F}}_{\text{out}} = 10\,\mathrm{mPa\,s}$, the fluid shear stress is given by 10 mPa, which should result in a tumbling motion of the cell.

The numerical model recovers the tumbling behavior. Its response can be thought to be almost insensitive with respect to the stress-free reference state. This is demonstrated by Figure 6.3 and Figure 6.4, which show the results for the two most extreme configurations RBC975SF and RBC975. In both cases, a solid-like behavior of the erythrocyte model can be seen and the shape of the cell stays almost unchanged during the rotation.

Beside the qualitative match, differences in the rotation velocity can be seen comparing Figure 6.3 and Figure 6.4. The unstressed biconcave configuration RBC975SF needs between 4 s and 5 s for a rotation of 90°, whereas the same rotation of RBC975 takes about 1 s longer. The differences in rotation velocity is due to a relative motion of

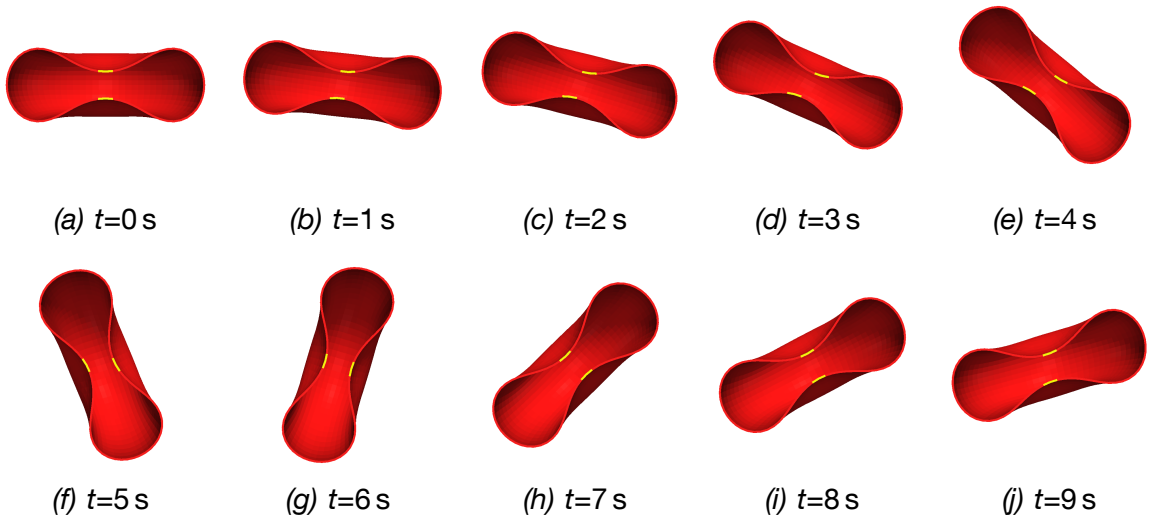

(a) t=0 s *(b)* t=1 s *(c)* t=2 s *(d)* t=3 s *(e)* t=4 s

(f) t=5 s *(g)* t=6 s *(h)* t=7 s *(i)* t=8 s *(j)* t=9 s

Figure 6.4: *Motion of* RBC975 *in slow shear flow with shear rate* $\dot{\gamma} = 1\,\mathrm{s}^{-1}$ *and fluid viscosity* $\mu_{\text{out}}^{\mathcal{F}} = 10\,\mathrm{mPa\,s}$

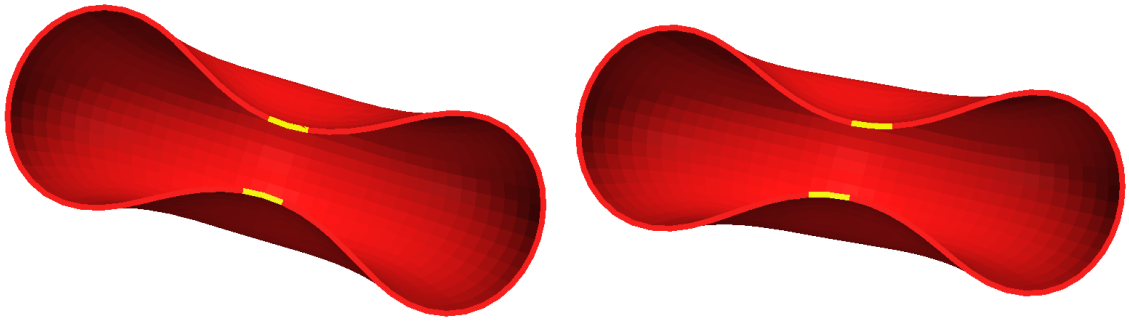

(a) RBC975SF *(b)* RBC975

Figure 6.5: *Detailed view on cells in slow shear flow at time* $t = 1.5\,\mathrm{s}$*. Elements initially positioned at the dimple of the cell are colored in yellow.*

the cell membrane around the biconcave cytosol domain, as becomes apparent from the enlarged views of the cells at time $t = 1.5\,\mathrm{s}$, cf. Figure 6.5. The rotation of the initially unstressed biconcave cell is very close to a perfect rigid-body rotation. The dimple of the cell is formed by the same elements throughout the whole simulation. In contrast, Figure 6.5(b) shows that there is a very small relative movement of the cell membrane around the almost unchanged biconcave cytosol domain for the pre-stressed configuration RBC975. The relative motion of the membrane oscillates around its initial position, i.e. a tank-treading motion cannot be found.

The results of the other pre-stressed configurations RBC960 and RBC900 are skipped at this point, since they are indistinguishable from Figure 6.4. Consequently, independent of the pre-stressing, a solid-like tumbling motion for the given boundary conditions is predicted by the proposed model.

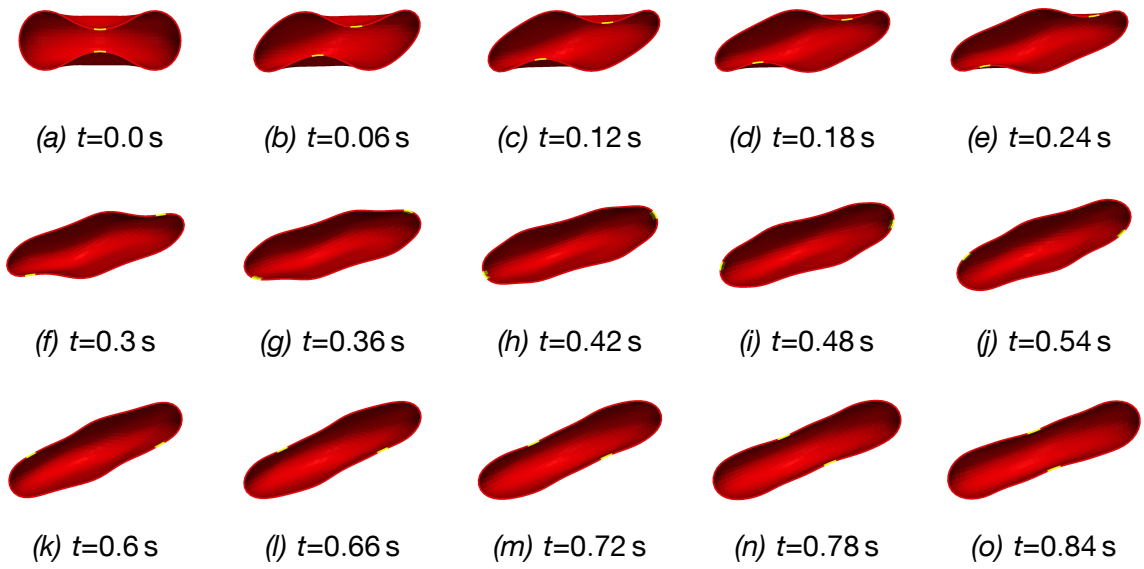

(a) t=0.0 s *(b)* t=0.06 s *(c)* t=0.12 s *(d)* t=0.18 s *(e)* t=0.24 s

(f) t=0.3 s *(g)* t=0.36 s *(h)* t=0.42 s *(i)* t=0.48 s *(j)* t=0.54 s

(k) t=0.6 s *(l)* t=0.66 s *(m)* t=0.72 s *(n)* t=0.78 s *(o)* t=0.84 s

Figure 6.6: *Motion of* RBC975SF *in fast shear flow with shear rate* $\dot{\gamma} = 12\,\mathrm{s}^{-1}$ *and fluid viscosity* $\mu^{\mathcal{F}}_{\mathrm{out}} = 150\,\mathrm{mPa\,s}$

6.2.2 Results for the high shear stress regime

The response of the erythrocyte to high shear stress is investigated considering a shear rate of $\dot{\gamma} = 12\,\mathrm{s}^{-1}$ and a dynamic viscosity of $\mu^{\mathcal{F}}_{\mathrm{out}} = 150\,\mathrm{mPa\,s}$ for the surrounding fluid. The resulting shear stress of 1.8 Pa is reported to result in tank-treading motion of ellipsoidal shaped cells, as discussed the quantitative study on tank-treading behavior presented by Fischer [64].

Numerical results for configuration RBC975SF are depicted in Figure 6.6. The transition from a stress-free biconcave into a roughly ellipsoidal shape takes about 0.4 s under the considered flow conditions. This transition requires the inversion of curvature of points initially at the dimple and involves intermediate cell configurations with at least four regions of positive and four regions of negative curvature. After the transition, the membrane starts a tank-treading motion. Superimposed is a continuous deformation of the cell shape and a slight change of the inclination angle.

If the pre-stressed configuration RBC975 is considered, the transition from biconcave to an almost perfect ellipsoidal shape of the cell involves geometrically simpler intermediate shapes as demonstrated by Figure 6.7. It is completed in less than 0.25 s. Furthermore, Figure 6.7 shows that neither significant deformation of the shape nor changes of the inclination angle can be observed after the transition. The tank-treading frequency is found to be comparable for both configurations.

In agreement to the observations for low shear stresses in the previous section, there are no visible differences between the numerical responses of all pre-stressed configurations RBC975, RBC960, and RBC900. Thus, all four configurations under

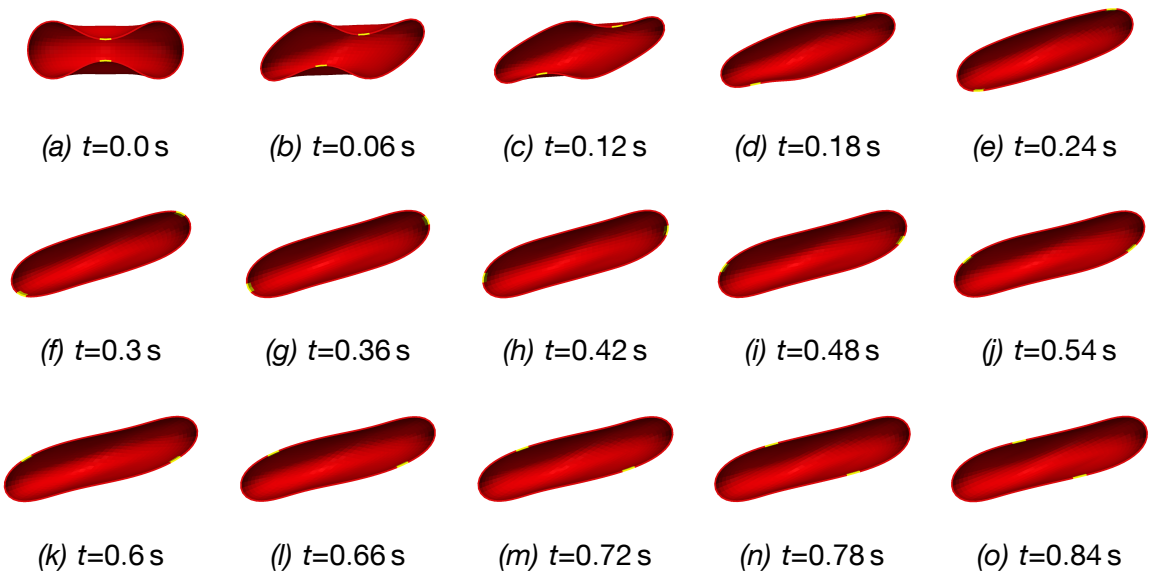

Figure 6.7: *Motion of* RBC975 *in fast shear flow with shear rate* $\dot{\gamma} = 12\,\mathrm{s}^{-1}$ *and fluid viscosity* $\mu^{\mathcal{F}}_{\mathrm{out}} = 150\,\mathrm{mPa\,s}$

consideration predict a tank-treading motion around a more or less ellipsoidal cell shape for shear stresses of 1.8 Pa.

6.2.3 Results for the medium shear stress regime

To study the response of the proposed FE erythrocyte model to the medium shear stress regime, shear stresses of 225 mPa and 450 mPa are considered. The viscosity of the surrounding fluid is fixed to $\mu^{\mathcal{F}}_{\mathrm{out}} = 75\,\mathrm{mPa\,s}$, whereas two different shear rates ($\dot{\gamma}_1 = 3.0\,\mathrm{s}^{-1}$, $\dot{\gamma}_2 = 6.0\,\mathrm{s}^{-1}$) are used.

To begin with, the behavior of the stress-free biconcave configuration RBC975SF is presented. The results of the simulations are shown in Figure 6.8 and Figure 6.9 for strain rates $\dot{\gamma} = \dot{\gamma}_1$ and $\dot{\gamma} = \dot{\gamma}_2$, respectively. The response of the erythrocyte to both shear stresses is a solid-like rotation of the whole cell. Additionally, an oscillating, relative motion of the membrane with respect to the cytosol domain is superimposed to the solid-like rotation, as indicated by the motion of elements initially positioned at the dimple of the cell, cf. Figure 6.8 and Figure 6.9. Tank-treading and swinging cannot be observed for configuration RBC975SF for the medium shear stress regime.

Next, the effect of residual stresses in the biconcave cell membrane is investigated. These stresses are lowest for configuration RBC900, which is first considered. As Figure 6.10 demonstrates, the low shear rate $\dot{\gamma} = 3\,\mathrm{s}^{-1}$ is not sufficient to induce tank-treading, although the membrane starts to rotate when subjected to shear flow. After about 1 s, however, this motion almost completely stops and is replaced by a solid-like rotation of the cell. This pattern is, hence, qualitatively similar to the previously

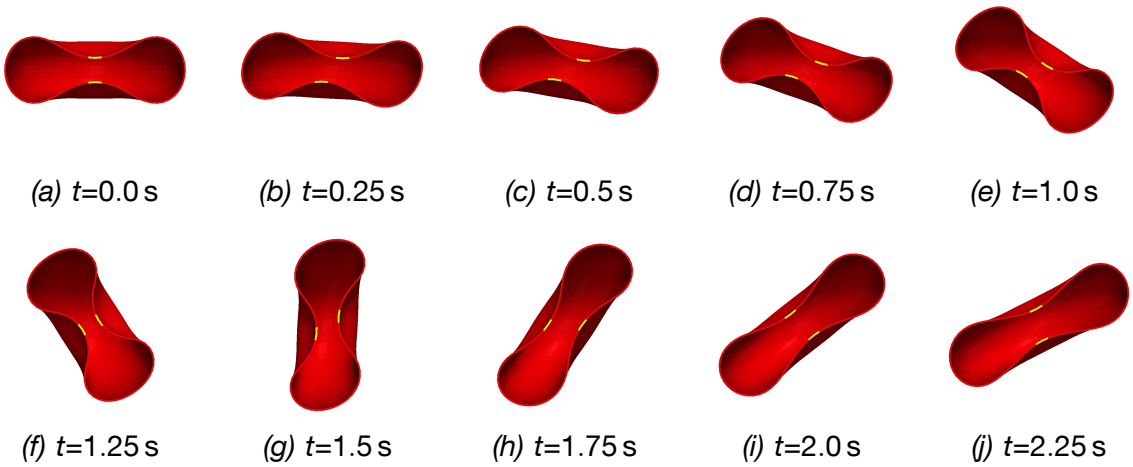

(a) t=0.0 s *(b)* t=0.25 s *(c)* t=0.5 s *(d)* t=0.75 s *(e)* t=1.0 s

(f) t=1.25 s *(g)* t=1.5 s *(h)* t=1.75 s *(i)* t=2.0 s *(j)* t=2.25 s

Figure 6.8: *Motion of* RBC975SF *in medium shear flow with shear rate* $\dot{\gamma} = 3\,\mathrm{s}^{-1}$ *and fluid viscosity* $\mu^{\mathcal{F}}_{\text{out}} = 75\,\mathrm{mPa\,s}$

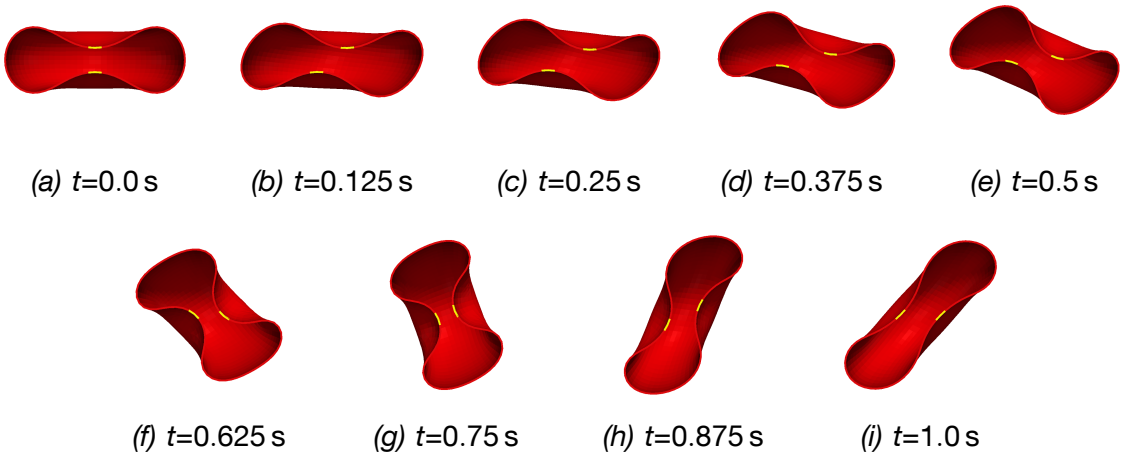

(a) t=0.0 s *(b)* t=0.125 s *(c)* t=0.25 s *(d)* t=0.375 s *(e)* t=0.5 s

(f) t=0.625 s *(g)* t=0.75 s *(h)* t=0.875 s *(i)* t=1.0 s

Figure 6.9: *Motion of* RBC975SF *in medium shear flow with shear rate* $\dot{\gamma} = 6\,\mathrm{s}^{-1}$ *and fluid viscosity* $\mu^{\mathcal{F}}_{\text{out}} = 75\,\mathrm{mPa\,s}$

described behavior ot the stress-free biconcave cell, although the relative motion of the membrane around the cytosol is significantly increased.

Doubling the shear rate to $\dot{\gamma} = 6\,\mathrm{s}^{-1}$ finally leads to tank-treading as presented in Figure 6.11. Due to the relatively high shear stresses, the cell shape is deformed in the course of the simulation, but remains biconcave. The first phase of the motion with a membrane rotation less the 90° is characterized by a constant cell shape and constant inclination angle. Thereafter, the cell rotates against the shear flow, while the tank-treading continues. A detailed study of the temporal variation of the inclination angle would require a longer simulation time, which could not be realized. Nevertheless, it seems reasonable to identify the change of inclination angle with experimentally

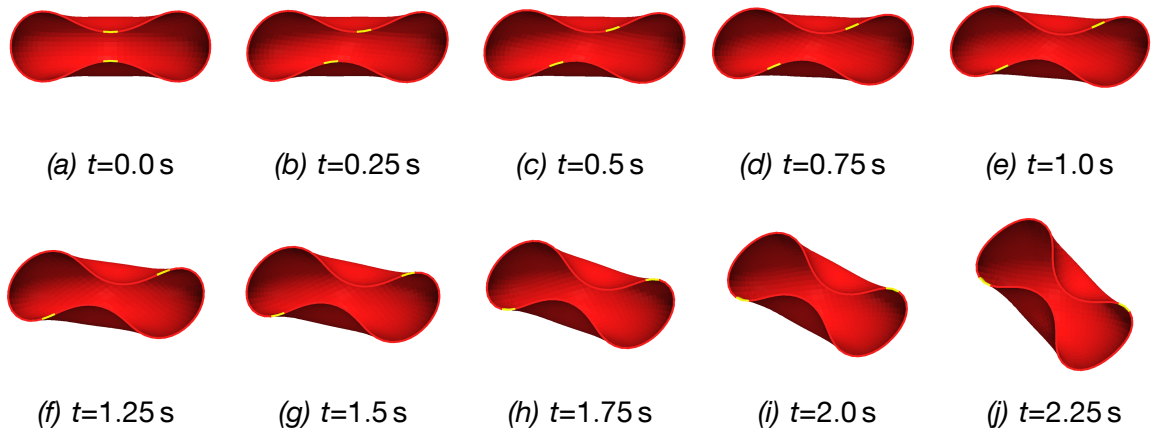

(a) t=0.0 s *(b)* t=0.25 s *(c)* t=0.5 s *(d)* t=0.75 s *(e)* t=1.0 s

(f) t=1.25 s *(g)* t=1.5 s *(h)* t=1.75 s *(i)* t=2.0 s *(j)* t=2.25 s

Figure 6.10: *Motion of* RBC900 *in medium shear flow with shear rate* $\dot{\gamma} = 3\,\mathrm{s}^{-1}$ *and fluid viscosity* $\mu^{\mathcal{F}}_{\mathrm{out}} = 75\,\mathrm{mPa\,s}$

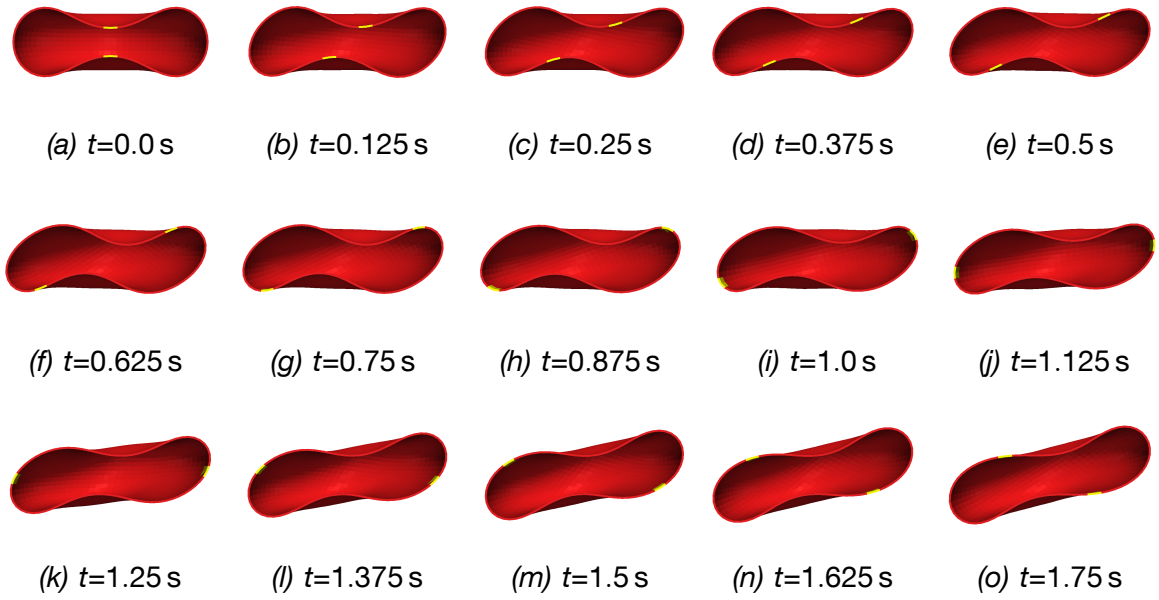

(a) t=0.0 s *(b)* t=0.125 s *(c)* t=0.25 s *(d)* t=0.375 s *(e)* t=0.5 s

(f) t=0.625 s *(g)* t=0.75 s *(h)* t=0.875 s *(i)* t=1.0 s *(j)* t=1.125 s

(k) t=1.25 s *(l)* t=1.375 s *(m)* t=1.5 s *(n)* t=1.625 s *(o)* t=1.75 s

Figure 6.11: *Motion of* RBC900 *in medium shear flow with shear rate* $\dot{\gamma} = 6\,\mathrm{s}^{-1}$ *and fluid viscosity* $\mu^{\mathcal{F}}_{\mathrm{out}} = 75\,\mathrm{mPa\,s}$

observed swinging motion as described by Abkarian et al. [1].

The numerical predicted erythrocyte responses obtained with configurations RBC900, RBC960, and RBC975 are again indistinguishable from each other for a shear rate of $\dot{\gamma} = 6\,\mathrm{s}^{-1}$. Thus, Figure 6.11 suffices to characterize the behavior of all considered pre-stressed configurations.

In contrast to these results for the higher shear rate $\dot{\gamma} = 6\,\mathrm{s}^{-1}$, the response to a shear rate of $\dot{\gamma} = 3\,\mathrm{s}^{-1}$ is significantly influenced by the residual stresses. This is demonstrated

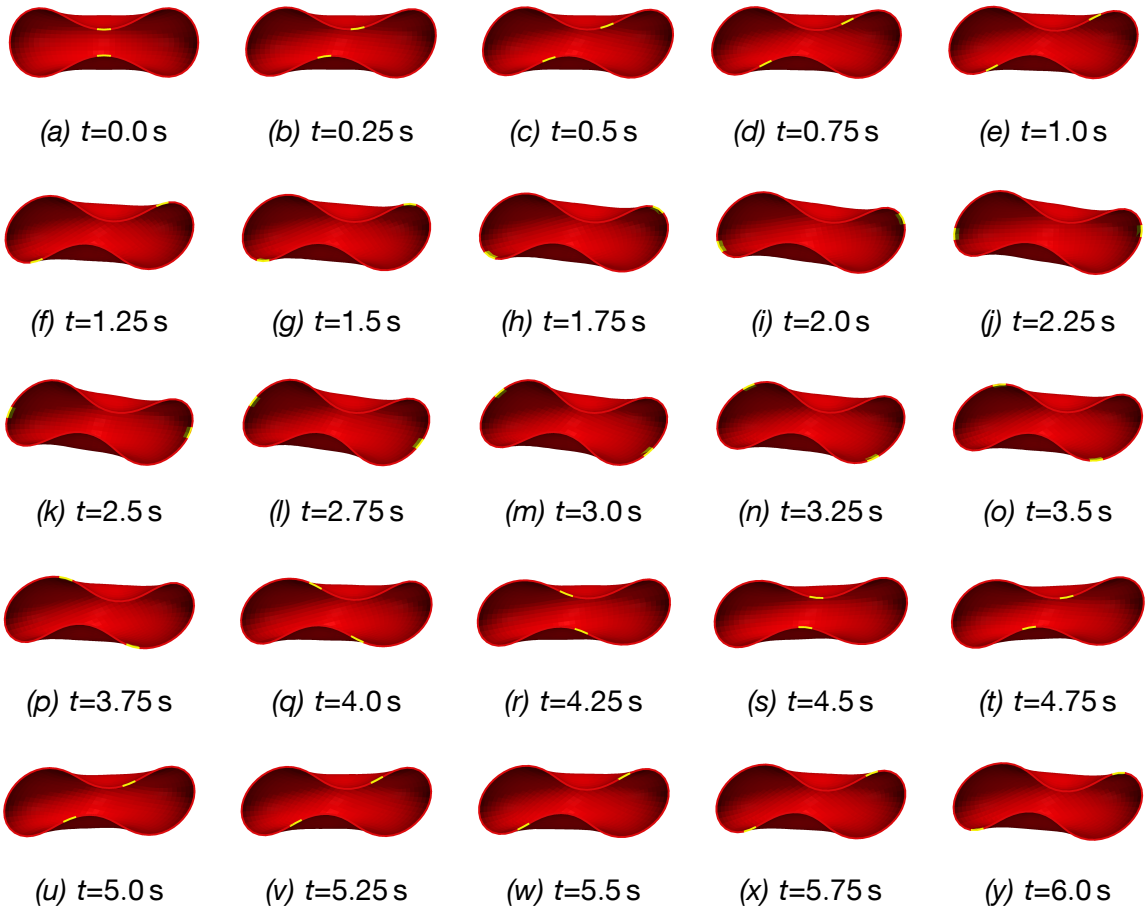

Figure 6.12: *Motion of* RBC960 *in medium shear flow with shear rate* $\dot{\gamma} = 3\,\mathrm{s}^{-1}$ *and fluid viscosity* $\mu^{\mathcal{F}}_{\mathrm{out}} = 75\,\mathrm{mPa\,s}$

by Figure 6.12, which shows that for configuration RBC960 this low shear rate suffices to induce a tank-treading motion. Although being slightly sheared, the cell shape stays biconcave during the course of the simulation. The inclination angle of the cell changes over time. For $t \leq 2\,\mathrm{s}$, the whole RBC slightly rotates in clockwise direction. When the tank-treading motion has reached an angle of 90°, the whole cell starts to rotate against the flow, i.e. in counterclockwise direction for the perspective in Figure 6.12.

Further increasing the residual stresses of the membrane further decreases the resistance of the cell against a tank-treading motion. This can be concluded from the numerical results of configuration RBC975, which are shown in Figure 6.13. An oscillating inclination angle of the cell, i.e. a swinging motion, is still undergone, but the magnitude of the oscillation is significantly reduced. The tank-treading frequency as well as the oscillating frequency of the motion is comparable to configuration RBC960.

Based on the experimental results of Abkarian et al. [1], the considered medium shear stresses in this subsection can be expected to induce a swinging motion of the human erythrocyte. The numerical simulations, on the other hand, only show swinging motion for those membrane configurations that have an almost spherical stress-free state.

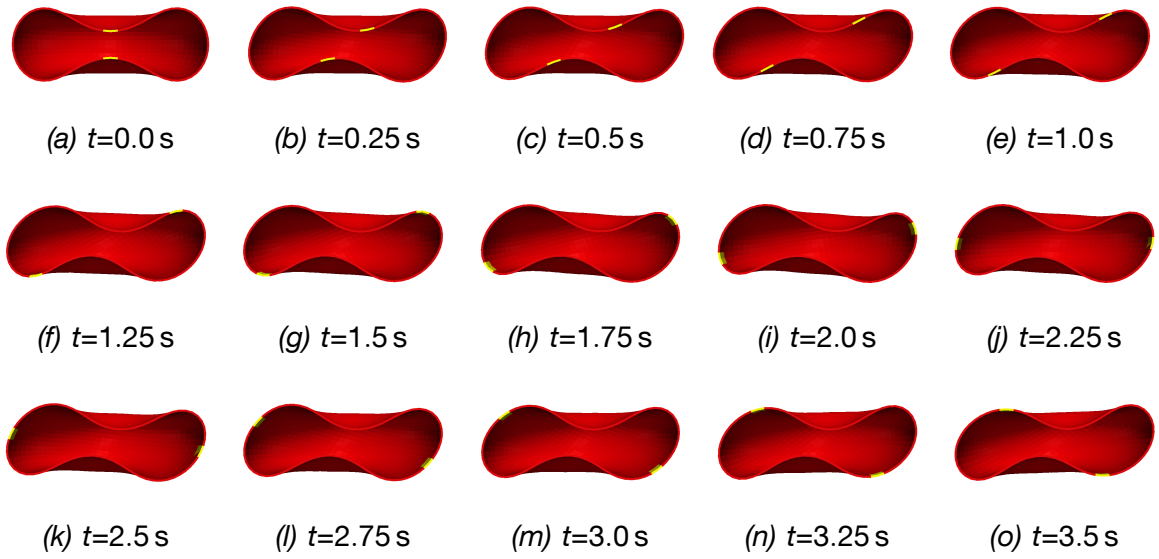

(a) t=0.0 s (b) t=0.25 s (c) t=0.5 s (d) t=0.75 s (e) t=1.0 s

(f) t=1.25 s (g) t=1.5 s (h) t=1.75 s (i) t=2.0 s (j) t=2.25 s

(k) t=2.5 s (l) t=2.75 s (m) t=3.0 s (n) t=3.25 s (o) t=3.5 s

Figure 6.13: *Motion of* RBC975 *in medium shear flow with shear rate* $\dot{\gamma} = 3\,\mathrm{s}^{-1}$ *and fluid viscosity* $\mu_{\mathrm{out}}^{\mathcal{F}} = 75\,\mathrm{mPa\,s}$

6.2.4 Discussion of the results for steady shear flow

The previous subsections show that all configurations considered in this thesis are able to recover the tumbling of a human erythrocyte subjected to very low shear stresses. Furthermore, high shear stresses deform the cells into ellipsoids and induce a tank-treading around a stationary shape, which is also in agreement with experimental measurements on human RBCs. Nevertheless, not all of the considered model configurations are able to adopt the swinging motion for medium shear stresses. The ability for a reasonable prediction of that particular cell motion can conclusively be related to a non-zero residual stress state of the biconcave membrane at rest.

Based on this considerations it becomes clear why numerical models found in literature are unable recover the swinging mode of the cell. None of them considers a stress-free membrane state other than a biconcave shape. This modeling assumption implies that the preferred (biconcave) state of the membrane has regions of positive and regions of negative curvature. At the beginning of tank-treading (or of any relative motion of the membrane with respect to the cytosol) the local curvature changes and the bending energy stored in the membrane increases. Consequently, in order to induce this motion, a bending energy barrier has to be overcome. As a results, the preferred response of a cell with a biconcave stress-free state to a medium shear flow is deformation rather than tank-treading. This behaviour has been reported for other numerical models of the cell and is found for RBC975SF as well.

In contrast, the symmetry of a perfectly spherical reference shape would imply that the overall bending energy stored in the membrane stays constant during tank-treading, since local changes in curvature balance out. Since none of the considered initial

configurations is perfectly spherical, which would contradict the assumption of shape memory of the cell addressed in the next section, tank-treading cannot be expected to preserve the bending energy of the membrane completely. The degree of energy necessary to induce any relative motion of the membrane around the biconcave shaped cytosol domain increases with the deviation of the initial shape from the sphere. Consequently, the required shear rates to overcome the bending energy barrier of the membrane can be assumed to increase with decreasing residual stresses. Numerically, this becomes most apparent in subsection 6.2.3, but is also indicated by the differences obtained in low (section 6.2.1) and in high shear rates (section 6.2.2).

The initial asymmetry of the cells also allows to interpret the swinging motion of the cell. For the first 90° of tank-treading, the bending energy stored in the membrane increases and the cell rotates with the shear flow. Subsequently, the membrane relaxes, i.e. the energy in the membrane decreases, and the inclination angle rotates against the shear flow. The results shown in Figure 6.12 and Figure 6.13 indicate a more pronounced swinging motion for more oblate reference shapes, which supports these argumentation. A similar interpretation was also given by Abkarian et al. [1]. Although a long-time numerical study cannot be provided in this thesis, the interpretation of the swinging in terms of bending energy suggest a swinging frequency twice as large as the tank-treading frequency, which agrees with the experimental observations in [1].

For a shear stress of 450 mPa, the swinging motion can be reproduced numerically by all considered pre-stressed configurations. Fluid shear stresses of 225 mPa, on the other hand, only suffice to induce tank-treading for almost spherical stress-free reference shapes, i.e. RBC960 and RBC975, although a very large relative membrane motion can be observed for the more oblate reference shape RBC900 as well. The simulations shown in this section only consider the first seconds of the shear flow. Thus, it might be possible that after half a solid-like rotation of RBC900 a tank-treading motion would be adopted. Such a behavior has been reported for the experiments performed by Viallat et al. [189]. In those, periods of tank-treading and tumbling alternate for a cell subjected to steady shear flow with medium shear stresses.

Thus, the results presented in this work do not allow to conclusively determine the stress-free state of the human RBC. Nevertheless, they demonstrate imposingly the influence of residual stresses in the membrane for the cell at rest. Moreover, they strongly indicate that the assumption of a stress-free biconcave shape is incorrect and probably spoils the results of numerical simulations of shear flow experiments.

6.3 Shape memory of the human erythrocyte

The existence of a shape memory of the human RBC has first been discovered rather recently with *go-and-stop* experiments by Fischer [65]. The recordings of the relaxation behavior of single cells did not only demonstrate the existence of this effect, but also allowed to investigate the mechanism behind it. A review of the experiments as well as of the bifurcation behavior of cells is given in the first subsection.

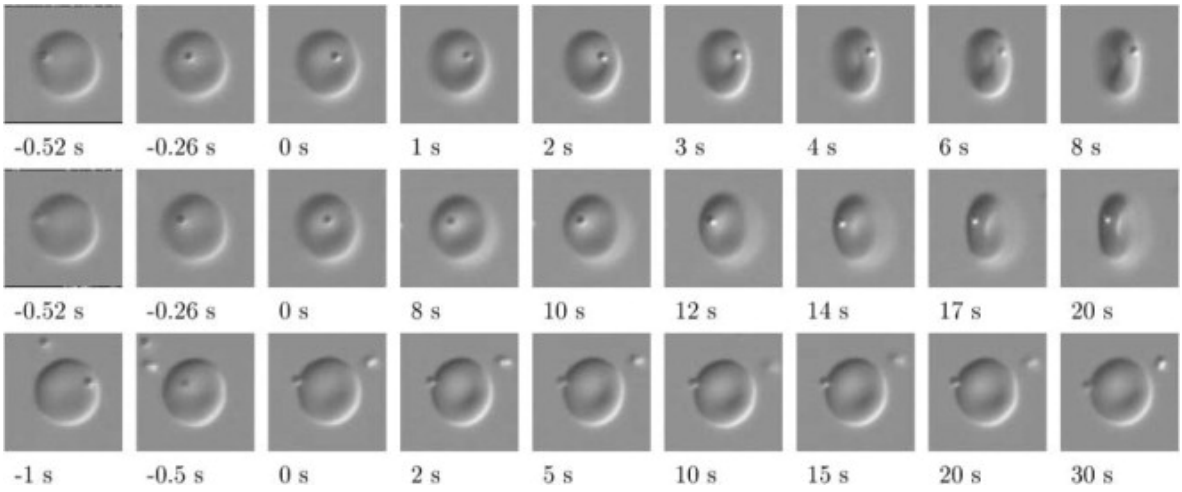

Figure 6.14: *Experimental results observed for go-and-stop experiments taken from [65]. At* $t = 0\,\mathrm{s}$ *the flow stops. At the end of the relaxation process, the latex sphere adhered to the membrane is always found at the rim of the cell, independent of its position at* $t = 0\,\mathrm{s}$.

The second subsection presents the numerical results obtained for go-and-stop experiments for the pre-stressed cell configurations. All considered cells show a relaxation behavior and shape memory. Almost spherical reference shapes (RBC975 and RBC960), however, lead to instabilities with respect to the biconcave shape. The section is completed by a discussion of the results.

6.3.1 Review on experimental observations and bifurcation behavior

In the go-and-stop experiments reported in [65], the cells were subjected to simple shear flow with a viscosity of the surrounding fluid of $\mu_{\text{out}}^{\mathcal{F}} = 12.9\,\mathrm{mPa\,s}$ and a shear rate of $\dot{\gamma} = 10\,\mathrm{s}^{-1}$, such that a tank-treading motion of the membrane was observed. Based on the above discussion and observations, a swinging motion can be expected for the resulting shear stresses. Since the focus of the experimental study was put on the relaxation behavior which was initiated by a sudden stop of the flow, a detailed description of the cell motion was not provided.

After the flow had stopped, the cell returned to its unloaded biconcave shape relatively fast. However, the relaxation was not completed by the shape transition. With latex spheres attached to the rim of the cell at rest, Fischer [65] could show that the membrane tended to tank-tread around the biconcave cell, until the marker was again positioned at the rim of the cell. A recording of the sphere motion taken from [65] is shown in Figure 6.14, where at time $t = 0\,\mathrm{s}$ the fluid flow stopped.

The rotation of the membrane during relaxation was much slower than the tank-treading induced by the shear flow and its direction exclusively depended on the phase difference, which is defined by the difference between the position of the latex sphere at $t = 0\,\mathrm{s}$ and at equilibrium. The relaxation is characterized by a bifurcation behavior, where the critical

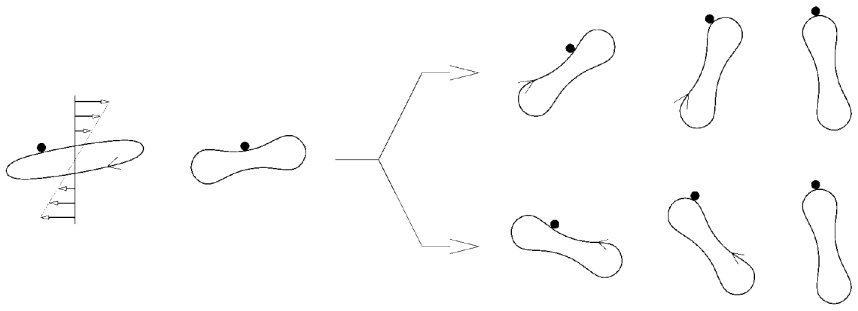

Figure 6.15: *Schematic drawing of the go-and-stop experiment taken from [65] demonstrating the bifurcating behavior and the tank-treading mode.*

phase difference is $\pi/2$, for which the sphere is positioned at the dimple of the cell. For greater phase differences, the membrane rotated in the direction of the flow induced tank-treading. Smaller differences lead to an opposite tank-treading. Both membrane motions were counterbalanced by a solid-like rotation of the whole cell. The observed relaxation behavior of the cell indicates a non-spherical stress-free configuration of the cell. A schematic drawing of this behavior taken from [65] is depicted in Figure 6.15.

The correspondence between Figure 6.14 and Figure 6.15 is remarkable. However, the schematic drawing starts with an initially ellipsoidal cell, which does not seem justified given the experimental observations and the presented numerical results at the end of the previous section.

6.3.2 Numerical results

Due to the non-symmetric stress-free reference state, all cell configurations discussed in this thesis have a shape memory. The motion of the membrane after the external fluid flow has stopped is driven by the derivative of the elastic energy stored in the membrane with respect to the phase difference between the current and the equilibrium state. Thus, it can be expected that the readiness to return to the state at rest and, thus, the transition speed should increase with decreasing pre-stressing of the cell at rest.

Being most critical in terms of shape memory, configurations characterized by an almost spherical reference state are considered first. Exemplarily, the numerical results for configuration RBC960 are considered here, where the tank-treading is initially induced by a shear flow with a fluid viscosity $\mu_{\text{out}}^{\mathcal{F}} = 75\,\text{mPa}\,\text{s}$ and a shear rate of $\dot{\gamma} = 3\,\text{s}^{-1}$. Figure 6.12 shows that the critical phase difference of $\pi/2$ is reached in between 2.25 s and 2.5 s. Thus, to answer the question, if the numerical model can recover the bifurcating behavior, two different simulations are performed. First, the flow is stopped after 2 s, such that the membrane is expected to start to rotate in opposite direction compared to the tank-treading motion induced by the fluid flow. In the second simulation, the membrane should tank-tread in the same direction as before, since the flow is stopped after 2.5 s. In the following, the time $t = 0\,\text{s}$ refers to that point in time,

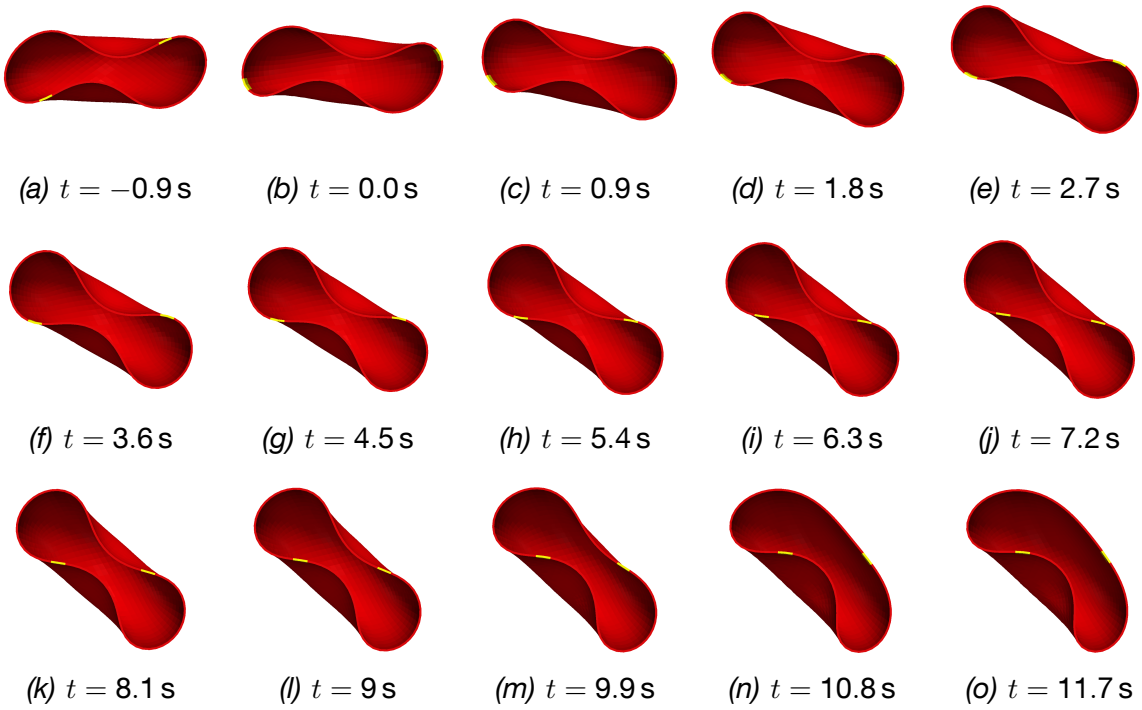

Figure 6.16: *Relaxation of erythrocyte model* RBC960 *in fluid. Shear flow is stopped before the critical phase difference* $\pi/2$ *is reached.*

when the flow is stopped.

The numerical results for the go-and-stop experiments with configuration RBC960 are depicted in Figure 6.16 and Figure 6.17. Within the first second after the stop, the cell returns to an undeformed biconcave shape that is indistinguishable from its shape at rest. Nevertheless, the results also show that the membrane has not found its equilibrium state yet. The membrane begins to rotate, such that the elements initially positioned around the dimple of the cell move towards the nearest dimple. If the flow stops before the critical phase difference is reached, the membrane rotates counterclockwise and this motion is counterbalanced by a clockwise rotation of the whole cell, cf. Figure 6.16. If the membrane has already passed the phase difference of $\pi/2$ as in Figure 6.17, the directions of rotation interchange, i.e. the membrane motion is clockwise and the cell rotates counterclockwise. The same behavior can also be observed for configuration RBC975, which is, thus, omitted here.

Beside the existence of a shape memory effect, the results presented in Figure 6.16 and Figure 6.17 also show an instability of the biconcave shape for a cell with almost spherical reference shape. After about 8 s of relaxation, the rotation of the membrane stops, although the elements initially positioned at the dimple have not yet reached that position again. The cell transforms from a biconcave into a cup-shaped cell, a so-called *stomatocytes*. A further tank-treading motion of the membrane cannot be observed.

The stress-free states of configuration RBC960 and RBC975 seem to be too close to

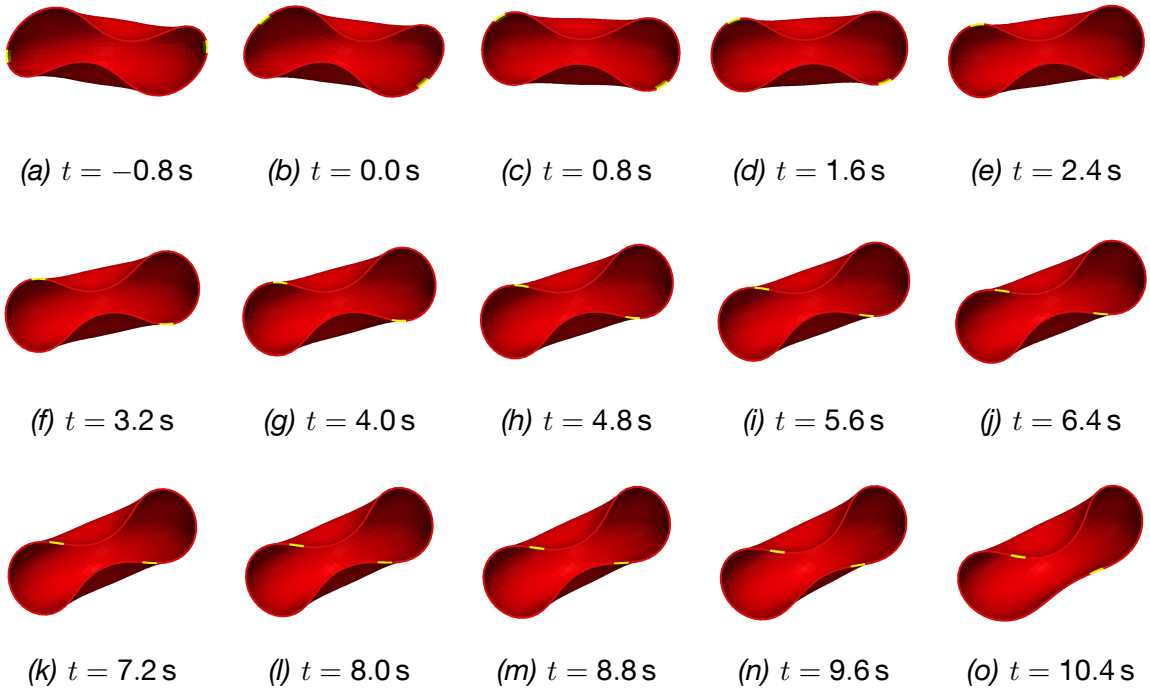

Figure 6.17: *Relaxation of erythrocyte model* RBC960 *in fluid. Shear flow is stopped after the critical phase difference* $\pi/2$ *is passed.*

a sphere in order to obtain a stable biconcave shape of the cell. Thus, the simulations of go-and-stop-experiments are repeated with configuration RBC900. In this case, a tank-treading behavior in steady shear flow has been obtained with a fluid viscosity $\mu^{\mathcal{F}}_{\text{out}} = 75\,\text{mPa s}$ and a shear rate $\dot{\gamma} = 6\,\text{s}^{-1}$, cf. Figure 6.11. Since the bifurcation behavior can already be observed for the more critical configurations RBC960 and RBC975, it suffices to consider the relaxation of RBC900 only for one case. Here, the flow is stopped after 1.0 s, i.e. before the critical phase difference in reached.

The numerically predicted relaxation is shown in Figure 6.18. Again, the transition from a sheared to an unloaded biconcave shape is completed within the first second after the flow has stopped. After a biconcave is adopted, the membrane begins to tank-tread and the motion is counterbalanced by a solid-like rotation of the cell. The membrane motions during the relaxation phase are much slower than the fluid induced tank-treading motion. However, due to the increase asymmetry of the initial stress-free shape, the induced rotation is slightly faster than the motion found for configuration RBC960. The equilibrium of the cell is reached after about $t = 7\,\text{s}$, as can be seen in Figure 6.18. In contrast to the previous results, the equilibrium shape of configuration RBC900 is still a biconcave cell, indicating that the biconcave shape is stable for this configuration.

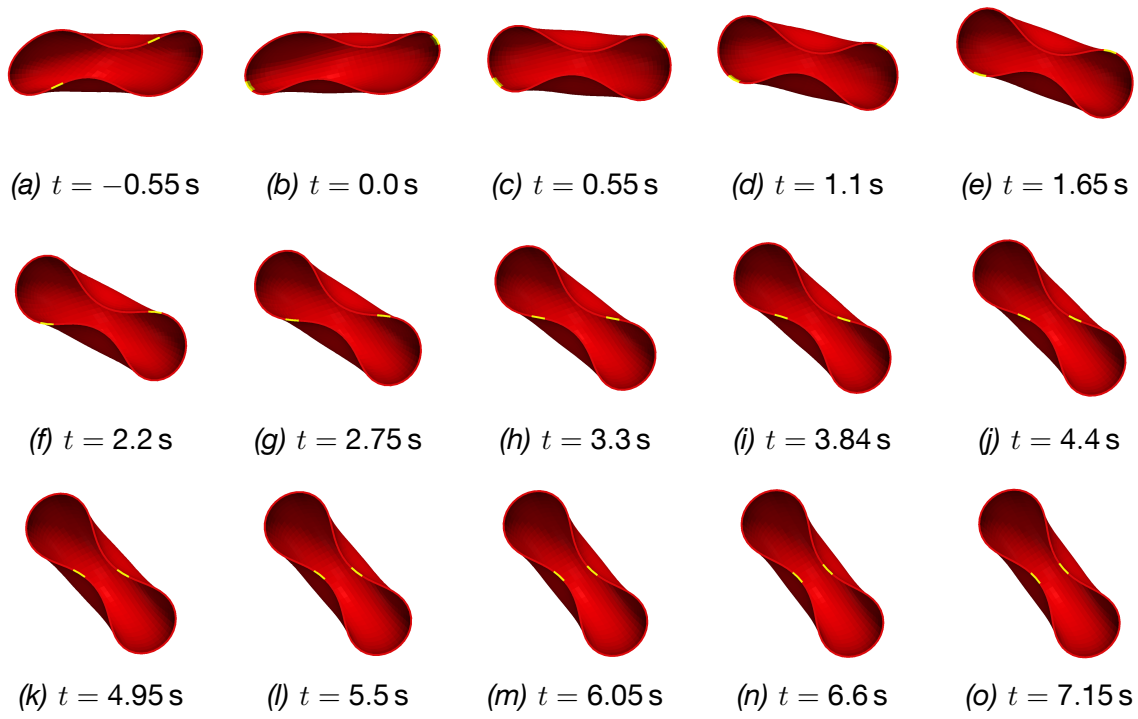

(a) $t = -0.55\,\mathrm{s}$ (b) $t = 0.0\,\mathrm{s}$ (c) $t = 0.55\,\mathrm{s}$ (d) $t = 1.1\,\mathrm{s}$ (e) $t = 1.65\,\mathrm{s}$

(f) $t = 2.2\,\mathrm{s}$ (g) $t = 2.75\,\mathrm{s}$ (h) $t = 3.3\,\mathrm{s}$ (i) $t = 3.84\,\mathrm{s}$ (j) $t = 4.4\,\mathrm{s}$

(k) $t = 4.95\,\mathrm{s}$ (l) $t = 5.5\,\mathrm{s}$ (m) $t = 6.05\,\mathrm{s}$ (n) $t = 6.6\,\mathrm{s}$ (o) $t = 7.15\,\mathrm{s}$

Figure 6.18: *Relaxation of erythrocyte model* RBC900 *in fluid. Shear flow is stopped before the critical phase difference* $\pi/2$ *is reached.*

6.3.3 Discussion of numerical results

This section demonstrates three interesting and important facts about the presented erythrocyte model. First, all considered configurations exhibit a shape memory effect. Following the argumentation in section 6.2.4, this property can easily be related to the bending energy stored in the membrane. Due to the asymmetry of all considered reference shapes, there always exists a unique membrane configuration with minimal bending energy. The additional bending energy developing in the membrane during the tank-treading motion suffices to induce membrane and cell rotations in the absence of external fluid flow. Being related to the bending energy, it is clear that the direction of the rotations is determined by the phase difference alone. Thus, the relaxation is characterized by the bifurcation behavior described by Fischer [65].

Second, the relaxation behavior is not only recovered qualitatively, but also quantitatively. During the relaxation phase the tank-treading motion is significantly slower than during the shear flow. The time needed for the relaxation into the equilibrium membrane state, which is found to only slightly increase with increasing pre-stressing, is in excellent agreement with the experimental observations in Fischer [65].

Third, the results also show a stability issue if the stress-free reference state of the numerical model is assumed to be almost spherical. Although the bending energy is strong enough to initiate the membrane motion within the first seconds of the relaxation phases, it is not large enough to stabilize the biconcave shape against a cup shape. This

observation is in agreement with the results of Li et al. [128], who concluded that for a spherical reference state the biconcave shape is only stable if an unphysiological high bending rigidity of the membrane is assumed. For the bending modulus employed in the presented models, configuration RBC900 is found to already have a stable biconcave shape, i.e. the critical configuration in terms of stability is somewhere between RBC900 and RBC960.

Even though resulting from a numerical defect, the behavior of the stomatocytic cells, i.e. the absence of a shape memory effect, agrees with experimental observations reported in [65]. In that experimental study, these non-biconcave cells accidentally evolved from initially healthy biconcave cells. This happened because of a wrong concentration of certain chemicals in the buffer solution the RBCs are suspended in. Although a thorough experimental study was not performed due to the relatively low number of these stomatocytes, go-and-stop-experiments indicate that those cells do not have a measurable shape memory. Consistent with the numerical results, no membrane rotation could be found for cup shaped cells.

Chapter 7

Conclusion and outlook

7.1 Conclusion

The goal of this thesis was to develop a comprehensive numerical model for the healthy human erythrocyte, also called red blood cell (RBC), which realistically accounts for the complex cell morphology. From a micromechanical point of view, the RBC is a liquid capsule enclosed by a two-layer biological membrane. None of the existing numerical models in literature accounted for all the key features that have been reported for the erythrocyte. In particular, a comprehensive model for the probably pre-stressed composite cell membrane was still missing. Thus, one main motivation for the development presented in this previous chapters was to identify the implication of such an incomplete model description and to relate it to the question, why some experimental observations could not be reproduced by numerical simulations so far.

In the developed model, the erythrocyte morphology was accounted for by a strongly coupled fluid-structure interaction (FSI) model, which included two fluid fields and one structure membrane. Since the erythrocyte membrane is composed of a lipid bilayer and a cytoskeleton network that show different mechanical characteristics, a two-layer membrane model was proposed accounting for both layers individually. Due to this construction, the model allows to easily access and modify single material parameters associated with a particular cell property. This flexibility provided by the model can prove beneficial for the investigation of altered cell mechanics caused by certain diseases and for possible extensions with regards to hemolysis prediction, as will be discussed in the following outlook.

The cytoskeleton, which provides shear elasticity to the membrane and shows a shear-hardening behavior, was modeled by a so-called Yeoh material, i.e. a third order compressible hyper-elastic constitutive relation. The mechanical description of the lipid bilayer was found to be more complex. First, to realize the relatively large bending resistance of this thin layer, an anisotropic material description was used, which assumed an additional stiffness in the surface normal direction. Second, the fluid-like character was accounted for by an incompressible viscoelastic constitutive

relation. Third, surface area preservation was controlled by a globally defined algebraic constraint.

The flow of both fluid fields, i.e. cytosol inside the membrane and blood plasma on the outside, was described with the arbitrary Lagrangean-Eulerian (ALE) version of the incompressible Navier-Stokes equations for Newtonian fluids. Since the cytosol is usually assumed to have a higher viscosity than the blood plasma, the material parameters were chosen individually for each field.

At the interface between fluid and structure fields, kinematic and dynamic boundary conditions were defined. Surface tractions acting on fluid and structure side of the interface, which have to match, could be identified with a Lagrange multiplier introduced to enforce the no-slip condition. This coupling condition prohibits both a mass flow across and a relative tangential movement at the interface.

The numerical model was created using the finite element method (FEM) to discretize the partial differential equation (PDE) resulting from the modeling process. For both, the incompressible fluid flow and the incompressible lipid bilayer membrane, stabilized, equal-order hybrid finite element (FE) formulations were employed. Of course, the particular stabilization techniques are tailored for the respective field description and discretization.

In order to avoid locking effects caused by the thinness of the elements in the lipid bilayer, the assumed natural strain (ANS) method was additionally introduced to obtain an incompressible solid shell FE formulation. The discretization of the cytoskeleton layer employed compressible solid shell finite elements, which are based on a combination of the ANS method and the enhanced assumed strain (EAS) approach.

The FE discretization of thin-walled structures with continuum-based elements brings about an ill-conditioning of the linear stiffness matrix, which limits the application of iterative linear solvers, in particular the usage of algebraic multigrid (AMG) preconditioners. The condition number of the stiffness matrix increases exponentially with increasing element aspect ratio. In this work, the reason for this ill-conditioning was investigated and a novel scaled thickness conditioning (STC) approach was presented to remedy the ill-conditioning problem. As a result, the example of a thin plate discretized with solid shell finite elements showed an almost constant conditioning of the problem for varying element aspect ratios.

Numerically, the interaction between membrane and the fluid fields was realized with a monolithic FSI scheme. The FSI coupling conditions were discretized using a dual mortar method, a numerical approach that is consistent with the FEM, the discretizations of the individual fields are based upon. In order to be able to eliminate the Lagrange multiplier degrees of freedom (DOFs) from the system by static condensation and to obtain the same block structure as in the conforming FSI case, dual shape functions were utilized for Lagrange multiplier field. Additionally, a repositioning algorithm for the fluid grid points at the interface was developed, which allows for the simulation of rotating structures embedded in a fluid domain.

To be able to investigate the influence of the pre-stressing state of the RBC membrane, different initial ellipsoidal stress-free shapes were considered. The biconcave shape found for the cell at rest numerically evolved by adjusting the ratio of enclosed volume and surface area. The stresses that emerged during the transition could be considered as residual stresses of the membrane.

The resulting FE-based model for the human RBC was validated based on laser trap experiments. The numerically obtained displacement over force diagrams for quasi-static deformations were found in excellent agreement with the experimental data taken from the literature. Furthermore, there was a close match between numerical and experimental data for the hysteresis behavior of the cell in fast moving laser traps. The deduced material parameters are within the literature range. Differences to other numerical studies have been discussed and have been attributed to deviating modeling assumptions for the membrane description and the boundary conditions.

Based on the deduced material parameters, the numerical model was able to accurately predict all experimentally observed motions of the human erythrocyte in steady shear flow. In contrast to other existing numerical models in literature, not only tumbling and tank-treading around an ellipsoidal cell could be recovered, but also the swinging motion for medium shear stresses was reproduced for the first time. The indispensable feature of the model to realize this tank-treading motion around a still biconcave cell was a stress-free reference shape different than the biconcave shape. Since all available models in literature assume a stress-free biconcave cell, none of them could predict the swinging motion of the cell. The simulations presented in this thesis covered only the first couple of seconds of the flow. Thus, a conclusive discussion on the ‘correct’ stress-free state of the human RBC was not yet possible.

The shape of the reference state and, in particular, its asymmetry were also found to control the oscillation of the inclination angle during the swinging motion. Tank-treading goes along with periodic bending energy fluctuations within the membrane. Increasing membrane energy leads to a cell rotation with the flow, relaxation to cell rotation against the flow, i.e. an oscillation of the inclination angle. Numerical results supported this interpretation and showed increased oscillation magnitudes with decreasing pre-stressing. Furthermore, the ratio of oscillation frequency to tank-treading frequency was found to be two, which is in agreement with the experimental measurements and the theoretical considerations stated above.

The shape memory effect of the erythrocyte is also caused by the particular form of the reference states. It came to light if the shear flow was stopped abruptly. Simulations showed that the asymmetry of all considered reference shapes was sufficient to induce a rotation of the membrane and, in order to counterbalance this motion, of the whole cell. In case of almost spherical stress-free reference states, the bending energies stored in the membrane did not suffice to stabilize the biconcave shape against the cup shape during the relaxation. Although still deviating from the equilibrium shape, the tank-treading stopped and the cell transformed into a stomatocytic cell. In case of more oblate reference shapes, however, the motion of the cell continued until the equilibrium

biconcave shape was reached, where the dimple of the cell was always formed by the same part of the membrane. The time needed for the relaxation process agreed very well with experimental measurements.

7.2 Outlook

Having developed a comprehensive and validated FE model for the human erythrocyte, its application to further experimental set-ups other than laser traps and shear flow is the logical next step. Furthermore, investigation of damaging scenarios and hemolysis prediction remain open tasks. Further simulations and possibly necessary modifications and extensions of the numerical model are discussed in the following.

The sliding ALE FSI approach cannot only be used for the investigation of shear flow, but also for the simulation of microfluidic devices. The projection based sliding of the fluid mesh on the channel walls is essential to avoid the distortion of the fluid grid due to large displacements. On the other hand, sliding may not be necessary on the erythrocyte membrane surface in this case. In terms of Algorithm 3.1 presented in section 3.7, the average translation $\bar{\Delta}\mathbf{t}_\Gamma^\mathcal{G}$ used to move the fluid interface relative to the wall is to be calculated with respect to the cell motion. The projection is to be performed onto the fixed channel wall. Due to the projection, the simulation is not restricted to flow through straight channels. This is demonstrated with a quasi-2D preliminary study of a vesicle flowing through a channel of oscillating width. The simulation is motivated by the experiments proposed by Braunmüller et al. [28]. The numerical results show that during the whole simulation the vesicle stays in the center of the fluid mesh, cf. Figure 7.1. The effect of the channel geometry on the deformation of the cell is depicted in Figure 7.2. The extension of this study to the 3D case should not pose any additional

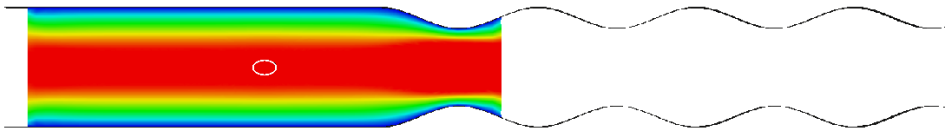

(a) initial position

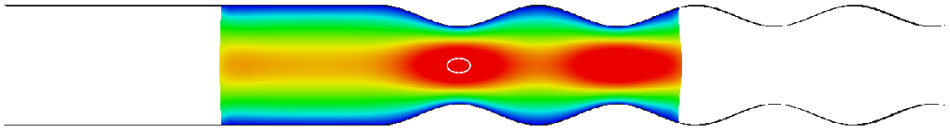

(b) cell has entered a constriction

Figure 7.1: *Sliding fluid domain for a vesicle in a channel of oscillating width*

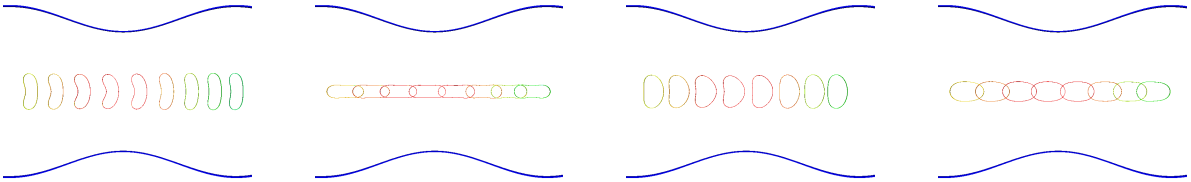

(a) slender vesicle vertically aligned *(b) slender vesicle horizontally aligned* *(c) bulky vesicle vertically aligned* *(d) bulky vesicle horizontally aligned*

Figure 7.2: *Shapes of vesicles flowing through a constriction of the channel in Figure 7.1. Shown is the deformed vesicle at different time steps*

(a) *(b)* *(c)* *(d)*

Figure 7.3: *Vesicle squeezing through narrow constriction*

numerical issues. It can serve to study migration behavior and deformation patterns of erythrocytes in capillaries.

Although the sliding ALE approach can deal with different channel geometries, a numerical study of the experiments with very narrow constrictions is beyond its capabilities. In order to simulate, for example, the experiments performed by Bow et al. [25], Braunmüller et al. [28], or Quinn et al. [167], contact between cell and rigid wall has to be numerically accounted for. If the fluid plasma is neglected, this is already possible due to the contact algorithm devised by Popp et al. [153, 154], as demonstrated in a preliminary 2D study of a vesicle squeezing through two trapezoidal pillars, cf. Figure 7.3.

For a comprehensive study, however, the influence of the fluid flow is of course not negligible. By definition, a deforming grid approach such as the presented ALE method is not suitable to describe the fluid between contacting structures, since it is incompatible with topology changes of the fluid domain. A remedy provides the recently developed fixed grid FSI approach, which has been proposed by Gerstenberger and Wall [78, 79] and is described in more detail in the thesis of Gerstenberger [80]. The employed fluid description is based on an *extended finite element method (XFEM)*. As shown by Mayer et al. [140], the approach can be combined with the contact algorithm mentioned above. However, at present, the XFEM based fluid-structure-contact interaction method is restricted to a partitioned coupling algorithm. To be applicable to balloon-type problems, such as the human RBC, it has to be extended to a monolithic formulation.

A robust and efficient method for fluid-structure-contact interaction would, furthermore,

allow for the simulations of a new class of problems: it would be perfectly suitable to investigate the behavior of multiple, possible contacting erythrocytes in fluid flow. For a realistic simulation including rouleaux formation and break-up, inter-cellular potentials, e.g. the formulations proposed by Neu and Meiselman [144] and Skalak et al. [177], have to be added to the model description. For example, the numerical models presented by Imai et al. [113] or Liu and Liu [134] combine a FSI simulation with simple inter-cellular potentials.

In addition to the simulation of new experimental set-ups, a fixed grid fluid approach could also improve the simulation results presented in this thesis. As chapter 6 shows, the sliding ALE formulation makes it possible to simulate increased rotations of an embedded structure in steady shear flow, but the methods fail to simulate long-time behavior of RBCs. Such a simulation would be important to conclusively discuss a realistic stress-free state of the cell. For some of the more oblate initial shapes, the relative membrane rotation has not exceeded the critical rotation of 90°. Nevertheless, it might be possible that after half a solid-like rotation a tank-treading motion would be adopted. Such a motion that alternates between tumbling and tank-treading has been reported by Viallat et al. [189]. In order to investigate this behavior, the method devised by Gerstenberger and Wall [78, 79] and also the related approach by Shahmiri et al. [174] seem to be very promising. The latter method combines an extended fixed-grid background fluid with a second fluid domain, which is possibly connected to a structure and can be formulated in an ALE framework.

So far, the discussed extensions and improvements of the model are motivated by further experimental set-ups. A change of the focus from purely mechanical questions to RBC damaging and hemolysis prediction would require further modifications and extensions of the numerical model. Some important aspects are discussed in the following paragraphs.

The atomic force microscope (AFM) experiments performed by a group in the biophysics department at the LMU showed a significant slower RBC relaxation if the cells were treated with a chemical called Latrunculin. The hypothesis explaining the altered relaxation behavior was that Latrunculin damages the connections between lipid bilayer and the cytoskeleton network. Since the proposed model accounts for the individual membrane constituents separately, it provides enough flexibility to test this hypothesis. A preliminary numerical study could show that a weakened connection between the layers increases both relaxation times. However, for a conclusive quantitative study, the simulations have to be further improved, in particular with respect to the boundary conditions applied to simulate the contact with the cantilever beam. Unfortunately, neither the strength of the adhesion nor the geometry of the contact surface are accessible in the experiments.

In contrast to damaging caused by diseases or certain chemicals, hemolysis occurs for healthy RBC due to external loading. As already mentiond in the introduction, the most promising approach to predict hemolysis numerically, at present, seems to be the tensor-based measure proposed by Arora et al. [3, 4]. It is defined by an empiric relation

between freed hemoglobin and the distortion of the cell, which is to be approximated based on fluid strain rate and vorticity. With the erythrocyte model at hand, it is possible to access strain state and distortion of the erythrocyte membrane in simple shear flow. A comparison of this results with the approximated values provided by a pure fluid simulation may serve as validation and calibration of the tensor-based measure and, thus, help to improve the hemolysis prediction.

The proposed erythrocyte model cannot only be used to validate the approximation for the cell distortion used in [3, 4], but it can be extended to simulate the relation between RBC deformation and hemoglobin leakage. For this purpose, the model should be combined with the multi-field scalar transport model recently proposed by Yoshihara et al. [202]. Within a FSI framework, the mass transport equations were formulated on the deformed fluid and solid domains. The transport from one field to the other was controlled by the interfacial permeability, attributed to the FSI interface. Considering the hemoglobin concentration as additional passive scalar field and employing a strain dependent permeability of the erythrocyte membrane would then allow to simulate the transport of hemoglobin through the erythrocyte membrane depending on the external loading.

Appendix A

Balance of angular momentum

As already stated in section 2.2.4, the angular momentum $\mathbf{A}(V(t)), \mathbf{x}_0)$ associated with a fixed spatial point $\mathbf{x}_0 \in \Omega_{\mathbf{x}}(t)$ and a balance volume $V(t) \in \Omega_{\mathbf{x}}(t)$ is defined as

$$\mathbf{A}(V(t)) = \int_{V(t)} \rho|_{\mathbf{x}}(\mathbf{x},t)\left((\mathbf{x}-\mathbf{x}_0)\times\mathbf{u}|_{\mathbf{x}}(\mathbf{x},t)\right)\,\mathrm{d}\mathbf{x}. \tag{A.1}$$

Its change over time can be calculated based on the transport theorem (2.36) and can subsequently be simplified using (2.44) to

$$\begin{aligned}\frac{\mathrm{d}\mathbf{A}(V(t))}{\mathrm{d}t} = \int_{V(t)} \rho|_{\mathbf{x}}(\mathbf{x},t)\,\Bigg(&\frac{\partial\left((\boldsymbol{\Phi}-\mathbf{x}_0)\times\mathbf{u}\right)|_{\boldsymbol{\chi}}}{\partial t}(\boldsymbol{\Phi}^{-1}(\mathbf{x},t),t) + \\ &+ \frac{\partial\left((\mathbf{x}-\mathbf{x}_0)\times\mathbf{u}|_{\mathbf{x}}\right)}{\partial\mathbf{x}}(\mathbf{x},t)\cdot\mathbf{c}|_{\mathbf{x}}(\mathbf{x},t)\Bigg)\,\mathrm{d}\mathbf{x}\end{aligned} \tag{A.2}$$

To further simplify the expression the partial time derivative is considered first. It can be rewritten as

$$\begin{aligned}\frac{\partial\left((\boldsymbol{\Phi}-\mathbf{x}_0)\times\mathbf{u}\right)|_{\boldsymbol{\chi}}}{\partial t} &= \left(\frac{\partial\boldsymbol{\Phi}|_{\boldsymbol{\chi}}}{\partial t}\times\mathbf{u}|_{\boldsymbol{\chi}}\right) + \left(\boldsymbol{\Phi}|_{\boldsymbol{\chi}}\times\frac{\partial\mathbf{u}|_{\boldsymbol{\chi}}}{\partial t}\right) \\ &= \left(\mathbf{u}^{\mathcal{G}}|_{\boldsymbol{\chi}}\times\mathbf{u}|_{\boldsymbol{\chi}}\right) + \left(\boldsymbol{\Phi}|_{\boldsymbol{\chi}}\times\frac{\partial\mathbf{u}|_{\boldsymbol{\chi}}}{\partial t}\right)\end{aligned} \tag{A.3}$$

using the product rule. Similarly, the spatial derivatives yield

$$\begin{aligned}\frac{\partial\left((\mathbf{x}-\mathbf{x}_0)\times\mathbf{u}\right)}{\partial\mathbf{x}}\cdot\mathbf{c} &= \left(\frac{\partial\mathbf{x}}{\partial\mathbf{x}_i}\times\mathbf{u}\right)\mathbf{c}_i + \left((\mathbf{x}-\mathbf{x}_0)\times\frac{\partial\mathbf{u}}{\partial\mathbf{x}_i}\right)\mathbf{c}_i \\ &= (\mathbf{e_i}\times\mathbf{u})\,\mathbf{c}_i + \left(\mathbf{x}\times\frac{\partial\mathbf{u}}{\partial\mathbf{x}_i}\right)\mathbf{c}_i = (\mathbf{c}_i\,\mathbf{e_i}\times\mathbf{u}) + \left((\mathbf{x}-\mathbf{x}_0)\times\frac{\partial\mathbf{u}}{\partial\mathbf{x}_i}\right)\mathbf{c}_i \\ &= (\mathbf{c}\times\mathbf{u}) + \left((\mathbf{x}-\mathbf{x}_0)\times\frac{\partial\mathbf{u}}{\partial\mathbf{x}_i}\right)\mathbf{c}_i \\ &= \left(-\mathbf{u}^{\mathcal{G}}\times\mathbf{u}\right) + \left((\mathbf{x}-\mathbf{x}_0)\times\frac{\partial\mathbf{u}}{\partial\mathbf{x}_i}\right)\mathbf{c}_i,\end{aligned} \tag{A.4}$$

where the observer $\cdot|_{\mathbf{x}}$ has been omitted for sake of brevity and the i-th Cartesian unit vector $\mathbf{e_i}$ has been introduced. Finally, the change of angular momentum can be reformulated to

$$\frac{\mathrm{d}\mathbf{A}(V(t))}{\mathrm{d}t} = \int_{V(t)} (\mathbf{x} - \mathbf{x}_0) \times \left(\rho|_{\mathbf{x}}(\mathbf{x},t) \left(\frac{\partial \mathbf{u}|_{\boldsymbol{\chi}}}{\partial t}(\boldsymbol{\Phi}^{-1}(\mathbf{x},t),t) + \frac{\partial \mathbf{u}|_{\mathbf{x}}}{\partial \mathbf{x}}(\mathbf{x},t) \cdot \mathbf{c}|_{\mathbf{x}}(\mathbf{x},t) \right) \right) \mathrm{d}\mathbf{x}. \tag{A.5}$$

The resultant moment acting due to the body force $\mathbf{b}$ and the traction $\mathbf{t}$ on the balance volume $V(t)$ and causing the change of angular momentum have been identified as

$$\frac{\mathrm{d}\mathbf{A}(V(t))}{\mathrm{d}t} = \int_{V(t)} (\mathbf{x} - \mathbf{x}_0) \times (\rho|_{\mathbf{x}} \mathbf{b}|_{\mathbf{x}})(\mathbf{x},t)\,\mathrm{d}\mathbf{x} + \int_{\partial V(t)} (\mathbf{x} - \mathbf{x}_0) \times \mathbf{t}|_{\mathbf{x}}(\mathbf{x},t,\mathbf{n}|_{\mathbf{x}})\,\mathrm{d}a. \tag{A.6}$$

Using the relation between the surface tension and the Cauchy stress given in (2.53) and Gauss' divergence theorem then leads to

$$\frac{\mathrm{d}\mathbf{A}(V(t))}{\mathrm{d}t} = \int_{V(t)} (\mathbf{x} - \mathbf{x}_0) \times (\rho|_{\mathbf{x}} \mathbf{b}|_{\mathbf{x}} + \mathrm{div}|_{\mathbf{x}}(\boldsymbol{\sigma}|_{\mathbf{x}}))(\mathbf{x},t) + \left(\boldsymbol{\sigma}|_{\mathbf{x}} - \boldsymbol{\sigma}^{\mathsf{T}}|_{\mathbf{x}}\right)(\mathbf{x},t)\,\mathrm{d}\mathbf{x}. \tag{A.7}$$

Comparing (A.5) and (A.7) and applying the ALE linear momentum conservation (2.56) show the symmetry of the Cauchy stress tensor

$$\boldsymbol{\sigma}|_{\mathbf{x}}(\mathbf{x},t) = \boldsymbol{\sigma}^{\mathsf{T}}|_{\mathbf{x}}(\mathbf{x},t) \tag{A.8}$$

since the equations hold for arbitrary balance volume $V(t)$.

Appendix B

Locking phenomena and remedies

In this chapter, some important locking phenomena associated with bending deformations of linear displacement-based thin structure finite elements are introduced and possible remedies are briefly discussed. The first section addresses the parasitic strains or stresses triggered in the element that cannot be compensated for by any other deformation mode of an element with linear shape functions.

The nature of the unwanted contributions, which lead to a too stiff element response, motivates the assumed natural strain (ANS) and enhanced assumed strain (EAS) methods, which are introduced in the subsequent sections B.2 and B.3.

B.1 Locking phenomena for thin walled structures

First, a bending deformation, i.e. a displacement $\mathbf{d} = [0, \beta\,\theta^2\theta^3, 0]^\mathsf{T}$, of an initially cuboid element with $\mathbf{X}^h = [\theta^1, \theta^2, h\theta^3]^\mathsf{T}$ is considered, cf. Figure 3.3. In Table B.1, the components of the resulting Green-Lagrange strain tensor $\mathbf{E}$ are given with respect to the material Cartesian frame. Beside a physically reasonable normal strain contribution E_{22}, also parasitic shear strains E_{23} emerge. In the small deformation limit, i.e. small values of β, the quadratic term can be neglected. Consequently, the parasitic component reduces

Table B.1: *Strain components E_{AB} with respect to the material Cartesion frame for a bending mode $(\mathbf{d} = [0, \beta\,\theta^2\theta^3, 0]^\mathsf{T})$ of a tri-linear hexahedral element with initial coordinates $\mathbf{X}^h = [\theta^1, \theta^2, h\theta^3]^\mathsf{T}$*

A	B	E_{AB}
1	1	0
2	2	$\frac{1}{2}\beta\,(2+\beta\theta^3)\,\theta^3$
3	3	$\beta^2/(2h^2)\,(\theta^2)^2$
1	2	0
2	3	$\beta/(2h)\,(1+\beta\theta^3)\,\theta^2$
3	1	0

Table B.2: *Parametric strain components* $\varepsilon_{\theta^i\theta^j}$ *for a bending mode* $(\mathbf{d} = [0, \beta\,\theta^2\theta^3, -\alpha\beta/h\,\theta^3]^\mathsf{T})$ *of a curved tri-linear hexahedral element with initial coordinates* $\mathbf{X}^h = [\theta^1, \theta^2 + \alpha\,\theta^2\theta^3, h\,\theta^3]^\mathsf{T}$

i	j	$\varepsilon_{\theta^i\theta^j}$
1	1	0
2	2	$\frac{1}{2}\beta\,(2 + (2\alpha + \beta)\theta^3)\,\theta^3$
3	3	$\alpha\beta\,(-1 + (\theta^2)^2) + \frac{1}{2}\beta^2\,(\alpha^2/h^2 + (\theta^2)^2)$
1	2	0
2	3	$\frac{1}{2}\beta\,(1 + (2\alpha + \beta)\theta^3)\,\theta^2$
3	1	0

to $E_{23} = \beta\theta^2/(2h)$. There is no other mode of the linear element that can counterbalance a shear strain E_{23} that is linear in θ^2, and the corresponding shear stress S_{23}. Thus, the element exhibits a too stiff behavior. This phenomenon is called *transverse shear locking*. The aspect ratio τ of the element, here $\tau = 1/h$, can be easily identified as the key parameter that controls this effect, since the parasitic strain component E_{23} scales linearly with the aspect ratio.

The second phenomenon discussed here is called *trapezoidal locking*. The name is motivated by trapezoidal shaped finite elements resulting from the discretization of curved structures with linear elements. Exemplarily, a thin element with material coordinates $\mathbf{X}^h = [\theta^1, \theta^2 + \alpha\,\theta^2\theta^3, h\theta^3]^\mathsf{T}$ is considered, i.e. the initial shape of the element resembles the deformed element depicted in Figure 3.3. A bending deformation is now characterized by displacements in tangential direction of the curved surface. In terms of the linear element, this is equivalent to displacements in normal direction with respect to the facets defined by $\theta^2 = \pm 1$. This displacement $\mathbf{d}$ can be expressed in terms of the parametric coordinates $\boldsymbol{\theta}$ as $\mathbf{d} = [0, \beta\,\theta^2\theta^3, -\alpha\beta/h\,\theta^3]^\mathsf{T}$.

Instead of considering the strains $\mathbf{E}$ within the material Cartesian frame, the parametric strain components $\varepsilon_{\theta^i\theta^j}$ are given in Table B.2. Naturally, the parasitic strains responsible for transverse shear locking can again be found. Additionally, an artificial normal strain component $\varepsilon_{\theta^3\theta^3}$ emerges, which reduces to $\alpha\beta\,(-1 + (\theta^2)^2)$ in the small deformation limit. Such a normal component as quadratic function in θ^2 cannot be compensated for by any other deformation mode of the linear element. The first key parameter is the curvature depending quantity α. Second, increasing the aspect ratio τ again additionally increases the locking effect, due to the transformation from parametric coordinates into the Cartesian material frame.

Both, transverse shear and trapezoidal locking are effects that can be related with the element geometry. By contrast, the third effect discussed here depends on the constitutive relation. The key parameter of the so-called *volumetric locking* is the dilatation modulus κ or, more general, the Poisson's ratio of the material under consideration. To characterize this locking effect, the response of an initially cuboid element to bending deformation is considered, cf. Figure 3.3 and Table B.1. For the small deformation limit

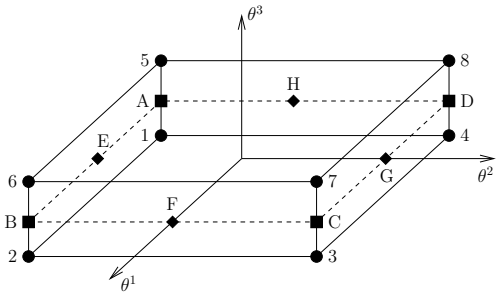

(a) Sketch of element with ANS sample points

ι	θ^1_ι	θ^2_ι	θ^3_ι
1	-1	-1	-1
2	1	-1	-1
3	1	1	-1
4	-1	1	-1
5	-1	-1	1
6	1	-1	1
7	1	1	1
8	-1	1	1

Λ	θ^1_Λ	θ^2_Λ	θ^3_Λ
A	-1	-1	0
B	1	-1	0
C	1	1	0
D	-1	1	0
E	0	-1	0
F	1	0	0
G	0	1	0
H	-1	0	0

(b) Parametric coordinates of nodes and ANS sample points

Figure B.1: *Hexahedral solid shell element with ANS sample points* $\mathsf{A}, \mathsf{B}, \mathsf{C}, \mathsf{D}$ *for normal strain and* $\mathsf{E}, \mathsf{F}, \mathsf{G}, \mathsf{H}$ *of shear strain*

the normal strain component E_{22} is linear both in the deformation β and in thickness direction θ^3. Since there is no normal strain component E_{33} in this limiting case, it is clear that bending always goes along with a local change in volume. Given a non-zero Poisson's ration, parasitic volumetric stresses are obtained that spoil the numerical results.

For an overview on further locking effects, the reader is referred to the theses of Koschnick [122] and Frenzel [72].

B.2 The Assumed Natural Strain approach

Transverse shear and trapezoidal locking can both be reduced by the so-called assumed natural strain (ANS) method. Instead of using the compatible strain values derived directly from the displacements, the critical strain components are interpolated based on particular sample points. This method was first developed in the context of shell and plate finite elements and was then extended to continuum based elements. Contributions to the development of this method have been made by Betsch et al. [15], Hughes and Liu [110], MacNeal [137], Simo and Hughes [175], Vu-Quoc and Tan [190, 191]. The particular ANS interpolation for the present solid shell element has first been proposed by Dvorkin and Bathe [51] (shear locking) and Betsch and Stein [14] (trapezoidal locking). The convention for the nodes and the sampling points are sketched in Figure B.1(a), together with their representation in local coordinates in Figure B.1(b).

Considering shear locking, the little survey in the previous subsection indicates that the parasitic shear stresses E_{23} vanish for $\theta^2 = 0$, cf. Table B.1. Naturally, transverse shear locking does not only occur for the depicted deformation, but also for a bending in the $\theta^1\theta^3$-plane, i.e. for a displacement $\mathbf{d} = [\beta\,\theta^1\theta^3, 0, 0]^\mathsf{T}$. This mode would result in

parasitic stresses E_{13} for $\theta^1 \neq 0$. The same is true for the parametric components $\varepsilon_{\theta^1\theta^2}$. Consequently, the ANS interpolation of the critical shear strain components is based on the sampling points E, F, G, H, i.e.

$$\varepsilon^{\text{ANS}}_{\theta^2\theta^3} = \tfrac{1}{2}\left(1-\theta^1\right)\varepsilon_{\theta^2\theta^3}(\boldsymbol{\theta}_H) + \tfrac{1}{2}\left(1+\theta^1\right)\varepsilon_{\theta^2\theta^3}(\boldsymbol{\theta}_F) \tag{B.1}$$

$$\varepsilon^{\text{ANS}}_{\theta^1\theta^3} = \tfrac{1}{2}\left(1-\theta^2\right)\varepsilon_{\theta^1\theta^3}(\boldsymbol{\theta}_E) + \tfrac{1}{2}\left(1+\theta^2\right)\varepsilon_{\theta^1\theta^3}(\boldsymbol{\theta}_G). \tag{B.2}$$

To find a new interpolation that does not suffer from trapezoidal locking effects, the normal strain component in thickness direction $\varepsilon_{\theta^3\theta^3}$ stated in Table B.2 is revisited. For an element that is curved and bent in the $\theta^2\theta^3$-plane, the parasitic component vanishes for $\theta^2 = \pm 1$. It is easy to see that a curvature and bending mode in the $\theta^1\theta^3$-plane would result also in parasitic strains $\varepsilon_{\theta^3\theta^3}$ except for $\theta^1 = \pm 1$. Thus, sampling points A, B, C, D on the edges are used. Constructing bilinear shape functions M_Λ as

$$M_\Lambda(\theta^1, \theta^2) = \tfrac{1}{4}(1+\theta^1_\Lambda\theta^1)(1+\theta^2_\Lambda\theta^2) \tag{B.3}$$

for $\Lambda \in \{A, B, C, D\}$, allows for the definition of an ANS interpolation of the critical strain component that reads

$$\varepsilon^{\text{ANS}}_{\theta^3\theta^3} = \sum_{\Lambda\in\{A,B,C,D\}} M_\Lambda(\theta^1, \theta^2)\varepsilon_{\theta^3\theta^3}(\boldsymbol{\theta}_\Lambda). \tag{B.4}$$

Replacing the respective standard components in the parametric strain tensor $\boldsymbol{\varepsilon}$ by $\varepsilon^{\text{ANS}}_{\theta^3\theta^3}$, $\varepsilon^{\text{ANS}}_{\theta^2\theta^3}$, and $\varepsilon^{\text{ANS}}_{\theta^1\theta^3}$, results in a modified tensor $\bar{\boldsymbol{\varepsilon}}$.

Finally, the modified Green-Lagrange strains $\bar{\mathbf{E}}$ can be defined by a co-ordinate transform of $\bar{\boldsymbol{\varepsilon}}$ into the material frame. Using the Voigt notation $\underline{\bar{\mathbf{E}}}$ as defined in (3.87), the complete ANS interpolation can be expressed as application of a modified operator $\underline{\bar{\mathbf{B}}}$:

$$\underline{\bar{\mathbf{E}}}(\boldsymbol{\theta}) = \underline{\bar{\mathbf{B}}}(\boldsymbol{\theta})\underline{\mathbf{d}}. \tag{B.5}$$

B.3 The Enhanced Assumed Strain approach

The enhanced assumed strain (EAS) method provides a remedy for some locking effects, in particular for the volumetric locking discussed in section B.1. This method enhances locally the element by strain components that are necessary for a locking free element, but that are not provided by the standard element formulation. For every element, a vectors of additional unknown EAS parameters $\underline{\boldsymbol{\alpha}}$ and of corresponding test functions $\delta\underline{\boldsymbol{\alpha}}$ are defined. The strain components to be enhanced define a matrix $\underline{\mathbf{M}}^\alpha$, such that the additional, locally enhanced strains $\tilde{\mathbf{E}}$ can be expressed as

$$\tilde{\mathbf{E}}(\boldsymbol{\theta}, t) = \underline{\mathbf{M}}^\alpha(\boldsymbol{\theta})\underline{\boldsymbol{\alpha}}(t) \tag{B.6}$$

$$\delta\tilde{\mathbf{E}}(\boldsymbol{\theta}) = \underline{\mathbf{M}}^\alpha(\boldsymbol{\theta})\delta\underline{\boldsymbol{\alpha}}. \tag{B.7}$$

For the solid shell element used for the discretization of the cytoskeleton, seven additional EAS parameter are utilized to improve the element behavior. The corresponding

matrix $\underline{\mathbf{M}}^{\alpha}$ reads

$$\underline{\mathbf{M}}^{\alpha} = \begin{bmatrix} \theta^1 & 0 & 0 & 0 & 0 & 0 & 0 \\ 0 & \theta^2 & 0 & 0 & 0 & 0 & 0 \\ 0 & 0 & \theta^3 & 0 & 0 & \theta^1\theta^2 & \theta^2\theta^3 \\ 0 & 0 & 0 & \theta^1 & \theta^2 & 0 & 0 \\ 0 & 0 & 0 & 0 & 0 & 0 & 0 \\ 0 & 0 & 0 & 0 & 0 & 0 & 0 \end{bmatrix} \tag{B.8}$$

With respect to the locking effects introduced above, the third and fourth row of $\underline{\mathbf{M}}^{\alpha}$ are of particular interest. A linear bending mode introduces normal strains only in the in-plane directions and, thus, leads to local volume changes. In order to compensate for the parasitic volumetric stresses, the normal strain component in θ^3-direction is enhanced, cf. third row of $\underline{\mathbf{M}}^{\alpha}$. Beside a linear polynom in θ^3, also two bilinear polynomials are introduced, in order to account for distorted element geometries. In-plane bending modes induce a parasitic shear component E_{12}. The effect is the same as the transverse shear locking, but is not accounted for by the ANS approach. Consequently, the shear strain is enhanced by a polynomial linear in θ^1 and θ^2.

A more detailed discussion on this particular EAS formulation can be found in the work of Vu-Quoc and Tan [190, 191] or the thesis of Frenzel [72]. In those references, the locking effects motivating the further enhancements found in (B.8) are also discussed.

Bibliography

[1] M. Abkarian, M. Faivre, and A. Viallat, Swinging of red blood cells under shear flow, *Physical Review Letters* **98**, 188302, 2007.

[2] D. Arora, *Computational Hemodynamics: Hemolysis and Viscoelasticity*, PhD thesis, Rice University, 2005.

[3] D. Arora, M. Behr, and M. Pasquali, A tensor-based measure for estimating blood damage, *Artificial Organs* **28**, 1002–1015, 2004.

[4] D. Arora, M. Behr, and M. Pasquali, Hemolysis estimation in a centrifugal blood pump using a tensor-based measure, *Artificial Organs* **30**, 539–547, 2006.

[5] F. P. Baaijens, Mixed finite element methods for viscoelastic flow analysis: a review, *Journal of Non-Newtonian Fluid Mechanics* **79**, 361–385, 1998.

[6] I. Babuška, The finite element method with Lagrangian multipliers, *Numerische Mathematik* **20**, 179–192, 1973-06-01.

[7] G. K. Batchelor, *An introduction to fluid dynamics*, Cambridge University Press, 2000.

[8] T. J. Batina, Unsteady euler algorithm with unstructured dynamic mesh for complex-aircraft aerodynamic analysis, *AIAA Journal* **29**, 7, 1991.

[9] M. Behr and D. Arora, Shear-slip mesh update method: Implementation and applications, *Computer Methods in Biomechanics and Biomedical Engineering* **6**, 113–123, 2003.

[10] M. Behr and T. E. Tezduyar, Shear-slip mesh update method, *Computer Methods In Applied Mechanics And Engineering* **174**, 261–274, 1999.

[11] M. Behr, D. Arora, O. M. Coronado, and M. Pasquali, Models and finite element techniques for blood flow simulation, *International Journal of Computational Fluid Dynamics* **20**, 175–181, 2006.

[12] M. Behr, *Stabilized Finite Element Methods for Incompressible Flows with Emphasis on Moving Boundaries and Interfaces*, PhD thesis, University of Minnesota, 1992.

[13] T. Belytschko, W. K. Liu, and B. Moran, *Nonlinear finite elements for continua and structures*, John Wiley & Sons, Inc, 2000.

[14] P. Betsch and E. Stein, An assumed strain approach avoiding artificial thickness straining for a nonlinear 4-node shell element, *Communications In Numerical Methods In Engineering* **11**, 899–909, 1995.

[15] P. Betsch, F. Gruttmann, and E. Stein, A 4-node finite shell element for the implementation of general hyperelastic 3d-elasticity at finite strains, *Computer Methods in Applied Mechanics and Engineering* **130**, 57–79, 1996.

[16] R. Bird, R. C. Armstrong, and O. Hassager, *Dynamics of Polymeric Liquids*, Volume 1: Fluid Mechanics, John Wiley & Sons Ltd, New York, 1987.

[17] M. Bischoff and E. Ramm, Shear deformable shell elements for large strains and rotations, *International Journal for Numerical Methods in Engineering* **40**, 4427–4449, 1997.

[18] M. Bischoff and E. Ramm, On the physical significance of higher order kinematic and static variables in a three-dimensional shell formulation, *International Journal Of Solids And Structures* **37**, 6933–6960, 2000.

[19] C. Bludszuweit, Model for a general mechanical blood damage prediction, *Artificial Organs* **19**, 583–589, 1995.

[20] D. Boal, Computer simulation of a model network for the erythrocyte cytoskeleton, *Biophysical Journal* **67**, 521–529, 1994.

[21] P. B. Bochev, C. R. Dohrmann, and M. D. Gunzburger, Stabilization of low-order mixed finite elements for the Stokes equations, *SIAM Journal on Numerical Analysis* **44**, 82–101, 2006.

[22] S. Boey, D. Boal, and D. Discher, Simulations of the erythrocyte cytoskeleton at large deformation. i. microscopic models, *Biophysical Journal* **75**, 1573–1583, 1998.

[23] P. B. Bornemann and W. A. Wall. An incompressible solid-shell element for finite deformations in statics. Technical report, Institute for Computational Mechanics, Technische Universität München, 2009. Internal report.

[24] T. Borsos, R. R. Dourmashkin, and J. H. Humphrey, Lesions in erythrocyte membranes caused by immune haemolysis, *Nature* **202**, 251–252, 1964.

[25] H. Bow, I. V. Pivkin, M. Diez-Silva, S. J. Goldfless, M. Dao, J. C. Niles, S. Suresh, and J. Han, A microfabricated deformability-based flow cytometer with application to malaria, *Lab on a Chip* **11**, 1065–1073, 2011.

[26] D. Braess, *Finite Elemente, Theorie, schnelle Löser und Anwendungen in der Elastizitätstheorie*, number XVI, Springer, 2003.

[27] H. Braess and P. Wriggers, Arbitrary Lagrangian Eulerian finite element analysis of free surface flow, *Computer Methods In Applied Mechanics and Engineering* **190**, 95–109, 2000.

[28] S. Braunmüller, L. Schmid, and T. Franke, Dynamics of red blood cells and vesicles in microchannels of oscillating width, *Journal of Physics: Condensed Matter* **23**, 184116–, 2011.

[29] F. Brezzi, On the existence, uniqueness and approximation of saddle-point problems arising from Lagrangian multipliers, *RAIRO - Analyse numérique* **8**, 129–151, 1974.

[30] F. Brezzi and M. Fortin, *Mixed and hybrid finite element methods*, Springer Series in Computational Mathematics, Springer, 2002.

[31] F. Brezzi and J. Douglas, Stabilized mixed methods for the Stokes problem, *Numerische Mathematik* **53**, 225–235, 1988.

[32] A. N. Brooks and T. J. Hughes, Streamline upwind/petrov-galerkin formulations for convection dominated flows with particular emphasis on the incompressible Navier-Stokes equations, *Computer Methods in Applied Mechanics and Engineering* **32**, 199–259, 1982.

[33] N. Büchter, E. Ramm, and D. Roehl, 3-dimensional extension of nonlinear shell formulation based on the enhanced assumed strain concept, *International Journal For Numerical Methods In Engineering* **37**, 2551–2568, 1994.

[34] P. Canham, The minimum energy of bending as a possible explanation of the biconcave shape of the human red blood cell, *Journal of Theoretical Biology* **26**, 61–81, 1970.

[35] C. Chee, H. Lee, and C. Lu, Using 3d fluid-structure interaction model to analyse the biomechanical properties of erythrocyte, *Physics Letters A* **372**, 1357–1362, 2008.

[36] S. Chien, K. Sung, R. Skalak, S. Usami, and A. Tozeren, Theoretical and experimental studies on viscoelastic properties of erythrocyte membrane, *Biophysical Journal* **24**, 463–487, 1978.

[37] S. Chien, Shear dependence of effective cell volume as a determinant of blood viscosity, *Science* **168**, 977–979, 1970.

[38] S. Chien, S. Usami, R. J. Dellenback, and M. I. Gregersen, Blood viscosity: Influence of erythrocyte deformation, *Science* **157**, 827–829, 1967.

[39] S. Chien, S. Usami, R. J. Dellenback, M. I. Gregersen, L. B. Nanninga, and M. M. Guest, Blood viscosity: Influence of erythrocyte aggregation, *Science* **157**, 829–831, 1967.

[40] J. Chung and G. M. Hulbert, A time integration algorithm for structural dynamics with improved numerical dissipation: The generalized-alpha method, *Journal of Applied Mechanics* **60**, 371–375, 1993.

[41] O. M. Coronado, D. Arora, M. Behr, and M. Pasquali, Four-field galerkin/least-squares formulation for viscoelastic fluids, *Journal of Non-Newtonian Fluid Mechanics* **140**, 132–144, 2006.

[42] O. M. Coronado, D. Arora, M. Behr, and M. Pasquali, A simple method for simulating general viscoelastic fluid flows with an alternate log-conformation formulation, *Journal of Non-Newtonian Fluid Mechanics* **147**, 189–199, 2007.

[43] H. A. Cranston, C. W. Boylan, G. L. Carroll, S. P. Sutera, J. R. Williamson, I. Y. Gluzman, and D. J. Krogstad, Plasmodium falciparum maturation abolishes physiologic red cell deformability, *Science* **223**, 400–403, 1984.

[44] M. Dao, J. Li, and S. Suresh, Molecularly based analysis of deformation of spectrin network and human erythrocyte, *Materials Science and Engineering: C* **26**, 1232–1244, 2006.

[45] C. Degand and C. Farhat, A three-dimensional torsional spring analogy method for unstructured dynamic meshes, *Computers & Structures* **80**, 305–316, 2002.

[46] D. E. Discher and N. Mohandas, Kinematics of red cell aspiration by fluorescence-imaged microdeformation, *Biophysical Journal* **71**, 1680–1694, 1996.

[47] D. E. Discher, N. Mohandas, and E. A. Evans, Molecular maps of red cell deformation: hidden elasticity and in situ connectivity, *Science* **266**, 1032–1035, 1994.

[48] D. E. Discher, D. H. Boal, and S. K. Boey, Simulations of the erythrocyte cytoskeleton at large deformation. ii. micropipette aspiration, *Biophysical Journal* **75**, 1584–1597, 1998.

[49] C. Dohrmann and P. Bochev, A stabilized finite element method for the Stokes problem based on polynomial pressure projections, *International Journal for Numerical Methods in Fluids* **46**, 183–201, 2004.

[50] J. Donea and A. Huerta, *Finite Element Methods for Flow Problems*, Wiley, New York, 2003.

[51] E. N. Dvorkin and K.-J. Bathe, A continuum mechanics based four-node shell element for general non-linear analysis, *Engineering Computations* **1**, 77–88, 1984.

[52] A. Ehrl, A. Popp, V. Gravemeier, and W. A. Wall, A mortar approach with dual Lagrange multipliers within a variational multiscale finite element method for incompressible flow, to be published in *Computer Methods in Applied Mechanics and Engineering*.

[53] E. A. Evans and Y.-C. Fung, Improved measurements of the erythrocyte geometry, *Microvascular Research* **4**, 335–347, 1972.

[54] E. A. Evans and R. M. Hochmuth, Membrane viscoelasticity, *Biophysical Journal* **16**, 1–11, 1976.

[55] E. A. Evans and R. Waugh, Osmotic correction to elastic area compressibility measurements on red cell membrane, *Biophysical Journal* **20**, 307–313, 1977.

[56] R. Fåhraeus and T. Lindqvist, he viscosity of the blood in narrow capillary tubes, *The American Journal of Physiology* **96**, 562–568, 1931.

[57] J. Fang and R. G. Owens, Numerical simulations of pulsatile blood flow using a new constitutive model, *Biorheology* **43**, 637–660, 2006.

[58] C. Farhat, C. Degand, B. Koobus, and M. Lesoinne, Torsional springs for two-dimensional dynamic unstructured fluid meshes, *Computer Methods in Applied Mechanics and Engineering* **163**, 231–245, 1998.

[59] D. A. Fedosov, *Multiscale modeling of blood flow and soft matter*, PhD thesis, Brown University, Providence, 2010.

[60] D. A. Fedosov, B. Caswell, and G. E. Karniadakis, Systematic coarse-graining of spectrin-level red blood cell models, *Computer Methods in Applied Mechanics and Engineering* **199**, 1937–1948, 2010.

[61] D. A. Fedosov, B. Caswell, and G. E. Karniadakis, A multiscale red blood cell model with accurate mechanics, rheology, and dynamics, *Biophysical Journal* **98**, 2215–2225, 2010.

[62] F. Feng and W. Klug, Finite element modeling of lipid bilayer membranes, *Journal of Computational Physics* **220**, 394–408, 2006.

[63] M. A. Fernández and M. Moubachir, A Newton method using exact jacobians for solving fluid-structure coupling, *Computers & Structures* **83**, 127–142, 2005.

[64] T. M. Fischer, Tank-tread frequency of the red cell membrane: Dependence on the viscosity of the suspending medium, *Biophysical Journal* **93**, 2553–2561, 2007.

[65] T. Fischer, Shape memory of human red blood cells, *Biophysical Journal* **86**, 3304–3313, 2004.

[66] T. Fischer, M. Stohr-Lissen, and H. Schmid-Schonbein, The red cell as a fluid droplet: tank tread-like motion of the human erythrocyte membrane in shear flow, *Science* **202**, 894–896, 1978.

[67] B. Flemisch and B. I. Wohlmuth, Stable Lagrange multipliers for quadrilateral meshes of curved interfaces in 3D, *Computer Methods in Applied Mechanics and Engineering* **196**, 1589–1602, 2007.

[68] C. Förster, W. A. Wall, and E. Ramm, On the geometric conservation law in transient flow calculations on deforming domains, *International Journal For Numerical Methods In Fluids* **50**, 1369–1379, 2006.

[69] C. Förster, *Robust methods for fluid–structure interaction with stabilised finite elements*, PhD thesis, Universität Stuttgart, 2007.

[70] L. P. Franca, T. J. R. Hughes, and R. Stenberg, Stabilized Finite Element Methods, *Incompressible Computational Fluid Dynamics – Trends and Advances*, M. D. Gunzberger and R. A. Nicolaides (eds.), Cambridge University Press, 1993.

[71] L. P. Franca and T. J. Hughes, Two classes of mixed finite element methods, *Computer Methods in Applied Mechanics and Engineering* **69**, 89–129, 1988.

[72] M. Frenzel, *Advanced Structural Finite Element Modeling for Patient-Specific Arterial Walls*, PhD thesis, Technische Universität München, 2009.

[73] P. Gaehtgens, C. Duhrssen, and K. Albrecht, Motion, deformation, and interaction of blood cells and plasma during flow through narrow capillary tubes, *Blood Cells* **6**, 799–817, 1980.

[74] P. Gamnitzer, *Residual-based variational multiscale methods for turbulent flows and fluid-structure interaction*, PhD thesis, Technische Universität München, 2010.

[75] M. W. Gee, *Effiziente Lösungsstrategien in der nichtlinearen Schalenmechanik*, PhD thesis, University of Stuttgart, 2004.

[76] M. W. Gee, E. Ramm, and W. A. Wall, Parallel multilevel solution of nonlinear shell structures, *Computer Methods In Applied Mechanics And Engineering* **194**, 2513–2533, 2005.

[77] M. W. Gee, U. Küttler, and W. A. Wall, Truly monolithic algebraic multigrid for fluid-structure interaction, *International Journal for Numerical Methods in Engineering* **85**, 987–1016, 2011.

[78] A. Gerstenberger and W. A. Wall, Enhancement of fixed-grid methods towards complex fluid-structure interaction applications, *International Journal for Numerical Methods in Fluids* **57**, 1227–1248, 2007.

[79] A. Gerstenberger and W. A. Wall, An extended finite element method / Lagrange multiplier based approach for fluid-structure interactions, *Computer Methods in Applied Mechanics and Engineering* **197**, 1699–1714, 2008.

[80] A. Gerstenberger, *An XFEM based fixed-grid approach to fluid-structure interaction*, PhD thesis, Technische Universität München, 2010.

[81] M. Gitterle, A. Popp, M. W. Gee, and W. A. Wall, Finite deformation frictional mortar contact using a semi-smooth Newton method with consistent linearization, *International Journal for Numerical Methods in Engineering* **84**, 543–571, 2010.

[82] R. Glowinski and P. Le Tallec, *Augmented Lagrangian and operator splitting methods in nonlinear mechanics*, SIAM, 1989.

[83] H. L. Goldsmith and J. Marlow, Flow behaviour of erythrocytes. i. rotation and deformation in dilute suspensions, *Proceedings of the Royal Society of London. Series B, Biological Sciences* **182**, 351–384, 1972.

[84] G. Gompper, Fluid vesicles with viscous membranes in shear flow, *Physical Review Letters* **93**, 258102, 2004.

[85] V. Gravemeier, *The variational multiscale method for laminar and turbulent incompressible flows*, PhD thesis, Universität Stuttgart, 2003.

[86] P. Gresho and R. Sani, *Incompressible flow and the finite element method advection-diffusion*, Volume 1, Wiley, 2000.

[87] P. Gresho and R. Sani, *Incompressible flow and the finite element method, isothermal laminar flow*, Volume 2, John Wiley & Sons, Inc, 2000.

[88] M. Grigioni, C. Daniele, G. D'Avenio, and V. Barbaro, A discussion on the threshold limit for hemolysis related to reynolds shear stress, *Journal of Biomechanics* **32**, 1107–1112, 1999.

[89] M. Grigioni, C. Daniele, U. Morbiducci, G. D'Avenio, G. D. Benedetto, and V. Barbaro, The power-law mathematical model for blood damage prediction: Analytical developments and physical inconsistencies, *Artificial Organs* **28**, 467–475, 2004.

[90] R. D. Groot and P. B. Warren, Dissipative particle dynamics: Bridging the gap between atomistic and mesoscopic simulation, *The Journal of Chemical Physics* **107**, 4423–4435, 1997.

[91] M. M. Guest, T. P. Bond, R. G. Cooper, and J. R. Derrick, Red blood cells: Change in shape in capillaries, *Science* **142**, 1319–1321, 1963.

[92] M. Gurtin, *An introduction to continuum mechanics (mathematics in science and engineering)*, Volume 158, Academic Press, 1981.

[93] E. Hairer and G. Wanner, *Solving ordinary differential equations II, stiff and differential-algebraic problems - series: Springer series in computational mathematics*, Volume 14, Springer, 2004.

[94] E. Hairer, S. Horsett, and G. Wanner, *Solving ordinary differential equations I, nonstiff problems - series: Springer series in computational mathematics*, Volume 8, Springer, 2000.

[95] P. Hansbo and A. Szepessy, A velocity-pressure streamline diffusion finite element method for the incompressible Navier-Stokes equations, *Computer Methods in Applied Mechanics and Engineering* **84**, 175–192, 1990.

[96] D. Hartmann, A multiscale model for red blood cell mechanics, *Biomechanics and Modeling in Mechanobiology* **9**, 1–17, 2010.

[97] S. Hartmann, S. Brunssen, E. Ramm, and B. Wohlmuth, Unilateral non-linear dynamic contact of thin-walled structures using a primal-dual active set strategy, *International Journal for Numerical Methods in Engineering* **70**, 883–912, 2007.

[98] M. Heil, An efficient solver for the fully coupled solution of large-displacement fluid-structure interaction problems, *Computer Methods in Applied Mechanics and Engineering* **193**, 1–23, 2004.

[99] V. Heinrich, K. Ritchie, N. Mohandas, and E. A. Evans, Elastic thickness compressibilty of the red cell membrane, *Biophysical Journal* **81**, 1452–1463, 2001.

[100] W. Helfrich, Elastic properties of lipid bilayers: theory and possible experiments, *Z. Naturforsch* **28c**, 693–703, 1973.

[101] W. Helfrich and H. J. Deuling, Some theoretical shapes of red blood cells, *Le Journal de Physique Colloques* **36**, C1–327–C1–329, 1975.

[102] S. Henon, G. Lenormand, A. Richert, and F. Gallet, A new determination of the shear modulus of the human erythrocyte membrane using optical tweezers, *Biophysical Journal* **76**, 1145–1151, 1999.

[103] M. A. Heroux, R. A. Bartlett, V. E. Howle, R. J. Hoekstra, J. J. Hu, T. G. Kolda, R. B. Lehoucq, K. R. Long, R. P. Pawlowski, E. T. Phipps, A. G. Salinger, H. K. Thornquist, R. S. Tuminaro, J. M. Willenbring, A. Williams, and K. S. Stanley, An overview of the trilinos project, *ACM Transactions on Mathematical Software* **31**, 397–423, 2005.

[104] R. Hochmuth, Measuring the mechanical properties of individual human blood cells, *Journal of Biomechanical Engineering* **115**, 515–519, 1993.

[105] R. Hochmuth, P. Worthy, and E. Evans, Red cell extensional recovery and the determination of membrane viscosity, *Biophysical Journal* **26**, 101–114, 1979.

[106] G. Holzapfel, *Nonlinear Solid Mechanics. A Continuum Approach for Engineering*, Wiley, Chichester, UK, 2000.

[107] G. Holzapfel and T. Gasser, A viscoelastic model for fiber-reinforced composites at finite strains: Continuum basis, computational aspects and applications, *Computer Methods in Applied Mechanics and Engineering* **190**, 4379–4403, 2001.

[108] P. J. Hoogerbrugge and J. M. V. A. Koelman, Simulating microscopic hydrodynamic phenomena with dissipative particle dynamics, *Europhysics Letters* **19**, 155, 1992.

[109] S. Hüeber and B. Wohlmuth, A primal-dual active set strategy for non-linear multibody contact problems, *Computer Methods in Applied Mechanics and Engineering* **194**, 3147–3166, 2005.

[110] T. J. R. Hughes and W. K. Liu, Nonlinear finite element analysis of shells: Part i. three-dimensional shells, *Computer Methods in Applied Mechanics and Engineering* **26**, 331–362, 1981.

[111] T. J. R. Hughes and G. Sangalli, Variational multiscale analysis: the fine-scale green's function, projection, optimization, localization, and stabilized methods, *SIAM J. Numerical Analysis* **45**, 539–557, 2007.

[112] T. J. R. Hughes, *The finite element method linear static and dynamic finite element analysis*, Dover Publications, 2000.

[113] Y. Imai, K. Nakaaki, H. Kondo, T. Ishikawa, C. Teck Lim, and T. Yamaguchi, Margination of red blood cells infected by plasmodium falciparum in a microvessel, *Journal of Biomechanics* **44**, 1553–1558, 2011.

[114] A. Iolov, A. S. Kane, Y. Bourgault, R. G. Owens, and A. Fortin, A finite element method for a microstructure-based model of blood, *International Journal for Numerical Methods in Biomedical Engineering*, n/a–n/a, 2011.

[115] M. V. Kameneva, P. F. Marad, J. M. Brugger, B. M. Repko, J. H. Wang, J. Moran, and H. S. Borovetz, In vitro evaluation of hemolysis and sublethal blood trauma in a novel subcutaneous vascular access system for hemodialysis, *Asaio Journal* **48**, 34–38, 2002.

[116] V. Kantsler and V. Steinberg, Transition to tumbling and two regimes of tumbling motion of a vesicle in shear flow, *Physical Review Letters* **96**, 036001–4, 2006.

[117] C. Katnik and R. Waugh, Alterations of the apparent area expansivity modulus of red blood cell membrane by electric fields, *Biophysical Journal* **57**, 877–882, 1990.

[118] K. Khairy, J. Foo, and J. Howard, Shapes of red blood cells: Comparison of 3d confocal images with the bilayer-couple model, *Cellular and Molecular Bioengineering* **1**, 173–181, 2008.

[119] T. Klöppel and W. A. Wall, A novel two-layer, coupled finite element approach for modeling the nonlinear elastic and viscoelastic behavior of human erythrocytes, *Biomechanics and Modeling in Mechanobiology* **10**, 445–459, 2011.

[120] T. Klöppel, M. W. Gee, and W. A. Wall, A scaled thickness conditioning for solid- and solid-shell discretizations of thin-walled structures, *Computer Methods in Applied Mechanics and Engineering* **200**, 1301–1310, 2011.

[121] T. Klöppel, A. Popp, U. Küttler, and W. A. Wall, Fluid-structure interaction for non-conforming interfaces based on a dual mortar formulation, *Computer Methods in Applied Mechanics and Engineering* **200**, 3111–3126, 2011.

[122] F. Koschnick, *Geometrische Lockingeffekte bei Finiten Elementen und ein allgemeines Konzept zu ihrer Vermeidung*, PhD thesis, Technische Universität München, 2004.

[123] U. Küttler, *Effiziente Lösungsverfahren für Fluid-Struktur-Interaktions-Probleme*, PhD thesis, Technische Universität München, 2009.

[124] U. Küttler, C. Förster, and W. A. Wall, A solution for the incompressibility dilemma in partitioned fluid-structure interaction with pure Dirichlet fluid domains, *Computational Mechanics* **38**, 417–429, 2006.

[125] O. A. Ladyzhenskaya, *The mathematical theory of viscous incompressible flow*, Gordon and Breach Science Publishers, 1969.

[126] Y. Lefebvre, E. Leclerc, D. Barthès-Biesel, J. Walter, and F. Edwards-Levy, Flow of artificial microcapsules in microfluidic channels: A method for determining the elastic properties of the membrane, *Phys. Fluids* **20**, 123102–10, 2008.

[127] A. Leuprecht and K. Perktold, Computer simulation of non-Newtonian effects on blood flow in large arteries, *Computer Methods in Biomechanics and Biomedical Engineering* **4**, 149–163, 2001.

[128] J. Li, M. Dao, C. T. Lim, and S. Suresh, Spectrin-level modeling of the cytoskeleton and optical tweezers stretching of the erythrocyte, *Biophysical Journal* **88**, 3707–3719, 2005.

[129] X. Z. Li, D. Barthès-Biesel, and A. Helmy, Large deformations and burst of a capsule freely suspended in an elongational flow, *Journal of Fluid Mechanics Digital Archive* **187**, 179–196, 2006.

[130] C. T. Lim, M. Dao, S. Suresh, C. H. Sow, and K. T. Chew, Large deformation of living cells using laser traps, *Acta Materialia* **52**, 1837–1845, 2004.

[131] C. T. Lim, M. Dao, S. Suresh, C. H. Sow, and K. T. Chew, Corrigendum to "large deformation of living cells using laser traps" [acta materialia 52 (2004) 1837-1845], *Acta Materialia* **52**, 4065–4066, 2004.

[132] G. H. W. Lim, M. Wortis, and R. Mukhopadhyay, Stomatocyte-discocyte-echinocyte sequence of the human red blood cell: Evidence for the bilayer-couple hypothesis from membrane mechanics, *Proceedings of the National Academy of Sciences of the United States of America* **99**, 16766–16769, 2002.

[133] A. Linke, Collision in a cross-shaped domain - a steady 2d Navier-Stokes example demonstrating the importance of mass conservation in cfd, *Computer Methods in Applied Mechanics and Engineering* **198**, 3278–3286, 2009.

[134] Y. Liu and W. K. Liu, Rheology of red blood cell aggregation by computer simulation, *Journal of Computational Physics* **220**, 139–154, 2006.

[135] P. C. Lu, H. C. Lai, and J. S. Liu, A reevaluation and discussion on the threshold limit for hemolysis in a turbulent shear flow, *Journal of Biomechanics* **34**, 1361–1364, 2001.

[136] D. Luenberger, *Linear and nonlinear programming*, Kluwer Academic Pub, 2003.

[137] R. H. MacNeal, Simple quadrilateral shell element, *Computers & Structures* **8**, 175–183, 1978.

[138] P. L. Maffettone and M. Minale, Equation of change for ellipsoidal drops in viscous flow, *Journal of Non-Newtonian Fluid Mechanics* **78**, 227–241, 1998.

[139] J. Marsden and T. J. R. Hughes, *Mathematical foundations of elasticity*, Dover, 1994.

[140] U. Mayer, A. Popp, A. Gerstenberger, and W. Wall, 3d fluid-structure-contact interaction based on a combined XFEM fsi and dual mortar contact approach, *Computational Mechanics* **46**, 53–67, 2010.

[141] B. L. McClain, I. J. Finkelstein, and M. D. Fayer, Vibrational echo experiments on red blood cells: Comparison of the dynamics of cytoplasmic and aqueous hemoglobin, *Chemical Physics Letters* **392**, 324–329, 2004.

[142] J. Mills, L. Qie, M. Dao, C. Lim, and S. Suresh, Nonlinear elastic and viscoelastic deformation of the human red blood cell with optical tweezers, *MCB: Molecular & Cellular Biomechanics* **1**, 169–180, 2004.

[143] N. Mohandas and P. G. Gallagher, Red cell membrane: past, present and future, *Blood* **112**, 3939–3947, 2008.

[144] B. Neu and H. J. Meiselman, Depletion-mediated red blood cell aggregation in polymer solutions, *Biophysical Journal* **83**, 2482–2490, 2002.

[145] H. Noguchi, Dynamic modes of red blood cells in oscillatory shear flow, *Physical Review E* **81**, 061920–, 2010.

[146] H. Noguchi and G. Gompper, Shape transitions of fluid vesicles and red blood cells in capillary flows, *Proceedings of the National Academy of Sciences of the United States of America* **102**, 14159–14164, 2005.

[147] H. Noguchi and G. Gompper, Swinging and tumbling of fluid vesicles in shear flow, *Physical Review Letters* **98**, 128103, 2007.

[148] R. G. Owens, A new microstructure-based constitutive model for human blood, *Journal of Non-Newtonian Fluid Mechanics* **140**, 57–70, 2006.

[149] H. Parisch, *Festkörper-Kontinuumsmechanik: Von den Grundgleichungen zur Lösung mit Finiten Elementen*, Teubner, 2003.

[150] R. Paul, J. Apel, S. Klaus, F. Schügner, P. Schwindke, and H. Reul, Shear stress related blood damage in laminar couette flow, *Artificial Organs* **27**, 517–529, 2003.

[151] Z. Peng, R. J. Asaro, and Q. Zhu, Multiscale simulation of erythrocyte membranes, *Physical Review E* **81**, 031904–, 2010.

[152] I. V. Pivkin and G. E. Karniadakis, Accurate coarse-grained modeling of red blood cells, *Physical Review Letters* **101**, 118105–4, 2008.

[153] A. Popp, M. W. Gee, and W. A. Wall, A finite deformation mortar contact formulation using a primal-dual active set strategy, *International Journal for Numerical Methods in Engineering* **79**, 1354–1391, 2009.

[154] A. Popp, M. Gitterle, M. W. Gee, and W. A. Wall, A dual mortar approach for 3D finite deformation contact with consistent linearization, *International Journal for Numerical Methods in Engineering* **83**, 1428–1465, 2010.

[155] C. Pozrikidis, The axisymmetric deformation of a red blood cell in uniaxial straining Stokes flow, *Journal of Fluid Mechanics* **216**, 231–254, 1990.

[156] C. Pozrikidis, Effect of membrane bending stiffness on the deformation of capsules in simple shear flow, *Journal of Fluid Mechanics* **440**, 269–291, 2001.

[157] C. Pozrikidis, Numerical simulation of the flow-induced deformation of red blood cells, *Annals of Biomedical Engineering* **31**, 1194–1205, 2003.

[158] C. Pozrikidis, Axisymmetric motion of a file of red blood cells through capillaries, *Physics of Fluids* **17**, 031503, 2005.

[159] A. R. Pries, K. Ley, M. Claassen, and P. Gaehtgens, Red cell distribution at microvascular bifurcations, *Microvascular Research* **38**, 81–101, 1989.

[160] A. R. Pries, T. W. Secomb, p. Gaehtgens, and F. J. Gross, Blood flow in microvascular networks : experiments and simulation, *Circulation Research* **67**, 9, 1990.

[161] A. R. Pries, T. W. Secomb, T. Gessner, M. B. Sperandio, J. F. Gross, and P. Gaehtgens, Resistance to blood-flow in microvessels in-vivo, *Circulation Research* **75**, 904–915, 1994.

[162] A. R. Pries, T. W. Secomb, and P. Gaehtgens, Biophysical aspects of blood flow in the microvasculature, *Cardiovascular Research* **32**, 654–667, 1996.

[163] M. A. Puso, A 3D mortar method for solid mechanics, *International Journal for Numerical Methods in Engineering* **59**, 315–336, 2004.

[164] M. A. Puso and T. A. Laursen, A mortar segment-to-segment contact method for large deformation solid mechanics, *Computer Methods in Applied Mechanics and Engineering* **193**, 601–629, 2004.

[165] M. A. Puso and T. A. Laursen, A mortar segment-to-segment frictional contact method for large deformations, *Computer Methods in Applied Mechanics and Engineering* **193**, 4891–4913, 2004.

[166] C. Queguiner and D. Barthès-Biesel, Axisymmetric motion of capsules through cylindrical channels, *Journal of Fluid Mechanics* **348**, 349–376, 1997.

[167] D. Quinn, I. Pivkin, S. Wong, K.-H. Chiam, M. Dao, G. Karniadakis, and S. Suresh, Combined simulation and experimental study of large deformation of red blood cells in microfluidic systems, *Annals of Biomedical Engineering* **39**, 1041–1050, 2011.

[168] F. Risso, F. Collé-Paillot, and M. Zagzoule, Experimental investigation of a bioartificial capsule flowing in a narrow tube, *Journal of Fluid Mechanics* **547**, 149–173, 2006.

[169] E. Rothe, Zweidimensionale parabolische randwertaufgaben als grenzfall eindimensionaler randwertaufgaben, *Mathematische Annalen* **102**, 650–670, 1930.

[170] H. Schmid-Schönbein and R. Wells, Fluid drop-like transition of erythrocytes under shear, *Science* **165**, 288–291, 1969.

[171] T. Secomb, Flow-dependent rheological properties of blood in capillaries, *Microvascular Research* **34**, 46–58, 1987.

[172] P. Seeman, Transient holes in the erythrocyte membrane during hypotonic hemolysis and stable holes in the membrane after lysis by saponin and lysolecithin, *Journal of Cell Biology* **32**, 55–70, 1967.

[173] V. Seshadri, R. M. Hochmuth, P. A. Croce, and S. P. Sutera, Capillary blood flow: Iii. deformable model cells compared to erythrocytes in vitro, *Microvascular Research* **2**, 434–442, 1970.

[174] S. Shahmiri, A. Gerstenberger, and W. A. Wall, An XFEM based embedding mesh technique for incompressible viscous flows, *International Journal for Numerical Methods in Fluids* **65**, 166–190, 2011.

[175] J. C. Simo and T. J. R. Hughes, On the variational foundations of assumed strain methods, *Jurnal of Applied Mechanics* **53**, 51–54, 1986.

[176] R. Skalak and P. I. Branemark, Deformation of red blood cells in capillaries, *Science* **164**, 717–719, 1969.

[177] R. Skalak, P. Zarda, K. Jan, and S. Chien, Mechanics of rouleau formation, *Biophysical Journal* **35**, 771–781, 1981.

[178] G. Strang and G. J. Fix, *An analysis of the finite element method*, Wellesley Cambridge Press, 2008.

[179] S. Suresh, J. Spatz, J. Mills, A. Micoulet, M. Dao, C. Lim, M. Beil, and T. Seufferlein, Connections between single-cell biomechanics and human disease states: gastrointestinal cancer and malaria, *Acta Biomaterialia* **1**, 15–30, 2005.

[180] S. Svetina and B. Zeks, Membrane bending energy and shape determination of phospholipid vesicles and red blood cells, *European Biophysics Journal* **17**, 101–111, 1989.

[181] X. Tan and L. Vu-Quoc, Efficient and accurate multilayer solid-shell element: non-linear materials at finite strain, *International Journal for Numerical Methods in Engineering* **63**, 2124–2170, 2005.

[182] T. Tezduyar, M. Behr, and J. Liou, A new strategy for finite element computations involving moving boundaries and interfaces - the deforming-spatial-domain/space-time procedure: I. the concept and the preliminary numerical tests, *Computer Methods in Applied Mechanics and Engineering* **94**, 339–351, 1992.

[183] T. Tezduyar, M. Behr, S. Mittal, and J. Liou, A new strategy for finite element computations involving moving boundaries and interfaces - the deforming-spatial-domain/space-time procedure: Ii. computation of free-surface flows, two-liquid flows, and flows with drifting cylinders, *Computer Methods in Applied Mechanics and Engineering* **94**, 353–371, 1992.

[184] T. Tezduyar, S. Mittal, S. Ray, and R. Shih, Incompressible flow computations with stabilized bilinear and linear equal-order-interpolation velocity-pressure elements, *Computer Methods in Applied Mechanics and Engineering* **95**, 221–242, 1992.

[185] G. Thurston, Viscoelasticity of human blood, *Biophysical Journal* **12**, 1205–1217, 1972.

[186] R. Tran-Son-Tay, S. Sutera, and P. Rao, Determination of red blood cell membrane viscosity from rheoscopic observations of tank-treading motion, *Biophysical Journal* **46**, 65–72, 1984.

[187] C. Truesdell and W. Noll, *The non-linear field theories of mechanics*, Springer, 2004.

[188] C. Truesdell and K. Rajagopal, *An introduction to the mechanics of fluids*, Modern Birkhäuser Classics, Springer, 2009.

[189] A. Viallat, M. Socol, and J. Dupire, Full dynamic of red blood cells in a shear flow: Rolling, tumbling, tanktreading, In *Book of Abstract: Euromech Colloquium 521, 29–31 August, ETH Zurich, Zurich, Switzerland*, 2011.

[190] L. Vu-Quoc and X. G. Tan, Optimal solid shells for non-linear analyses of multilayer composites. i. statics, *Computer Methods in Applied Mechanics and Engineering* **192**, 975–1016, 2003.

[191] L. Vu-Quoc and X. G. Tan, Optimal solid shells for non-linear analyses of multilayer composites. ii. dynamics, *Computer Methods in Applied Mechanics and Engineering* **192**, 1017–1059, 2003.

[192] W. A. Wall, *Fluid-Struktur-Interaktion mit stabilisierenden Finiten Elementen*, PhD thesis, Universität Stuttgart, 1999.

[193] W. A. Wall and M. W. Gee. BACI - a multiphysics simulation environment. Technical report, Technische Universität München, 2010.

[194] J. Walter, A.-V. Salsac, D. Barthès-Biesel, and P. Le Tallec, Coupling of finite element and boundary integral methods for a capsule in a Stokes flow, *International Journal for Numerical Methods in Engineering* **83**, 829–850, 2010.

[195] R. Waugh and E. Evans, Thermoelasticity of red blood cell membrane, *Biophysical Journal* **26**, 115–131, 1979.

[196] B. I. Wohlmuth, A mortar finite element method using dual spaces for the Lagrange multiplier, *SIAM J. Numer. Anal* **38**, 989–1012, 2000.

[197] B. I. Wohlmuth, *Discretization methods and iterative solvers based on domain decomposition*, Springer-Verlag Berlin Heidelberg, 2001.

[198] P. Wriggers, *Nonlinear Finite Element Method*, Springer, 2008.

[199] K. K. Yeleswarapu, *Evaluation of Continuum Models for Characterizing the Constitutive Behavior of Blood*, PhD thesis, University of Pittsburgh, 1996.

[200] O. Yeoh, Characterization of elastic properties of carbon-black-filled rubber vulcanizates, *Rubber chemistry and technology* **63**, 792–805, 1990.

[201] Y.-Z. Yoon, J. Kotar, G. Yoon, and P. Cicuta, The nonlinear mechanical response of the red blood cell, *Physical Biology* **5**, 036007, 2008.

[202] L. Yoshihara, A. Comerford, G. Bauer, T. Klöppel, and W. A. Wall, A combined fluid-structure interaction and multi-field scalar transport model for simulating mass transport in biomechanics, *to be submitted*, 2012.

[203] Q. Zhu, C. Vera, R. J. Asaro, P. Sche, and L. A. Sung, A hybrid model for erythrocyte membrane: A single unit of protein network coupled with lipid bilayer, *Biophysical Journal* **93**, 386–400, 2007.

[204] R. Zienkiewicz and R. Taylor, *The finite element method, Vol. 1 - the basis*, Butterworth-Heinemann, 2000.

[205] R. Zienkiewicz and R. Taylor, *The finite element method, Vol. 2 - solid mechanics*, Butterworth-Heinemann, 2000.